SCUOLA
NORMALE
SUPERIORE

2D VERTICAL HETEROSTRUCTURES:

GROWTH, PROPERTIES AND APPLICATIONS

ANTONIO ROSSI

Advisor

Dr. Camilla Coletti

Supervisor

Prof. Giuseppe Carlo La Rocca

FOREWORD

This thesis is the result of my research activity at NEST laboratory of Scuola Normale Superiore in Pisa: I started my studies on two dimensional materials and their vertical heterostructure at the end of 2014. My interest in nanotechnologies applied to novel materials has matched with the research activity of the group I joined. This work was performed within a joint PhD program sponsored by Scuola Normale Superiore and Istituto Italiano di Tecnologia.

LIST OF ABBREVIATION

2d	Two dimension
2DEG	Two Dimension Electron Gas
AFM	Atomic Force Microscopy
ALD	Atomic Layer Deposition
ARPES	Angle Resolved Photoemission Spectroscopy
BZ	Brillouin Zone
CB	Conduction Band
CES_s	Constant Energy Surface
CLPES	Core Level Photoelectron Spectroscopy
CVD	Chemical Vapor Deposition
DFT	Density Functional Theory
DOS	Density of State
DS	Doniach Sunjic
EBL	Electron Beam Lithography
E_c	Conduction Band Minimum
EDC_s	Energy Distribution Curves
EDX	Energy Dispersive X-ray Spectroscopy
E_f	Fermi Energy
EG	Epitaxial Graphene
E_v	Valence Band Maximum
FFT	Fast Fourier Transform
FOV	Field of View
FS	Fermi Surface

FWHM	Full Width Half Maximum
h-BN	Hexagonal Boron Nitride
HPSI	High Purity Semi-insulating
HSQ	Hydrogen Silsesquioxane
IMFP	Inelastic Mean Free Path
LDOS	Local Density Off States
LEED	Low Energy Electron Diffraction
LEEM	Low Energy Electron Microscopy
LJ	Lennard Jones
LPE	Liquid Phase Exfoliation
MBE	Molecular Beam Epitaxy
MEM	Mirror Mode
MLG	Monolayer graphene
MOCVD	Metal Organic Chemical Vapor Deposition
MPI	Max Plank Institute
NEC	Negative Electron Compressibility
NEMS	Nanoelectromechanical System
PDMS	Polydimethylsiloxane
PES	Photoelectron Spectroscopy
PL	Photoluminescence
PPC	Persistent Photocurrent
QFMLG	Quasi-Free Standing Monolayer Graphene
RT	Room Temperature
SPELEEM	Spectroscopic Photoemission and Low Energy Electron Microscope

SPM	Scanning Probe Microscopy
STM	Scanning Tunneling Microscopy
STV	Starting Voltage
TFET	Tunneling Field Effect Transistor
TMD_s	Transition Metal Dichalcogenides
tr-ARPES	Time resolved ARPES
UHV	Ultrahigh Vacuum
UPS	UV Photoelectron Spectroscopy
UV	Ultraviolet
VB	Valence Band
vdW	Van der Waals
vdWE	Van der Waals Epitaxy
vdWH	Van der Waals Heterostructures
XPEEM-	X-Ray Photoemission Electron Microscopy
XPS	X-Ray Photoemission Spectroscopy
μ-XPS	Micro XPS
PDOS	Projected Density of States

CONTENTS

INTRODUCTION

Since its discovery, graphene has gathered increasing interest thanks to its outstanding properties such as astonishing carrier mobilities (up to 3,000,000 $cm^2/V\ s$)[1] and a thermal conductivity substantially higher than diamond (up to 5000 W/m K)[2]. In addition, it is practically transparent (it absorbs 2.3% of white light)[3], it possesses an amazing impermeability to most gases and liquids[4], unprecedented flexibility, mechanical strength and Young modulus[5]. What is truly outstanding is that these enticing properties are displayed by a real two-dimensional (2d) system, i.e., a honeycomb lattice of carbon atoms extending on a plane. Graphene is the first atomic-thick material to have been experimentally demonstrated and studied, but is not the only character in the world of 2d materials, which has been recently named *Flatland*[6]. Traditional layered materials such as transition metal dichalcogenides, hexagonal boron nitride, and black phosphorus can be isolated in their monolayer form, showing a number of interesting properties such as high spin-orbit coupling[7], direct band gap[8], charge density waves[9], superconductivity[10], and topological phases[11]. This plethora of 2d materials can be further expanded by arranging them together in vertical heterostructures. This allows for devising and implementing a new class of materials with potentially countless applications. Heterostructures are at the key of modern electronics. They have been at the center of semiconductors research for more than 50 years. Having materials with different properties combined together allows creating functional devices with non-trivial properties. The most common are covalent heterostructures, with chemical bonds between different layers[12]. However, combining materials with different lattice parameters creates defects, dislocations and even lattice breaking at the interface, which can alter the crystal structure in a detrimental way

for the electronic properties of the system. Despite covalent heterostructures have allowed for reaching performances such as $35x10^6$ cm^2/Vs of carrier mobility[13], the need to create chemical bonds limits the selection of materials, not always cheap or available on the large scale. Indeed, this new class of 2d heterostructures, namely van der Waals (vdW) heterostructures[14], offers a solution to this problem. By vertically staking monolayer vdW materials such as graphene, transition metal dichalcogenides (TMDs) and hexagonal boron nitride (h-BN), constrains on the matching of the lattice parameters are released by the lack of covalent bonds between the layers. Hence, one can potentially combine any kind of layered material to form the desired heterostructure and engineer the properties of the new material. However, research on this field is still at the beginning, and many steps forward need to be made before novel electronic and optoelectronic devices with real-world potential can be demonstrated. A first compelling issue that needs to be solved is that of the scalable synthesis of 2d materials and vdW heterostacks more in general. In fact, to date, most of the 2d heterostructures studied have been realized by mechanically exfoliating bulk materials[15,16]. Mechanical exfoliation is a technique that is effective in obtaining highly crystalline 2d materials but is cumbersome, and lacking in scalability. Second, specific vdW heterostacks with enticing prospects in (opto)electronics need to be fully studied. Indeed, the lack of scalable materials is a hurdle towards a thorough characterization with conventional surface science techniques. Finally, scalable (opto)electronic devices need to be devised and demonstrated.

OBJECTIVE AND RESULTS OF THE THESIS

The overarching goal of this work is: (i) to demonstrate the scalable synthesis of highly crystalline 2d heterostacks appealing for

optoelectronic applications; (ii) to investigate their fundamental properties; (iii) to demonstrate novel high-performance scalable optoelectronic devices.

The 2d heterostacks that are investigated in this thesis are those obtained by vertically stacking the TMD tungsten disulfide (WS_2) with graphene or h-BN. WS_2 has been selected as the TMD of choice as it displays a number of extremely appealing properties for optoelectronics. It exhibits large carrier mobility[17], high photoluminesce emission[18], significantly large spin-orbit splitting[19] and long exciton life and coherence times[20]. 2d exfoliated heterostructures obtained by vertically stacking graphene (or h-BN) and WS_2 have demonstrated high carrier mobility, remarkable light responsivity and significant spin-orbit coupling[21–23]. Hence, in first place, this thesis reports on the scalable synthesis of WS_2 on graphene and WS_2 on h-BN, by using chemical vapor deposition (CVD). To date, CVD has been accepted as the most suitable technique for the growth of highly-crystalline 2D materials over large areas[24,25]. CVD of TMDs from solid precursors has been demonstrated by a number of works on bulk substrates such as silicon oxide (SiO_2) and sapphire[24,26], but reports on the synthesis of large areas TMDs on 2d materials were lacking at the time when this work started. A large part of this thesis is devoted to the study of CVD WS_2 on epitaxial graphene (EG) grown via thermal decomposition on silicon carbide (SiC), an ideal system for carrying on fundamental studies and proof-of-principle devices.

The electronic structure of the WS_2/EG heterostructure has been investigated via angle resolved photoemission spectroscopy (ARPES) measurements performed at the Elettra synchrotron facility in Trieste (Italy) and at the Max-Planck-Institut für Festkörperforschung in Stuttgart (Germany). These measurements have yielded the first band structure

visualization of the system[27]. Chemical analysis of the synthetized heterostack has been carried on via X-ray photoemission spectroscopy (XPS) and X-ray photoemission electron microscopy (XPEEM) at the same facilities. Structural and electronic characterization of the system have been also carried out via low energy electron diffraction (LEED), low energy electron microscopy (LEEM), and scanning tunnel microscopy (STM), respectively.

STM studies have allowed for studying the nanotribological properties of the WS_2/graphene heterostack and resolving at atomic level the surface of WS_2 in order to identify the nature and the distribution of the surface defects. Notably, in the course of this study, a phenomenon which has not been reported until now for vdW heterostacks containing a TMD has been observed: superlubricity.

By adopting the WS_2/EG heterostructure, photodetectors capable of collecting light in the visible range have been fabricated. To this end, a synthetic method has been developed to obtain the patterned growth of WS_2 on EG, which paves the way for obtaining WS_2/graphene optoelectronic devices in a scalable manner. The devices demonstrated display remarkable responsivities and response times.

Finally, this work reports on the optical properties of bilayer WS_2 on: (i) EG; (ii) graphene grown via CVD on copper (Cu) foil; (iii) h-BN. As a direct consequence of giant spin-orbit coupling and spin-valley locking, bilayer WS_2 presents an astonishing preservation of polarization at room temperature (RT)[28], *i.e.* when a polarized light is shined on the material, its photoluminescence (PL) emission preserves the polarization of the impinging light. This implies that the carriers are promoted in two non equivalent valleys. Due to spin-valley locking this means that excited

photocarriers are also spin-polarized. Our findings indicate that such robust preservation of polarization exists for CVD WS_2 synthesized on h-BN and on buffer layer graphene on SiC[29]. These findings open the route for the realization of novel all-2d opto-spintronic devices.

THESIS OUTLINE

Chapter 1 discusses the fundamental properties of the 2d materials adopted in this work. The main electronic and structural features of graphene, h-BN and WS_2 are reported. Also, an overview of the principal synthetic techniques currently adopted for these materials is given. Finally, a discussion on the general properties, synthetic methods and possible applications of vertical vdW heterostacks (vdWH) is reported.

Chapter 2 gives a presentation of the experimental techniques used in this work to study the properties of 2d materials. As the techniques used are a considerable number, only the most relevant to this work are thoroughly discussed while the others are treated in more general terms.

Chapter 3 focuses on the synthetic techniques used to obtain graphene and WS_2 and reports the first experimental results of this work in this direction. Thermal decomposition of SiC and growth of graphene on Cu foil are discussed and the experimental approaches adopted in this work to obtain graphene of high crystallinity are presented. In this case, my contribution was limited to performing or assisting a well-defined protocol which has been developed in my group for obtaining graphene on SiC and Cu, respectively. Subsequently, WS_2 growth from solid precursors is presented. The experimental approach adopted to grow WS_2 on a wide number of substrates was entirely developed by myself during the past years. The approach chosen is discussed in parallel with the modeling of the reaction mechanisms that lead to the formation of 2d

crystals. Notably, the part relative to the growth of WS_2 on 2d substrates is a pioneering part of my work and will be further elaborated in the following chapters.

Chapter 4 reports an electronic and micro-structural study of monolayer WS_2 grown on EG on SiC. To this end, surface science techniques such as ARPES, XPS, LEED, LEEM and XPEEM are adopted. Notably, LEED measurements assign the zero-degree orientation as the preferential azimuthal alignment for WS_2/EG. The valence-band (VB) structure emerging from this alignment is presented and discussed in detail. Remarkably, we find that the spin–orbit splitting of monolayer WS_2 on EG is larger than what reported to date for other substrates[27]. We present the density functional theory (DFT) calculations performed which confirm the experimental band structure to an excellent degree. Finally, we discuss the XPEEM measurements performed on single WS_2 crystals, which confirm the van der Waals nature of the interface coupling between the EG and the WS_2 layer. The results reported in this chapter indicate that this system is promising for applications in the realm of opto-electronics, an aspect that will be deepened further on in this thesis.

Chapter 5 reports a study of the nanotribological properties of monolayer WS_2 on EG on SiC performed with scanning probe techniques. Our experimental findings show that WS_2 flakes are prone to slid over graphene surfaces when scanned over with a STM tip. Atomistic force field based molecular dynamics simulations indicate that the vdW interaction between the scanning tip and WS_2 is enough to overcome the energy activation barrier and to trigger a sliding of the flake that is superlubric. Atomically resolved investigations show that the interface is atomically sharp and that the WS_2 lattice is strain-free. These results help to shed light on nanotribological phenomena in van der Waals heterostacks and

suggest that the applicative potential of the graphene/WS_2 interface can be extended by novel mechanical prospects.

Chapter 6 is centered on the implementation of WS_2/EG-based high-performing photodetectors. An original approach for the fabrication of efficient optoelectronic devices from scalable 2d vertical heterostructures is presented. This approach allows for the patterned growth of WS_2 on graphene and facilitates the realization of ohmic contacts. Indeed, graphene areas are left uncovered and ready for contact deposition. Photodetectors fabricated with WS_2 on EG on SiC present, when illuminated with red light, a maximum responsivity R ~ 220 A/W, a detectivity of $D^* \sim 1.6 \times 10^{10}$ $Jones$ and a -3dB bandwidth of 250 Hz. The retrieved detectivity is 3 orders of magnitude higher than that obtained with graphene-only devices at the same wavelength. For shorter illumination wavelengths, a persistent photocurrent is observed, with a nearly complete charge retention, which originates from deep trap levels in the SiC substrate. This work ultimately demonstrates that WS_2/graphene optoelectronic devices with promising performances can be obtained in a scalable manner.

Chapter 7 reports on the optical properties of continuous bilayer WS_2 film on h-BN, CVD graphene and EG. Spectroscopic and microscopic analysis are implemented to address the quality of the material. The sample is shone with polarized light and photoluminescence measurements show a remarkable conservation of polarization of the emitted light with respect to the incident one at room temperature, peaking 74% for the entire WS_2 film. Furthermore, we present a scalable bottom-up approach for the design of photoconductive and photoemitting patterns. These findings indicate that bilayer WS_2 synthetized on graphene and h-BN is an ideal

platform for light-matter transduction and hence an enticing material for the fabrication of novel valley-spintronic devices.

Finally, in **Summary and perspective** the major scientific findings of this work are summarized and a series of perspectives for additional research in the field are proposed.

1 INTRODUCTION TO GRAPHENE, OTHER 2D MATERIALS, AND THEIR VERTICAL HETEROSTRUCTURES

In this chapter the main structural, chemical and electronic properties of graphene, h-BN and WS_2 (as representative of TMDs) will be discussed. The state-of-the-art synthetic methods for each material will be reported. In the end, a description of the materials arranged to form vertical heterostructures will be addressed in order to introduce the core of this thesis.

1.1 GRAPHENE, A CARBON HONEYCOMB LATTICE

Graphene, a single layer of carbon (C) atoms disposed in a hexagonal lattice, can be considered the base-structure for materials with other dimensionalities belonging to the family of carbon allotropes Fig. 1.1[30]:

- 0d Fullerene (C60): graphene wrapping on itself in a spherical form
- 1d Carbon nanotubes: graphene rolled to form a tube
- 3d Graphite: multiple graphene layers stacked on top of each other

The first theoretical study on graphene was published in 1947[31]. Nevertheless, this 2d carbon honeycomb was considered, until very recently, just a "model system". It was believed that, as proposed by Landau and Peierls, atomic-thick materials could not be stable for thermodynamic reasons[32,33]. The calculations reported in these works suggested that the thermal fluctuations in low-dimensional crystals would make such structures unstable, being the atomic displacement comparable with interatomic distances.

However, all of this was reconsidered in 2004, when Andre Geim and Konstantin Novoselov managed to isolate and investigate graphene[34]. Its

unconventional electronic, optical and mechanical properties, which will be discussed in detail in the following paragraph, strongly influenced both fundamental research and technology. In 2010, "*for groundbreaking experiments regarding the two-dimensional material graphene*" Geim and Novoselov were awarded the the Nobel Prize in Physics[35].

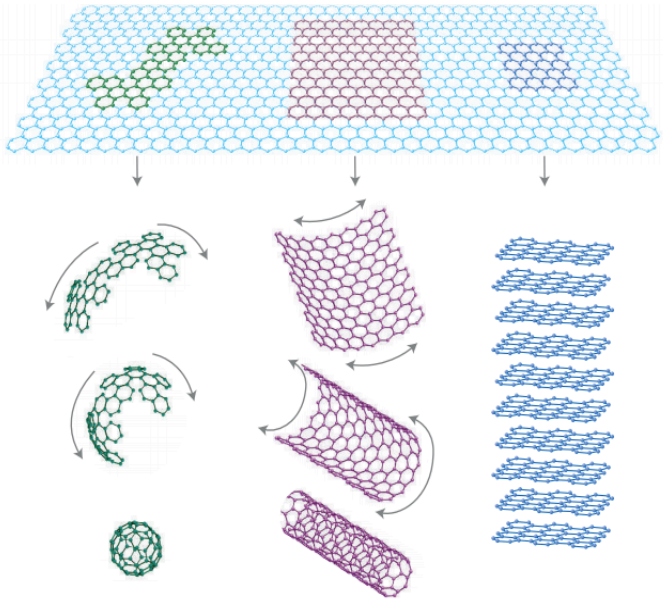

Fig. 1.1 Graphene depicted as the building block in the family of carbon allotropes. It can be wrapped up into 0D buckyballs, rolled into 1d nanotubes or stacked into 3d graphite. Adapted from [30]

1.2 GRAPHENE PROPERTIES AND SYNTHESIS

1.2.1 STRUCTURE

Graphene is constituted by carbon atoms disposed in a honeycomb lattice and each carbon atom has four valence electrons. Three of them form in-plane σ bond, whereas the last one fills the p_z orbital and it gives rise to the π bond, which is orthogonal to the crystal plane.

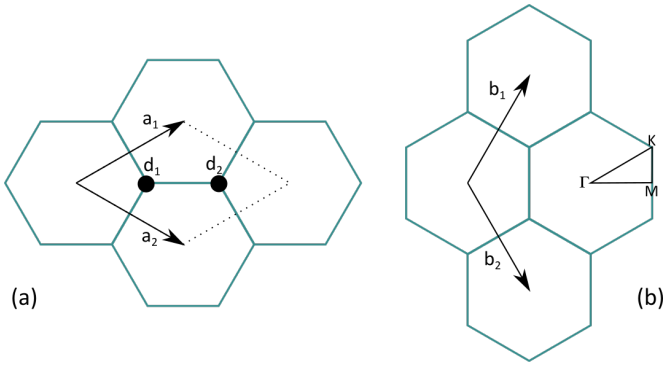

Fig. 1.2 (a) Graphene lattice structure, with the d_1 and d_2 base atoms and a_1 a_2 base vectors. (b) Representation of graphene lattice in reciprocal space, with Γ–M–K–Γ the irreducible area of BZ.

The graphene lattice is spanned by the vectors:

$$\mathbf{a_1} = \frac{a}{2}(\sqrt{3}, 1) \quad \mathbf{a_2} = \frac{a}{2}(\sqrt{3}, -1) \qquad (1)$$

Where $a = 2.461$ Å is the lattice parameter. The base atoms are placed in position:

$$\mathbf{d_1} = (0,0) \qquad \mathbf{d_2} = (0, c) \qquad (2)$$

Where $c = 1.42$ Å is the C=C bond length. The reciprocal lattice in k-space is represented by the reciprocal vectors:

$$\mathbf{b_1} = \frac{2\pi}{a}\left(\frac{1}{\sqrt{3}}, 1\right) \quad \mathbf{b_2} = \frac{2\pi}{a}\left(\frac{1}{\sqrt{3}}, -1\right) \qquad (3)$$

The two different atoms in the base form two distinct sublattices. The structure in real and reciprocal space is depicted in Fig. 1.2(a) and (b) respectively. The unit cell is defined by the dashed lines in panel (a). The electronic properties of graphene can be fully described by the irreducible

area in the Brillouin Zone (BZ) delimited by the path $\mathbf{\Gamma - M - K - \Gamma}$ highlighted in panel (b).

1.2.2 TIGHT-BINDING APPROXIMATION

The electronic band structure of crystals can be quite straightforwardly described by adopting the so-called "*tight binding*" approach. Such approach is based on the assumption that a crystal is formed by many atoms that can be treated as isolated, with the exception for valence wave functions which overlap with the first (or n-th) neighbor around. It essentially deals with the fact that this overlap is enough to require correction to the *isolated-atoms* picture, but not enough to make the atomic description negligible[36]. Wallace adopted this approach in 1947 to study a single layer of graphite[31], thus providing the first description of the electronic dispersion in graphene. For the sake of simplicity, the full calculation will be omitted and final result will be presented only.

The starting point is trivially the tight-binding Hamiltonian of the single electron:

$$\mathcal{H} = -t \sum_{<i,j>,\sigma} \left({a^{\dagger}}_{\sigma,j} b_{\sigma,j} + \text{H.C.} \right) - t' \sum_{\ll i,j \gg,\sigma} \left({a^{\dagger}}_{\sigma,i} a_{\sigma,j} + {b^{\dagger}}_{\sigma,i} b_{\sigma,j} + \text{H.C.} \right) \tag{4}$$

where ${a^{\dagger}}_{\sigma,i}$ $({a}_{\sigma,j})$ creates (annihilates) an electron with spin $\sigma = \uparrow , \downarrow$ on the i-th site on sublattice A (an equivalent definition is used for sublattice B); $t \approx 2.8\, eV$ is the nearest-neighbor hopping energy, i.e. the energy needed for one electron to move from one lattice site to the next one, in this case belonging to a different sublattice; t' $(0.02t \leq t' \leq 0.2t)$ is the next

nearest-neighbor hopping energy, representing the hopping in the same sublattice[37].

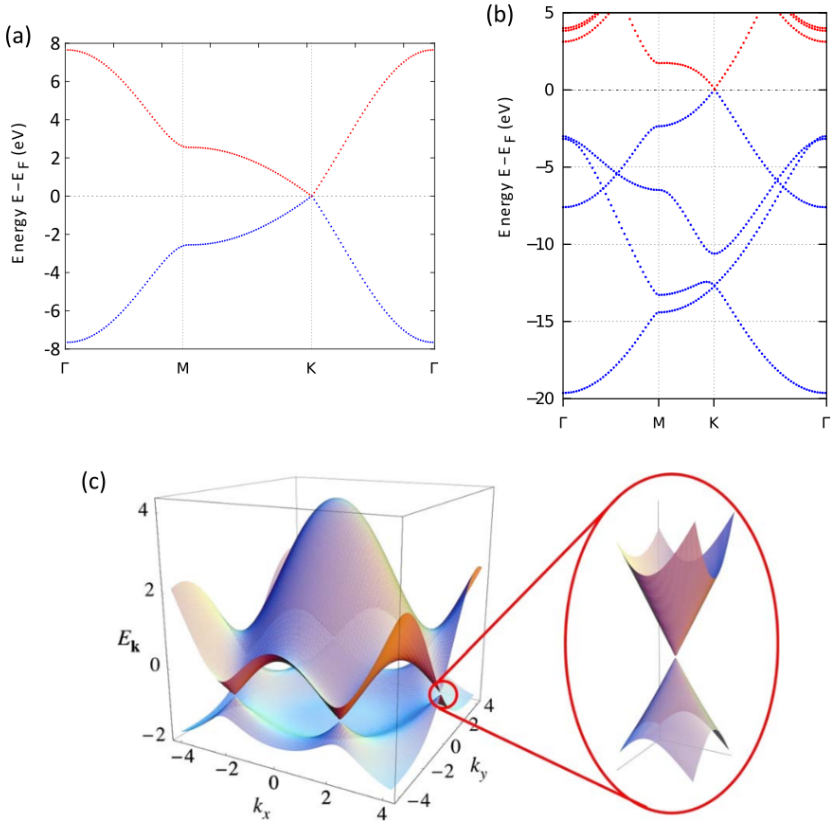

Fig. 1.3(a) Graphene $\boldsymbol{\pi}$ bands in tight binding approximation. (b) Graphene band structure from density functional theory calculations. (c) Three dimensional band structure of π-bands in tight-binding approximation. Panel (c) adapted from [37]

The resulting energy dispersion is

$$E_{\pm}(\mathbf{k}) = \pm t\sqrt{3 + f(\mathbf{k})} - t' f(\mathbf{k}) \tag{5}$$

with

$$f(\mathbf{k}) = 2\cos\left(\sqrt{3}k_y a\right) + 4\cos\left(\frac{\sqrt{3}}{2}k_y a\right)\cos\left(\frac{3}{2}k_x a\right) \qquad (6)$$

The Fermi level lies of the system lies at the crossing of the bands in the special point **K.** Fig. 1.3 reports the energy dispersion for π bands along the path of the irreducible area in the Brillouin zone (BZ), calculated using Eq. (6). If one expands the full band structure near the **K** (or **K'**) point of the BZ such that **k=K+q** the expression takes the linear form

$$E_{\pm}(\mathbf{q}) \approx \pm v_F|\mathbf{q}| + O[(q/K)^2] \qquad (7)$$

where $v_F \sim 10^6$ ms^{-1} is the Fermi velocity defined as $v_F = 3ta/2$. The $\pm$ sign arises from having two different sublattices and identifies the $\pi(+)$ or $\pi^*(-)$ band. If the second nearest neighbor interaction is neglected, the conduction (CB) VB become symmetric (Fig. 1.3(a,c)). However, for a more accurate description, ab initio calculations are needed (Fig. 1.3(b)). The point in which π and π^* cross each other is called Dirac point and the density of states in that point is 0. Since, the electrons populating the two bands belong to different sublattices, the degeneracy at the Dirac point is not lifted and no gap is opened. It is worth mentioning that a second order expansion of Eq. (7) brings a direction dependence in momentum space. Constant energy maps, i.e. maps of the $\mathbf{k}_{x,y}$ taken at constant energy, show a three-fold symmetry, called trigonal warping. It is interesting to note that Eq. (7) resembles the linear dispersion typical for massless high-energy fermions of quantum electrodynamics (QED). Indeed, the eigenstates of the system near the Fermi level obey the Dirac equation

$$-iv_F\boldsymbol{\sigma}\cdot\nabla\psi(r)=E\psi(r) \tag{8}$$

where $\boldsymbol{\sigma}=(\sigma_x,\sigma_y)$ is the Pauli matrix and $\psi(r)$ the electron wave function, which can be identified as spinors. However, in graphene there is not a real correspondence with spin, therefore the notion of '*pseudospin*' is used instead. Eq (8) describes the behavior of massless particle in high-energy physics. This implies that graphene provides a table-top low-energy platform to test the relativistic nature of electrons[38,39].

The eigenstates that solve Eq. 8 are

$$\psi_{\pm,\mathbf{q}}=\frac{1}{\sqrt{2}}\begin{pmatrix}e^{-i\vartheta_{\mathbf{q}}/2}\\ \pm e^{-i\vartheta_{\mathbf{q}}/2}\end{pmatrix} \tag{9}$$

Where $\vartheta_{\mathbf{q}}=\arctan\left(\frac{q_x}{q_y}\right)$ is a phase factor. When it is rotated by 2π the wave function is rotated by π, acquiring the so-called Barry phase. Moreover, states in **K** are mapped in **K'** by time-reversal symmetry.

Another important quantity is the chirality, i.e. the projection of the pseudospin over the momentum **q**. The pseudospin vector is either parallel or antiparallel to the momentum, therefore it can have positive or negative chirality respectively. Around the Dirac point the chirality is well defined and becomes a good quantum number. This introduces a suppression of backscattering. In fact, when backscattering occurs the momentum changes sign. This means that the chirality is not conserved, unless also the pseudospin is flipped. A phenomenon which justifies the analogy with QED is the Klein paradox. It describes the perfect tunneling for massless particles when scattering against an arbitrarily high and wide

barrier. This has been observed for graphene[39] and finds its explanation in the suppression of backscattering just described.

1.2.3 SYNTHESIS OF GRAPHENE

Graphene can be obtained through a variety of different routes which substantially belong to two different families: (i) a top-down approach that basically consists in splitting graphite into individual atomic planes (i.e., exfoliation techniques); (ii) bottom-up synthesis on top of suitable crystals (see growth methods section 3.1). In the following text the most relevant techniques will be presented.

Mechanical exfoliation is the technique that led to the isolation of graphene in 2004[34]. It can be performed in two ways, either rubbing the crystal against another surface or in the most well-known way of peeling graphene off by means of a sticky tape. The first process can be described as "*drawing with chalk on blackboard* "[40]. In the peeling method, the structured surface has to be pressed against a layer of a fresh wet photoresist spun[34]. After baking, the sample becomes attached to the photoresist layer, which allows using a common scotch tape repeatedly to peel graphite flakes off. The flakes remaining on the photoresist are then released in acetone and put on a SiO_2 wafer. Subsequently, ultrasound cleaving in propanol is used to remove flakes with thickness larger than 10 nm, (the others attach strongly to SiO_2)[34]. As demonstrated in their work[40], Geim and Novoselov took advantage of this method to isolate monolayer of other 2d materials such as h-BN and TMDs. Thus, in principle, it can be applied to any layered material. The primary identification of the specimens produced in this way is performed using an optical microscope. The two-dimensional crystals are visible when they are above a surface of SiO_2/Si^{++} with specific thickness of the oxide

(300 or 90 nm), in such a way as to allow a phase contrast of light reflected between the 2d crystal and the plane of the graphene oxide. A direct determination of the thickness of the exfoliated crystals is possible via atomic force microscopy (AFM). To date, mechanical exfoliation is still the technique that allows to obtain 2d crystals of the highest quality, ideal for fundamental studies. However, the limited lateral dimension of the produced flakes, the cumbersomeness of the technique and its high cost make this approach unfeasible for technological applications.

Automation of the exfoliation process can be implemented by adopting a wet-chemistry approach[41]. For example, in liquid phase exfoliation (LPE) the solubility of graphite in specific solvents is exploited. Graphite is immersed in N-methylpyrrolidone (NMP) and subsequently sonicated, centrifugated and filtered[42]. This technique, with the right choice of solvents, can be in principle applied to any layered material[43]. This approach is highly scalable and can lead to the implementation of 2d flexible electronics[44]. However, the quality of the materials is lower than those obtained via mechanical exfoliation, or other bottom-up synthetic techniques. The most popular bottom-up synthetic techniques to produce graphene, are: (i) CVD on a metallic substrate and (ii) thermal decomposition of SiC. In the very early days of 2d materials, thermal decomposition of SiC was put under the spotlight as an alternative technique to produce graphene. It relies on the high temperature annealing of SiC in vacuum[45] or in high-pressure inert environment[46]. When heated up, Si atoms sublimate from the SiC surface leaving behind a carbon layer. If this process occurs on the C-terminated face of SiC, graphene is immediately formed on the surface. For the Si-terminated face of SiC instead, the first rich carbon layer forms covalent bonds with the substrate and does not show the typical features of graphene[47,48]. This layer is called

"buffer layer". If the thermal decomposition of the substrate keeps going another buffer layer is formed below the first one, which, now decoupled from SiC, becomes a graphene layer. Thermal decomposition of SiC is treated in detail in paragraph 3.1.1 In the CVD approach, methane (CH_4) is flown within a high-temperature CVD growth reactor towards a heated surface (~1000°C). The heat will cause the CH_4 to "*crack*" and to release on the surface C atoms that – under appropriate growth conditions - rearrange to form graphene. When a metallic surface such as Cu is used as a substrate, the exposed area behaves as a catalyzer by lowering the activation energy for graphene formation. On Cu, once the surface is fully covered, the growth process is self-terminating and under appropriate conditions might lead to large area single crystal graphene[49,50]. To date, significant steps further have been carried on which allow to obtain single crystals of graphene (up to centimeter scale[51]) with quality comparable to that of exfoliated flakes. Once the process is over, for most application graphene has to be transferred on a different substrate, typically SiO_2. Therefore, it is necessary to detach it from the metallic substrate and deposit it elsewhere. At present, scalable high-quality transfer of CVD graphene is the major bottleneck which prevents the successful adoption of this material in wafer-scale optoelectronic applications. CVD growth of graphene on metallic substrates is discussed in detail in paragraph 3.1.3.

1.3 TUNGSTEN DISULFIDE, PROPERTIES AND SYNTHESIS

Within the large portfolio of 2d materials, a great deal of attention has been lately paid to TMDs[52–55]. In fact, they offer enticing optoelectronic and spintronic properties which make them ideal platforms for fundamental studies and for developing novel 2D opto-electronic and opto-spintronic applications [54–57]. This paragraph first introduces the general structure of

TMDs, and then focuses on the properties of WS_2, which is the TMD studied in this thesis.

1.3.1 STRUCTURE

A single TMD layer is constituted by two layers of chalcogen atoms sandwiching another layer of a transition metal. They have the chemical formula MX_2, where M is a transition metal (W, Mo, V, etc) and X is a chalcogen (S, Se and Te). The two most common structural phases are the hexagonal (2H) and octahedral (1T), which differ in the stacking: ABA and ABC respectively (Fig. 1.4)

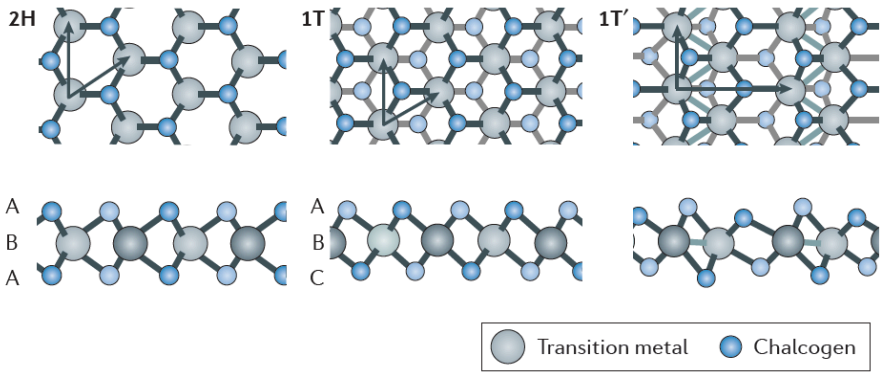

Fig. 1.4 Lattice structure of TMDs in the three most stable phases. Top view in the top panels and side view in the bottom panels. Adapted from [58]

In the 2H phase, the two chalcogen atoms in different atomic planes occupy the same position on top of each other. The 1T phase instead can be regarded as a structural transition from the 2H phase where the X atoms on one side of the M atoms are shifted to coincide (in the top view) with the centers of the hexagons formed by M atoms and other X atoms[59]. Depending on the atomic species, one of the two structure is stable and the other either absent or metastable[58]. In addition to 2H and 1T also the 1T'

(distorted octahedral) can occur. It is similar to 1T, however it shows a distortion in the W coordination which alters its electronic properties[60]. The most studied classes of TMDs are the ones having Mo and W as transition metals. In WS_2 and MoS_2 the most stable is the 2H phase[53], whereas WTe_2 is stable in 1T in bulk form at room temperature and 1T' in monolayer form.

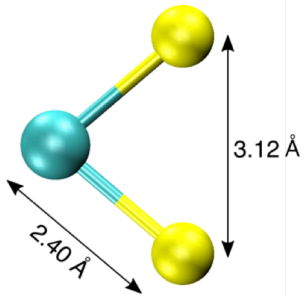

Fig. 1.5 Side view of WS_2 unit cell. The atomic distances are reported

The WS_2 unit cell is formed by two atoms of S and one of W displaced as shown in Fig. 1.5. Qualitatively, it has the same lattice vectors of graphene, hence the same BZ. However, their sizes differ as WS_2 lattice parameter is $a = 3.16$ Å[61]. The base atoms of S and of W are placed in position d_{s1} d_{s2} and d_w , respectively

$$\mathrm{d}_{s1} = \left(0, \frac{a}{\sqrt{3}}, \frac{-h}{2}\right) \quad \mathrm{d}_{s2} = \left(0, \frac{a}{\sqrt{3}}, \frac{-h}{2}\right) \quad \mathrm{d}_w = (0,0,0) \tag{2}$$

where $h = 3.12$ Å is the height of the layer.

1.3.2 ELECTRONIC PROPERTIES

Due to the wide plethora of chemical species, TMDs show a broad range of electronic properties from (semi)metallic to insulating. In the text below,

the electronic properties of WS_2 will be discussed, which qualitatively speaking are similar to those of MoS_2, MoS_2 and WSe_2. [53]. Bulk WS_2 is an indirect semiconductor with a band gap of ~1.3 eV[62], with the maximum of the VB in **Γ** and the minimum of the conduction band (CB) in **K**. In **Γ**, the *d*-orbitals of W hybridize with the p_z-orbitals of the chalcogen atoms. This out-of-plane displacement is strongly affected by the number of layers. It lowers in energy going towards the monolayer form. The states in **K** are purely in-plane, therefore they remain unaffected when lowering the dimension of the system[61]. At the monolayer limit the system displays a direct band gap whose magnitude is ~2 eV (see Fig. 1.6)[62].

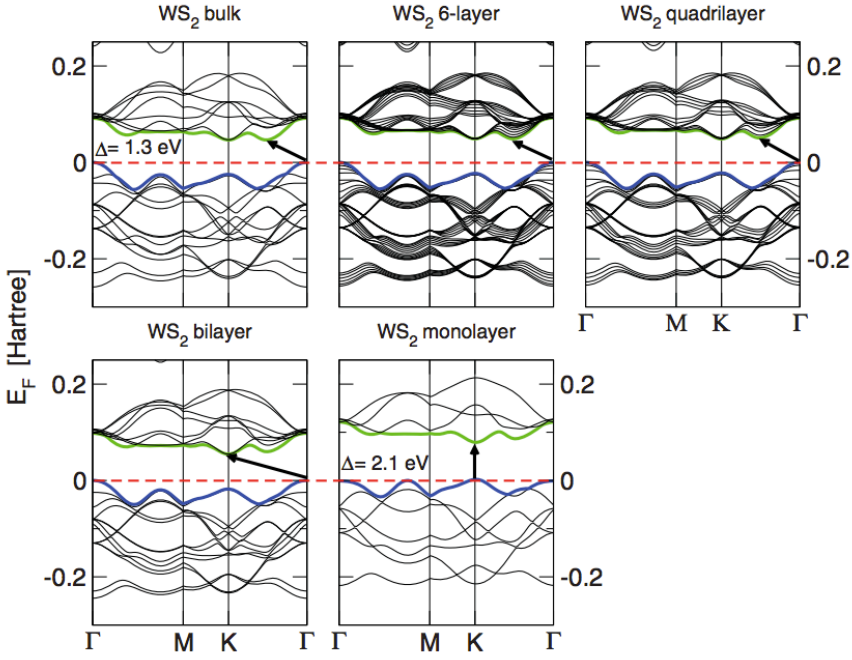

Fig. 1.6 Evolution of the band structure of WS2 with the number of layers, the band gap turns from indirect to direct passing from bulk to monolayer. Adapted from[62].

This transition has been explored in terms of PL, i.e. the emission of light consequent to the recombination of an electron in the CB with a hole in the

VB. Indeed, PL increases mowing towards the single layer as displayed in Fig. 1.7[63].

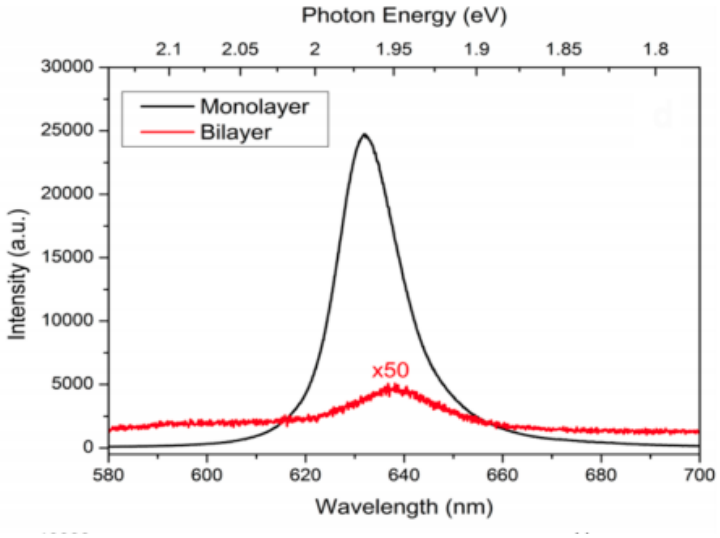

Fig. 1.7 PL spectra collected from WS_2 monolayer (black) and bilayer crystals (red). The shift in the PL emission energy is due to the shrinking of the band gap in the bilayer crystal. Adapted from [63].

In 2d materials with hexagonal lattice structure, the **K** and **K′** valleys are connected by time reversal symmetry. To access one valley or the other it is necessary to have a measurable physical quantity that has odd parity under time reversal. The valley degree of freedom behaves as the spin. Up and down states have the same time reversal relationship of the valleys in 2d materials and they are distinguished by opposite values of magnetic moment. Therefore, the magnetic field can be used to select one of the two states.

As said before WS_2 has a direct band gap in **K** and **K′** when monolayer. This suggests that polarized light can be used to access one valley or the other (Fig. 1.8) since selection rules at the base of optical transition have the right parity to discriminate valleys[64]. Optical pumping of valley-polarized

exciton has already been demonstrated[65] where PL is found to be strongly polarized with the same circular polarization as the incident light. Intervalley scattering is suppressed by the large momentum separation, leading to robust valley polarization.

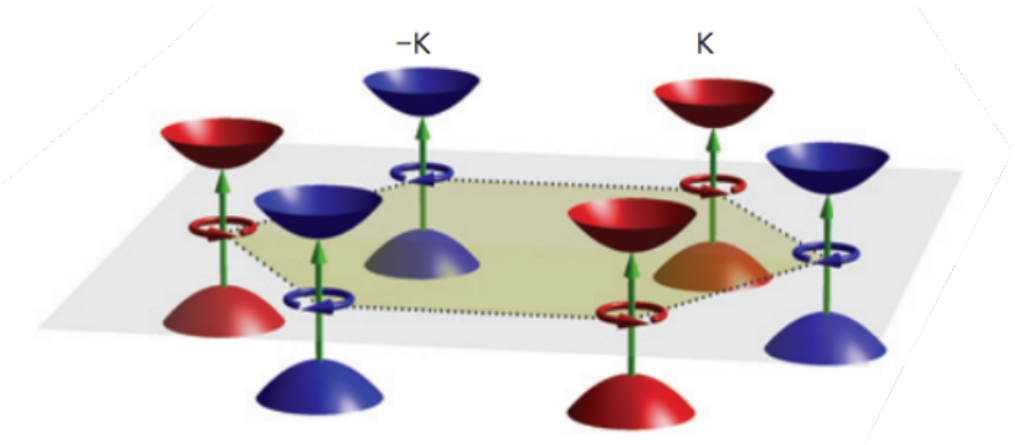

Fig. 1.8 Optical selection rules in **K** and **K′**. Light with different polarization promotes carriers in different valleys. Adapted from [55].

It is important to mention that WS_2 manifests a big spin-orbit coupling. This implies that at the **K** point the bands display a splitting that lifts the degeneracy of the spin. Considering the inversion symmetry breaking and the selection rules mentioned before, the spin degree of freedom is locked to the valley, meaning that the excited carriers resulting from optical pumping will also be spin-polarized[55].

1.3.3 SYNTHESIS OF WS_2

When bulk, WS_2 is a layered material as graphene and as graphene it can be exfoliated applying the same method of scotch tape exfoliation. However, as explained previously, this approach lacks of scalability. Other techniques have been used to synthesize monolayer WS_2[66,67]. Among them, CVD[65,68,69] and metalorganic-CVD (MOCVD)[70–72] are definitely the most

adopted to obtain highly crystalline and large area monolayer WS_2. CVD is the technique adopted in this work to grow WS_2 and it will be extensively described in chapter 3. It relies on the reduction and subsequent sulfurization of tungsten trioxide (WO_3) powder[24]. The S, at first solid, is evaporated in a controllable way in order to be delivered next to the W source. After the reaction, the WS_2 molecules diffuse on the target substrate where they form the 2d crystal. The process is cost-effective and of simple implementation.

MOCVD relies on the delivery of reactants in gas from, starting from vapor phase metal-organic complex molecules. They contain the desired atom, surrounded by a volatile compound that facilitates the material delivery. Once in contact with the hot substrate, they denaturize into more light byproducts, which are pumped away, leaving the metal behind. The metal atoms then react with chalcogen atoms deposited in the same fashion[67]. Typically used compounds are $M(CO)_6$ - where M is a metal such as W – and $(C_2H_5)S$ – where S is a chalcogen such as sulfur. This technique can lead to fully covered substrates such as SiO_2/Si^{++}. However, dealing with metal-organic compounds is not trivial and the chemistry behind the reaction can be more complicated than expected.

Other effective techniques for the production of TMDs are LPE and sulfurization of tungsten oxide layers deposited by atomic layer deposition (ALD). The former is very similar to the technique used for graphene as it uses sonication in common solvents such as NMP or isopropanol (IPA) with subsequent centrifugation and decantation. This approach is ideal to have large scale production of 2d materials for low-tech applications such as reinforcement of composite materials[66]. ALD offers the possibility of depositing a layer of a selected oxide on a substrate by exposing its surface to alternate gaseous species; the difference with CVD is that chemical

species are delivered sequentially. Song and coworkers demonstrated the successful growth of WS_2 using this approach[73].

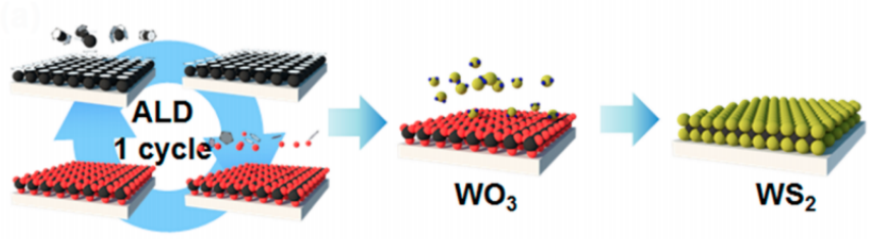

Fig. 1.9 ALD of WS_2, starting from WO3 subsequently sulfurized. Adapted from [73]

Fig. 1.9 reports the synthesis scheme. First a layer of W is deposited starting from the chemical precursor $WH_2(iPrCp)_2$ that decomposes leaving metallic atoms on the substrate. Subsequently, using oxygen plasma it is possible to oxidize the structure leading to a layer of WO_3. The material now is sulfurized at high temperature by means of a gas mixture of argon (Ar) and H_2S. This technique allows for high thickness uniformity over the entire substrate but presents drawbacks such us the use of dangerous precursors and the formation of many grain boundaries (e.g., grain size of tens of nanometers). However, carrier mobilities of about 4 cm^2/Vs have been recently reported[73], indicating a rapid development in the growth control. By offering significant prospects in terms of scalability, in the future this technique shall be optimized to produce wafer scale 2d semiconductors.

Another technique which has been adopted, although in a limited way, to obtain TMDs, is molecular beam epitaxy (MBE). MBE is performed in ultra-high vacuum (UHV) (10^{-10} bar), with the reactants introduced in the form of molecular beams by vaporizing a source solid material. The UHV

environments allows for the ballistic transport of the chemical species on the substrate. Nevertheless, TMDs produced via MBE typically present poor crystal quality and low coverage[74,75].

1.4 HEXAGONAL BORON NITRIDE, PROPERTIES AND SYNTHESIS

h-BN is constituted by nitrogen (N) and boron (B) atoms arranged in a hexagonal lattice. Its lattice parameter is $a = 2.51$ Å, slightly larger than that of graphene. When bulk, h-BN is a layered material kept together by vdW forces.

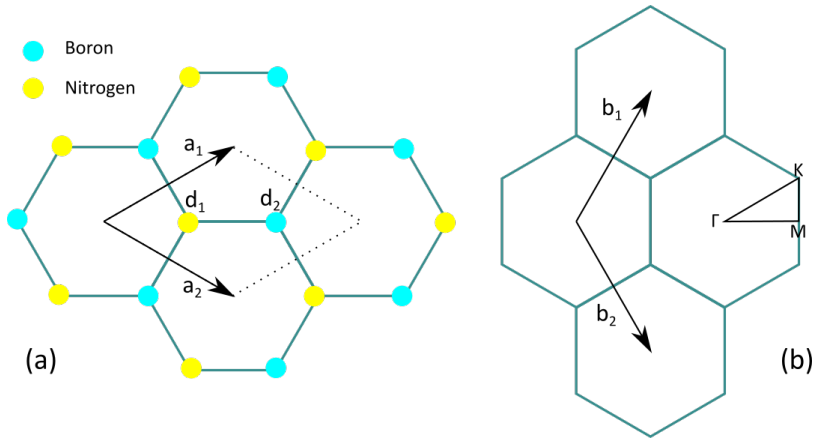

Fig. 1.10 h-BN lattice structure, with the d1 and d2 base atoms of B in yellow and N in cyan. a1 a2 are the base vectors. (b) Representation of h-BN lattice in reciprocal space, with Γ−M−K−Γ the irreducible area of the BZ.

The absence of dangling bonds makes this structure extremely flat. Also in this case the sp^2 hybridization is responsible for the planar structure of the σ bond, However, with respect to graphene, h-BN is formed by two inequivalent sublattices formed by the two different chemical species. This leads to a wide band gap opening at the K-point of the BZ[76]. Fig. 1.10 shows

the h-BN crystal structure and its relative reciprocal lattice, with the irreducible area of the BZ highlighted by the special points **Γ-M-K-Γ**.

1.4.1 ELECTRONIC PROPERTIES

h-BN is a wide gap semiconductor[77,78]. It does not show any light absorption in the visible range, however in the ultraviolet region it displays good adsorption and photoluminescence[79]. In Fig. 1.11 h-BN band structure is displayed including the projected density of states (PDOS) over B and N states. Conduction and valence bands are due to B and N states, respectively.

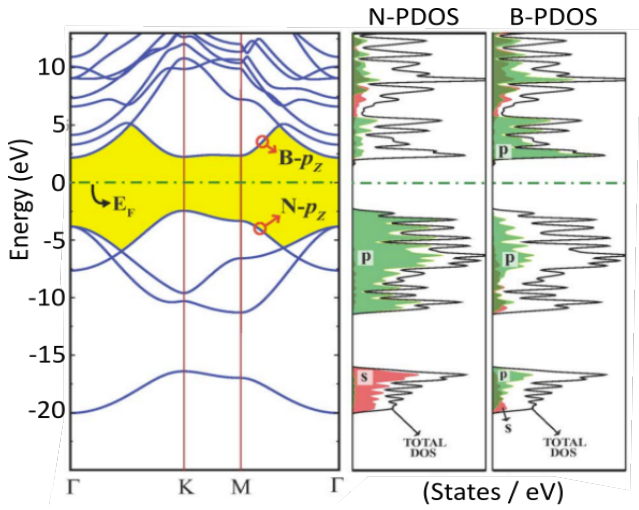

Fig. 1.11 h-BN band structure and projected density of states on N and B orbitals. Adapted from ([78])

1.4.2 PREPARATION OF H-BN

Nowadays, a lot of effort is being put on implementing techniques such as LPE[80] and CVD[81] to produce single layer h-BN. LPE, as in the case of graphene, has the advantage of scalability (at the expenses of crystallinity) which makes it the technique of choice for low-tech applications (e.g.,

insulating coatings/inks). Instead, CVD attempts on catalytic substrates typically yield polycrystalline multilayer h-BN[82,83]. Vacuum synthesis on catalytic substrates has yielded h-BN monolayers[84], although in this case, transfer from the substrate and scalability remain significant issues. Hence, to date, the most popular technique to produce high-quality monolayer h-BN remains mechanical exfoliation[21] (performed as reported in paragraph 1.2.3). When h-BN crystals tens of nanometers thick are requested, mechanical exfoliation is carried on by placing large bulk crystals on top of a commercially available scotch tape (blue tape semiconductor grade). Subsequently, the blue tape is back-folded in order to place the h-BN between two adhesive limbs, which are then pealed apart leaving on each side h-BN flakes of various thickness[85].

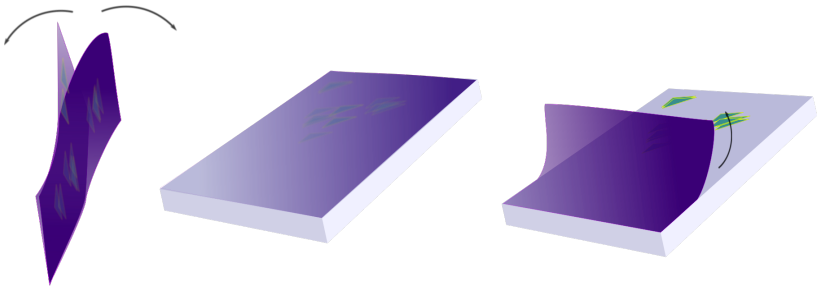

Fig. 1.12 Scheme of exfoliation process and deposition on a substrate. From left to right: Exfoliation of the crystal using two limbs of scotch tape. Deposition of one limb of scotch tape on a substrate. Pealing off of the scotch tape leaving the crystals on the surface.

The latter can be further reduced by repeating the process many times on a new patch of scotch tape. The h-BN flakes are transferred on the desired substrate by pressing it against the adhesive tape (Fig. 1.12). Solvent cleaning is finally adopted to remove glue residues. With this method, a fine control over the number of layers is not possible. The high-pressure method presented by Watanabe and Taniguchi[86] allows for obtaining bulk h-BN crystal with high crystallinity, still limited by the exfoliation issues.

Hopefully, in the next years, significant step forwards in synthetic techniques will yield high quality monolayer material thus speeding-up the development of all-2d-based technologies.

1.5 2D VERTICAL HETEROSTRUCTURES

Fig. 1.13 reports a comparison between a standard covalent heterostructure – the center of semiconductors research for more than 40 year[87,88] – and a vdW heterostructure. In covalent heterostructures chemical bonds exist between different materials. Classical methods to produce covalent heterostructures are molecular CVD or MBE. If the thin film which is deposited has the same chemical composition of the bulk underneath, this method is known as homo-epitaxy; hetero-epitaxy otherwise[12]. In hetero-epitaxy, to ensure that the thin top-layer has high crystalline quality, its lattice structure should be as close as possible to that of the substrate. The epitaxial registry is very important to control the defects at the interface. Namely, combining materials with different lattice parameters creates defects, dislocation and even lattice breaking at the interface and this can be harmful for the performance of the device. In standard AlGaAs heterostructures, solutions like modulation doping are used in order to tune the electronic properties of the material without introducing defects. In such a way it is possible to obtain a 2d electron gas (2DEG) that can reach mobilities of $\mu \sim 35 \times 10^6$ cm^2/Vs[13]. The current silicon technology is based on the capability to create a sharp interface between doped Si and SiO_2 keeping low the fabrication costs. Nevertheless, having chemical bonds limits the selections of materials available. vdW heterostructures – formed by staking 2d layered materials such as graphene, TMDs and h-BN – hold promises to overcome the abovementioned hurdles. Indeed, the lack of covalent bonds between the layers (see Fig. 1.13(b)) relaxes the constraints on the matching of the

lattice parameters. Hence, one can – in principle – combine any kind of layered material to form the desired heterostructure. In vdWH the properties of each constituting layer might be either significantly changed or remain seemingly unaltered. For instance, when placing TMDs on graphene, a gap is opened at the Dirac point in graphene as a consequence of the spin-orbit proximity effect[23].

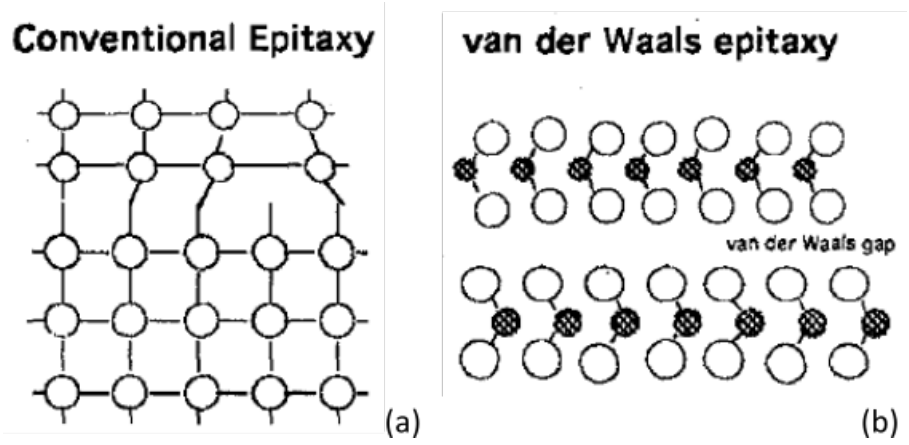

Fig. 1.13 Representation of a covalent heterostructure (a) and of a vdW heterostructures (b). In the first there are no chemical bonds between layers. Adapted from [89]

In other cases, due to the weak interaction between the constituting layers, the electronic structure of each material is not altered. Therefore, within the full system, the properties of each single layer are preserved. For instance, when stacking graphene on h-BN, the electronic properties of the former are greatly enhanced as first demonstrated by Dean et al[21]. Recently, Banszerus and co-workers[1] have demonstrated a record mobility for graphene (i.e., μ=3,000,000 $cm^2/(Vs)$) by encapsulating it between two h-BN layers. On the contrary, on SiO_2, the typical substrate adopted to realize graphene backgated devices, graphene transport properties are

inferior (e.g., typically a few thousands of $cm^2/(Vs)$)[90]. In fact, SiO_2 displays a significant surface roughness that increases electron scattering in graphene. The extreme flatness and the absence of dangling bonds in h-BN, make it the perfect candidate to suppress undesired scattering.

In the following chapters the electronic properties of the vdWH WS_2 on graphene will be investigated and discussed in depth.

1.5.1 SYNTHESIS OF 2D VERTICAL HETEROSTACKS

Fabrication of 2d vertical heterostructures can be carried on with different approaches. As for every 2d material, the first to be demonstrated was mechanical exfoliation.

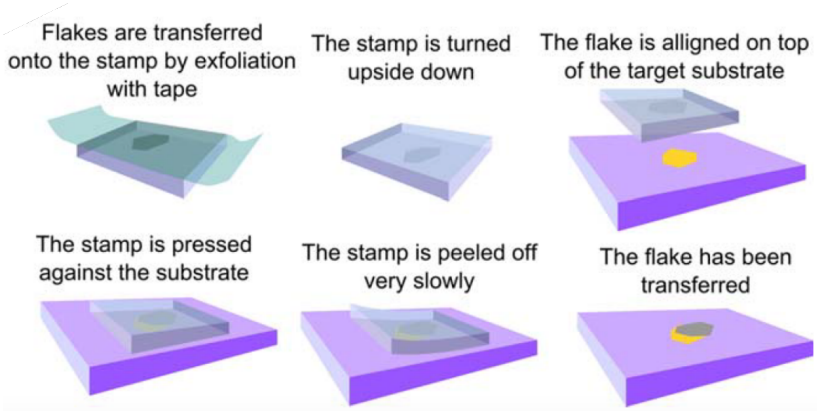

Fig. 1.14 Diagram of the steps involved in the preparation of the viscoelastic stamp and the deterministic transfer of an atomically thin flake onto a user-defined location (for instance another atomically thin flake). Adapted from [91]

Nowadays, by using Polydimethylsiloxane (PMDS) stamps, it is possible to transfer exfoliated 2d materials one on top of each other in a very clean and controlled way[91,92]. The stamp is a thin layer of commercially available viscoelastic material which is adhered to a glass slide to facilitate its

handling. The crystals to be transferred are deposited onto the viscoelastic layer by mechanical exfoliation. The surface of the stamp is inspected under the optical microscope to select the thinner flakes due to their faint contrast under normal illumination. The stamp is then attached to a three-axis manipulator with the flakes facing towards the sample. As the stamp is transparent, one can see the sample through it and thus it is possible to align the desired flake on the target surface at sub-micrometer resolution[91]. In Fig. 1.14 the various steps of the transfer method are depicted.

The advantage of this technique is its versatility as it can be applied to transfer any layered material (even obtained in different ways). However, this method is extremely cumbersome and does not offer any scalability, since the heterostructures are literally hand-made one by one. CVD synthesis offers nice advantages for the production of vdW heterostacks. By being a bottom-up approach, CVD synthesis offers a fully scalable way to produce heterostacks. Furthermore, this approach allows for a van der Waals epitaxy (vdWE), i.e., the synthesis of azimuthally aligned heterostructures. As a 2d layer is grown on top of another, it is influenced by the crystal structure of the substrate which might therefore induce on it a well-defined register. The concept of vdWE has been introduced almost 20 years ago[93] by A. Koma, Before this work a few groups demonstrated vdWe of 2d heterostacks[65,85,94,95]. For instance, Li and coworkers[96] demonstrated the epitaxial growth of GaSe on graphene via CVD. Structural analysis (Fig. 1.15) revealed that approximately 50% of the GaSe domains were oriented with a ~10° interlayer rotation with respect to the underlying graphene (the most energetically stable azimuthal orientation as also confirmed by theoretical calculations). Nevertheless, the fine control over the heterostack formation process remains a huge challenge.

At the time when this work started, no work had reported the synthesis of WS2 on graphene. In fact, although graphene growth had matured to a level where the synthesized films and the mechanically exfoliated ones had comparable quality, WS_2 synthesis had still to be perfected and implemented on 2d substrates.

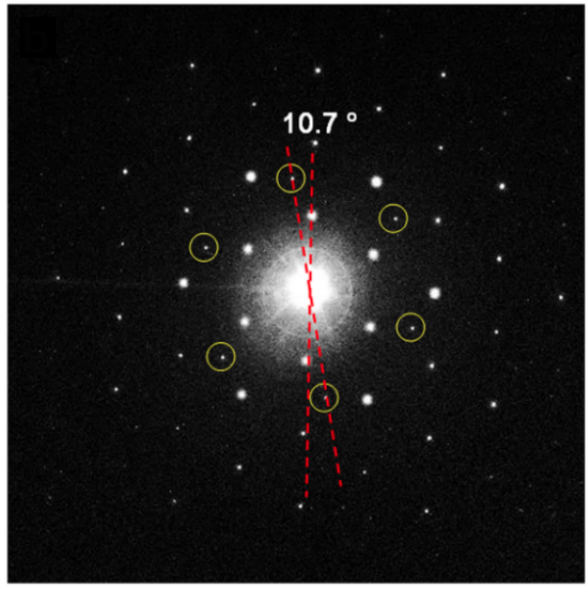

Fig. 1.15 SAED pattern of GaSe on graphene obtained via TEM analysis. The two crystals are misaligned by 10.7°. Adapted from (47)

The synthesis of WS2 over graphene and h-BN is thoroughly discussed in Chapter 4.

1.6 APPLICATIONS OF VAN DER WAALS HETEROSTRUCTURES

To date, a large number of potential applications for vdW heterostacks have been proposed, spanning from flexible electronics to DNA detection[97]. In the following, vertical tunnel field effect transistor (TFET) for low power and fast electronics and light detection will be discussed. Despite not having specifically treated TFETs in this thesis, their working principle

relies on the epitaxial alignment extensively studied for 2d vertical heterostructures in the following chapters. Conversely, the topic light detection is discussed as vdW-based photodetectors are reported in chapter 6. Indeed, for both these applications the crystalline quality and the epitaxial alignment of the grown heterostacks are extremely relevant. To date, most devices for (opto)electronics have been demonstrated using mechanically exfoliated flakes. In exfoliated vertical stacks no control on the epitaxial alignment can be operated, while CVD synthesis offers – as discussed- the possibility to implement vdWE.

1.6.1 TUNNELING DEVICES FOR LOW-POWER ELECTRONICS APPLICATIONS

The possibility to combine two-dimensional semiconductor, conductor and insulating materials in a vertical stack regardless of their lattice parameter opens to route to a new class of electronic devices. Vertical tunneling transistors are devices that modulate the tunnel barrier between metals and semiconductors rather than the thermoionic emission barrier. This allows this class of devices to be faster and to consume less power with respect to traditional bulk materials-base- transistor[98]. In a classical vertical tunneling transistor graphene is piled with h-BN which acts as a tunnel barrier (Fig. 1.16)[99]. h-BN is ideal for this purpose, having a wide band gap and a flat surface. Also, other materials with a non-negligible band gap can be interfaced with graphene and used as tunnel-barrier, such as for example the TMD studied in this work, WS_2[100]. Azimuthal alignment between the two conductive layers separated by the barrier plays a major role, since for tunneling to occur the momentum conservation has to be fulfilled, therefore the BZs of the layers have to be aligned. When the lattices of the two materials forming the vertical heterostack are strongly misoriented with respect to each other, tunnel is not efficient and might

involve phonons or impurities at the interface. Hence, in order to realize efficient vertical tunneling transistors made of graphene and a TMD, it is crucial to understand and control the band structure alignment within the heterostructure. This work explores this aspect in chapter 4.

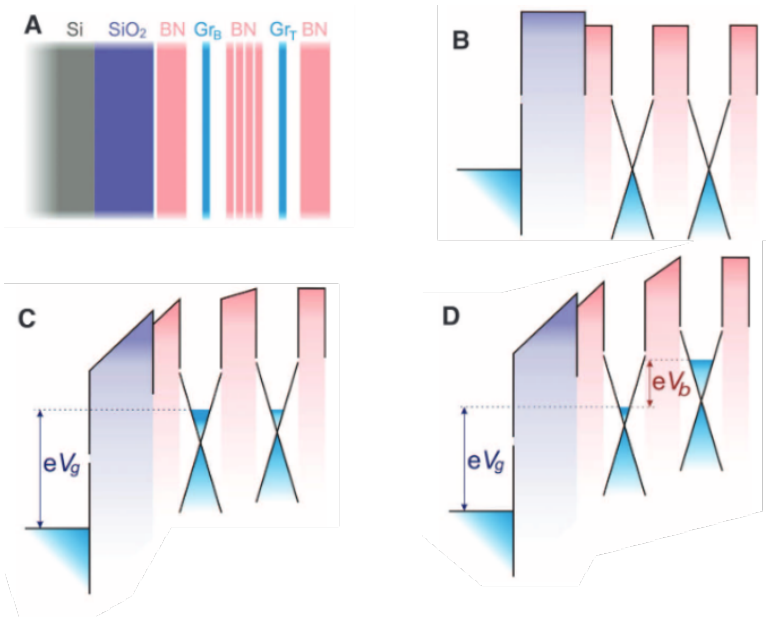

Fig. 1.16 Graphene field-effect tunneling transistor. (A) Schematic structure the experimental devices. (B) The corresponding band structure with no gate voltage applied. (C) The same band structure for a finite gate voltage Vg and zero bias Vb. (D) Both Vg and Vb are finite. Adapted from [99]

1.6.2 VAN DER WAALS HETEROSTRUCTURES FOR LIGHT DETECTION

Another class of devices that can be realized with vdWH are those dedicated to light detection. 2d materials that possess a direct band gap, such as monolayer TMDs, can be used to fabricate photodetectors active in the infrared and visible range. By combining TMDs' optical absorbance

with the outstanding transport properties of graphene efficient photodetectors have been demonstrated[22]. The simplest device structure is that obtained by vertically stacking graphene, as the channel material, and a TMD, as the optically active layer. This is an efficient architecture for phototransistors (Fig. 1.17). The charge transfer from the optically active layer to the channel ensures a fast detection of the incident light[101]. A part of this work is focused on the fabrication of photodetectors based on the interface graphene/WS_2 (see Chapter 6).

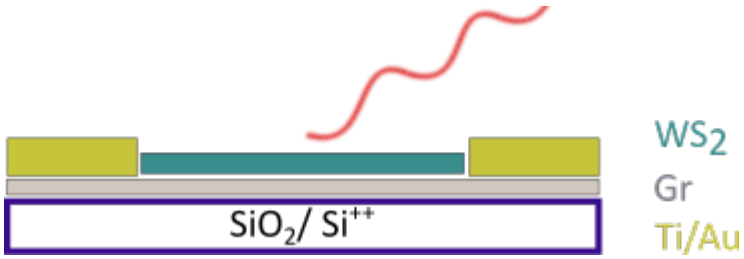

Fig. 1.17 Scheme of a hybrid WS~~2~~/Gr based device, WS_2 is the active material, whereas graphene acts as fast channel.

2 EXPERIMENTAL TECHNIQUES

This chapter introduces the experimental technique used in this work. Particular focus is put in the discussion of surface science techniques such as angle resolved photoemission spectroscopy (section 2.2), low energy electron diffraction (section 2.4) and microscopy (section 2.5) since they led to one of the major results reported in this work, mostly obtained at the ELETTRA synchrotron facility in Italy. Other routinely used techniques such as Raman spectroscopy are also addressed. In particular, one entire section (2.8) is devoted to Raman applied to graphene and other 2d materials as this discussion is instrumental for a better understanding of the data presented in this thesis.

2.1 PHOTOELECTRON SPECTROSCOPY

Photoelectron spectroscopy (PES) is a technique used to study the electronic state and the chemical composition of the surface region of a sample (solids, liquids or gases). Its working principle is based on the photoelectric effect discovered by Hertz in 1887 and explained by Einstein in 1915. The photoelectric effect is a phenomenon involving the expulsion of electrons from a material when it absorbs light with sufficient energy. Specifically, the term PES refers to a number of techniques depending on the source of the exciting radiation. The excitation source is a high-energy radiation spanning from ultraviolet light (for instance generated by a helium (He) lamp) to X-ray (for instance coming from a synchrotron source). The electromagnetic radiation is directed towards the target material. Once the radiation impinges on the material, emitted (photo)electrons are generated. Such electrons are then adsorbed by an *analyzer* whose work function sets the reference for the measurement of the kinetic energy. The energy conservation law allows calculating the

binding energy of the electron starting from its kinetic energy and, therefore, information about the energy levels of the material can be extracted.

$$E_{kin} = h\upsilon - \phi_A - E_B = h\upsilon - E_{vac} \qquad (1)$$

Where $h\upsilon$ is the energy of the incident photon, E_B is the binding energy calculated with respect to the Fermi Level and ϕ_A is the work function of the analyzer referred to the Fermi energy of the system (the same of the sample as long as they are put in electrical contact). E_{vac} is the energy of the vacuum level. In the energy distribution of the relevant spectra, shown in Fig. 2.1, N(E) is the DOS in the sample (lower left) and for the revealed photo emitted electrons (upper right).

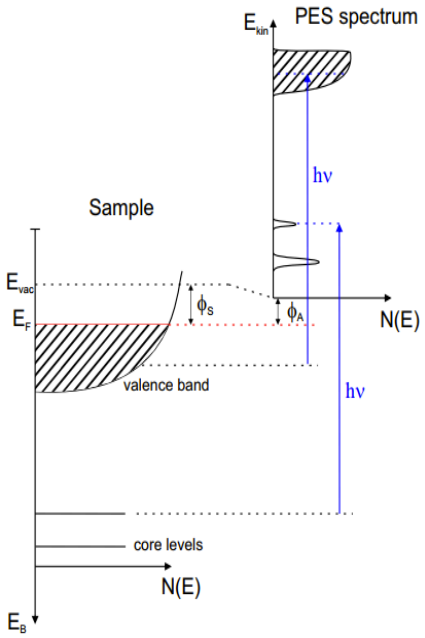

Fig. 2.1 Scheme of the energies involved in a photoelectron emission process from a solid. N(E) is the energy distribution of the photoemitted electrons. Adapted from [102]

The non-dispersive states represent the core levels of the system. The collected electrons are shifted up in energy by the photon energy minus the work function necessary to inject the electrons in the analyzer from vacuum. This scheme is very simple and does not take into account the presence of inelastic scattering events, which would give rise to additional features at different binding energies.

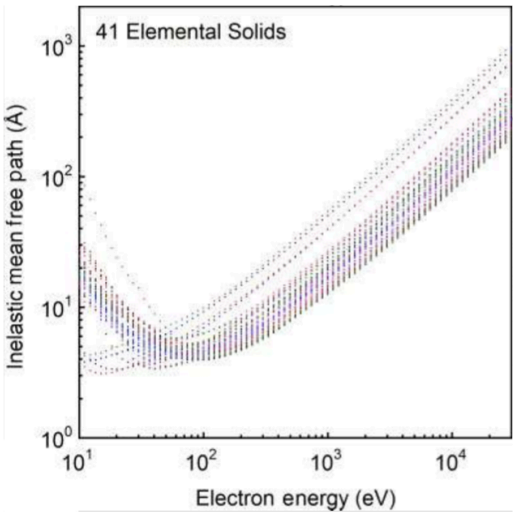

Fig. 2.2 Inelastic mean free path in function of impinging electron energy calculated for 41 materials. From [103]

The electrons that experience multiple inelastic scattering events are called *secondary* and are present mainly in the lower part of the kinetic energy spectrum. The inelastic scattering puts a limit to the distance that electrons can travel before escaping the substrate. It strongly depends on the kind of material and on the energy of the impinging electron. The average distance travelled by an electron before losing energy is called inelastic mean free path (IMFP). The IMFP for different elemental materials and in function of the impinging electron energy is displayed in Fig. 2.2 as calculated in Ref.[103].

In photoemission, the escape depth of the electrons is between 5 and 10 Å in the energy range 20–1000 eV. Therefore, for photoemission experiments, the sample surface should be atomically clean. UHV environment is typically required in order to avoid any unwanted scattering event with gaseous species in the chamber.

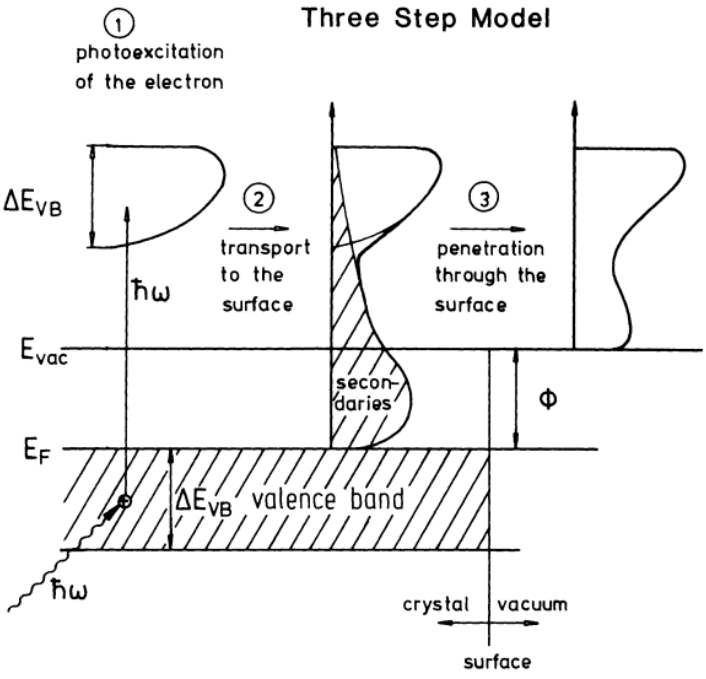

Fig. 2.3 Three step model describing the photoelectrons dynamics before escaping the material. 1) Photoexcitation of electron 2) transport to the surface 3) penetration through the surface. From [102]

The photoemission process can be phenomenologically described with the *three-step model* first proposed by Berglund and Spicer[104]. This model identifies three independent events within the full photoemission phenomenon. The three steps (sketched in Fig. 2.3) are:

(1) adsorption of the photon and consequent excitation of an electron in the solid

(2) Migration of the electron towards the surface

(3) Penetration of the electron into the barrier at the interface material-vacuum and escape into the vacuum

However, in order to simplify the description, the so called one-step model is here adopted, where the initial and final states only are taken into account[102].

When the electromagnetic field, described by the potential vector $\boldsymbol{A}$ impinges on the substrates it promotes one electron in its excited state. This process is described by the well-known *Fermi Golden Rule* [105]:

$$w_{if} \propto \frac{2\pi}{\hbar} |< \psi_f \, |\mathcal{H}_{int}| \psi_i >|^2 \delta(E_f - E_i - h\upsilon) \qquad (2)$$

Where $\mathcal{H}_{int}$ is the interaction Hamiltonian, ψ_f and ψ_i are the final and initial state respectively.

The approximated form for $\mathcal{H}_{int}$, neglecting second order processes, is

$$\mathcal{H}_{int} = \frac{e}{mc} A \cdot \mathrm{p} \qquad (3)$$

where p is the momentum operator.

The matrix element depends on the photon energy, but also on the experimental geometry. The matrix element is a fundamental quantity when considering polarized light and it could give a complete suppression of photocurrent. The polarization of the incident light is defined by the orientation of the electromagnetic field with respect to the *mirror plane*, i.e.

the plane orthogonal to the substrate where lies the wave vector. If the electromagnetic field is orthogonal to the mirror plane the beam is defined as *s-polarized*, if it lies on the mirror plane it is defined as *p-polarized*[106].

2.2 ANGLE-RESOLVED PHOTOELECTRON SPECTROSCOPY

ARPES is a PES technique that records the number of photoemitted electrons at a given kinetic energy and emission angle with respect to the sample. This technique takes advantage of ultraviolet or X-ray radiation to extract electrons from the investigated sample.

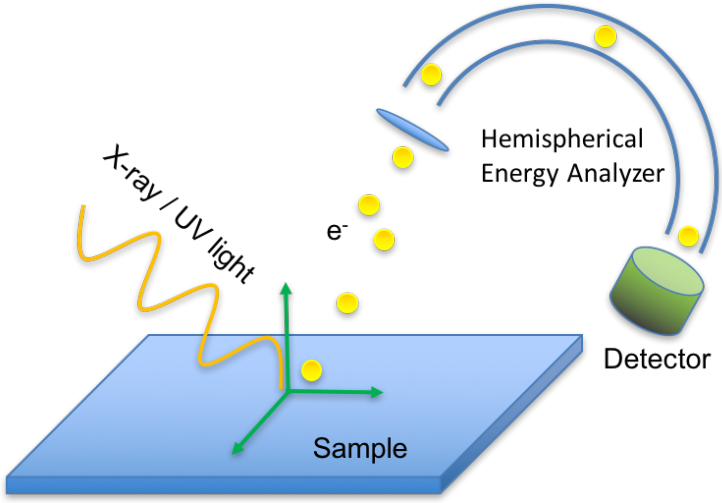

Fig. 2.4 ARPES set up scheme. Electromagnetic radiation provide enough energy to the sample to leave the first layers of the substrate and travel towards the analyzer.

As mentioned above, the radiation can be generated by a number of sources such as helium He lamp or synchrotron radiation. Thanks to the energy and momentum conservation laws it is possible to extract the kinetic energy and the momentum of the electrons before they are emitted from the crystal. In this way it is possible to obtain momentum-energy spectra, i.e., the electronic band structure of the explored materials. A

typical experimental set-up for ARPES measurement is sketched in Fig. 2.4. The radiation is shone over the sample. The photoemitted electrons are directed by means of magnetic lenses into a hemispherical analyzer. Here, the electrons are separated in trajectory according to their energy by means of an electrostatic field. Finally, the electrons are collected by a detector. The detectors are made by a fluorescent screen which emits light when hit. A CCD camera reconstructs the energy dispersion of the crystal subsequently collecting the outgoing light. With modern detectors it is possible to obtain 2d maps of the energy dispersion and also reconstruct the Fermi surface topology.

Photoemitted electrons can also be collected to obtain an image of the surface (photo-emitted electrons are originated from a very shallow layer). Variation in electron emission is used to generate image contrast. This technique is called photoemission electron microscopy (PEEM) or XPEEM when X-rays are used as excitation source.

During the electron extraction process, the parallel component $k_{||}$ is conserved, thanks to translation symmetry in the x-y plane across the surface. Making the assumption that the momentum carried by the photon $p_{ph} = h\upsilon/c$ is negligible compared to the crystal momentum of the electron $\hbar k \gg p_{ph}$, ensures a vertical transition in the reduced zone scheme, thus $\mathbf{k}_f = \mathbf{k}_i$. Hence, the von Laue equation $\mathbf{k}_f = \mathbf{k}_i + \mathbf{G}$ is fulfilled, where **G** is a base vector of the BZ. Indeed, experiments are usually performed using photon energy lower than 100 eV, which correspond to a momentum of $\frac{p}{\hbar} \simeq 0.05$ Å^{-1}. Another assumption made to simplify the description of the system is the so-called *sudden approximation,* namely the electron is supposed to be extracted instantaneously from the material with no time to interact with the remaining N-1 electrons. This allows us to

consider the obtained dispersion as the ground state of the system. Taking into account all of these approximations, and considering a 2-dimensional material, as all the systems studied in this work, the emitted photocurrent takes the form:

$$I(\mathbf{k}, E, h\upsilon) \propto \left|M_{i,f}\right|^2 A(k,E) f(E,T) + B \qquad (4)$$

Where $|M_{i,f}|$ is the matrix element of the transition from the initial (i) to the final (f) state, $A(k,E)$ is the so called spectral function, $f(E,T)$ is the Fermi-Dirac distribution and B is a background term coming from secondary electrons. The spectral function takes into account the angular dependence of the photo-emitted electrons.

When the electrons leave the material, they end in a free particle state. Considering the scheme in Fig. 2.5 and assuming the conservation of the electron parallel momentum, the following expression holds:

$$k_{||int} = k_{||ext} = \sqrt{\frac{2mE_{kin}}{\hbar^2}} \sin(\theta) \qquad (5)$$

Where θ is the emission angle and E_{kin} is the kinetic energy expressed in eV and $k_{||}$ in Å^{-1}. For immediate calculation Eq. (5) can be approximated as $k_{||int} = 0.5123\sqrt{E_{kin}}\sin(\theta)$.

When considering the perpendicular component, the description is not this simple, since it is not conserved when crossing the crystal surface[106]. From Eq. 5 is possible to obtain the resolution on the measurement of $k_{||}$

$$\Delta k_{||} = k_{||}\sqrt{\left(\frac{\Delta E}{2E_{kin}}\right)^2 + \left(\frac{\Delta\theta}{\tan(\theta)}\right)^2} \qquad (6)$$

where $\Delta\theta$ is the angular acceptance of the analyzer. In equation (6) the first term in the square root can be neglected, since ΔE is typically of the order of few meV for the most common analyzer system. For practical use the error can be computed $\Delta k_{||} = 0.5123\sqrt{E_{kin}}\cos(\theta)\Delta\theta$.

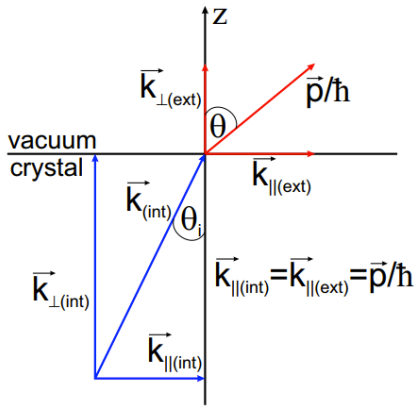

Fig. 2.5 Scheme of the momentum component conservation at the crystal-vacuum interface. The parallel component $\boldsymbol{k}_{||}$ only is conserved. From[107]

2.3 CORE LEVEL PHOTOELECTRON SPECTROSCOPY

Core level photoelectron spectroscopy (CLPES) is a technique used to study the core levels of atoms in molecules and crystals. The incident photon energy in this case is ~1 keV[107]. Therefore all the assumptions made for ARPES do not hold in this case. This means that the relations between energy and angle are not trivial, thus the signal is integrated over the angle.

The chemical environment affects the core levels of an atom dramatically. Indeed, core electrons of an element might differ in binding energy by a value (called chemical shift, ΔE_B) which depends on the elemental chemical bonding. The binding energy is affected by the effective potential due to the different distribution of electrons in the material, thus it changes with ligands having different electronegativity. A typical use of this technique is to reveal the presence of an oxide. As a matter of fact, oxygen is a highly electronegative element and the chemical shift is quite strong. In metal oxide compounds, the electrons from the metal will fill the 2p shell of oxygen. This means that the electrons left on the metal will experience a stronger Coulomb potential, since the core is less screened due to the different charge distribution, resulting in a higher binding energy. This effect can be of the order of a few eV, partially overlapping to another similar peak. Therefore, the fitting procedure is crucial to obtain reliable results.

The line shape of a singular core level is a convolution of a Lorentzian and a Gaussian distribution (the first is linked to the lifetime of the transition and the second to thermal effects), each with different weights. This line-shape is called *Voigt profile*[108]

$$V(x,\sigma,\gamma) = \int_{-\infty}^{+\infty} \frac{e^{\frac{-x\prime^2}{2\sigma^2}}}{\sqrt{2\pi\sigma^2}} \cdot \frac{\gamma}{\pi[(x-x')^2+\gamma^2]}\,dx \tag{7}$$

where σ^2 is the variance of the Gaussian distribution and γ is the scale parameter of the Lorentzian.

Under certain circumstances, typically in the case of metals, the core level peak shows a broad tail towards high binding energies and a sharp decay

at lower binding energies. In metals this behavior finds explanation in the energy loss due to the readjustment of the screening potential resulting from the formation of electron-hole pairs in the Fermi sea. This effect lowers the energy of the escaping electron. The line shape that takes into account what described is called *Doniach-Šunjić* (DS)[109]

$$f_{DS}(E) = \frac{\Gamma(1-\alpha)\cos[\frac{\pi\alpha}{2} + (1-\alpha)\tan^{-1}(\frac{E-E_0}{\gamma})]}{[(E-E_0)^2+\gamma^2]^{\frac{1-\alpha}{2}}} \quad (8)$$

Where E_0 is the kinetic energy of the main peak, γ is the scale parameter of the Lorentzian and α is the asymmetry coefficient of the distribution, whereas Γ is the Euler's Γ function. Nevertheless, the DS function is just an asymmetric Lorentzian, therefore it has to be convoluted with a Gaussian to get the actual spectrum. Moreover, the spin-orbit splitting of the core levels has be taken into account. The ratio in intensity between the two branches is described with the so-called *branching ratio l/(l+1)* where *l* is the angular momentum. Finally, to obtain reliable fitting parameters, the signal coming from the background has to be addressed to take into account noise coming from inelastic scattering.

2.4 LOW ENERGY ELECTRON DIFFRACTION

LEED is a technique used to determine the surface structure of a crystalline material. It is based on the diffraction process and uses incoming electrons with an energy in the 10-300 eV range to bombard the target surface and the diffracted back-scattered electrons can be observed in a fluorescent screen. As the previous ones, also this technique is performed in high vacuum, avoiding the scattering events of scanning electrons with gases. The electrons are generated with an electron gun, i.e. by supplying enough

voltage to a metallic filament, which subsequently expels electrons. The beam is collimated and accelerated by means of electromagnetic lenses.

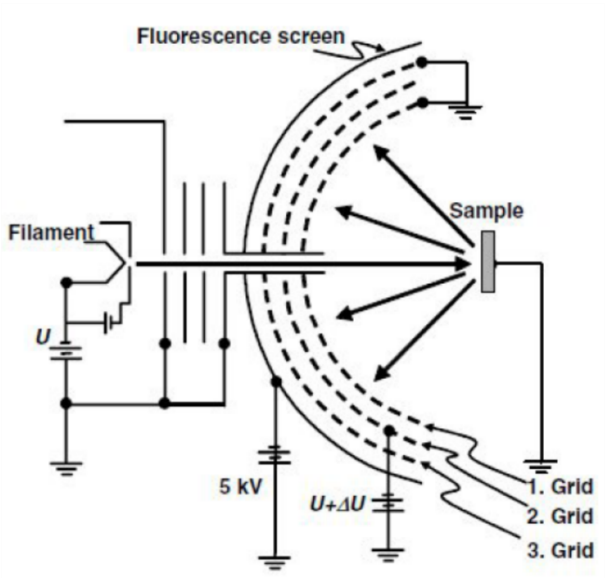

Fig. 2.6 LEED setup scheme. The electrons are accelerated towards the sample. The backscattered electrons impinge over the fluorescent screen, generating a light signal.

The sample is grounded in order to discharge incoming electrons. A scheme of the system is shown in Fig. 2.6. Considering the exponential decay of the primary electron beam intensity given by the Lambert-Beer law, LEED is a surface sensitive technique, therefore it is particularly efficient for 2d materials, such as graphene and TMDs.

Its basic principle is founded on de Broglie hypothesis, whereby a particle, in this case an electron, has a wavelength associated with its kinetic energy:

$$\lambda = \frac{h}{\sqrt{2mE}} \qquad (10)$$

The incoming electron beam is characterized by a wave vector $k_0 = 2\pi/\lambda_0$ and the scattered one by the wave vector $k = 2\pi/\lambda$.

The condition for constructive interference will occur if the Laue equation is fulfilled

$$\boldsymbol{k}_{||} - \boldsymbol{k}_{\boldsymbol{0}||} = \boldsymbol{G}_{||} \qquad (11)$$

where $\boldsymbol{G}_{||}$ is a base vector of the reciprocal space.

Only elastic scattering is considered, therefore only electrons coming from the first layers will contribute. However, information about the vertical stacking can be extracted by the *I-V* curves[110], i.e. how the intensity of a particular diffraction point changes with respect to the electron energy. The curve is also affected by the potential experienced by the electrons in the crystal, shifting the energy of the intensity maxima.

2.5 LOW ENERGY ELECTRON MICROSCOPY

LEEM is a technique that exploits slow electrons to reconstruct the image of the scanned surface. A cathode filament held at a negative potential with respect to the sample produces an electron beam, accelerated at tens of keV and collimated with electromagnetic components. In this case the sample is set with a bias voltage. The difference between the voltage needed for electron extraction and the sample bias, is called starting voltage (STV). This parameter allows tuning the kinetic energy of the electrons before they reach the surface. The electrons are surface sensitive and they explore up to the first few Å of the sample (see Fig. 2.2). They are slowed down to ~10 eV. Once the electrons hit the surface they experience diffraction and then they are elastically backscattered. The focal plane can be placed either

on the image place (imaging) or on the diffraction place. Using small aperture, it is possible to shine electrons over regions of few μm^2. The resulting diffraction patter will be characteristic of the area probed. This allows filtering the image for the specific crystal lattice forming the relative diffraction patter (μ-LEED). By means of an aperture is possible to select electrons coming from a single diffraction spot. In particular, if we take into account the *0-order* point, we talk about *bright field microscopy*. Conversely, if any other non-*0-order* point is selected we talk about *dark field microscopy*. Electrons can be decelerated enough not to penetrate the material and get collected before experience any scattering, hence diffraction. This is called *mirror mode imaging*. In mirror electron microscopy (MEM) the surface is illuminated with electrons at very low energy, so that the electrons interact very weakly with the surface (this occurs at the transition MEM–LEEM). Under these conditions the contrast is due to work function differences and topography variations.

2.5.1 NANOSPECTROSCOPY @ ELETTRA

The techniques explored so far have been exploited for a number of results in this work. Most of those experiments have been performed at Elettra Synchrotron in Trieste (Italy). A synchrotron is an accelerator facility which can be used to produce a coherent and tunable beam. At Elettra, a X-ray beam is collected in a *beam-line* called "*Nanospectroscopy*". Here by means of a monochromator, the wanted wavelength is selected and subsequently shone on the sample. Moreover, it is possible to select the polarization of the incident beam. The system is equipped with a bandpass energy filter, allowing carrying out laterally resolved ultra-violet (UV) and soft X-ray photoelectron spectroscopy. In imaging mode, the lateral resolution approaches 30 nm, the energy resolution 300 meV. It is possible to obtain XPEEM data that evaluated at core level energies yield

microscopic photoelectron spectroscopy (μXPS) spectra. The system is illuminated with photons linearly polarized in the synchrotron's ring plane. The sample is mounted vertical with respect to that plane and the photon beam impinges at 16◦ onto the sample. The light is therefore mostly p-polarized. This setup allows also carrying out microprobe (also known as microspot) ARPES (μARPES) measurements[111]. With this technique, the band structure of the system can be probed on areas as small as ~2 μm in diameter, allowing the imaging of the angular distribution of photoemitted electrons. However, the ARPES analysis carried out in this setup is slightly different. In the μ-ARPES mode (or diffraction mode), the diffraction pattern, formed at the back focal plane of the objective lens, is imaged.

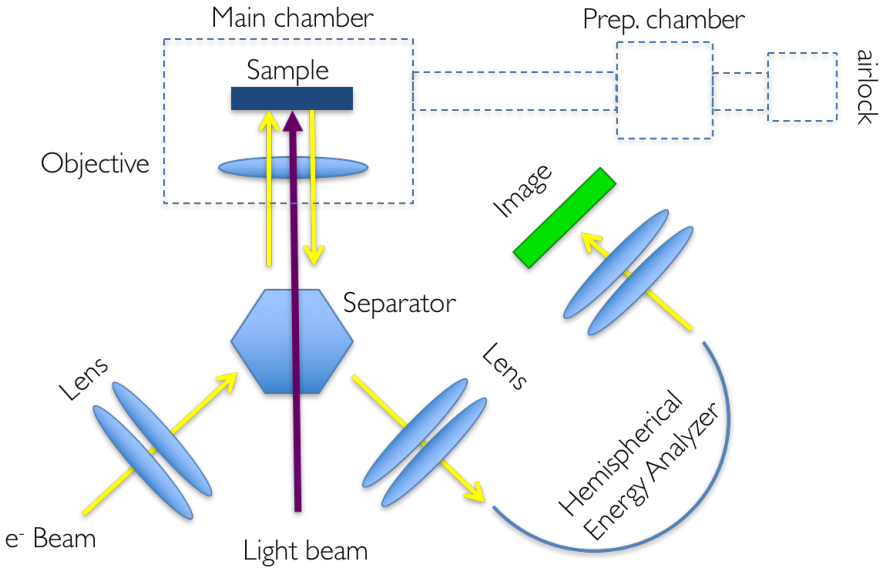

Fig. 2.7 SPELEEM end-station scheme at *Nanospectroscopy* . LEEM/PEEM analysis are available within the same endstation.

The diffraction pattern carries information about the BZ in reciprocal space of the analyzed sample. By collecting images at different energies, it is possible to reconstruct the energy dispersion, thus the band structure of

the crystal. Even though the result obtained in this way is the same of the "standard" ARPES, in this case, we are not looking at the angular distribution of the photoelectrons, but the diffraction pattern is taken into account. In addition, the *Nanospectroscopy* end-station is equipped with a LaB_6 gun used to generate a collimated electron beam. The lateral resolution of the microscope in LEEM is better than 10 nm[112,113]. Along with imaging, μLEED measurements (also known as microprobe-LEED) are performed using illumination apertures to restrict the electron beam to a minimum size of 500 nm. Inasmuch as *Nanospectroscopy* end-station(schematized in Fig. 2.7) allows for Spectroscopic Photoemission and Low Energy Electron Microscope (SPELEEM), it is possible to obtain a full characterization of the same selected μ-area.

2.6 ATOMIC FORCE MICROSCOPY

AFM is the technique of choice to obtain information about the surface morphology and thickness of 2d materials. Its working principle is based on probing the vdW forces acting on a sharp tip when placed in contact with a substrate. This kind of interaction is described by the Lennard-Jones potential:

$$V_{LJ} = \varepsilon \left[\left(\frac{r_0}{r} \right)^{12} - 2 \left(\frac{r_0}{r} \right)^{6} \right] \qquad (12)$$

where ε is the depth of the well potential depicted in Fig. 2.8 and r_0 is the equilibrium distance.

In AFM a cantilever with a sharp tip is dragged over the sample surface (Fig. 2.8(a)). The tip displacement is measured by a laser beam that is

reflected off the cantilever and directed to a photodetector (Fig. 2.8(b)). AFM can work in two main modes:

- Contact Mode
- Tapping Mode

In the first, the cantilever is kept fixed and the tip, dragged over the sample, is deflected by the corrugation of the substrate. In this mode, it is possible also to measure the torsion of the tip when it probes substrates with different friction coefficient. Therefore, it is possible to obtain information about the height and the kind of material analyzed.
In the tapping mode instead, the tip is kept oscillating around its resonance frequency by piezoelectric motors. When the morphology of the substrate changes, the vibration frequency changes accordingly, since it depends on the distance from the substrate. The phase of the oscillation changes when changing the probed material. Additionally, adhesion force can be measured.

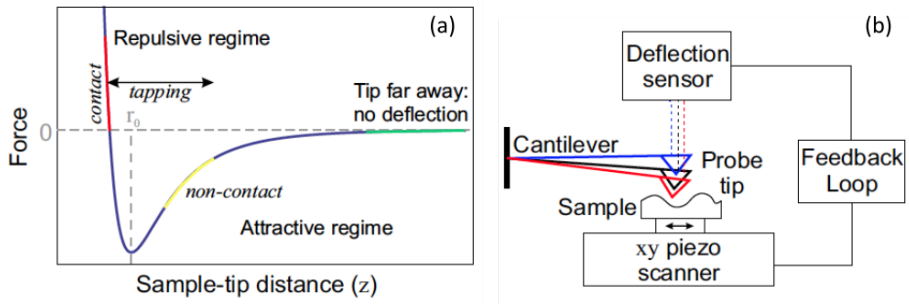

Fig. 2.8 (a) Qualitative profile of the Lennard-Johns potential. (b) AFM scheme.. The piezoelectric motor and the deflection sensor form a feedback loop which controls the movements for the tip to approach the cantilever.

Both of these modes will be exploited to characterize the materials studied in this thesis.

2.7 SCANNING TUNNELLING MICROSCOPY

STM is a scanning probe technique that allows imaging the surface of a material with atomic resolution. The working principle comes from basic quantum mechanics as it exploits the tunneling effect between a surface and a metallic tip which act as electrodes (see Fig. 2.9). The distance of the tip from the surface determines the different tunneling barrier, thus the different detected current depends on the morphology of the system. The tunneling current J_T is a function of the gap between the electrodes[114].

$$J_T \propto {V_T}^{-A\phi^{1/2}s} \tag{13}$$

Where ϕ is the tunnel barrier identifiable also with the work function (in eV), A is a constant ~ 1 and s is the distance sample-tip Å. Thanks to the exponential decay, with small distance variations, the tunneling current changes dramatically. The resulting tunneling current is a function of tip position, applied voltage, and local density of states (LDOS) of the sample. The LDOS of a material surface is measured as a function of lateral (x-y) position on the sample surface and energy. The LDOS is proportional to the differential increase in tunneling current given a differential increase in bias voltage. A direct measure of the LDOS can be obtained by measuring $\mathrm{d}J_T/\mathrm{dV}$ curves via scanning tunneling spectroscopy (STS).

Thanks to the small tip (ideally one-atom sharp), it is possible to obtain very high resolutions, up to the atomic level (as shown later in this work).

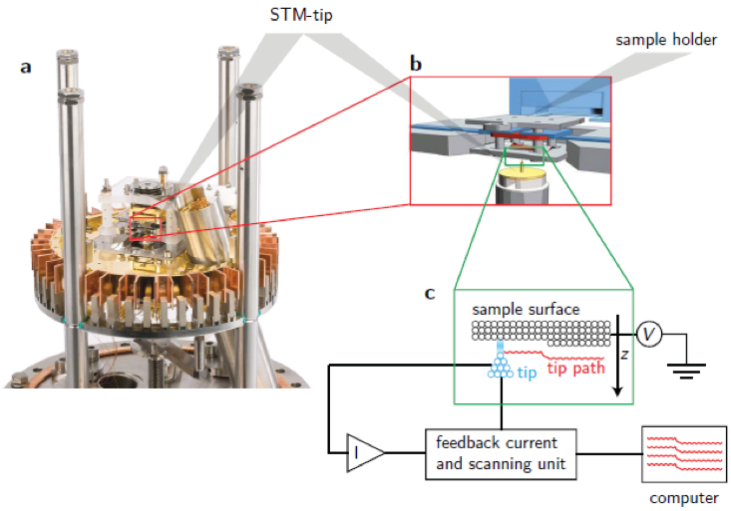

Fig. 2.9 (a) Scanning tunneling microscopy set-up (b) Scheme of the actual tip/feedback loop system

2.8 RAMAN SPECTROSCOPY

Raman spectroscopy is a technique, which relies on inelastic scattering, and is used to observe vibrational, rotational and generally low-frequency modes in a material. It has been proved to be a reliable tool to characterize graphene in terms of crystal quality, number of layers, doping and strain[115]. With this technique, the modes of a crystal are probed by means of a monochromatic light source, usually in the visible range. As the impinging light interacts with molecular vibrations, or other excitations in the system, the energy of the laser photons is shifted.

The greatest challenge in this technique is to separate the weak Raman scattering (only one in every 10^6 - 10^8 photons scatters) from the strong elastic scattering component (Rayleigh scattering). Rayleigh scattering is a

process in which an electron in the ground level is excited and falls to the original ground level. Thus, Rayleigh scattered light has the same energy as incident light (see Fig. 2.10). Raman scattering can be classified as two types, Stokes Raman scattering and anti-Stokes Raman scattering.

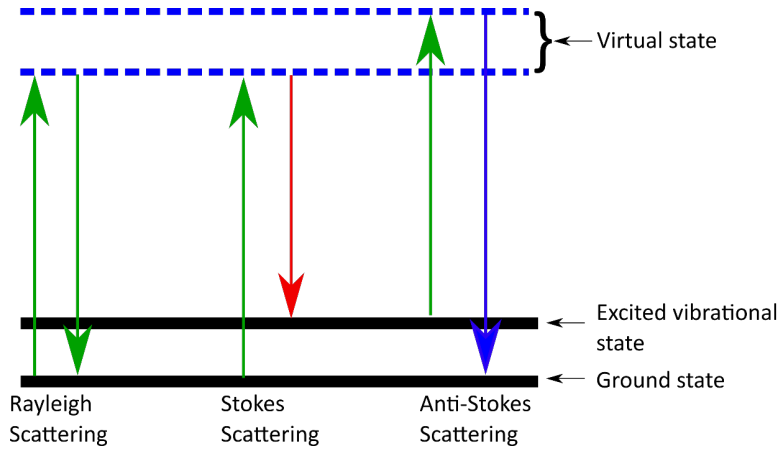

Fig. 2.10 Scheme of the Raman active transition. In black the electronic ground state and its excited vibrational state. In blue the virtual states involved in the transition.

Stokes Raman scattering is a process in which an electron is excited from the ground level and falls into an excited vibrational level.

It involves energy absorption by the system thus Stokes Raman scattered light has less energy (longer wavelength) than incident light. Conversely, anti-Stokes Raman scattering is a process in which an electron is excited from an excited vibrational level to the ground level. It involves an energy transfer to the scattered photon thus, anti-Stokes Raman scattered light has higher energy (shorter wavelength) than incident light. In the experimental set-up, the radiation incoming from the illuminated spot is collected through a lens, sent through a monochromator, filtered with a notch-filter (to eliminate the elastic scattering component), and dispersed into a detector.

2.8.1 RAMAN ON GRAPHENE AND 2D MATERIALS

Graphene has two atoms per unit cell, this implies six normal modes two of which are doubly degenerate at Γ in the BZ. Its Raman spectrum is very similar to the graphite one, however peaks such as that labeled C, which is present in graphite and represents the shearing force between different layers, are absent in single layer graphene. The main peaks for single layer graphene are the ones related to the E_{2g} and A_{1g} normal modes depicted in Fig. 2.11.

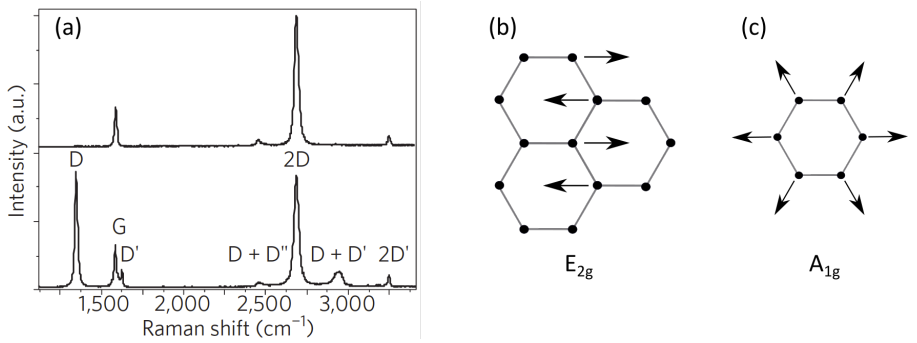

Fig. 2.11 Raman spectrum of pristine graphene showed on the top. On the bottom the Raman spectrum of defective graphene is depicted. The D and D' peaks are observable just in presence of defects. From[115]. The normal modes responsible for the G (E2g) and 2D (A1g) peak are sketched on the right.

The G peak corresponds to the high-frequency E_{2g} phonon at the **Γ** point of the BZ. The D peak is due to the A_{1g} breathing modes related to transvers optical phonons at the corner K of the BZ of six-atom rings. Due to conservation of momentum, it requires a defect to be activated. In samples with defects, the overall momentum conservation can be satisfied by adding an electron-defect scattering event to the process.[115]. The mechanism involved in this process is called double resonance and it consists in an intravalley process that connects two points belonging to the same cone around K (or K′). This is the same mechanism that gives the so-

called D′ peak. The 2D peak is the most important peak for graphene and gives useful information about quality, doping and number of layers. It is a D-peak overtone, (in the same way 2D′ peak is the D′ overtone). Because the 2D and 2D′ peaks originate from a process where momentum conservation is satisfied by two phonons with opposite wave vectors, no defects are required for their activation, and are thus always present[115]. The position of the 2D peak is centered at ~2700 cm^{-1} and the G peak at ~1580 cm^{-1}. Doping, defects[116] or strain[117] affects the relative position of the two peaks. Raman spectroscopy has been proven to be a good technique also to investigate TMDs[118–120]. In this work, it is extensively used to probe WS_2 layers. Raman signal is strongly dependent from the wavelength and in some cases partially overlaps with the photoluminescence emission of the material[121]. The Raman active mode of WS_2 are reported in Fig. 2.12. The A_{1g} mode is an out-of-plane vibration involving only the chalcogen atoms while the E_{2g}^1 mode involves in-plane displacement of transition metal and chalcogen atoms[121,122]. Moreover, another Raman active mode is a zone-edge mode activated by disorder, which has been identified as the longitudinal acoustic mode at the M point, LA(M). WS2 is usually studied by using different wavelengths (i.e., 633 nm, 473 nm and 532 (or 514) nm). Depending on the wavelength, to evaluate the number of layers one has to consider different quantities, such as the distance between the main peaks, relative height and the full-width-at-half-maximum (FWHM). However, in this work the 532 nm laser only has been used therefore, only those features will be summarized. The main peaks are in the following positions:

- 2LA @ 352 cm^{-1}
- A_{1g} @ 417 cm^{-1}
- E_{2g}^1 @ 355 cm^{-1}

2LA and E_{2g}^1 peaks partially overlaps. This makes quite difficult to identify the right position of the two with the proper fit. However, once recognized E_{2g}^1 position and height, the number of layers is extrapolated from the relative intensity with respect to the SiO_2 peak at 520 cm^{-1}. Nevertheless, if the substrate is Si-free another useful quantity is the relative height of 2LA and A_{1g} peak[121].

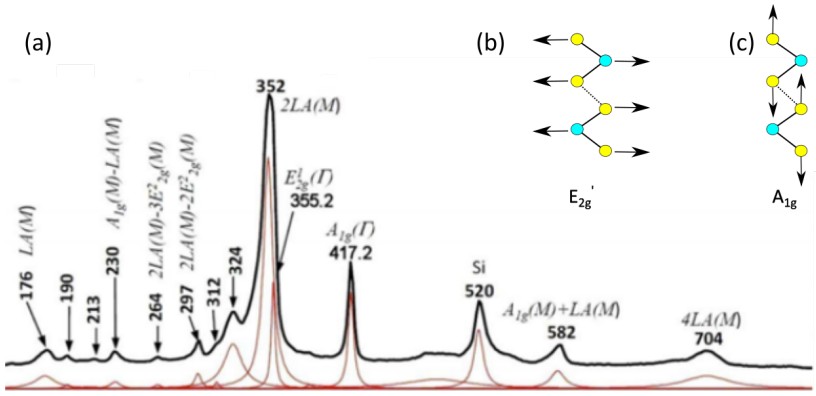

Fig. 2.12 WS_2 Raman spectrum take with 514nm excitation light. All the main peaks and their overtone are highlighted From [121]. On the left the two main phonon modes.

2.9 PHOTOLUMINESCENCE

PL is light emission from any form of matter after the absorption of electromagnetic radiation. Light with energy $\hbar\omega > E_g$ is shone on the sample, where E_g is the band gap energy which, for TMDs, spans in the visible range[8,53]. The charged carriers will occupy an excited state adsorbing a photon and subsequently relax on the ground state emitting another photon. The nature of the emitted photons depends on the energy gap and on the binding energy of the electron-hole pair (exciton) that will be created after the excitation of the electron in upper states. The

hydrogen-like particle will therefore form an energy level below the minimum of the conduction band at energies:

$$E_{X(n)} = \frac{(m_r/m_0)}{\varepsilon^2}\frac{1}{n^2}Ry \qquad (14)$$

where $m_r = \frac{m_e \cdot m_h}{m_e + m_h}$ is the reduced mass of electrons (m_e) and holes (m_h), ε is the dielectric constant, n is an integer number which identifies the number of the electronic level and $Ry = 13.6$ eV is the energy of the ground state of the hydrogen atom. For TMDs, thanks to very low electronic screening, $E_{X(n)}$ can be of the order of hundreds of meV[123,124]. Also, the photon emission subsequent to the recombination of the electron hole caused by the electrostatic potential can preserve the information carried by the polarization of the incident light[65]. Moreover the exciton lifetime is related to the carrier dynamics in the material and can provide an important picture of the excited states in 2d semiconductors[20]. This feature is particularly interesting in TMDs; thanks to the peculiar selection rules imposed by the symmetry of the system and to the strong spin-orbit coupling, it is possible to promote selectively spin-polarized carriers from one of the two valleys in K or K'. Photoluminescence experiments can therefore provide useful information regarding the spin-polarized carrier dynamics in the system.

2.10 TRANSMISSION ELECTRON MICROSCOPY

TEM is a microscopy technique that provides high-resolution information regarding the structure of the investigated material. In TEM electrons are transmitted through the sample to form an image that is magnified and focused into an imaging device. Since the electrons collected are the ones

transmitted through the sample, the latter has to be very thin (max 100 nm) and suspended on a grid. TEM instruments are capable of imaging with a resolution high enough to resolve a single column of atoms, owing to the small de Broglie wavelength of electrons. Also, by adopting a TEM set-up a number of different analyses such as, for instance, selected area electron diffraction (SAED), can be performed. SAED is used in this work and performed by selecting the area of the specimen from which one can obtain a diffraction image.

2.11 SCANNING ELECTRON MICROSCOPY

Scanning electron microscopy (SEM) allows to obtain images of a sample by scanning its surface with a focused beam of electrons. The initial mechanism of electron acceleration towards the sample surface is very similar to that operated in LEEM. The electron beam is accelerated by mean of an electromagnetic field in high vacuum to a few keV on the selected area. The difference with LEEM is that the electrons are not slowed down and impinge on the substrate with relatively high energy. The impinging electron beam penetrates the substrate in a *pear*–like shaped volume, called interacting volume, whose size depends on the incoming electron energy, atomic number and density of the specimen.

The image is reconstructed collecting the outcoming electrons that can be distinguished according to the different kind of interaction that they experience. The two principal detection modes are *backscattering* and *secondary electrons*. Backscattered electrons experience elastic scattering with the nucleus. Therefore, they are sensitive to the atomic number of the target. Collecting electrons at different angles allows also reconstructing a topological image of the system. Conversely, *secondary electrons* mode involves particles that are emitted by core levels of the investigated

material, originated by inelastic scattering with the incident beam. Their energy is < 50 eV, thus considering the IMFP described above, they come from the first few nm of the material and deliver information about the topography of the surface.

2.12 ENERGY-DISPERSIVE X-RAY SPECTROSCOPY

Energy dispersive X-ray spectroscopy (EDX) is an analytical technique used for chemical characterization. It relies on x-rays emitted from core levels of the atoms of the investigated specimen, consequent to the extraction of a core electron by means of another energetic electron (~10keV) or x-ray radiation. The hole left behind attracts another electron that will recombine in the lower empty level emitting highly energetic radiation, which is detected and its energy is unique for a given atomic specie. The EDX set-up used in this work exploits a source of electrons as means of atomic excitation. The detectors are embedded in a SEM set up. Therefore, it is also possible to perform imaging of the selected target. SEM electromagnetic lens allows for the investigation of a very small spot size, down to 1μm diameter.

3 2D MATERIALS SYNTHESIS

Since the time graphene has proven to be an outstanding material, capable of facing the modern challenges of technology development, a major goal of the scientific community has been to scale up its production. As already introduced, exfoliation is cumbersome and not scalable[125]. Recently, advances in CVD-based techniques have allowed for producing graphene with qualities comparable to those of the mechanically cleaved flakes[1]. Also, the peculiar electronic properties and applicative prospects of other 2d materials such as TMDs have triggered a massive research in large-scale production for these materials as well[24,67,126,127]. However, at the early times of this research work, results on the synthesis of 2d vertical heterostacks were lacking. In section 3.1, large-scale synthesis of graphene is discussed and the experimental approaches used in this work are reported. In paragraph 4.2, focus is given to the CVD growth of WS_2 on bulk substrates and ultimately on 2d layers, the first novel contribution of this research work.

3.1 GRAPHENE GROWTH

As introduced in paragraph 1.2.3, there are mainly two ways to produce scalable graphene with high-crystallinity[43].

- Thermal decomposition of SiC
- CVD on metals

In the following sections, these bottom-up production techniques will be discussed as they have been extensively adopted in this work. paragraph 3.1.1 introduces the basic principles behind thermal decomposition of SiC,

discusses the quality of EG and presents hydrogen intercalation as a solution to improve the transport properties EG on SiC(0001). Paragraph 3.1.2 presents the experimental approach particularly adopted in this work to obtain EG on SiC(0001) and to intercalate it with hydrogen. EG on SiC(0001) was used as the substrate to synthesize WS2 in the studies reported in Paragraph 4.2 and in all the following Chapters. Intercalated EG samples were adopted in appendix C. In 3.1.3 and 3.1.4 the state-of-the-art for the CVD of graphene on metals and our experimental approach are presented, respectively. Large-grain CVD graphene crystals in Chapter 7.

3.1.1 *GRAPHENE FROM THERMAL DECOMPOSITION OF SILICON CARBIDE*

The production of graphite from SiC has been known for a long time[128,129]. Whereby, it is straightforward to think that by tuning the growth parameters, it is possible to obtain a single graphite layer, i.e. graphene. The mechanism behind the formation of graphene involves the desorption of Si atoms from the topmost surface. Such decomposition of the SiC crystal is triggered by heating it in vacuum at temperatures above 1050°C. At this temperature Si starts to sublimate and leaves behind a C rich layer. This process has been first reported by Berger et. al.[45] for the Si-face of SiC and then extended to the C-face[130]. Subsequently, Emtsev and coworkers have demonstrated how to obtain high quality and wafer scale graphene from SiC(0001) by implementing the process in a high pressure of Ar[46].
SiC is a crystal formed by silicon and carbon atoms, whose basic unit is made of a Si atom placed at the center of a tetrahedral structure with C at the vertexes with side of 3.08 Å (Fig. 3.1(a)). The Si atoms at the center of the tetrahedron and the carbon atoms forming the base on which the tetrahedron stands form the so-called bilayer Fig. 3.1(a).

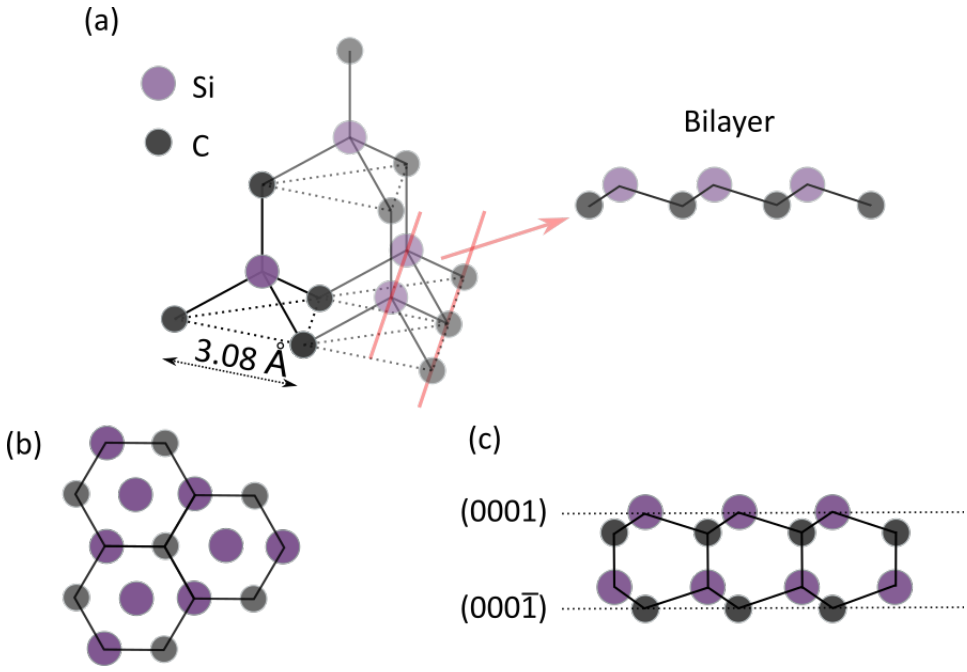

Fig. 3.1SiC crystal structure (a) top view of the plane orthogonal to the (0001) direction. (b) side view of the crystal with the (0001) and (000$\bar{1}$) planes, representing the Si and C face respectively.

The tetrahedrons can be stacked in different ways, whose sequence determines the so-called polytype. There are more than 250 polytypes that can be grouped, according to their symmetry, in cubic, hexagonal and rombohedral[131]. For symmetry reasons, the most used to obtain graphene are the hexagonal ones known as 4H- and 6H-SiC. 4H-SiC is determined by a stacking order ABCB while 6H-SiC by a stacking order ABCACB (Fig. 3.2(a)and (b), respectively). 4H- and 6H-SiC show different features such as different band gaps, namely 3.26 eV for 4H and 3.02 for 6H[132,133].

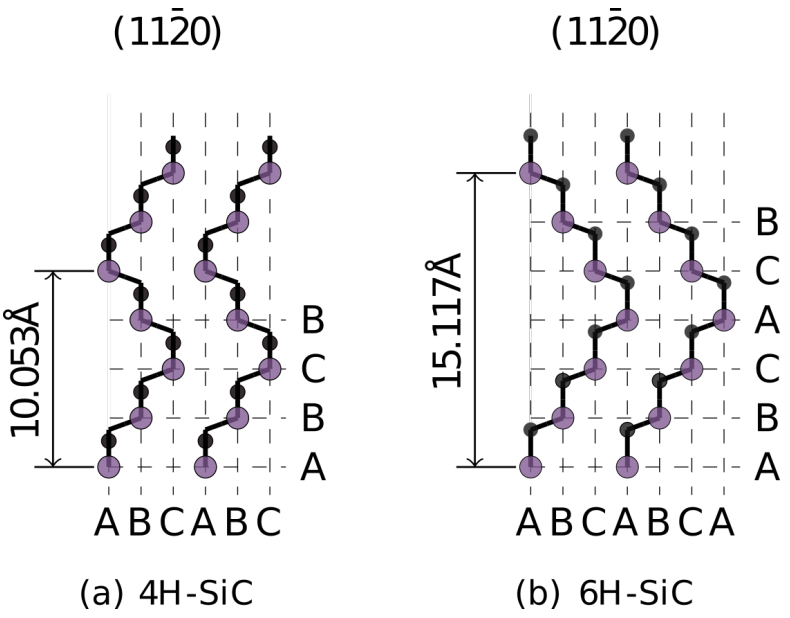

Fig. 3.2 Two SiC politypes used for graphene synthesis. SiC-4H (a) and SiC-6H (b). They show ABCB and ABCACB stacking respectively

The Miller indices (0001) and (000$\bar{1}$) determine a hexagonal in-plane crystal structure terminated with silicon (i.e., Si-face) and carbon atoms (i.e., C-face), respectively (Fig. 3.1 (b)). Three Si-C bilayer slabs are needed to have enough C atoms to form a single graphene layer. When applying the thermal decomposition process on the Si-face of SiC, the first carbon layer generated via thermal decomposition does not show the typical electronic properties of graphene[47] (Fig. 3.3(a)). This first carbon-rich layer, called buffer layer or zero layer, has the same topological configuration as graphene, although about 30% of its carbon atoms are partially covalently bonded to the topmost Si-atoms of the SiC reconstruction underneath[48].

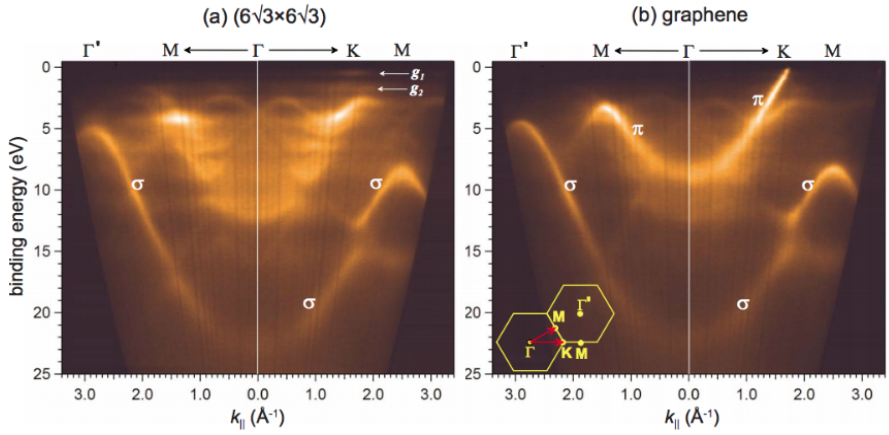

Fig. 3.3 Band structure measured via ARPES of buffer layer on top of SiC(0001) (a) and of graphene on top of buffer layer and SiC (0001). The inset shows the hexagonal BZ of graphene. Adapted from [47].

This gives an epitaxial register to the top structure. The different crystal structure between the underlying SiC crystal and the zero layer gives rise to a superperiodicity called $6\sqrt{3} \times 6\sqrt{3}\,R30$, whose length of the unit cell is 32 Å, which corresponds to 13 graphene cells (Fig. 3.4). By prolonging the growth time, Si sublimation keeps proceeding. At this time, underneath the buffer layer, another carbon rich structure forms, and the one who was previously addressed as the zero layer, now unbonded from the substrate, displays the typical features of graphene such as the Dirac cone (Fig. 3.3(b)).

This growth process is an inside-out process that gradually consumes the SiC substrate and it is substantially different from standard epitaxial techniques where materials are deposited on a substrate. In Fig. 3.5 the full system is reported. It shows the buffer layer partially bonded to the SiC substrate and the graphene layer standing on top.

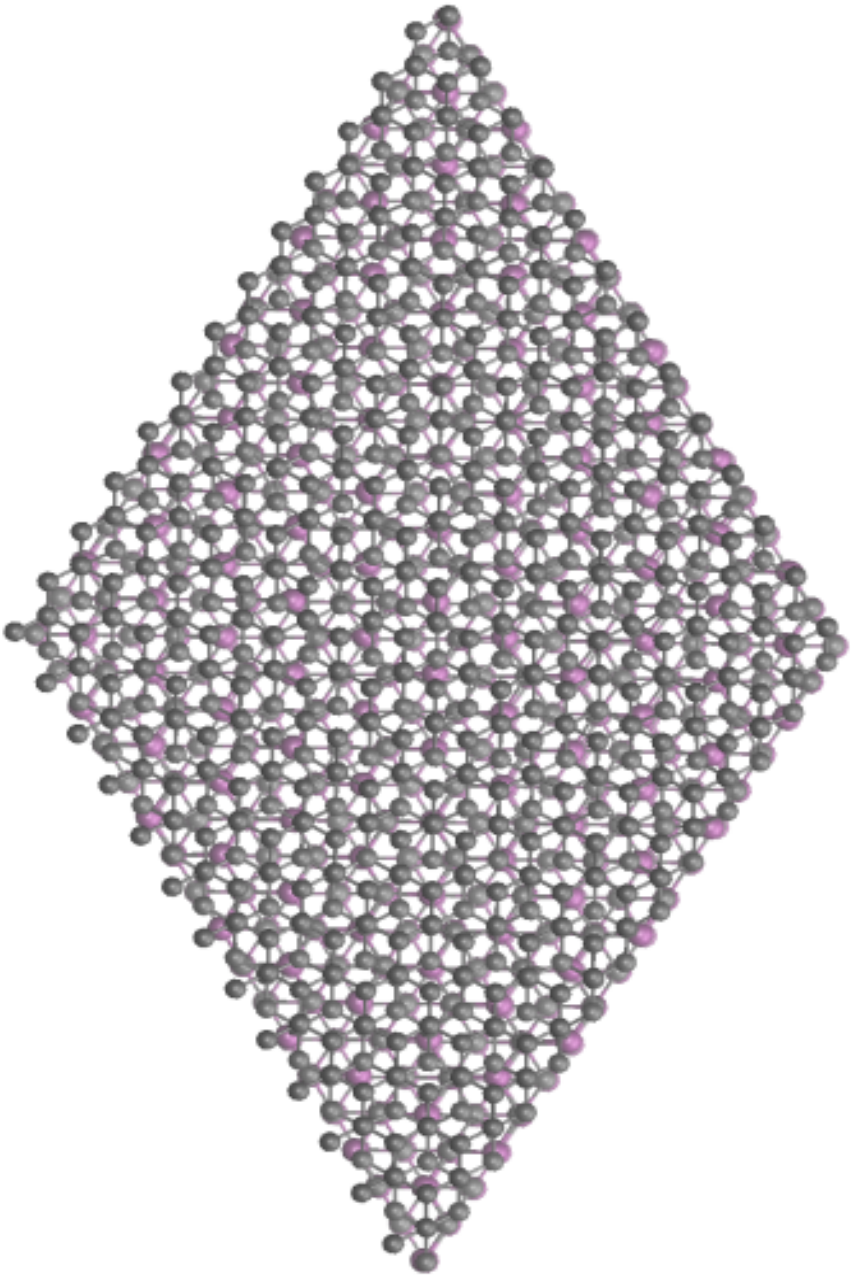

Fig. 3.4 $\mathbf{6\sqrt{3}}$ cell relative to the reconstruction of Buffer layer on top of SiC (0001)

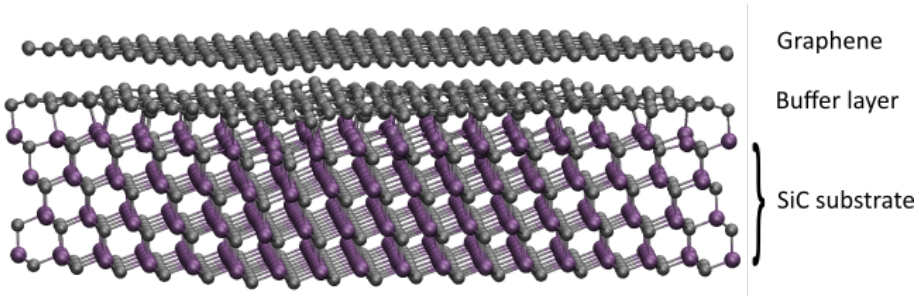

Fig. 3.5 Full slab displaying the SiC(0001) topmost surface, the buffer layer and a graphene monolayer.

The graphene grown in this way present a distinct n-type doping and typical carrier mobilities at room temperature of about 1000 cm^2/Vs [134], far from the theoretical limit of few hundreds of thousands[135]. Indeed, it has been shown that the presence of the buffer layer is detrimental to the transport properties of monolayer graphene on SiC(0001)[136]. This is mainly due to phonon scattering arising from the coupling with the buffer layer, which is also responsible for the pinning of the Fermi level in graphene 450 meV higher than the neutrality point[46,137].

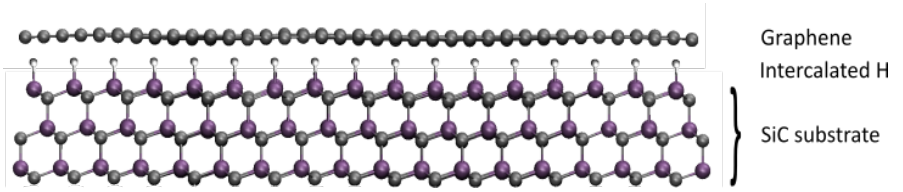

Fig. 3.6 Structure of QFMLG. White atoms represent H intercalants

A way to overcome this issue has been proposed by Riedl and co-workers with the introduction of the hydrogen-intercalation technique, which consists in annealing a buffer layer at high temperature (>900°C) in hydrogen atmosphere[138]. In this way hydrogen intercalates between the

SiC substrate and the buffer-layer so that C-Si bonds are replaced with H-Si bonds (Fig. 3.6). Hence, the buffer layer becomes a *quasi-free standing monolayer graphene* (QFMLG). Charge carriers in intercalated graphene are no longer influenced by the phonons in the buffer layer, now absent. QFMLG displays carrier RT mobilities up to 11000 $cm^2/(Vs)$[139].

3.1.2 PREPARATION OF GRAPHENE ON SIC (0001): *EXPERIMENTAL DETAILS*

Commercially available 4H- and 6H-SiC(0001) wafers typically present mechanical scratches and damages (as well as chemical contaminants) coming from wafer polishing. This implies that their surfaces have to be properly prepared (i.e., cleaned and smoothed) to improve the quality and homogeneity of the graphene obtained.

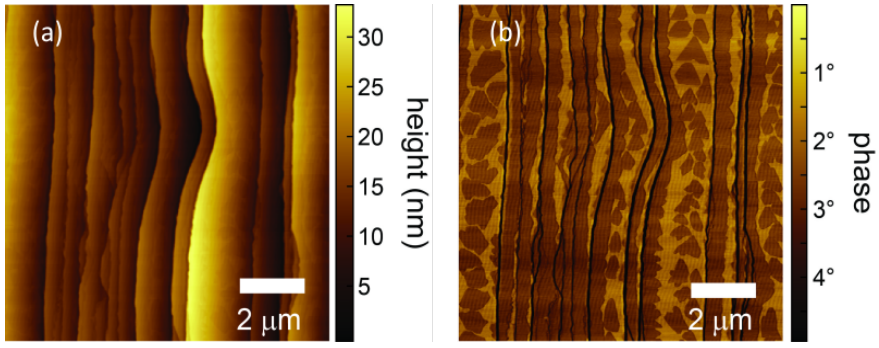

Fig. 3.7 AFM scan of partial grown graphene on SiC (0001). (a) Height signal showing the terraces arising from the hydrogen etching. (b) Phase signal in which the contrast is due either to graphene (darker) or buffer layer (brighter).

In this work SiC surface preparation was carried on with a standard process which involves three steps. The first is a treatment with piranha solution (H_2SO_4:H_2O_2 - 3:1 for 10 minutes) in order to remove organic contaminants. Then the sample was put in hydrofluoridric acid (HF) in a

HF:H_2O solution 1:10 for 1 minute. This is functional for removing native oxide on the surface[140]. Subsequently, in order to create atomically flat surfaces, the sample was placed in a resistively heated cold wall reactor (HT-BM, Aixtron) and etched at 1250°C for ~5 minutes in H_2/Ar environment[141,142]. Hydrogen etching is a well-known technique used to produce atomically flat surfaces[141] and has been optimized by our group in the specific Aixtron reactor used[143]. Fig. 3.7(a) reports a typical AFM micrograph of a SiC surface subjected to etching. Atomic terraces are evident, whose width is determined by the miscut angle with respect to the basal plane (0001), and whose height (in absence of stacking faults) is a multiple of the "unit cell" of the adopted polytype. In the same reactor, monolayer graphene was obtained by heating the substrate at 1400°C in an Ar environment (750mbar) for approximately 10 minutes. This recipe was adapted in our reactor from that originally developed by Emtsev and coworkers[46]. In Fig. 3.7(b) an AFM phase-scan of a partial growth of graphene obtained in our reactor is reported. It is possible to observe that graphene growth (darker contrast) consistently starts from the edges of the atomic terraces. This is in agreement with what reported in reference[144]. However, in our case, preferential desorption also in the center of the terraces was observed (i.e., graphene island formation). Raman analysis on the sample (Fig. 3.8(a) confirms the presence of monolayer graphene at the terrace edges and locally in central islands as visualized via AFM. Panel (c) indeed displays the typical graphene spectrum (as introduced in paragraph 2.8.1). Within the areas where no graphene was grown, the typical Raman spectrum of SiC was measured (Fig. 3.8(b)).

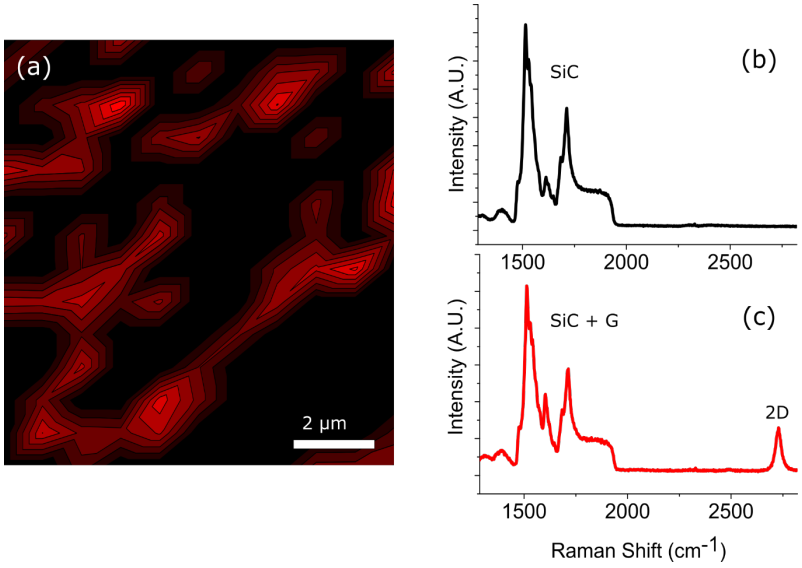

Fig. 3.8 (a) Raman map of graphene on SiC(0001) of graphene 2D peak. (b) and (c) Raman spectrum from buffer layer area (black) and graphene areas (red)

In order to move from partial to continuous monolayer graphene coverage the growth time was prolonged. When QFMLG has been adopted in this work, it was produced in the following way. The as-grown buffer layer graphene grown on SiC sample was introduced in the HT-BM reactor and annealed at 900 °C for 20 minutes in H_2/Ar with a flow of 500 s.c.c.m. for both gases.

3.1.3 GRAPHENE VIA CVD ON METALS.

Graphene from thermal decomposition of SiC is a fully scalable technique to obtain graphene. However, due to the high cost of SiC wafers, such approach is not cost-effective. Furthermore, one of the major challenge that has to be faced nowadays is the integration of graphene technology in existing semiconductor fabrication processes, mostly oriented on standard Si-based CMOS technology. This has led to other approaches to

synthetize graphene, in particular taking advantage of the catalytic behavior of transition metals, which facilitates the formation of graphene films by lowering the activation energy of the involved reactions. Metallic substrate such as, platinum (Pt)[145] iridium (Ir)[146] nickel (Ni)[147,148] or Cu[50,149] have been proven to be good candidates for graphene growth. Also, both single-crystals specimens and polycrystalline foils have been largely adopted and clearly influence crystallinity of the resulting graphene. To date, because of cost, and easiness in substrate etchability, Ni and Cu foils are the most popular choices. The growth mechanism on the two substrates is very different. Ni has a very high carbon solubility[150,151]. At the high temperatures needed for graphene growth, a high number of C atoms are absorbed in the Ni foil. Such atoms will subsequently segregate on the surface forming the graphene layer[49]. On the other hand, C solubility is low on Cu. This means that growth of graphene on Cu is mostly a surface-mediated process with an almost negligible contribute from carbon segregation.

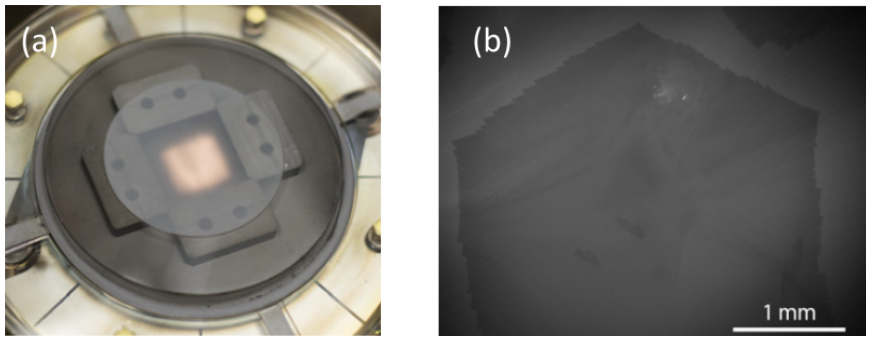

Fig. 3.9 (a)Quartz enclosure. (b) SEM image of a single crystal grain 3mm wide. From [50]

Therefore, thanks to the self-terminating nature of the process, monolayer graphene is typically obtained. In recent works, it has been shown that

oxygen contained within the foil as well as adsorbed on the Cu surface, plays a relevant role for the obtainment of large single-grain graphene[152]. After appropriate Cu foil preparation, such as electropolishing and thermal annealing, and in-situ (or ex-situ) Cu oxidation, it is nowadays possible to produce large single-crystal monolayer graphene of millimeter or even centimeter dimension[51]. Such crystals present remarkable mobilities[1].

3.1.4 PREPARATION OF GRAPHENE ON CU FOIL: EXPERIMENTAL DETAILS

In this work, graphene deposition was performed on electropolished 25 μm thick Cu foils (Alfa Aesar, purity 99.8%). The foils were oxidized as a consequence of the electropolishing and extensively annealed in an inert atmosphere (i.e., Ar) within a 4-inch cold-wall CVD system (Aixtron BM)[50]. Graphene films were subsequently synthesized in the same reactor at a pressure of 25 mbar. CH_4 was used as carbon precursor and Ar as carrier gas with fluxes of 1 s.c.c.m. and 900 s.c.c.m., respectively. Growth temperature was kept as close as possible to the Cu melting point (i.e., growth T~1040°C) as this allows for improving the quality of the grown graphene[50]. To achieve more reproducible atmospheric and thermal conditions and to reduce the effective gas flow, the sample was contained in a custom-made quartz enclosure as shown in Fig. 3.9(a)[50]. Limiting the carbon impingement flux on the Cu foil by adopting such enclosure and/or a "Cu-pocket" configuration[153] was found to be instrumental to reduce graphene nucleation. Ultimately, single-crystal graphene grains with lateral dimensions up to 3 mm (Fig. 3.9(b)) were synthetized in just 3 hours[50] by: (i) using *ex situ* oxidized foils; (ii) reducing the C impingement flux; (iii) annealing in inert atmosphere.

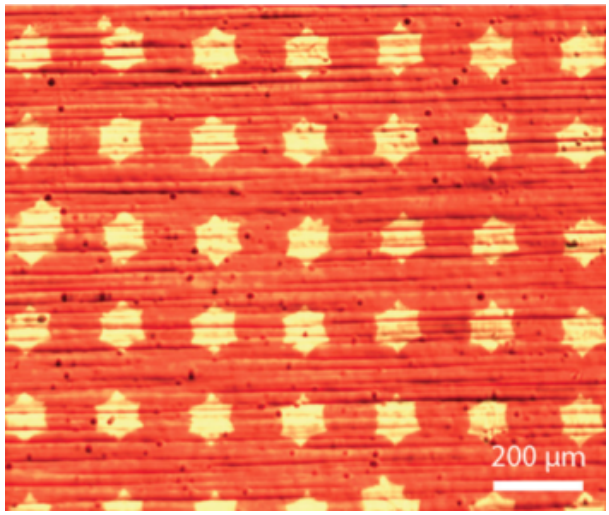

Fig. 3.10 Optical image of Gr array on Cu foil obtained with deterministic patterning growth. Adapted from [154]

Besides large graphene crystals, CVD graphene was also grown in a deterministic way, by creating large area graphene arrays. Such arrays were grown by adopting the patterned deterministic approach recently developed by our group[154]. Nano-disks of chromium (Cr), 25 nm thick and 5µm wide, were evaporated on the Cu foil by means of optical lithography. Such nano-disks acted as patterned nucleation points for graphene. By adopting a growth process similar to that described above, graphene arrays with controlled lateral size were obtained (Fig. 3.10). Interestingly Cr seeds were completely removed during the growth[154]. The CVD graphene grown on Cu foil used on this work was transferred either on SiO_2 or on SiC substrates by adopting the semi-dry transfer process described in [50].

3.2 TUNGSTEN DISULPHIDE GROWTH

The growth of TMDs has been being a major task in the last years within the 2d materials community and various approaches have been attempted

with different results (as discussed in paragraph 1.3.3). Here we focus on the approach used in this work, namely CVD growth. In particular, after a general introduction to the general CVD growth mechanisms, we report and discuss the approach developed to grow WS_2 on classical bulk substrates. These growths were performed to benchmark our process with others present in literature[18,24,26,68]. Then, we report on the growth of WS_2 on the 2d substrates EG, CVD graphene and h-BN. We discuss how growth can be tuned to obtain either single crystals, continuous monolayer and continuous bilayer WS_2. Single crystal WS_2 on EG is used for fundamental studies in Chapters 4 and 5. Continuous ML WS_2 on EG is adopted to implement optoelectronic devices in Chapter 6. Continuous BL on EG, CVD graphene and h-BN is adopted for optical studies in Chapter 7.

3.2.1 CHEMICAL VAPOR DEPOSITION

In this work we implement CVD growth of WS_2 from solid precursors. The strengths of this technique are cost-effectiveness and a typically rather simple growth chemistry. In the past, a number of works have reported the successful synthesis of WS_2 on typical bulk crystals such as SiO_2 and sapphire[18,24,26,155]. Typically, as already introduced in chapter 1, S and WO_3 powders are adopted as precursors[68], although in a few works metallization of the target substrate and subsequent sulfurization are reported[73,156].The reaction is generally carried on within horizontal quartz tubes and the position of the target substrate has been shown to affect the quality of the result. The process that takes place is a two-step reaction involving a redox and a substitution process. Starting from W and S, the reaction is the following:

$$WO_3 + S \rightarrow WO_2 + SO + WS_2$$

The SO is volatile and pumped away while the WS_2 molecules form the layer on the substrate. The reaction between WO_3 and S occurs in vapor phase similarly to what reported for MoS_2[67].

There are many factors whose variability influences the ultimate quality and crystallinity of the obtained WS_2 material. Here are listed the most relevant:

1) The substrate. Its nanoscale morphology and crystallinity are crucial and clearly different results are obtained when using, for instance, SiO_2, SiC, or graphene.
2) The temperature. This parameter affects mostly the atom/molecule mobility on top of the substrate. With a temperature that is too high, the surface diffusion is fast enough for the adatoms to reach the most energetically favorable sites, eventually leading to the formation of a 3d island, or in the worst scenario, to the desorption of the molecules. Conversely, if the temperature is too low, it is the reaction itself that is not taking place.
3) Precursor vapor pressure. This parameter is directly linked to the amount of solid precursors adopted and to the flux and nature of the carrier gas. Indeed, the vapor pressure of the reactants has to be properly balanced and high enough to enable the reaction to take place.

At the time when this research started, the existent literature reported on the synthesis of single grain (up to 370 μm) WS_2 on SiO_2[68], and continuous polycrystalline WS_2 films on SiO_2[26]. SiO_2 is the ideal substrate for direct growth if a back-gated device wants to be implemented, although the amorphous nature of the surface is not ideal as a template for the growth of a crystalline film. Concerning 2d materials, Okada et al reported in August 2014 on the growth of micron-sized single-grains WS_2 on h-BN[94].

On the other hand, at that time, no report of WS2 synthesis on graphene was present.

3.2.2 PROCESS DEVELOPED FOR THE CVD SYNTHESIS OF WS_2

In this section, we discuss the approach developed specifically to synthetize WS_2 on a number of substrates, ranging from bulk to 2d. First, we concentrate on the growth of WS_2 on a classical bulk substrate such as SiO_2. This task was carried on as a first step instrumental to the definition of a working recipe necessary to undertake the more challenging task of synthesis on 2d substrates.

To synthesize WS_2 on SiO_2, we adopted a classical vapor-phase approach using as precursors S (Sigma Aldrich, 99.998%) and WO_3 (Sigma Aldrich, 99.995%) powders. The process was performed within a 2.5-inches horizontal hot-wall furnace (Lenton PTF) (Fig. 3.11). The furnace comprises an inner hot zone, in which WO_3 was spread over a crucible, and a cooler outer zone in which S was placed (about ~15 cm away from the hot-zone edge). A resistive heating belt was wrapped around the upstream zone where S was kept to separately control its temperature. Supplying a voltage, it can reach 200°C in a few seconds, ensuring the right conditions to keep S in gas form. During growth optimization, temperature, chamber pressure and target substrate were varied once at the time, while all the other parameters and geometrical aspects were kept fixed and chosen according to literature (process time 1 hr, distance of the substrate from WO_3 powder at 2 cm). The growth temperature within the hot-zone was varied between 850°C and 950°C. The highest value was dictated by a technical limit of the furnace, the lowest by the chemistry of the reaction. The final temperature was reached at a rate of 10°C/s. The substrates were placed face-up next to the WO_3 powder.

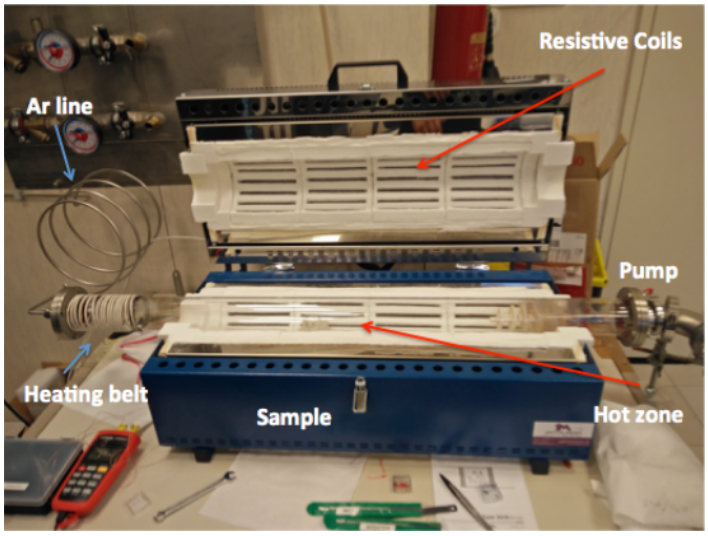

Fig. 3.11 Lenton furnace used to synthetize WS_2 with highlighted components. S is placed inside the heating belt, whereas the WO3 powder is placed upstream next to the substrate.

Before the temperature ramp up, the chamber was pumped down to a pressure of ~$5x10^{-2}$ mbar. Argon was flowed during the temperature ramp-up with a flux of 500 s.c.c.m., leading to a pressure of 4.6 mbar, which keeps the sulfur solid. After reaching the target temperature, the Ar flow was suddenly reduced, lowering the chamber pressure in a very short time frame, and thus initiating sulfur evaporation and WO_3 sulfurization. At each different temperature, experiments with Ar flows spanning from 8 s.c.c.m. to 500 s.c.c.m, corresponding to chamber pressures of 0.6 mbar and 4.6 mbar, respectively, were performed. In all these initial growths SiO_2 was adopted as a substrate. The syntheses performed by changing the process parameters were instrumental to model the growth mechanism in this specific furnace and in particular to investigate how temperature and carrier gas flow influenced the growth efficiency. The flux of the carrier gas not only determines the delivery

rates of the reactants but also sets the pressure in the chamber and sulfur evaporation.

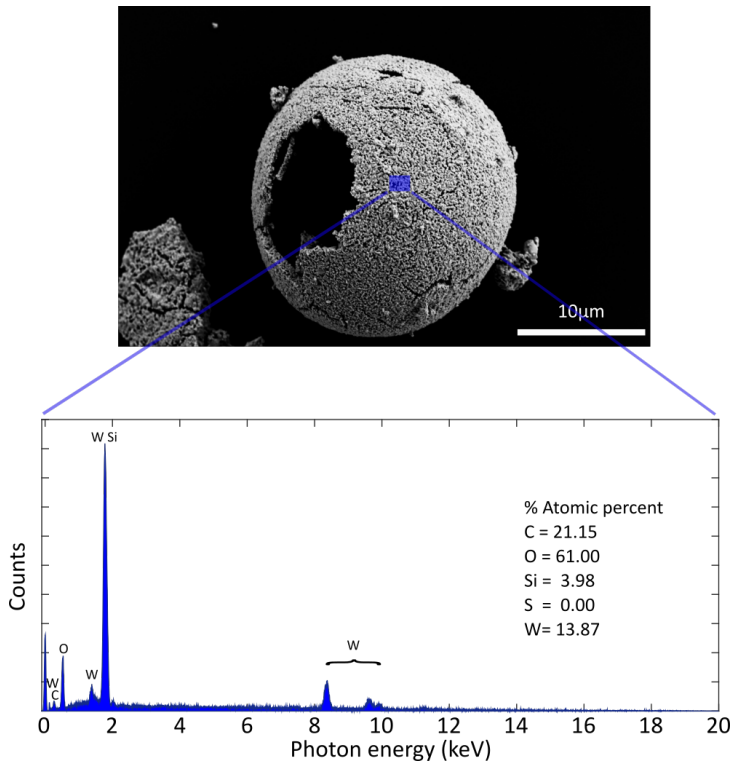

Fig. 3.12 SEM image of WOx micro particle delivered on the substrate. Its composition is determined by EDX analysis (Bottom panel)

For a higher chamber pressure, the sulfur evaporation rate is lower, therefore the reaction stoichiometry shall be unbalanced towards a lack of sulfur. When combining a maximum Ar flux (i.e., 4.6 mbar chamber pressure) with a low growth temperature of 850 °C we observed that on the SiO_2 surface byproducts were always formed. Fig. 3.12 reports the SEM micrograph and the EDX spectrum of a hollow particle, a typical byproduct obtained in these experimental conditions. The particle appears to be mainly a WO_x compound, thus confirming that the growth environment was suffering –as expected – of sulfur deficiency.

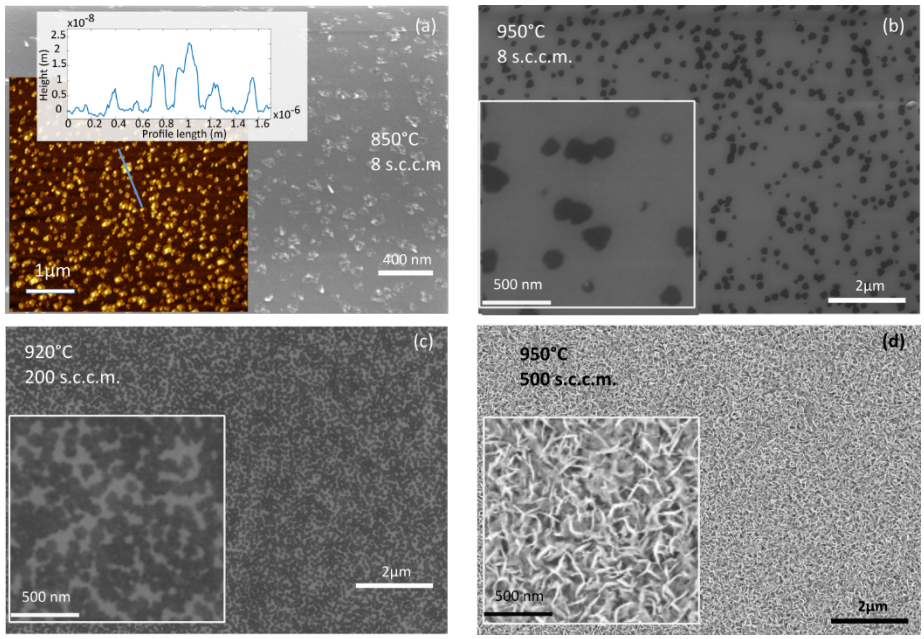

Fig. 3.13 SEM images of samples grown at different conditions (a) 850°C 8 s.c.c.m (inset showing AFM topography image with relative height profile); (b) 950°C, 8s.c.c.m; (c) 920°C, 200 s.c.c.m; (d) 950°C, 500 s.c.c.m. Insets of (b-d) showing zoom-in of the relative panel.

However, for the experiments performed at 850°C, a sensible decrease in chamber pressure was not much beneficial towards the synthesis of WS_2. Indeed, within our system, such a low temperature approach never worked, differently from what reported in[25], where seeds are used to trigger the growth. Even in abundance of sulfur, when the pressure was set to 0.6 mbar (Ar flow = 8 s.c.c.m.) causing S faster evaporation, a large number of byproducts were observed. Fig. 3.13(a) reports a representative SEM image obtained when growing at 850°C at 0.6 mbar. As it can be seen, three-dimensional structures of ~100 nm are present. Their height is around 15 nm, as measured via AFM. The Raman spectrum collected on this sample shows a small peak located at around 540 nm and a faint and broad PL peak at around 620 nm (Fig. 3.14(a)), indicating that

WS_2 is present in low amount. Hence, such low temperatures do not favor the reaction leading to the formation of WS_2. Indeed, when increasing the temperature up to 950°C (Ar flow kept at 8 s.c.c.m.) larger grains with a diameter of about 200 nm WS_2 were formed (Fig. 3.13(b)).

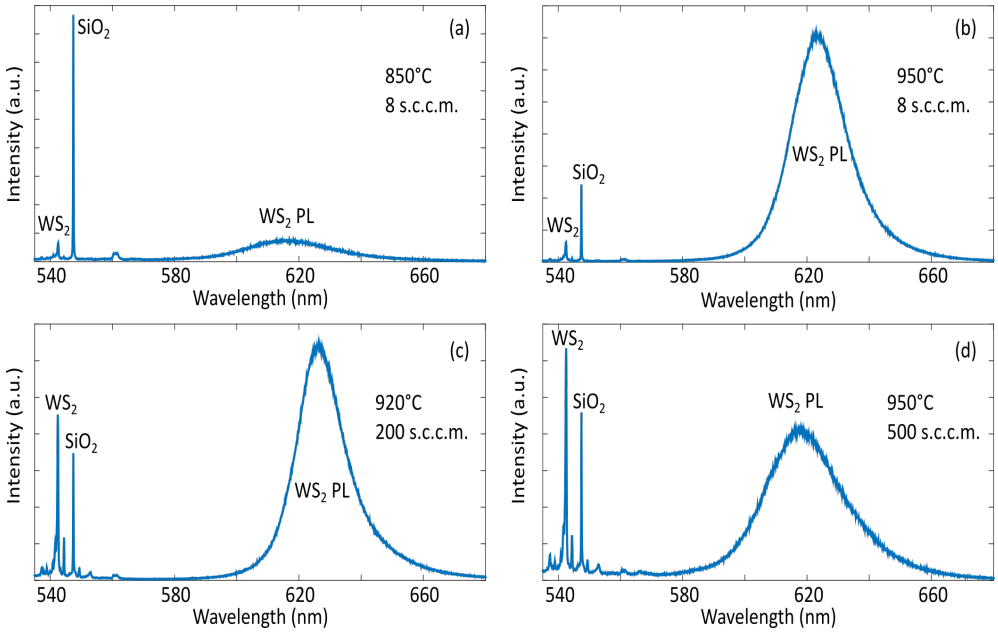

Fig. 3.14 Raman spectrum collected from samples grown under different conditions

The SEM zoomed-in image reported in the inset evidences that the grains are typically triangular – as expected for single-crystal WS_2[68] – therefore suggesting a successful synthesis of the TMD. The Raman spectrum collected on the sample (Fig. 3.14(b)) shows higher 2LA-WS_2/Si modes with respect to that observed in panel (a). This confirms that indeed the triangular crystals are WS_2. In addition, a very strong photoluminescence (PL) peak is visible which indicates that the TMD is monolayer. The WS_2 single-crystals obtained in this way have a lateral size which is however, smaller than that reported by other groups[26]. During this work, a different approach to increase the grain size of WS_2 was developed, leading to a

maximum size of about 10 μm. Such approach consists in inserting a 1 inch one-side sealed quartz-tube within the chamber to increase the growth pressure as described in detail in appendix A.

In order to create a continuous WS_2 film, we played with pressure and temperature to affect the molecule mean free path (λ) on a surface, the distance that the molecule can travel before scattering on another molecule and eventually taking part in the crystal formation. Considering the ideal gas picture, the relation $\lambda \propto \frac{T}{P}$ holds. By providing more energy to the system in terms of temperature, it is possible for the molecule to explore more than one site and stick to the most energetically favorable. In the extreme case, when the temperature is sufficiently high the molecules will start accumulating at the edge of the sample and start expanding from there. It is important to keep in mind that if enough energy to the system is given, but the mean free path is kept low (i.e., by setting high values of pressure), the molecules can start extending in the vertical direction rather than on the 2d plane. Interestingly, in agreement with the ideal picture, we observed an increased nucleation density when increasing the pressure and lowering the temperature (Fig. 3.13(c)). Indeed, the sample imaged in panel (c), grown at 920 °C and 2 mbar, presents more nucleation points than the sample imaged in panel (b), grown at 950 °C and 0.6 mbar. This is because the mean free path of the molecule is not high enough to reach the most favorable nucleation points and the molecules will therefore stick to higher relative minimum in the energy potential landscape. The Raman spectrum of the sample grown at 920 °C and 2 mbar is reported in Fig. 3.14(c) and shows a lower (than that in Fig. 3.14(b)), yet still very intense PL peak, probably due to bilayer patches (visible also in the inset of Fig. 3.13(c)). In addition, the 2LA intensity ratio of WS_2 over SiO_2 is higher than that in Fig. 3.14(b) because

of the higher coverage of WS_2 in the area probed by the Raman laser (i.e., about 1 μm). After these preliminary experiments, we found that the optimal temperature and pressure parameters to obtain a continuous film on SiO_2 are 880°C and 1 mbar, respectively. In the extreme condition of high temperature (950°C) and high pressure (4.6 mbar) the process proceeds towards the formation of vertical platelets (Fig. 3.13(d)). Despite being a structure far from the ideal triangular-flat-shape of WS_2, the Raman signal coming from this area (Fig. 3.14(d)) has the typical spectrum of mono-bilayer WS_2[121]. These kinds of structures have already been observed for MoS_2[157], however, a deeper study is required to understand the exact nature of what observed in Fig. 3.13(d).

Let's now investigate the influence of the substrate on WS2 growth. As described above, the synthesis is triggered by the evaporation of sulfur. The WS_2 molecule is first formed in vapor phase, and then is deposited on the substrate. At this point, the molecule-substrate interaction is fundamental to direct the crystal growth. Let us take into account the first molecule that is deposited on the surface. The mobility on the surface is bound to the quality of the substrate. An atomically flat and clean surface would offer the chance for the molecule to explore a wide area before finding a point that can trap it, and which would act as seeding point for the following molecules. This picture leads to the formation of isolated crystal that will grow with incoming "nutrients" (vapor phase WS_2 molecules). At fixed temperature and pressure, the higher is the roughness of the surface the higher is the nucleation point density[158]. This effect can be appreciated taking into account SiC as substrate for the growth. As described in section 3.1, hydrogen-etched SiC surfaces are atomically flat and therefore adopted for graphene growth. Conversely, commercially available SiC substrates present a rough surface with a

number of scratches arising from the mechanical polishing of the surface. In this case, it is easy to compare the different results obtained under the same growth condition. In Fig. 3.15(a) a SEM image of the hydrogen-etched SiC surface after WS_2 growth performed at 900°C and 1 mbar pressure is reported.

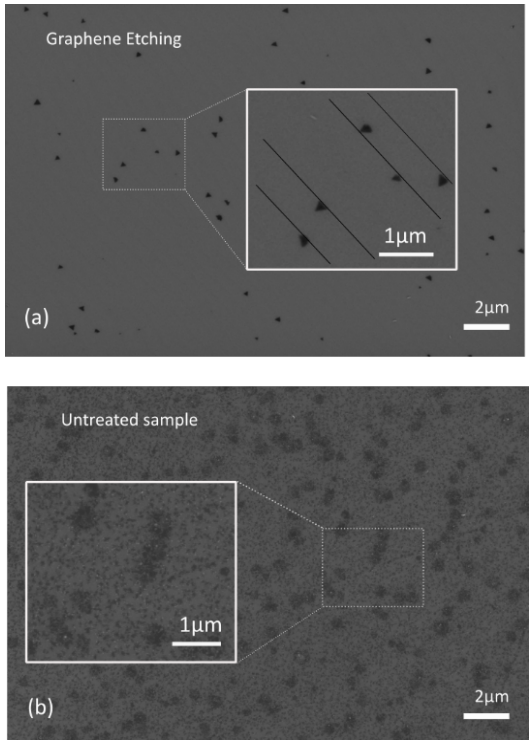

Fig. 3.15 SEM images of WS_2 grown on (a) SiC after H-etching, and (b) before surface preparation

The nucleation density is low and the WS_2 cover the 1-2% of the surface. In Fig. 3.15(b), WS_2 was grown with the same parameters on commercially available SiC. The nucleation points are significantly higher in number and preferentially located along the polishing scratches, with smaller grains occasionally forming darker clusters.

After having developed the growth of WS_2 on conventional bulk substrates, we now direct our attention to the growth of WS_2 on 2d materials such as graphene and h-BN. Ideally, these 2d surfaces are flat and with no dangling bonds. Given their extreme flatness, for the picture described above, one should expect an extremely inefficient growth. However, when using the same parameters reported for the growth on bare SiC (i.e., 900 °C and 1 mbar), on 2d substrates we surprisingly obtained a very efficient growth. Fig. 3.16(a) reports the growth of WS_2 obtained on EG on SiC. Large grains up to 1 μm are clearly visible and the TMD coverage on the EG substrate is estimated to be about 35%. A similar behavior is observed for WS2 on CVD graphene grown on Cu foil and subsequently transferred on SiC substrates (Fig. 3.16(b)). The TMD coverage on graphene is in this case about 50%. Even higher WS2 coverages are obtained on h-BN flakes exfoliated on SiC (Fig. 3.16(c)). For both CVD graphene and h-BN flakes, the WS_2 growth on the 2d material is remarkably more effective than on the SiC substrate around. In order to explain this unexpected behavior, one has to take into account the real morphology of the substrate. Indeed, in all these samples a relatively high number of "defective" points can be found. In the case of EG, preferential nucleation points are represented by the atomic terraces generated by the hydrogen etching process.

In the case of CVD graphene, they are represented by the wrinkles formed during the growth on Cu[159], and by stress-lines and chemical residues left from the transfer process. Analogously, the edges of the h-BN flake, its atomic lines and contaminants from the exfoliation step can act as a seeding point and trigger the nucleation of WS_2. Our experimental findings highlight that the growth of WS_2 on 2d materials is in fact extremely favorable. To tune WS_2 coverage also another parameter was modified in

our experiments: the distance of the substrate from the reactants. A preliminary study on the dependence of WS_2 growth with such distance is reported in appendix B.

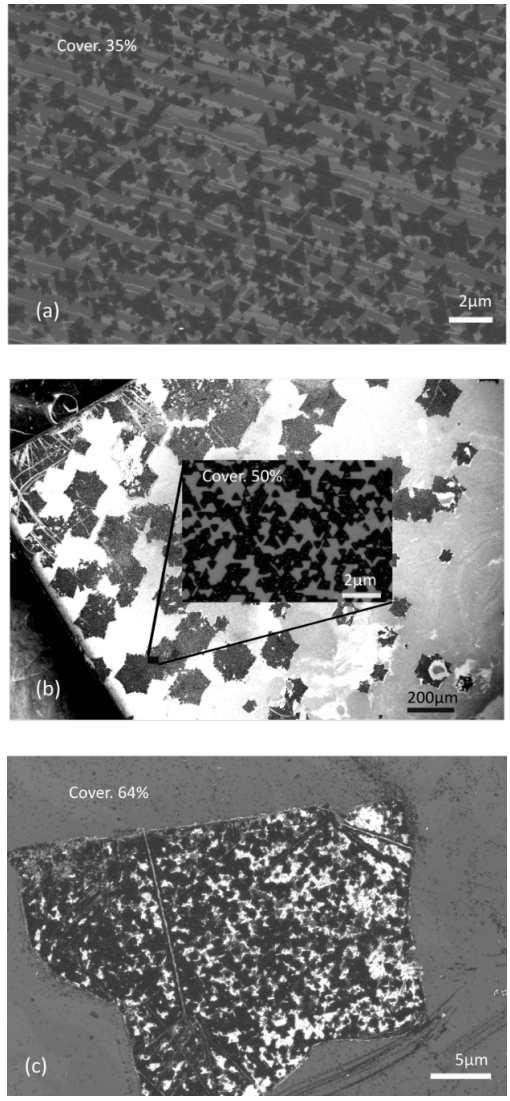

Fig. 3.16 SEM micrograph of (a) WS_2 on epitaxial graphene, (b) WS_2 on CVD graphene transferred on SiC and (c) WS_2 on h-BN exfoliated on SiC. Every growth is performed at 900°C and 80 s.c.c.m. Ar flow.

Generally, it holds the rule that the further the sample is placed the lower is the WS_2 coverage. As the sample is placed very close to the WO_3 powder (i.e., < 1 cm), bilayer WS2 growth occur. However, modelling the growth with respect to the substrate/powder distance is not straightforward since the fluid dynamics of the carrier gas has to be considered and the laminar flow approximation holds only in a limited range of gas flow.

Table 3.1 Parameters used for WS_2 growth studied in the different chapter of this thesis.

Chapter	**Substrate**	**Growth**	**Temperature**	**Pressure**	**Distance**
4,5	EG	Isolated monolayer crystal	900 °C	1 mbar	2 cm
6	EG	Continuous monolayer	920 °C	0.6 mbar	1.5 cm
7	h-BN, CVD graphene and EG	Continuous bilayer	900 °C	1 mbar	< 1 cm

In Table 3.1 the growth parameters adopted to obtain isolated monolayer grains, continuous monolayer and continuous bilayer (the samples studied in the different chapters) are reported.

The growth performed to prepare samples for experiments reported in chapter 4,5 and 7 were carried out at the very beginning of my thesis work. With set up aging, the process parameters had to be recalibrated to take into account vacuum pump low performance, for instance. Therefore,

growth parameters used to obtain continuous film used in chapter 6 deviate from the ideal pictures of the growth mechanism we described so far.

3.3 CONCLUSIONS

In this chapter, the state-of-the-art and the experimental details of the main techniques adopted to produce large scale graphene and WS_2 have been discussed. While the growth of graphene on SiC and Cu has been achieved by simply implementing growth processes developed in the group, WS_2 growth on a number of substrates has been developed from scratch. The growth mechanism has been discussed in light of its dependence on parameters such as growth temperature and carrier gas flow. Indeed, it has been found that the growth of WS_2 in either continuous films or isolated crystals depends dramatically on the substrate roughness, and growth temperature and pressure. Particular conditions of high pressure and high temperature have been found to lead to the formation of vertical platelets of WS_2, as suggested by SEM analysis. In the opposite situation of low pressure and low temperature, unwanted byproducts have been retrieved as also confirmed by EDX spectroscopy. By analyzing Raman spectra and PL emission it has been possible to assess WS_2 presence and coverage. It has been possible to explore the influence of substrate roughness on WS_2 growth by comparing growths performed on h-etched and commercially available SiC. Finally, growth on h-BN, epitaxial graphene and CVD graphene has been introduced. It has been surprisingly found that growth of WS_2 on such 2d substrates is favored and strongly effective. It is reasonable to assume that such efficient growth is triggered by the presence of defects on the 2d substrate.

Furthermore, it has been discussed that the continuity and thickness of WS_2 on 2d substrates can be controlled. This will be further demonstrated in the following chapters.

4 MICRO-STRUCTURAL, ELECTRONIC AND CHEMICAL PROPERTIES OF SINGLE-LAYER WS_2 ON EPITAXIAL GRAPHENE ON SILICON CARBIDE

In the previous chapter the growth of WS_2 on a number of substrates has been addressed. However, as introduced in chapter 1, what makes 2d materials unique is the possibility to combine them in vertical structures relaxing the condition of lattice parameter matching between different layers. As already discussed in this work, the vdW heterostack mostly studied to date is that resulting from the stacking of graphene and h-BN. Indeed, h-BN is a great substrate and encapsulating layer for enhancing graphene electrical properties[160,161]. Due to the challenges met in terms of scalability for h-BN, other 2d materials acting as encapsulants and which might open novel research avenues are being actively sought for. In this respect, WS_2 combined with graphene is a vdW heterostack which hosts a great appeal for applications in optoelectronics. For example, the mobility of graphene encapsulated between WS_2 and h-BN is very promising[162], i.e. about 60000 cm^2/Vs. Improving the mobility of graphene by providing an extremely flat substrate and a defect-free interface is only one possible application out of plenty that might emerge. WS_2 has a thickness dependent band gap and when going from 2 layers to 1 layer, it exhibits a transition from indirect- to direct- gap semiconductor[163,164]. The gap in single layer WS_2 measures about 2.1 eV[163,165,166] at the two non-equivalent K-points of its BZ. The neutral exciton in WS_2 has a large binding energy[167], making it a good candidate for the realization of exciton-polariton lasers[168]. In virtue of such a long-lived exciton, WS_2 shows a remarkably high room-temperature photoluminescence[18]. In the vicinity of the two K valleys the bands are energy separated because of spin-orbit coupling. The spin-valley coupling is robust enough to observe spontaneous

magnetoluminescence at zero magnetic field[169]. Combining semimetallic graphene and semiconducting single-layer WS_2 in a vertical heterostack brings together massless Dirac particles with long spin lifetimes and strongly spin-polarized electrons with great potential for spintronics and optospintronics. Indeed, when placed in close contact, these materials have already shown interesting results in this direction. For instance, the high spin-orbit interaction in WS_2 has been observed to induce an enhancement of the intrinsic graphene spin-orbit coupling via proximity effect[23]. Moreover, single-layer WS_2 was observed to preserve the polarization of impinging light in photoluminescence experiments[29]. Charge transfer between WS_2 and graphene was seen to be fast and efficient under optical pump[170]. Very recently, a first evidence of tunable spin-injection for stacked flakes of WS_2 and graphene has been reported[56]. The system has therefore a serious appeal for a wide number of applications, ranging from photodetection[171] to flexible and transparent electronics[15], to optospintronics[61]. Indeed, an in-depth investigation of the electronic properties of such heterostack would be instrumental for many of the abovementioned applications. To date, the analysis of the electronic properties of WS_2/graphene with conventional surface science techniques (such as ARPES) has been mainly hindered by the limited areas of available crystalline stacks. The steps forwards carried on in the synthetic approach introduced in chapter 3, allow to have highly crystalline 2d heterostacks ideal for this kind of investigations. In this chapter we address the microstructural and chemical features and thoroughly discuss the electronic properties of WS_2 on EG on SiC(0001) synthesized over large areas via CVD. Investigations are carried out using synchrotron-based XPEEM for chemical and electronic-structure characterization, combined with structurally sensitive LEEM[172]. The electronic structure is further probed using ARPES, which provides higher energy resolution.

The experimental results are supported by Density Functional Theory calculations. LEED measurements assign the zero-degree orientation as the preferential azimuthal alignment for WS_2/EG. The VB structure emerging from this alignment is investigated by means of photoelectron spectroscopy measurements, with both high space and energy resolution. We find that the spin-orbit splitting of monolayer WS_2 on graphene is of 462 meV, larger than what is reported to date for other substrates. We determine the value of the work function for the WS_2/EG to be 4.5 ± 0.1 eV. A large shift of the WS_2 VB maximum is observed as well, due to the lowering of the WS_2 work function caused by the donor-like interfacial states of EG. DFT calculations carried out on a coincidence supercell confirm the experimental band structure to an excellent degree. XPEEM measurements performed on single WS_2 crystals confirm the van der Waals nature of the interface coupling between the two layers. In virtue of its band alignment and large spin-orbit splitting, this system gains strong appeal for optical spin-injection experiments and opto-spintronic applications in general.

4.1 METHODS

4.1.1 EXPERIMENTAL DETAILS

Nominally on-axis Si-face polished 6H-SiC(0001) purchased from SiCrystal GmbH was used as a substrate for all the experiments. EG was grown by thermal decomposition as described in chapter 3, adapting the recipe of Emtsev and coworkers[46] in an Aixtron Black Magic reaction chamber. WS_2 was synthesized by CVD in a hot-wall quartz furnace, by adapting the approach described in chapter 3 to the desired results, *i.e.* μm-size isolated crystals. Specifically, growth was carried on from solid WO_2 and S precursors at 900°C, at a pressure of 1 mbar and for 1 hour.

The microscopy measurements were carried out at the Nanospectroscopy beamline (Elettra Synchrotron, Italy) using the SPELEEM set-up. The SPELEEM combines LEEM with energy filtered XPEEM. In this set-up, a focused, collimated electron beam is generated by a LaB6 gun; the electron energy is precisely set by applying a voltage bias, referred to as STV, to the sample[1]. The lateral resolution of the microscope in LEEM is better than 10 nm[112,113]. Along with imaging, μLEED measurements are performed using illumination apertures to restrict the electron beam to a minimum size of 500 nm. The SPELEEM is equipped with a band-pass energy filter, allowing carrying out laterally resolved ultra-violet (UV) and soft X-ray photoelectron spectroscopy. In imaging mode, the lateral resolution approaches 30 nm, the energy resolution 300 meV. XPEEM data at core level energies were evaluated to obtain μXPS spectra. The system is illuminated with photons linearly polarized in the synchrotron's ring plane. The sample is mounted vertical with respect to that plane and the photon beam impinge at 16° onto the sample. The light is therefore mostly p-polarized. The SPELEEM allows also to carry out μARPES measurements[111] With this technique the band structure of the system can be probed on areas as small as ~2 μm in diameter, allowing the imaging of the angular distribution of photoemitted electrons. In order to resolve the spin-orbit splitting of the WS_2 bands at the K-point, we carried out ARPES measurements at the Max Planck Institute (MPI) for Solid State Research in Stuttgart. There, ARPES spectra were recorded with a hemispherical SPECS Phoibos 150 electron analyzer in combination with a Scienta VUV5000 lamp. A monochromator selects the He I emission line

[1] The actual electron energy can be defined by performing a LEEM-IV scan. In particular, the electron energy is defined as the start voltage minus the start voltage of the MEM-LEEM transition.

of the lamp ($h\nu$ =21.22 eV). 2d dispersion sets E(k) were recorded with the display detector, through a 0.2 mm entrance slit in low angular dispersion mode, corresponding to $\pm$13° range. With this technique the probed area is of the order of 1 mm^2. The mapping of the WS_2 BZ was done by measuring single spectra perpendicularly to the high-symmetry direction and varying the photoemission angle. The spectra were acquired at different azimuthal orientations along the **Γ-K, Γ-M, M-K** directions. The three different band branches were then put together via software. In this geometrical configuration, the graphene π-bands intersect the WS_2 VB for a small portion. Considering their low cross section at 21 eV and the high emission angle needed close to **K**, the π-bands are not to be seen unless the contrast is strongly enhanced. XPS spectra were acquired with a Kratos hemispherical analyzer coupled to a monochromatized Al Ka X-Ray source. AFM images were acquired with a Bruker Dimension Icon microscope used in ScanAsyst tapping mode. Spatially averaged LEED measurements were carried out using an ErLEED system from SPECS GmbH. All measurements were performed at room temperature.

4.1.2 CORE-LEVEL FITTING PROCEDURE

In section 4.3 we display spectroscopy results from local XPEEM measurements. For every spectrum, a Shirley-type background was considered. We used the reference position of the C 1s peak of SiC in monolayer graphene (MLG) on SiC(0001) (i.e., 283.7 eV[47]), in order to align the binding energy of the spectra extracted for the XPEEM scans. The symmetric peaks were fitted with Voigt functions. To take into account the asymmetry of the peaks coming from conductive layers, such as graphitic carbon, a Doniach-Šunji´c (DS) line shape was used. The C 1s on MLG was fitted taking into account the following components: SiC (Voigt), graphene

(DS), S1 (Voigt) and S2 (Voigt), where S1 and S2 are the components associated with the buffer layer[47,144,173].

4.1.3 COMPUTATIONAL METHODS

The electronic band structure of the system was evaluated within the DFT framework, using the code Quantum ESPRESSO[174]. The simulation setup is similar to the one we previously used and tested for similar systems[175]. We used a plane wave expansion of the wavefunctions within the pseudopotential[176,177] approach and a PBEsol[178] vdW corrected[179] density functional, both scalar and fully relativistic for spin orbit calculations, using a calculation setup which was previously well tested in similar systems[175,180]. Both the isolated (i.e. free-standing) WS_2 and WS_2 on top of graphene were studied. To match the graphene and WS_2 lattice parameters a supercell was used, with a periodicity of (7×7) with respect to WS_2 and (9×9) with respect to graphene. At variance with similar previous calculations[181] we included vdW corrections, which were proven of utmost importance in reproducing inter-layer interactions in graphene-based systems[175]. The model systems, the supercells and all the simulation setup information are reported in the following. Two different series of DFT calculations were performed: one with the unit cell of WS_2 and one for the graphene plus WS_2 system using the consensus supercell, namely the (9 × 9) for graphene and the (7 × 7) for WS_2, which includes 162+147=309 atoms. The initial thickness of the graphene-WS_2 system is 8.40 Å (distance between the graphene layer and the top of the WS_2 layer), which corresponds to the upper limit suggested by the experimental measurement. All cells and their Brillouin zones are reported in Fig. 4.1, with the relative location of symmetry points. The cell parameters used are reported in Table 4.1.

Table 4.1 Calculation setup and parameters for the WS_2 unit cell and for the graphene-WS_2 system

	WS_2 unit cell	Consensus supercell
a (Å)	3.16	22.14
c (Å)	25.0	30.0
Atoms	3	309
k-points (scf)	15×15×1	Γ
Sampling for band calculation	200	72
Gaussian smearing	0.01	0.01
Convergence threshold	10^{-8}	10^{-8}
Spin treatment	Collinear Spin-orbit coupling	Collinear

Convergence checks on energy were performed using the WS_2 unit cell (see Fig. 4.2(a) and (b)). A good convergence is achieved at 30 Ry. The density cutoff was set 10 times larger than the wave function cutoff in any case. The convergence vs. the k point sampling was also tested (Fig. 4.2(c) and (d)). The final choice was to use a 15 × 15 × 1 grid for the unit cell. For

the complete system we performed Γ point calculations, which were proven sufficient for structure convergence in our previous calculations for smaller supercells[180].

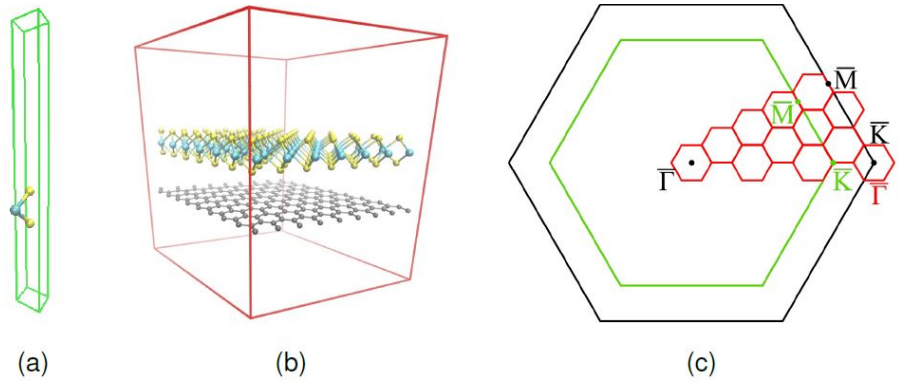

Fig. 4.1 WS_2 unit cell and (b) graphene- WS_2 supercell used in calculations: cell boundaries in green (unit cell) and red (supercell), structures in ball and stick representation (C = grey, S = yellow and W = cyan). (c) Brillouin zones of graphene (black), of WS_2 (green) and of the supercell (red), with symmetry points reported. As it can be seen upon refolding, the K point of the graphene unit cell is remapped onto the Γ point of the consensus supercell.

The band structure was evaluated on a sufficiently dense set of points along the main symmetry directions. In order to compare the isolated WS_2 bands with those of the combined system and with the experiment, an unfolding procedure was applied to the band calculations of the latter, using the method developed by Popescu and Zunger[182]. For each supercell state, defined by **k** point and band index, the spectral weight, namely the probability of finding a set of states of the unit cell contributing to the supercell state, is calculated. Then for each point within the unit cell in k-energy space, the spectral function is calculated averaging the contribution of all supercell k points that belong to the same symmetry

class. This yields a blurred plot of the band structure. The code used is part of the Quantum ESPRESSO project[174]. The remapping of points upon refolding is illustrated in Fig. 4.1(c). Beside the neutral supercell system, the n-doped system was studied to emulate the polarization effect of the SiC substrate.

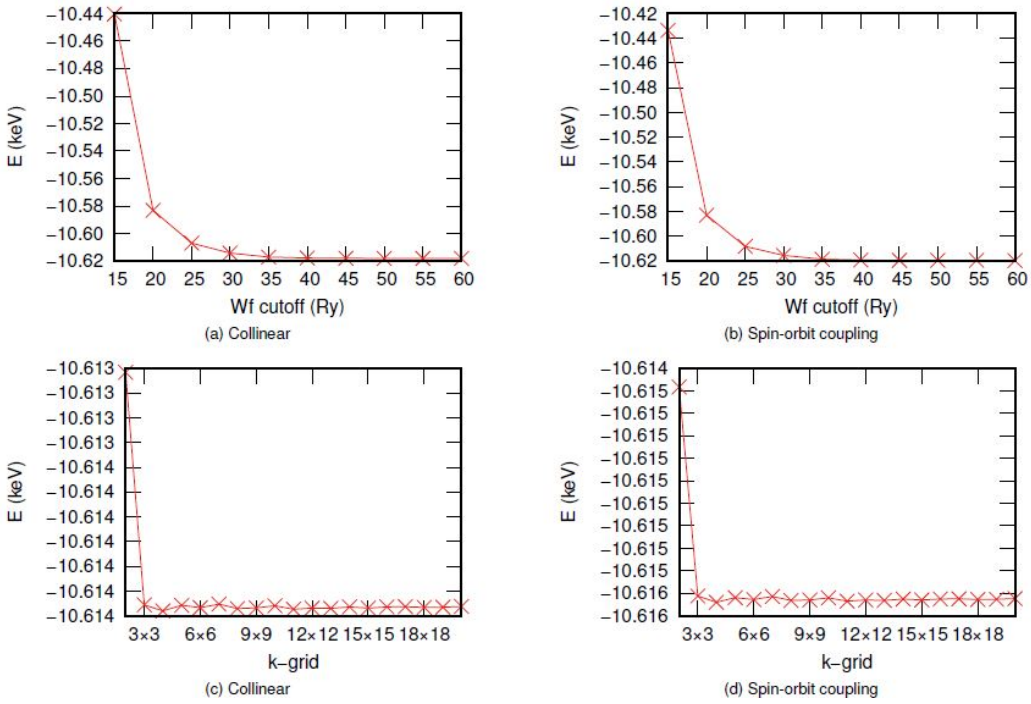

Fig. 4.2 Wave function cutoff energies and k-grids for the collinear and spin-orbit pseudopotentials. Each plot shows the total energy as a function of (a)-(b) the wave function cutoff energy and (c)-(d) the reciprocal space sampling. The total energy depends on the pseudopotential used, hence it does not have a straight physical meaning and values from collinear and spin-orbit calculations cannot be directly compared.

A negative charge of 0.5 electrons per supercell, corresponding to $\sim 10^{13}$ cm^{-2} and a shift of 15 meV of the Dirac point and 122 meV of the WS_2 bands, was added to the cell, while a compensating positive background charge was added to restore charge neutrality. Structural optimization

was performed both without and with the vdW corrections, with convergence thresholds of 10^{-3} a.u. for forces and 10^{-4} Ry for the total energy. For the unit cell, the relaxed WS_2 layer has a thickness of 3.12 Å and the W-S bond length is equal to 2.40 Å (Fig. 4.3). The graphene-WS_2 relaxation gives almost the same thickness of the WS_2 layer (3.11 Å) and a negligible change in the bond lengths (within 10^{-3} Å). However, the system thickness depends on the vdW corrections: when they are present. The optimized graphene- WS_2 distance is 3.14 Å from graphene to the bottom of WS_2 and 6.25 Å to the upper side of the WS_2 layer, while in absence of vdW corrections, the configuration remains basically the starting one, namely with 5.11 Å of interlayer distance and 8.35 Å of total thickness. WS_2 and graphene layer energies were also calculated separately, with the same structures of the relaxed full system, in order to evaluate the van der Waals interaction energy between the layers, which results to ~240 meV per superficial S atom (i.e. half of the supercell S atoms), or equivalently ~72 meV per C atom with vdW corrections.

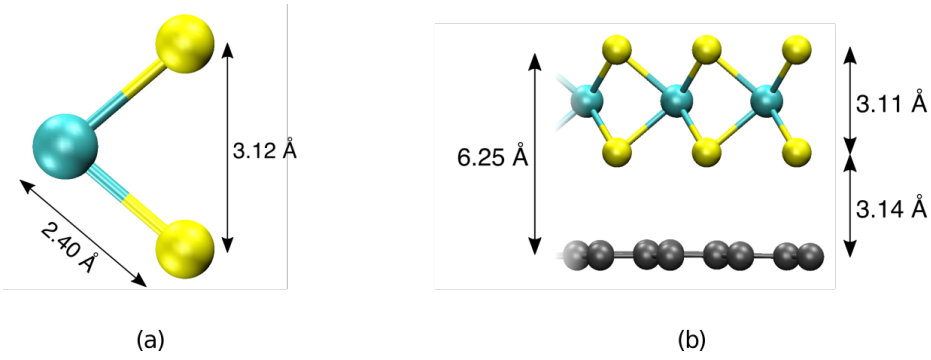

Fig. 4.3 Relaxed structured and main distances of (a) WS_2 unit cell and (b) graphene-WS_2 supercell with vdW corrections.

The van der Waals interaction energy evaluated in the experimental structure is lower, namely ~50 meV per superficial S atom and ~15 meV per C atom.

4.2 RESULTS AND DISCUSSION

4.2.1 STRUCTURE AND MORPHOLOGY

The experimental study of structure and morphology of the system has been carried out via LEEM/LEED and AFM analysis. Fig. 4.4(a) displays a representative image of the typical μm-sized triangularly-shaped WS_2 single-crystals obtained with our growth approach. This LEEM micrograph, acquired at STV 3.5 eV over a field of view (FOV) of 30 mm, indicates that the great majority of the WS_2 crystals are aligned along the same crystallographic direction. In Fig. 4.4(b) we show an AFM image with a WS_2 triangle to highlight the morphology of the system. The average height of the single-layer WS_2 is estimated to be 0.84 nm. The LEEM micrograph in panel (c) is a zoom-in of the image of panel (a) on a single triangle over a 6 mm FOV. The image was extracted at STV 4.8 eV, hence the different color contrast. μLEED measurements were performed on the same region, the results of which are shown in panels (d) and (e) for WS_2 and graphene, respectively. Because of the very low intensity of the graphene spots when measured on the triangle, we show a measurement acquired outside of the triangle, on a MLG region nearby it. Both measured regions are indicated with dashed circles on the figure. In μLEED, the (10) spots of WS_2 are 3-fold symmetric, resulting from the broken inversion symmetry of the real space lattice, as visible from the sketch in panel (g). In spatially averaged LEED measurements shown in panel (f), the 3-fold symmetry is lost because of the presence of crystals rotated by $n\pi/3$, as visible in panel (a).

The preferential alignment of the WS_2 along the graphene's crystalline axes is apparent by looking at the (10) diffraction spots of WS_2, indicated

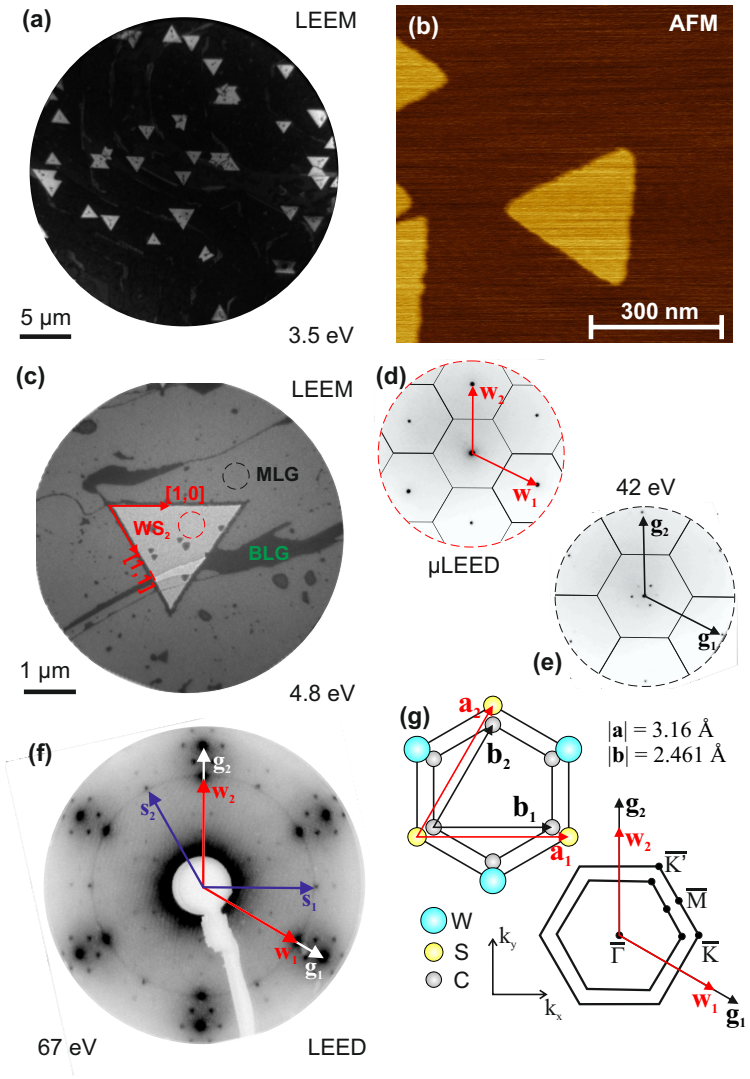

Fig. 4.4 (a) LEEM micrograph recorded at STV 3.5 eV on a 30 μm FOV. (b) AFM image centered on a single WS_2 triangle on MLG over a (770 × 770) nm 2 area. (c) LEEM micrograph of a single WS_2 crystal imaged at STV 4.8 eV on a 6 μm FOV. Areas with different contrast are labeled MLG, BLG and WS_2, respectively. (d) and (e)μLEED pattern acquired on the dashed-circle areas for WS_2 and MLG, respectively. (f) LEED pattern at electron energy of 67 eV. WS_2, graphene and SiC reciprocal lattice vectors are indicated as w,g and s, respectively. (g) Real and reciprocal space sketch derived from μLEED. Crystal directions are drawn in panel (c), according to this sketch.

by $w_{1;2}$ in the figure. The minority orientations are visible as a ring passing through the (10) spots of WS_2. The ring is very faint in intensity and its diameter is slightly smaller - about 2.6% - than the SiC reciprocal lattice vectors ($s_{1;2}$ in the figure). Moreover, the (10) spots of WS_2 appear to be slightly elongated along the polar direction, possibly suggesting an equilibrium position fluctuating about the zero-degree orientation. In panel (g) we display the 2D projection of the real and reciprocal space structures of the system as derived from the μ-LEED and LEED measurements, assuming the equilibrium value of the graphene's lattice parameter to be 2.461 Å and that of SiC to be 3.08 Å. We find the WS_2 lattice parameter to be 3.16 ± 0.1 Å. However, no evidence of superperiodicity (moirè) was found in μ-LEED (at higher energies as well), in contrast with WS_2/gold(Au)(111)[183]. From diffraction measurements we also determine that the edges of the triangular WS_2 crystals on epitaxial graphene are aligned along the [1,0] (zigzag) direction, as apparent by comparing panels (c) and (g).

4.2.2 ELECTRONIC PROPERTIES

The band structure of WS_2/MLG was measured by means of μ-ARPES on a single WS_2 crystal. In particular, the results for the triangle of Fig. 4.4(c) obtained with photons of 70 eV are shown in Fig. 4.5(a). The graphene $\pi-$ and $\pi*-$bands are well visible and also highlighted by orange dots, corresponding to the DFT calculated bands on the graphene single cell. Calculated graphene s-bands are not superimposed as in the experimental data they are not detectable due to their low intensity.

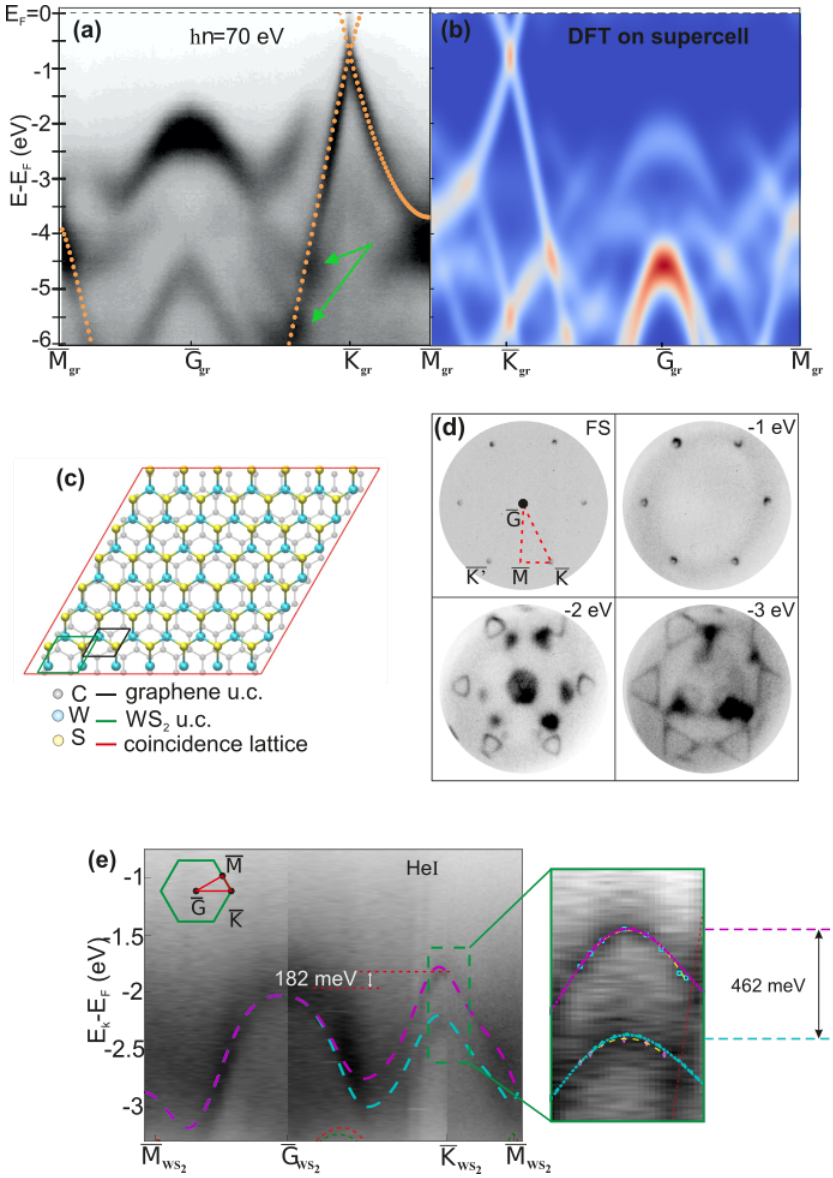

Fig. 4.5 Band structure of WS_2/MLG. (a) μARPES measured on a single WS_2 triangle with photons of 70 eV. (b) Theoretical DFT band structure evaluated on the WS2/graphene supercell depicted in panel (c) and unfolded into graphene BZ. (c) Coincidence supercell (7 × 7) over (9 × 9) of WS_2/graphene. (d) Experimental ARPES CESs recorded with p-polarized photons at 27.5eV (e) Experimental ARPES band structure of WS_2/EG measured with He I light along the path indicated in the inset by the red line. DFT calculated bands including spin–orbit effects are overlapped to the raw data. On the right: zoom-in of the region around K_{WS2} (green-dashed line in panel (e)). Both DFT calculated bands and experimental band fit are over imposed to the raw data. The orange-dashed line is on the graphene π-bands.

The bands visible in Γ belong to WS_2 as also indicated by DFT calculations. Interestingly, at the points where the bands of graphene and WS_2 cross (indicated by green arrows in the panel), no apparent splitting or gap is observed. In order to confirm this finding, DFT calculations were carried out, the result of which is summarized in Fig. 4.5(b), where we display the bands "unfolded" onto graphene's BZ, for better readability. The smallest coincidence lattice for the WS_2/graphene system was found to be (7×7) WS_2 unit cells (u.c.) on (9×9) of graphene, as sketched in Fig. 4.5(c). DFT calculations were carried out on this supercell and as a result, no mini-gap opening was predicted for this system (Fig. 4.6), contrary to what was recently observed for MoS_2 on graphene[184]. The band structure was evaluated in the isolated WS_2 unit cell and in the interacting graphene-WS_2 system, in the neutral and doped, vdW corrected and uncorrected system. The comparison between the bands without vdW correction and larger thickness (Fig. 4.6(a-b)) and those with corrections and smaller thickness (Fig. 4.6(c-f)) shows an average ~0.4 eV upward shift of the filled band system and ~0.6 eV of the empty bands, and a ~4 meV gap opening at the **K**-point. The gap opening can be attributed to the stronger interaction between the two layers in the closest configuration. To better match the experimental data the DFT spectrum was artificially "doped" by an energy shift of about 200 meV. The results of the calculations displayed in panel (b) do not include matrix element effects depending on the incident photons and thus the intensity distribution cannot be directly compared with the experimental ARPES data. To better visualize the relation between the graphene p-bands and the WS_2 bands, we show constant energy surfaces (CESs) in Fig. 4.5(d), extracted starting from the Fermi surface (FS) at binding energies indicated in the figure. The CESs in this case are small volumes in k space integrated over about 250 meV, corresponding to the resolution of the instrument.

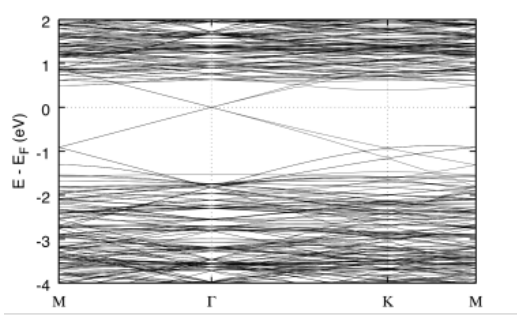

(a) Without vdW correction (experimental distance)

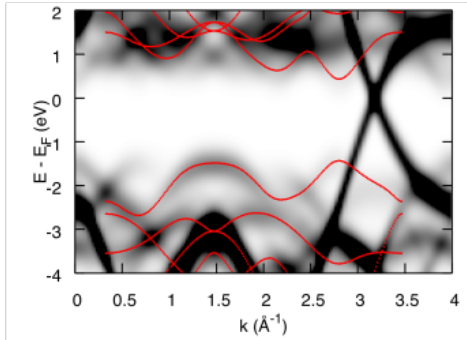

(b) Without vdW correction, unfolded

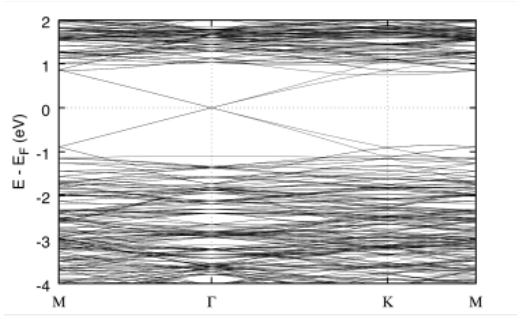

(c) With vdW correction (DFT optimized structure)

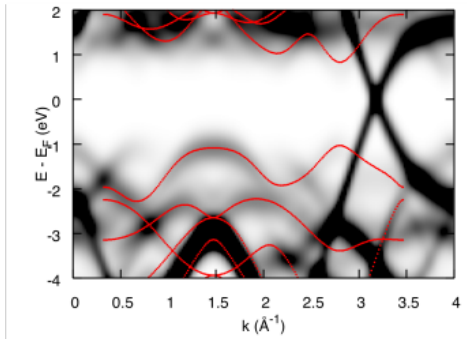

(d) With vdW correction, unfolded

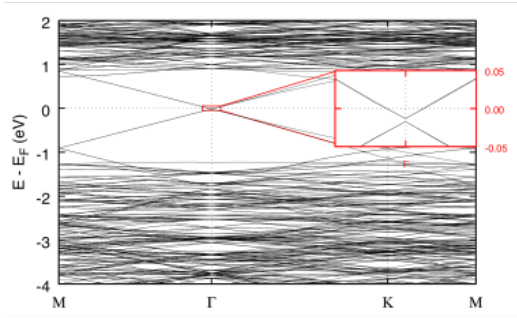

(e) n doped with vdW correction (DFT optimized structure)

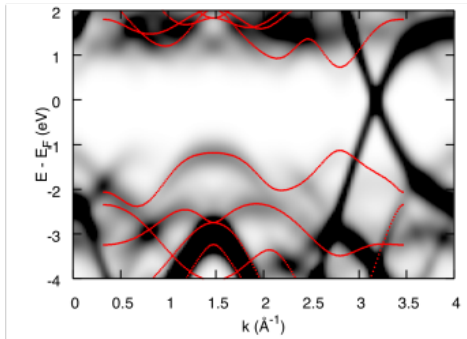

(f) n doped with vdW correction, unfolded

Fig. 4.6 Energy bands of the different models: (a)-(b) optimized without vdW corrections, (c)-(d) optimized with vdW corrections and (e)-(f) with doping. Bands (a)-(c)-(e) are the consensus supercell, while (b)-(d)-(f) are those obtained upon unfolding to compare with experiment. The bands of the WS_2 unit cell are superimposed as red lines, manually aligned to the unfolded interacting system top of valence band of gamma point located at 1.47 Å−1.

The data were acquired with photon energy of 27.5 eV in order to maximize the intensity of the WS_2 bands with respect to graphene. We display the results of the ARPES measurements recorded at the MPI with He I radiation in Fig. 4.5(e), together with the DFT-calculated bands including spin-orbit coupling. The image was obtained by scanning the BZ of the system along the red line traced within the green hexagon in the inset. Note that in this image the high symmetry points are for the WS_2 BZ, whereas for panels (a) and (b) we referred to graphene BZ. Single spectra were measured perpendicular to the red line. We have fitted the experimental data in proximity ($\pm \sim 0.1$ Å^{-1}) of K with a parabolic function in order to extract the effective mass values of the holes. The result along the **Γ–K–M** direction is displayed on the right side of Fig. 4.5(e), representing the zoom-in of the region framed with a green-dashed line in the panel. We find $m_{h1} \approx 0{:}39 m_e$ for the low energy band and $m_{h2} \approx 0{:}53 m_e$ for the high energy band, confirming the asymmetry reported in other publications[183]. The spin-orbit splitting of the WS_2 bands in **K** was retrieved from integrated energy distribution curves (EDCs) to be 462 ± 5 meV. Notably, this value is about 10% larger than what was measured for monolayer WS_2 on Au(111) and Ag(111)[183,185]and about 7% larger than the highest value reported so far[186]. The value measured on our system is comparable only with measurements carried out on bulk WS_2[187].

In Fig. 4.7(a) we show LEEM-IV spectra recorded on WS_2, MLG and bilayer graphene (BLG) areas, as labeled in Fig. 4.4(c).LEEM-IV curves give information about the electronic properties of the system for energies above E_F and their dips, at least in the case of graphene, indicate the number of layers [188–190]. In the WS_2 spectrum we observe three dips modulated by a linear decay of the intensity, possibly reflecting the three-layer structure of the single-layer WS_2. LEEM-IV curves can also provide a

direct and local measurement of the surface potential difference between different regions looking at the transition between MEM and LEEM[113]. In the inset of the figure we show a zoom-in of the MEM-LEEM transition region with an energy scale-bar of 50 meV. We observe that the WS_2/MLG exhibits a value of work function slightly larger (about 150 meV) than of pristine (or as grown) MLG.

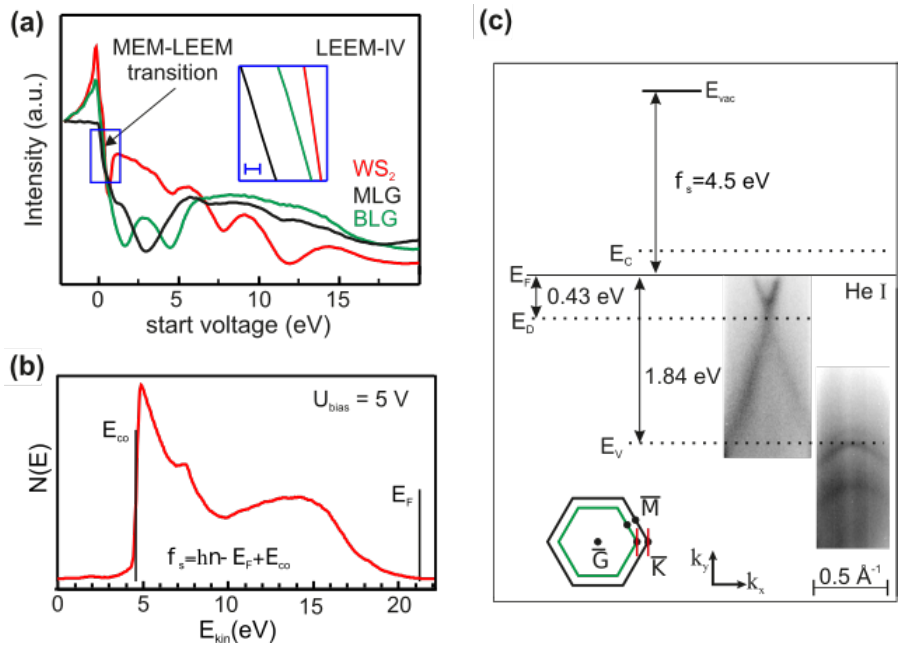

Fig. 4.7 (a) LEEM-IV curves measured on and outside the triangle on the MLG, BLG and WS_2 regions defined in Fig. 4.4(c). In the inset, the bar is 50 meV. (b) Experimental UPS data acquired with a 5 V bias voltage applied to the sample. (c) Scheme of the band alignment derived from the ARPES spectra measured with He I light along the red lines shown in the inset.

The value of the work function instead, was obtained over the entire sample from HeI UV photoelectron spectroscopy (UPS) measurements of

the VB. The VB spectrum is shown in panel (b) and was acquired with the sample biased at 5 V in order to access the secondary electrons cut-off energy. The work function of the analyzer is constant and the acquisition software compensate for it in a way that the kinetic energy of the electrons at the Fermi level, essentially coincide with the photon energy. The work function of the sample ϕ_S is then $h\nu$-E_F+E_{co}, where E_{co} is the cut-off energy beyond which no electron is emitted from the sample. The value obtained in this way is 4.35 ± 0.05 eV. By combining these information, we could determine the band alignment of the system, which is displayed in Fig. 4.7 (c). Although the role of the substrate requires further investigation, in Fig. 4.8(a) we provide a first proof of its relevance. On the left side of panel (a) we show the ARPES spectrum of WS_2 grown directly on 6H-SiC(0001). The bands are recorded in K. On the right side, we show again the ARPES of WS_2/MLG as in Fig. 4.7(c).

The energy difference between the two valence band maxima (E_v) is about 830 meV. This indicates that the WS_2, when grown on SiC(0001), exhibits a band alignment very close to the one expected for isolated WS_2, i.e. Fermi level in the middle of the bandgap. For the size of the bandgap we refer to recent time-resolved ARPES measurements[185], which set the bandgap value for single layer WS_2 at 2.1 eV. To make this visually more clear, in Fig. 4.8(b) we show a scheme of the band alignment for the three situations: isolated WS_2, WS_2/SiC(0001) and WS_2/MLG. On top of every sketch, a simple ball-stick model of each system is shown. For the WS_2/MLG, the conduction band minimum (E_c) lays then $\sim$260 meV above the Fermi level. In the case of WS_2/SiC(0001) instead, E_v is found at 1.00 ± 0.05 eV below E_F, which means that the donor states of the graphene/buffer layer system[191,192] "pin" the Fermi level of WS_2 on MLG, thereby lowering its work function. The spin-orbit splitting of the bands

in **K** remains instead unaltered. Indeed, for the WS_2/SiC(0001), the ΔE between the fitted maxima of the peaks of the integrated intensity yields 458 ± 5 meV. The population of the conduction band via transfer of negative charge to TMDs leads to unconventional phenomena as negative electronic compressibility (NEC), as observed in WSe_2 [193] and more recently also in WS_2 [186].

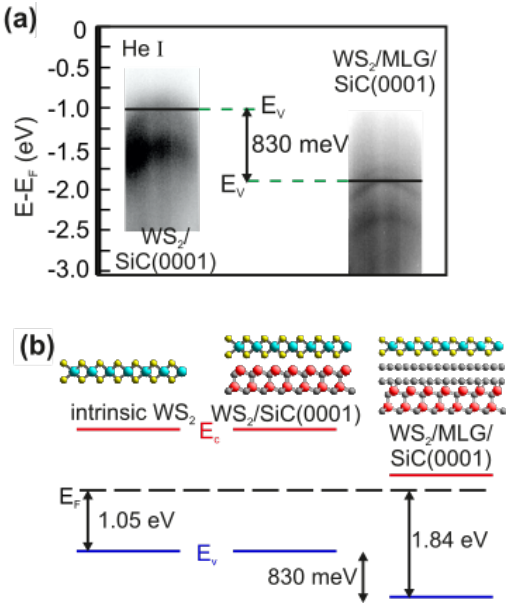

Fig. 4.8 (a) On the left, bands of WS_2/SiC(0001) and on the right WS_2/MLG/SiC (0001). Both measurements are aligned to the Fermi energy and the energy scale is the same. (b) Simple scheme of the different energy alignments for intrinsic (ideal) WS_2, WS_2/SiC(0001) and WS_2/MLG. On the top, a schematic representation of each considered system.

The NEC reduces the size of the gap and since bilayer WS_2 has a smaller band-gap, it could be readily metallic on EG, opening up the possibility for the observation of predicted exotic phenomena such as the transition to a superconductive phase[194,195]. In addition, the energy difference between the maxima of the VB in Γ and K is found to be $\Delta_{\Gamma K}$=182 meV (Fig. 4.5(e)), about a third of what was observed for the same material on Au(111)[183],

possibly implying the occurrence of many-body renormalization effects of the bands or due to the graphene-WS_2 interaction. As a comparison, we note that for the WS_2/SiC(0001) system the same quantity was found to be $\Delta_{\Gamma K}$ = (250±20) meV (not shown). Despite the recent popularity of vdW vertical heterostructures and the variety of investigated TMDs, the system presented and studied in this work represents an unicum as referred to the potential applications in opto-spintronics. Graphene has a large spin relaxation time[196], but the electrical injection of spin in graphene suffers of problems arising from the quality of the contacts, defects at the interfaces, minority spin injection or the definition of a tunnel barrier to minimize it[197]. A cleaner way to inject spin polarized carriers into graphene would be optically, i.e. by exploiting the optical selection rules introduced by the use of photons with a specific helicity. We propose that the WS_2/MLG described in this work has the ideal band alignment for such applications using photons in the visible range.

4.3 CHEMICAL PROPERTIES

The chemical properties of the system are investigated locally, i.e. measuring each core level spectrum on and outside a single WS_2 crystal, by means of XPEEM. The outcome of those measurements is summarized in Fig. 4.9(a-e). In Fig. 4.9(a) and (b) we compare the C 1s spectra recorded on MLG and WS_2/MLG, respectively. Intensities are area normalized so that line-shape and peak positions can be better compared.

It is important to point out that, within the experimental error, the positions of the C 1s components do not shift. In particular, the sp^2 graphitic peak remains at 284.4±0.1 eV, confirming the absence of doping variation in graphene and at the same time excluding strong chemical interaction between the two 2D layers. Because their shape is not

explicitly evident at this particular photon energy, the S1 and S2 components - characterizing the buffer layer - were assigned from literature data[47]. We find S1 at 284.7±0.2 eV and S2 at 285.2±0.1 eV. Again, their positions are stable on and outside the WS_2 island. The SiC component is found at 283.7±0.1 eV in both cases, meaning that the WS_2 layer does not induce any band bending of the SiC core-level bands. Such a fact is further confirmed by the Si 2p peak, shown in Fig. 4.9(c).

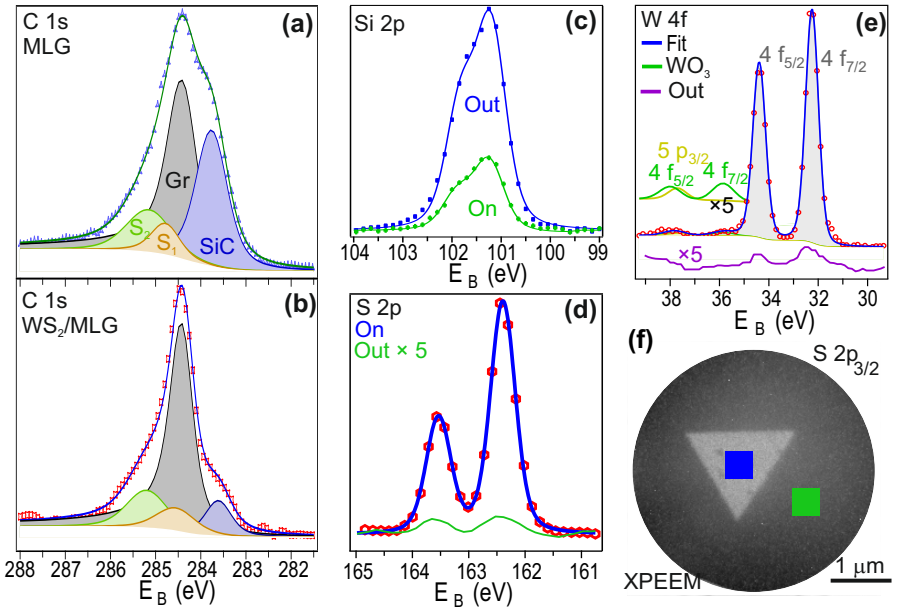

Fig. 4.9 Panels (a –e): Core level photoemission spectroscopy spectra extracted from XPEEM scan at 400 eV. The label "out" indicates that the spectrum was recorded outside the triangle. (f) XPEEM snapshot of S 2p extracted on the high-spin component highlighting the areas from which the spectra are extracted. The same areas are valid for the W 4f spectra.

Also in that case, the 2p doublet remains at 101.2±0.1 eV. Panels (d) and (e) display the S 2p and W 4f spectra, respectively. The S 2p is well fitted with a single Voigt doublet with Lorentian width 0.09 eV and Gaussian width 0.2 eV, with the $2p_{3/2}$ component centered at 262.2±0.1 eV. This is

symptomatic of the fact that the sulfur atoms of both top and bottom layers are in the same chemical environment and the interaction with the graphene p_z orbitals does not induce a measurable chemical shift. The W 4f contains a visible second component that we ascribe to a high-oxidation state, namely WO_3. The intensity of the oxide doublet is about 4.5% of that of the 4f disulfide doublet.

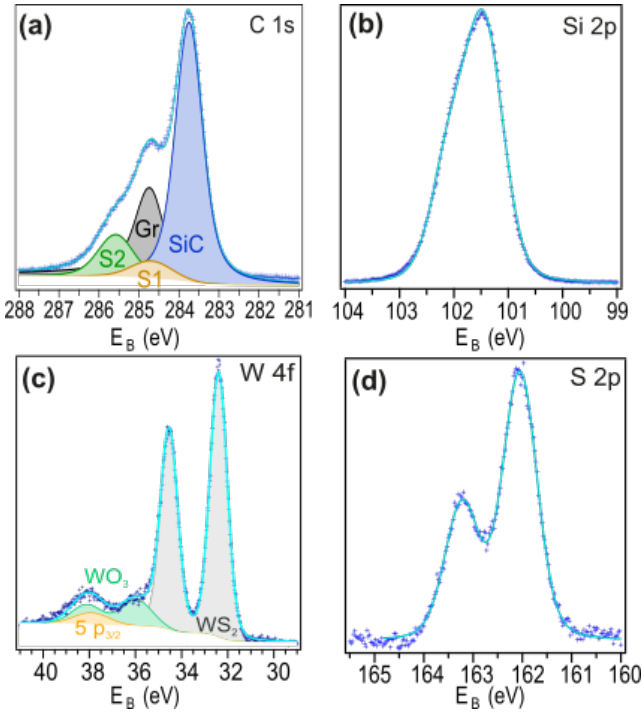

Fig. 4.10 XPS spectra recorded at room temperature on a Kratos Al-Kα-laboratory system.

The energy position of the WS_2 W $4f_{7/2}$ component is measured as 32.2±0.1 eV and the spin-orbit splitting 2.15±0.05 eV. As for the other peaks, we measured W 4f and S 2p also outside the WS_2 triangle and we

report those spectra with intensity multiplied by a factor 5 in the figures. We find some sulfur and tungsten with energies compatible with those of WS_2. The WO_3 was instead detected only on the island, leading us to the conclusion that some unreacted material is embedded into the WS_2 or underneath it. In panel (f) we display the XPEEM snapshot acquired at the S $2p_{3/2}$ energy, showing the regions where the spectra in and outside the triangle were acquired from. In order to have a statistical comparison with the full sample, laterally averaged chemical properties were instead collected via XPS, as described in the methods section and the data are summarized in Fig. 4.10 with a photon beam spot of 2×3 mm^2 in size. The C 1s and Si 2p spectra (panels (a) and (b), respectively) do not show any peculiar feature deviating from the results expected from a MLG/SiC(0001). The W 4f peak confirms the XPEEM measurements shown in Fig. 4.9(e) Here, the WO_3/WS_2 components ratio is slightly higher (Fig. 4.10(c)), indicating a possible inhomogeneity in the WO_3 concentration throughout the sample. Given the higher surface sensitivity of the XPEEM at lower photon energies compared with the XPS, it could also indicate that the WO_3 is actually underneath the WS_2 and not on top. However, its contribution remains very little. The sulfur component was fitted with a single Voigt doublet in this case as well (Fig. 4.10d)), as it was the XPEEM peak shown in Fig. 4.9(d).

4.4 CONCLUSIONS

In this chapter we investigated the properties of CVD-grown WS_2 crystals on epitaxial graphene on SiC(0001) by means of microscopy techniques such as LEEM/PEEM and AFM as well as laterally averaging methods as ARPES and XPS. The set of measurements we carry out converge on defining the WS_2/MLG a low-interacting system. Indeed, μLEED does not show moiré-like diffraction spots and neither μARPES nor ARPES show

replica bands. DFT calculations support the experimental findings by evidencing the absence of gaps (either due to band anticrossing or to superperiodicity effects), which have instead been recently reported for a similar system, e.g. MoS_2/graphene[198]. The analysis of core level data excludes substantial chemical shifts and line-shape modifications such as peak broadening or splitting, further confirming the weak interaction between WS_2 and graphene. The band alignment between WS_2 and graphene is determined. We find that the position of the MLG Dirac point does not change behavior observed also for MoS2 on MLG[199], and the E_v of WS_2 is located 1.84 eV below E_F. This strong downshift of about 830 meV of the E_v depends on the substrate and it alters the value of work function for the WS_2. The band structure of the system is measured through the entire BZ. We extract the effective masses in K, finding $m_{h1} \approx 0.39m_e$ for the low energy band and $m_{h2} \approx 0.53$me for the high energy band. The spin-orbit splitting of the VB at K is found to be 462 meV, the highest values reported for this material in its monolayer form. Together with the observed 0° azimuthal alignment of the two crystals, the band structure of the system results to be promising for applications in the realm of opto-electronics, which will be explored in chapter 6.

5 SUPERLUBRICITY OF EPITAXIAL MONOLAYER WS_2 ON GRAPHENE

In chapter 4, the electronic properties of WS_2 on epitaxial graphene have been explored. This chapter focuses on the nanotribological properties of this system. It should be mentioned that to date minor attention has been paid to the tribological properties of vdW heterostacks at the nano/microscale while most research work has investigated their electronic and optical potential. Here we report the superlubric sliding of monolayer WS_2 nanoflakes over single-layer EG triggered by an STM tip. WS_2 was synthesized on graphene on SiC adopting the same approach reported in Chapter 4. In comparison to heterostacks obtained via mechanical exfoliation, this entirely heterostack presents a WS_2/graphene interface free of resist and solution residuals, and it is thus ideal for nanotribology investigations. Our experimental findings show that WS_2 single-crystalline flakes are prone to slide over graphene surfaces when perturbed by a scanning probe microscope (SPM) tip. Atomistic force field based molecular dynamics simulations indicate that the vdW interaction between the scanning tip and WS_2 is enough to overcome the energy activation barrier and to trigger an ultra-low friction roto-translational displacement of the flake, that is superlubric. Rotation angles of $n\pi/3$ between graphene and WS_2 are found to be the most energetically stable. Atomically resolved investigations show that the interface is atomically sharp and that the WS_2 lattice is strain-free. These results help to shed light on nanotribological phenomena in vdW heterostacks and suggest that the applicative potential of the WS_2/graphene heterostructure can be extended by novel mechanical prospects. In this chapter we first discuss the concept of superlubricity and give an overview of the superlubric studies carried on to date on vdW

stacks (section 5.1). We then report experimental details and discuss how modeling and simulations were carried on (section 5.2 and 5.3, respectively). Section 5.2 describes the sliding experimentally observed during SPM analyses while paragraph 5.3, reports classical dynamics simulation results which are instrumental to model the observed sliding. Finally, paragraph 5.6 reports atomically resolved images of WS_2 on graphene.

5.1 SUPERLUBRICITY AND TMD/GRAPHENE HETEROSTACKS: AN OVERVIEW

Both graphite and bulk WS_2 are known as effective lamellar lubricant with a hexagonal structure. During the years, a number of tribological experiments have been carried out on both graphite and bulk molybdenum disulfide (MoS_2), whose structure is analogous to WS_2[200,201]. Interestingly, novel phenomena as self-retraction and superlubricity have been reported [201,202]. Superlubricity has been predicted by a number of studies in vertical homo- and heterostacks of 2D materials [201,203]. In the early 90s, Hirano et al[204] related friction to "commensuration" between crystal surfaces, involving the difference between lattice parameters, symmetry and relative rotation of surfaces. Later on, it was recognized, that the relaxation of the atoms at the surface have a fundamental role, that is the introduction of an energy dissipation mechanism. The dissipation was related to surfaces flexibility[205] by the parameter $\lambda=u/(Ka^2)$, measuring the relative strength of the inter-surface interaction u (usually the vdW interaction) to the rigidity of the surfaces (K), with a being the lattice parameter. If the surfaces in contact are rather rigid (large K) and/or the inter-surface interaction u is small, the system is prone to superlubricity[206]. This work also showed an increase in friction with the temperature, attributed to an enhancement of commensurability

driven by fluctuations. On the other hand, if a stick-slip mechanism is assumed between surfaces, then the behavior is the opposite, i.e. friction decreases with temperature[207] and is related to the "relative corrugation" of the surfaces. In this case, activation barriers can be present for the motion[208]. The dependence of lubricity on the size is less studied. Clearly, friction is an extensive quantity: in general, the force needed to move a flake is proportional to its surface area, and the friction per unit area is constant. Superlubricity was observed in a graphene flake attached to an atomic force microscopy AFM tip sliding with incommensurate misaligned relation over a graphite substrate[209]. It was also reported in scanning STM experiments at temperatures as low as 5 K[210]. Very recently, friction tests on the sliding of a single-layer MoS_2 nanoflake on another incommensurate misaligned MoS_2 substrate have yielded ultra-low friction coefficients of about 10^{-4} indicating superlubricity[211]. Similarly, extremely low friction was measured when sliding a multilayer graphene–coated microsphere on graphite and bulk h-BN[212]. To date, however, the superlubricity between a TMD and graphene – a natural playground for nanotribological studies – has not yet been experimentally observed.

Despite the fact that to date there is still not broad consensus over the definition of the term superlubricity itself, in this work it is reasonably used to describe the sliding of flakes over a substrate without the need for a horizontal force.

5.2 EXPERIMENTAL

Graphene was obtained via solid state thermal decomposition of atomically flat nominally on-axis 6H–SiC(0001) substrate using a resistively heated cold-wall reactor as described in chapter 3. The as-grown graphene/SiC samples were then used as receiving substrates in a

tube-furnace low pressure CVD reactor, while sulfur and tungsten trioxide powders served as chemical precursors and argon as carrier gas. The growth recipe was tuned in order to obtain isolated crystals, in the same way implemented in chapter 4. STM measurements were carried out in an Omicron low-temperature STM system. After transfer to the UHV chamber, the sample was annealed via resistive heating to 400 °C for about 12 hours. The STM was operated in constant current mode using an etched tungsten tip. The tip voltage was varied between 0.1 V and 2.7 V, and the tunnel current between 10 pA and 300 pA. The pressure in the STM chamber was better than 5 x 10^{-11} mbar. Scanning electron microscopy (SEM) imaging was performed at 5 keV using a Zeiss Merlin microscope, equipped with a field emission gun. Atomic force microscopy was performed using an AFM+ by *Anasys*. The Gwyddion software package was used for the analysis of the STM and AFM images[213]. Low energy electron diffraction (LEED) measurements were carried with an ErLEED by SPECS.

5.3 MODELING AND SIMULATIONS

Molecular dynamics simulations were performed with a model system including a WS_2 triangular flakes of ~5nm, ~10 or ~20 nm in combination with simulation sufficiently large graphene rhombohedral supercells from 16 to 31 nm. The largest model system includes up to ~40500 atoms (see Table 5.1). All the interaction parameters were optimized in order to reproduce experimental data or data from higher order theories. The flake-substrate interactions were represented via vdW interactions. We used the Lennard Jones (LJ) potential with standard parameterization. A preliminary evaluation of vdW energy per S atom performed by means of a local optimization on the flat substrate at T=0 K indicate a vdW energy

per atom of about 110 meV/atom, larger (~4 fold) than the value obtained in chapter 4 by means of DFT calculations[27].

Table 5.1 Representation of the substrate (cut within the simulation supercell) and of the flakes of WS_2 (flakes are in scale between each other but not with the substrate structures). Substrates are considered both flat and corrugated with corrugation amplitude (bottom-to-top vertical displacement) of ~0.57Å at T=0K. Corrugations are highlighted with gray shadows (bright areas protrude, dark areas intrude)

	WS_2 flakes		
	~5nm (442 at)	**~10nm (1650 at)**	**~20nm (6767 at)**
		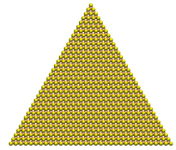	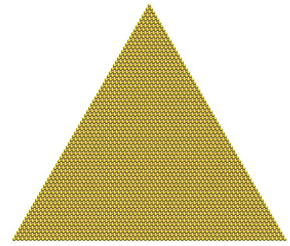
Graphene substrate (supercell boundaries)			**Combination**
			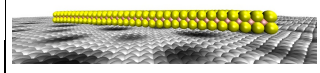
		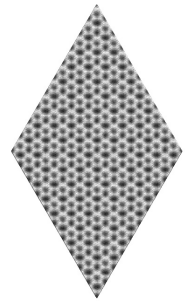	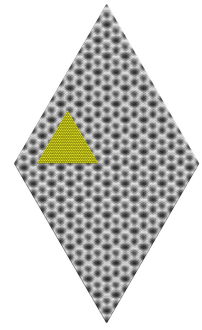

Table 5.2 Summary of the models parameters.

Graphene sheet		
Tethering potential	Harmonic, anchoring to the starting position	k_t=1.5 kcal/mole$Å^2$
Corrugation amplitude		0.57Å
Elastic Network	6th neighbor (r_{cut} = 5.2 Å)	k=800kcal/mole
WS_2 flakes		
Distance dependent Elastic Network: K=200 exp(-2.0*(r_0-2.4))		
	r_0 (Å)	**K (kcal/mole)**
First neighbor (S-W)	2.40	200
Second neigh (W-W)	3.160	~45
Second neighbor (S-S)	4.437	~44
Third neighbor (S-W)	5.076	~8.
Flake - graphene interaction		
Lennard Jones	**E (kcal/mole)**	**σ (Å)**
W-C	0.067	3.14
S-C	0.173	3.56

However, this value is also highly dependent on the corrugation of the flake and registry, therefore, in absence of a direct evaluation of the experimental value of this parameter, we preferred to use the standard values of the vdW parameters, previously used and tested. The parameters were adapted from a similar model reproducing phonons in 2D WS_2 systems[214].The whole parameter set is reported in Table 5.2. In order to speed up simulations, we represented the intra-molecular interactions of the flakes and the substrate with elastic network models, defined by two parameters: the elastic constant and the number of neighbors included in the network. For the flakes, up to the third neighbors were included. The elastic constant of graphene was fitted on fluctuation data derived by simulation with the Broido potential[215] previously observed to well reproduce phonons in graphene[216]. Graphene required a six-neighbor model, being single layer, as opposed to the three layers WS_2 flake. In order to emulate the SiC substrate effect, the graphene sheet atoms were anchored to their starting location with a tethering potential also maintaining the corrugation typical of graphene on SiC. The pattern of corrugation was built following the one obtained in our previous DFT calculations[175], reproducing the experimental one. The maximum amplitude and the value of the elastic constant were adjusted in order to reproduce the experimentally measured values of the vertical displacement measured at high temperatures. This simplified, few parameters representation of the substrate, therefore, has the advantage of being capable of reproducing the experimental structural features of the graphene sheet on SiC (corrugation and dynamical out of plane fluctuations) with a limited computational cost. Simulations were performed with the code DL_POLY[217], using in-house programmed software tools to create the input files and analyze the output. The simulation timestep was 1 fs and standard algorithms were used for

integration of equations of motion (Verlet and Nosé thermostat for constant temperature runs). Simulations were run on a 8-core workstation.

5.4 WS_2 SLIDING ON EG TRIGGERED BY SPM TIPS

In Fig. 5.1(a), we show a large-scale filled-state STM image of as-grown triangular WS_2 flakes on the graphene/SiC substrate. Within the field of view, a few WS_2 flakes are visible with an apparent height of ~7 Å (see line profile in the inset), confirming the monolayer thickness of the TMD. Most of the flakes lie smoothly across the SiC step edges (~8 Å in height). The size distribution of the WS_2 flakes is appreciably narrow. A simple inspection of the STM and SEM micrographs indicates, as already observed in Chapter 4, the existence of an epitaxial relation to the substrate. Most of the triangular flakes present parallel edges. As evidenced in panel (c), only a limited number of flakes – i.e., about 10% – were found to present edges rotated by 30°. LEED analysis – performed on a macroscopic area of about 1 mm^2 Fig. 5.1(b) reveals that the majority of the WS_2 flakes are perfectly aligned with the substrate as the highest intensity WS_2 diffraction spots are 0° oriented with respect to the graphene diffraction spots, confirming what reported in chapter 4.

We also note a faint complete circle in the LEED image belonging to WS_2 lattice vectors, which we attribute to a low percentage of WS_2 nanoflakes of stray orientation. The average area of the flakes analyzed in the sample is about 0.17μm^2, as confirmed by SEM analysis (see the histogram reported in Fig. 5.1(d)). Larger areas reported in the histogram are typically caused by merging of triangular grains (i.e., detected values are multiples of those retrieved for isolated crystals).

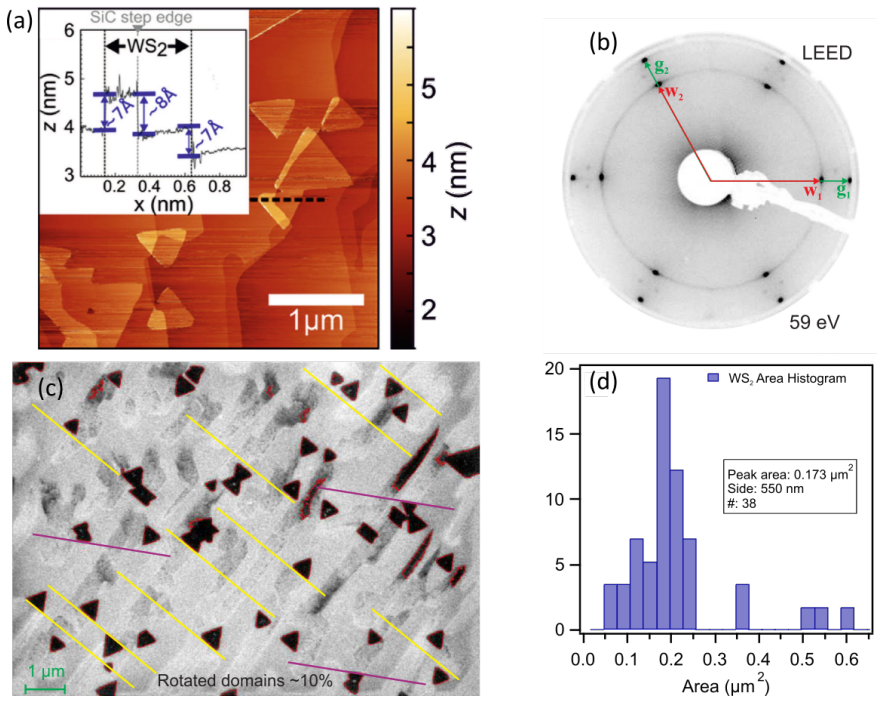

Fig. 5.1 Epitaxial WS_2 graphene-SiC heterostructure. a, Large scale STM image of WS_2 flakes on the graphene/SiC(0001) substrate, at a tip voltage 2.7 V and a constant current of 0.5 nA. The black dashed line marks the position of the line profile displayed in the inset. b, LEED pattern of the WS_2/graphene/SiC heterostructure recorded at a primary beam energy of 72 eV. The arrows mark the different diffraction spots. c, representative SEM micrograph showing a 10% of differently oriented grains. d, histogram of the grain area obtained from SEM analysis.

In Fig. 5.2(a-c), we show a typical behavior identified as superlubricity, observed when scanning with an STM tip over sample areas presenting WS_2 flakes. The three STM images of the same surface area display the same WS_2 flake in three different positions (marked by arrows). Initially, the WS_2 flake is located in the bottom right side of the image (panel (a)). In the subsequent image the flake has moved to the central left area of the micrograph (panel (b)) and finally, in the third scan, is found in the bottom left side (panel (c)). Hence, it appears that upon triggering of the STM tip

the flake slides by rotating and translating in random directions, not connected with the scanning direction.

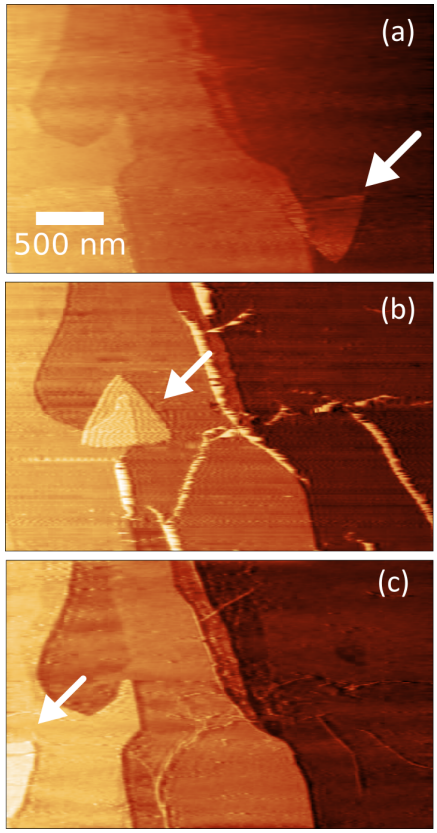

Fig. 5.2 Observation of the displacement of WS_2 flake due to superlubricity. (a-c), Three STM images of the same area revealing three different positions of a WS_2 flake (marked by arrows). Tip parameters: voltage of +2.7 V and constant tunneling current of 0.5 nA.,

It should be mentioned that the sliding of the WS_2 flake on top of the graphene substrate is not always observed when performing STM imaging. The scanned WS_2 flake might either sit still or move suddenly to another position, often several micrometers away with what appears to be a stochastic trigger, i.e. flake sliding becomes more likely the longer we scan over it. Fig. 5.3 reports what typically observed for larger scan areas,

where some of the flakes sit still while others slide around without preferential direction.

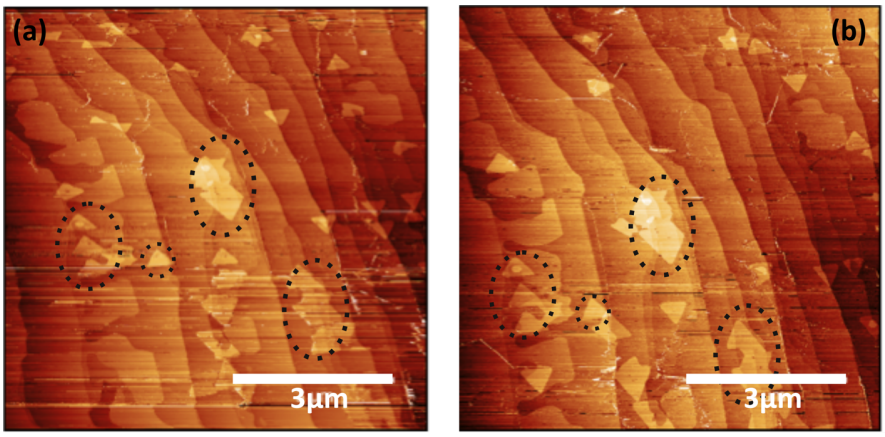

Fig. 5.3 Large area STM image showing WS_2 crystals moving around. Bigger crystals or clusters (dotted circles) seem to be steady during the scanning.

The locked flakes are often part of large clusters of flakes or sit across step edges. When sliding, after each transition, the WS_2 flakes are always found to sit in commensurate position with respect to the underlying graphene layer. They either maintain the same initial orientation or rotate by 60°, reasonably indicating the most stable stacking. In our experiments, we do not observe a trend in the moving probability as a function of tip voltage (while keeping the tip-sample distance constant). This rules out electrostatic effects being the triggering cause of the sliding as it is instead reported in electrostatic-manipulation STM (EM-STM) experiments[218,219]. A further confirmation of this is given by the observation of WS_2 superlubric sliding triggered by an AFM probe. When scanning in contact mode, some of the WS_2 flakes rotate and translate as shown in Fig. 5.4 and in agreement with the STM measurements. In contrast, no WS_2 flake movement is observed in tapping mode, which we attribute to the

strongly reduced time during which the van der Waals forces between tip and sample reach the full strength. Since during the AFM scan both sample and probe are grounded, electrostatic manipulation is not at the basis of the observed sliding.

Also, these observations are significantly different from those reported by Kobayashi et al., where WS_2 grains are manipulated and physically pushed with a nano-prober system[220]. Remarkably, the observation of superlubric sliding via AFM is an indication that the superlubric regime is achieved even under ambient conditions.

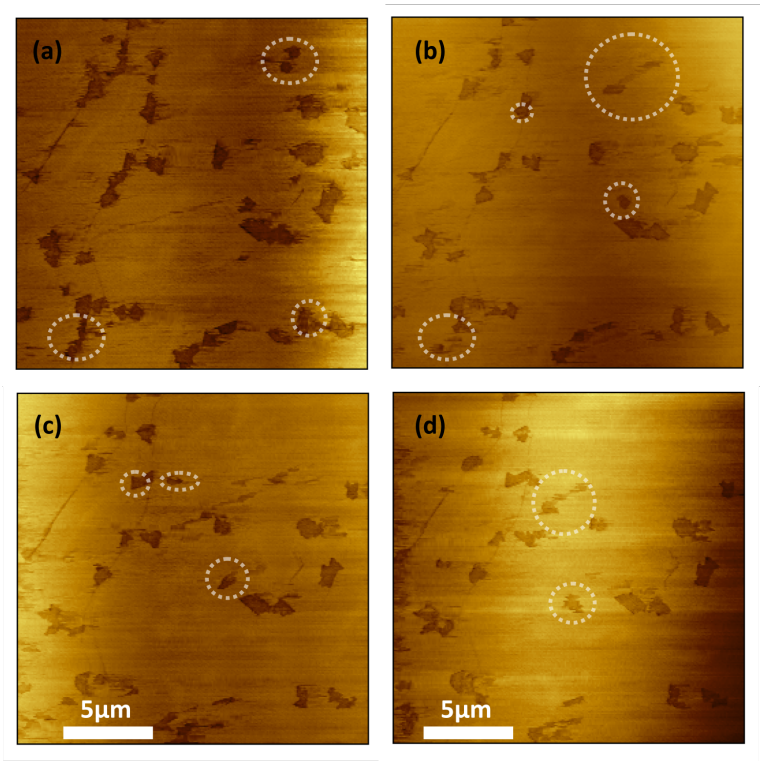

Fig. 5.4 AFM scan in contact mode (phase image). WS_2 flakes, highlighted with dotted circles, are sliding on top of graphene substrates during the scanning of the sample.

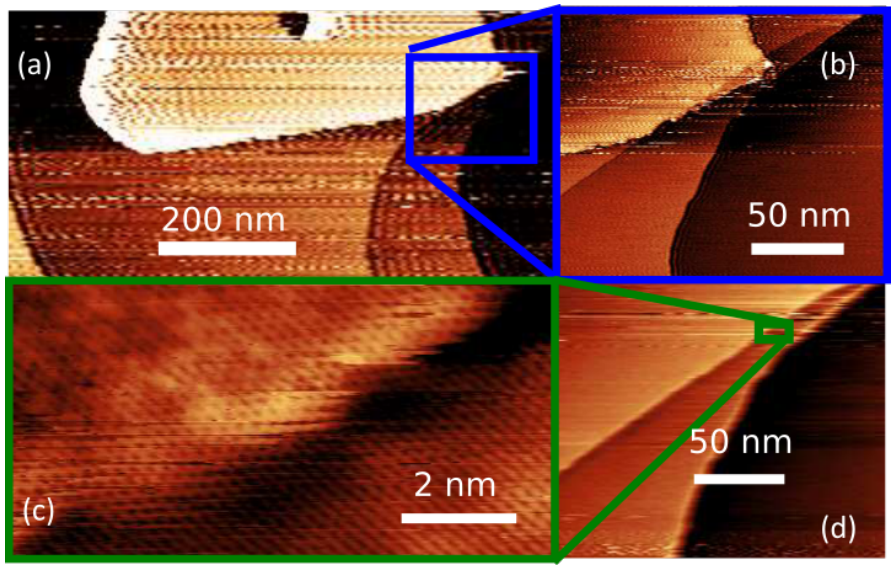

Fig. 5.5 STM images (2.5 V, 0.1 nA) of a surface area containing a WS_2 flake (partially seen in brighter color at the top end). The blue box shows a zoom in the selected area. The WS_2 flake is gone in a later scan. Green box shows the same area of atomically resolved graphene layer.

Sliding of the WS_2 flakes does not create defects in the underlying graphene, as shown in Fig. 5.5(a-d). Panel (a) shows a larger scan to clearly display the initial presence of the WS_2 flake, and panel (b) the zoom-in to one of its edges. In the micrograph reported in panel (d), acquired immediately after that reported in panel (b), the flake appears to have slid away. The corresponding zoom-in (panel (c)) does not only reveal an atomically flat graphene surface underneath where the WS_2 was previously located but also shows that the graphene layer does not get damaged, i.e. an intact graphene carpet stretches across the SiC step edge. The sliding behavior observed in this work appears very similar to what reported in reference[210] where superlubric sliding of graphene flakes on graphite was triggered by an STM tip. Anyhow, thermal fluctuation should

be first excluded as an activating cause of the transition. To this end, simulations were carried on whose main results are reported below.

5.5 MODELING WS_2 SLIDING TRIGGER

Simulation were performed using a slip-stick model. This model is used to describe an object dragged on a corrugated surface always on the minimum of the potential energy surface, and thermally dissipating all acquired energy at each step[207]. The model describes the sliding on a rigid substrate by a flexible "tip" characterized by an elastic constant K, and its behavior is governed by the already described parameter $\lambda = u/Ka^2$, being u the amplitude of corrugation of the potential describing the substrate and a its periodicity. If K is large or u small, the friction is low. In our case, this parameter is not easy to evaluate, both the substrate and the flake are flexible, therefore a combination of lattice parameters and lattice constants should be present at the denominator. However, using the parameters of simulation models, one gets values between 10^{-3} and 10^{-4}, suggesting that the system should display low friction, once the motion is activated. Activation of motion is governed by an Arrenius type equation for jumping probability from a given location[207],

$$\frac{d}{dt}P(t) = \frac{P(t)}{\tau}, \quad \tau = \frac{\exp\left(\frac{u}{KT}\right)}{f_0} \tag{1}$$

being u again the corrugation amplitude, i.e. the height of the barrier to be overcome to move the object and f_0 the "attempt frequency". In other words, the motion is activated either by decreasing the barrier u, which happens e.g. with an external dragging field or by an external pulse, or by increasing the temperature, or by altering the attempt frequency.

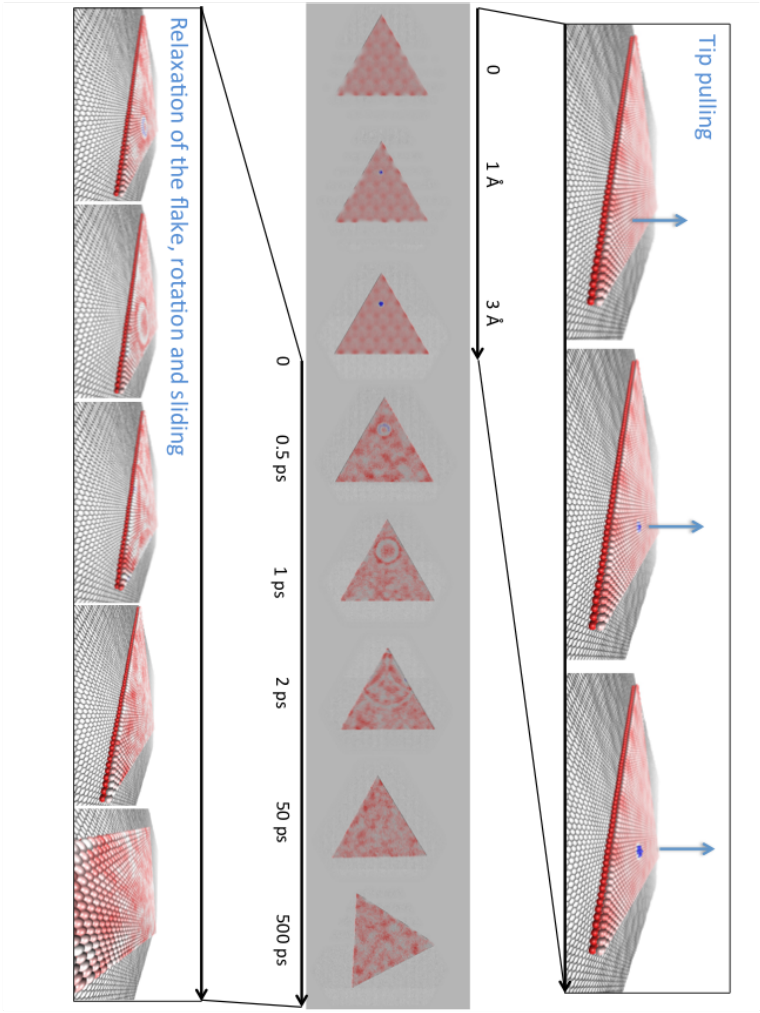

Fig. 5.6 Simulation of an event of pulling of the flake with the tip up to a deformation of about 3 Å, subsequent release and free dynamics. The whole simulation lasts for 1 ns, at room temperature. Only selected relevant snapshots are reported, in top view in the central strip, in perspective in upper and lower parts. Graphene is in grey; the flake is colored according to the vertical displacement (white and blue protruding).

The above equation predicts thermal activation of motion in an average time τ. Our interest here is to understand how, at given temperature, τ depends on the flake size. u is an intensive quantity (barrier per atom or per mole), therefore the exponential factor is independent from the size.

However, f_0 is associated to some frequency ω_0 of the system related to the transition path. In our case, it is likely that the modes involved are the so-called "flexural" i.e. those involving out of plane displacement. These have quadratic dispersion for 2D systems[221], therefore it is to be expected that the involved $f_0 \propto 1/L^2 \sim 1/S$ leading to an increase of the thermal activation time linearly with size.

In the following, molecular dynamics simulations performed for the WS_2/graphene system are shown to verify these statements. Calculations show that in the realistic case of a corrugated graphene, thermal fluctuations alone are sufficient for small WS_2 flakes (i.e., lateral size of 5 nm) to initiate a roto-translatory movement already at ~150K, while no motion is detected in a ~20ns run at 50K. A run at 0K with an external force slowly pulling force shows that the sliding barrier for motion in the harmchair direction of graphene is ~1 kcal/mole (~50 meV) for the 5nm flake. As the Arrenius model suggests, the sliding triggering temperature increases with the crystal size. Indeed, simulations with 10 nm flake locate the motion triggering temperature in the range 150-300K while a simulation of ~10 ns performed at RT with a 20nm flake do not show roto-translational motion but only fluctuations about the starting position. Therefore, as our flakes present a typical lateral size of about 600 nm, we can exclude thermal fluctuation as the cause for the observed transition. The dynamics activation kinetics is different if the motion is activated by the tip. We describe the event as a pulling of the tip of an area of the flake up to a given height with consequent deformation of the flake. When the tip detaches, the deformation energy is released, and transferred in translational motion after some flexural like oscillation propagating from the tip pulling location. This transition phase lasts for ~200ps, after which the flake starts to rotate and then to translate, at the starting velocity of

0.007nm/ps. The sequence of events is reported in Fig. 5.6. The total transferred energy from the tip to the flake is more than ΔE~2eV, which is subsequently distributed over the flake atoms, resulting in more than 1 meV per atom, and allowing to overcome the motion activation barrier in microscopic times. What is important to observe here is that the transferred energy ΔE depends on the deformation of the flake due to the pulling, which is basically independent on the size of the flake, being local. Conversely, as said, the macroscopic friction coefficient of the flake is proportional to the surface. Therefore, it is to be expected that smaller flakes are activated more easily and faster from the tip, while larger flakes might take macroscopic times or need stronger pulling to be activated in microscopic times.

5.6 ATOMICALLY RESOLVED IMAGING OF WS_2 ON GRAPHENE

Clearly, the reported superlubric sliding of WS_2 on graphene makes atomic resolution imaging of the heterostack extremely challenging. It should be mentioned that to date, no STM study has yet investigated the WS_2/graphene heterostructure, while WS_2 nanoclusters have been studied on Au(111) surfaces [183,222]. STM images for the more complex $Mo_{1-x}W_xS_2$ on graphite were reported in[223]. We report that in order to obtain atomically resolved micrographs, it is crucial to image small-scale frames entirely located within a WS_2 flake and not including a flake edge. In general, we observed an increased sliding probability when the tip was positioned for an extended period of time in close vicinity of an edge of the flake. In Fig. 5.7(a) we report an atomically resolved STM micrograph obtained with a sample bias of 0.1 V and a tunneling current of 0.25 nA. A number of defective sites can be observed, which can be reasonably attributed to sulfur vacancies, generated either during the CVD growth

process or to exposure of the sample to the electron beam for SEM imaging[224–226].

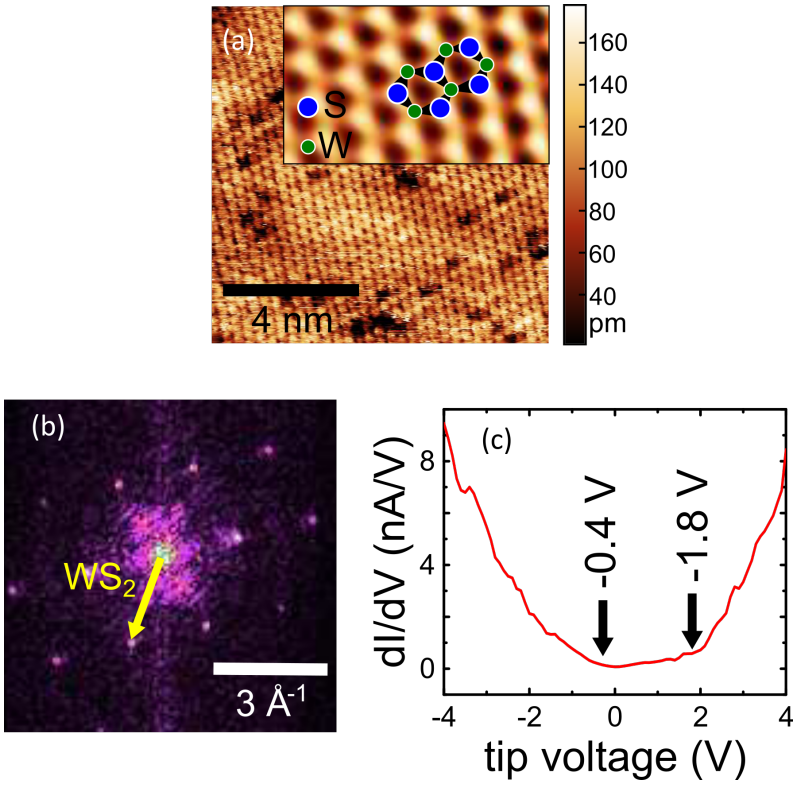

Fig. 5.7 Atomically resolved WS_2 on graphene. a, STM image (0.1 V tip voltage, 0.25 nA tunnel current) acquired on a WS_2 flake. Inset: zoom-in to the lattice (2D fast Fourier transformation (FFT) filtered), with atom position overlay. b, FFT of the raw image in a.c, Scanning tunneling spectroscopy data acquired on a WS_2 flake; the positions of the valence and conductance band edges are marked by arrows.

The epitaxial alignment of the two crystals, which exhibit different lattice parameters (i.e., 3.2 Å for WS_2 and 2.4 Å for graphene[61]), is expected to give rise to a well-defined moiré pattern, which should be possible to observe via STM. However, no moiré pattern is observed in Fig. 5.7(a). This can be explained by the electron-rich thickness of the S-W-S sandwich structure, which electronically screens the graphene from the STM tip. Also, even small lifting of the WS_2 flake by the tip could be

sufficient to significantly reduce the coupling with the graphene layer and favor an exclusive imaging of the top layer as observed for graphite[210]. The inset in panel (a) report a 2d Fast Fourier Transform (FFT) filtered zoomed-in image. We assign the brightest spots to the S atoms of the top-layer of the S-W-S sandwich structure and the lower intensity ones to the W atoms. Intuitively, this assignment would be in contradiction with the fact that in WS_2, the density of state contribution of the metal atom is significantly stronger than that of the S atom. However, simulated STM images for the filled states [227] indicate that geometrical effects dominate in such TMDs (the metal atoms are positioned about 1.5 Å below the S atoms). Hence, a stronger tunnel current contribution by the S atoms is obtained, which leads to the observed triangular pattern. By performing an FFT of the STM image, we obtain the hexagonal Brillouin zone of the WS_2 structure with a lattice parameter of 3.2 ± 0.1 Å, as shown in Fig. 5.7(b). This value is in agreement with what reported for strain-free WS_2[228], further indicating that the WS_2/graphene is a low-interacting system as already observed via ARPES measurements[27]. Scanning tunneling spectroscopy (STS) analysis is reported in Fig. 5.7(c) and retrieves a WS_2 bandgap of 2.2 V ± 0.2. The Fermi level shift towards the edge of the conduction bands indicates n-type doping of the WS_2 layer in agreement with what observed for the same system via ARPES in chapter 4.

5.7 CONCLUSIONS

In summary, we have reported the superlubric sliding of monolayer WS_2 on epitaxial graphene triggered by scanning probes. The as-grown WS_2/graphene heterostack presents a commensurate stacking and an atomically sharp interface as demonstrated by microscopic and diffraction studies. Sliding of the flakes is observed with a high incidence

although it appears to be stochastically triggered. We attribute the activation of the transition to tip-sample interactions, as also supported by calculations. The observation of the superlubric sliding of the WS_2 flakes on the graphene substrate is a further indication of the cleanliness of the CVD growth of WS_2, since contaminants like hydrogen can hinder superlubricity[229]. Furthermore, the reported superlubricity under atmospheric conditions opens the road to novel applicative prospects of this heterostack in nanomotors, nanoelectromechanical systems (NEMS) and advanced optoelectronic multifunctional devices. In order to employ the observed nanotribological properties in applications, further studies focusing on controlled unlocking and impressed directionality should be carried on.

6 PATTERNED WS_2/GRAPHENE HETEROSTRUCTURES FOR EFFICIENT MULTIFUNCTIONAL OPTOELECTRONIC DEVICE

The combination in vertical heterostructures of 2d layers paves the way for novel device concepts[14]. WS_2, in its monolayer form, shows a direct bandgap of 2.1 eV at the two non-equivalent **K**-point of the Brillouin zone[55]. Its optical properties can be thus used for photodetection to enhance the response of graphene. Indeed, when placed in vertical heterostacks[54], the charge transfer between WS_2 and graphene under optical pumping[101] was reported to be fast and efficient. Recently, many efforts have been devoted to create efficient hybrid graphene/TMD photodetectors[54,230,231]. Photoresponsivities as high as $R \sim 10^{10}$ A/W[232] and very fast response times (down to τ=130 μs)[233] have been demonstrated. Yet, one major issue that still has to be efficiently addressed is that of device scalability. Indeed, hybrid photodetectors are generally fabricated using exfoliated graphene/TMD heterostructures. Very recently, photodetectors obtained by combining one layer produced by chemical CVD with exfoliated flakes have been reported[233], but despite the good performances, they lack in scalability. Finally, in the studies involving only CVD grown materials at least one transfer step is required and the growth of the TMD is not continuous[234,235].

In this chapter we demonstrate fully scalable hybrid WS_2/EG photodetectors. The devices were realized with a novel approach implementing a patterned growth of WS_2 on EG, so that WS_2 is present only in the active areas for photodetection and the underneath graphene is accessible to metal deposition of ohmic contacts. Indeed, contacting the WS_2 directly would generate a Schottky barrier[236]. This approach allows minimizing the contact resistance and thus improving the photodetection

efficiency[54,222,231]. The implemented photodetectors display a maximum photoresponsivity R~220 A/W under continuous-wave illumination and a -3dB bandwidth of 250 Hz, remarkable values for fully scalable devices[54,231]. As we demonstrated in chapter 4, the WS_2 layer synthesized over graphene using the bottom-up approach described in chapter 3 and also implemented here, results to be azimuthally aligned with the underlying EG[27]. The precise band alignment and the atomically sharp interfaces of this heterostack are crucial to control the optoelectronic properties of the full structure. The photodetectors also display wavelength-dependent persistent photoconductivity (PPC). For shorter illumination wavelengths we observe a persistent photocurrent, with a nearly complete charge retention, which originates from deep trap levels in the SiC substrate. The explanation of this phenomenon has been possible in light of the results shown in chapter 4. The band alignment reported for the WS_2/graphene heterostructure allows for having a clear picture of the system exploited for the realization of the device.

6.1 METHODS.

6.1.1 SYNTHESIS AND PATTERNED MASKING OF GRAPHENE

As in the previous chapters, EG was grown on nominally on-axis 4H-SiC(0001) substrates (SICrystal GmbH) by adapting the approach reported by Emtsev and coworkers[46] in an Aixtron HT-BM reaction chamber[237]. Before proceeding with WS_2 deposition, the areas of graphene where contacts shall be subsequently deposited were masked by evaporating 100 nm of Au (Fig. 6.1(a)).

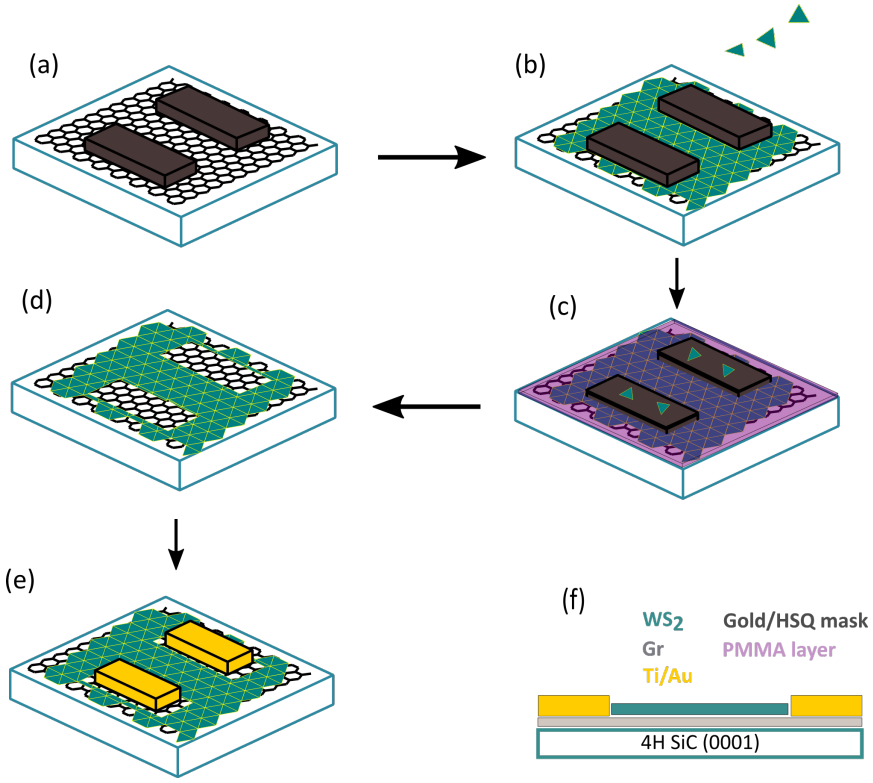

Fig. 6.1 Scheme of the fabrication process of the photodetector. (a) A mask, either Au or HSQ, is deposited on the Gr substrate to prevent the formation of WS_2 on selected areas, which allows to (b) obtain full coverage of WS_2 outside the mask by the deposition technique described in the text. (c) PMMA is spin coated and patterned to remove the WS_2 crystals on top of the mask. (d) The mask is removed either with KI, I2 solution. for Au or HF solution for HSQ This leaves a pattern behind, on which the contacts can be deposited(e). (f) Legend of the colors used in panels (a--(e) and side-view of the geometry of the device.

Au is a highly suitable mask material, because it can sustain high temperatures and it is inert to a sulfur (S) environment, therefore it remains basically unaltered during the growth process. The Au mask was obtained using a standard procedure: graphene coating with poly(methyl methacrylate) (PMMA) resist, followed by EBL, thermal evaporation of Au, and lift-off. It is important to mention that the same results, also in terms of graphene/contacts interface quality, could be achieved using temperature-resistant resist hydrogen silsesquioxane (HSQ) instead of Au

mask. This material, once exposed, turns into a film of silicon oxide that can sustain the WS_2 growth conditions as well. After the masking phase it can be etched using a 1:5 HF:H_2O solution. HSQ offers an alternative to the expensive Au. Indeed, the width needed for the latter in order to sustain growth environment is about 100 nm. Moreover, the choice of one instead of the other can be dictated considering the resistance of the substrate to the different etching method.

6.1.2 WS_2 SYNTHESIS

WS_2 was synthesized on partially masked graphene (Fig. 6.1(b)) using a growth process similar to that discussed in chapter 3. Specifically, in the present work, the protocol was adapted in order to obtain a continuous WS_2 monolayer film on EG. Sulfurization of WO_3 powder (Sigma Aldrich, 99.995%) was carried out within the usual horizontal hot-wall furnace (Lenton PTF). The growth temperature within the hot-zone was set to 920 °C and the growth time was 1 h. The EG substrate was placed face-up next to the WO_3 powder and within the same crucible. Argon was flown during the temperature ramp with a flux of 500 s.c.c.m., leading to a pressure of 4.5 mbar, which kept the S solid. After reaching 920 °C, the Ar flux was suddenly reduced to 8 s.c.c.m., which reduced the furnace pressure to 0.5 mbar, triggering S evaporation. In order to obtain sudden S evaporation, chalcogen crystals were heated up at 200°C by wrapping a heating belt around the quartz tube.

6.1.3 DEVICE FABRICATION

After the growth of WS_2, some crystals were deposited also on the Au mask (Fig. 6.1(c)). Removing these crystals before removing the mask is a crucial step to ensure a clean interface with the bare graphene. Therefore,

the top surface of the mask was exposed to reactive ion etching with O_2 and Ar plasma while protecting the active area with a PMMA layer. After a cleaning in acetone, the sample was immersed in a solution of potassium iodide for 3 minutes (H_2O:KI:I_2 in ratio 40:4:1) in order to remove the Au mask. This allowed for the creation of well-defined channels (Fig. 6.1(d)) with width of 30 μm and length of 2, 5 and 10 μm. If not differently specified, the results reported in this chapter are relative to devices with shorter channel length, namely 2 μm. Once the WS_2/graphene channels were defined, ohmic contacts were fabricated via standard EBL, followed by metal deposition (titanium(Ti)/Au 10/80 nm) and lift-off (Fig. 6.1(e)).

6.1.4 RAMAN AND PHOTOCURRENT MEASUREMENTS

Raman characterization of the synthetized films was carried out with a commercial Renishaw inVia system equipped with a 532 nm green laser.

Photocurrent measurements were performed at room temperature in a vacuum probe station (~$2x10^{-5}$ mbar) by applying a bias voltage of 1.8 V. Illumination was carried out through an optical window using laser diodes coupled into a fiber and focused on the sample in a spot size of approximately 1 mm. The devices were illuminated with blue (473 nm), green (532 nm) and red (638 nm) lasers. The photoresponsivity was assessed for photoexcitation intensities ranging from 16 to 680 mW/cm^2 both with continuous and temporally modulated light, referred as DC and AC in the following, respectively. For AC measurements, laser light was modulated either by a chopper or by modulating the drive current of the diode and acquired using a current preamplifier and a lock-in amplifier. Further photocurrent measurements were also carried out at a wavelength of 532 nm with the Renishaw inVia system used for Raman

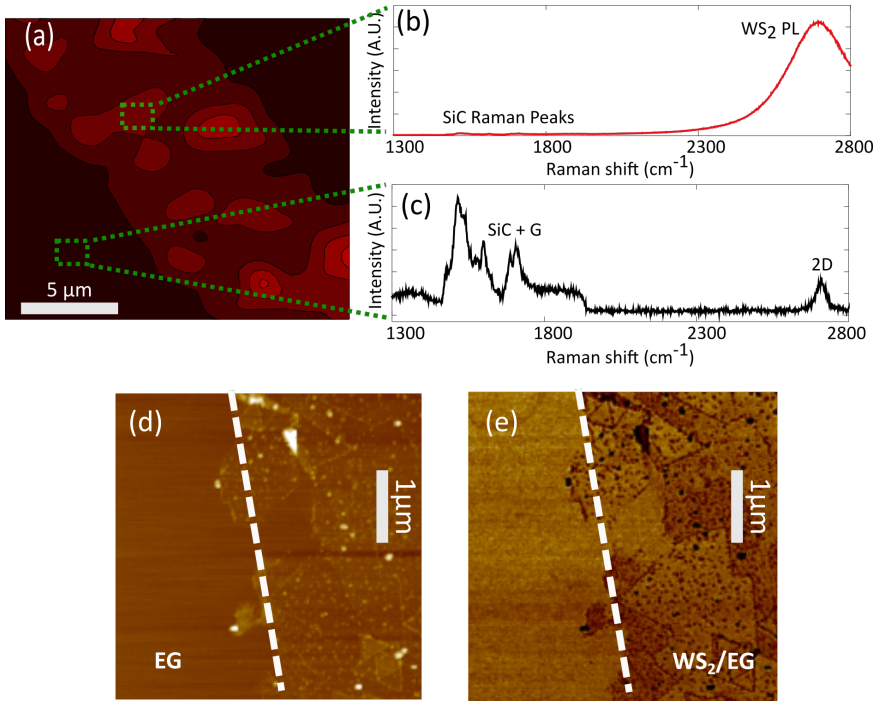

Fig. 6.2 (a) Raman/PL map of the active channel with WS_2 and graphene and of the contact area with graphene only. The map shows the integrated intensity in the range 2600 cm-1 and 2800 cm-1, in which both the PL of WS_2 and graphene 2D peak fall. (b-c) Representative WS_2/graphene (b) and graphene only spectra (c). (d-e) AFM scan in contact mode of the area at the edge between EG and WS_2/EG areas. (d) showing height scan and (e) adhesion micrograph.

characterization in order to ensure an illuminating spot size (variable between 4 µm and 15 µm) that is smaller than the device area.

6.2 RESULTS AND DISCUSSION

The process flow of our fabrication method is depicted in Fig. 6.1 a-e)) while the cross section of the measured devices is reported in panel (f). The quality of graphene outside the channels was assessed via Raman spectroscopy prior to contact deposition (Fig. 6.2(a-c)). Panel (b) and (c) report representative spectra measured inside and outside the channel, respectively.

In the channel, the photoluminescence of WS_2 (Fig. 6.2(b)) is clearly visible and overlapping the Raman signal of graphene (Fig. 6.2(c)). No appreciable D peak is retrieved and 2D peak position and full width at half maximum (FWHM) are entirely comparable to those of the as-grown material[238]. This confirms that the graphene quality is not affected by the processing. A further investigation has been carried out by means of AFM in contact mode. Panels (d-e) show the height and adhesion micrograph.

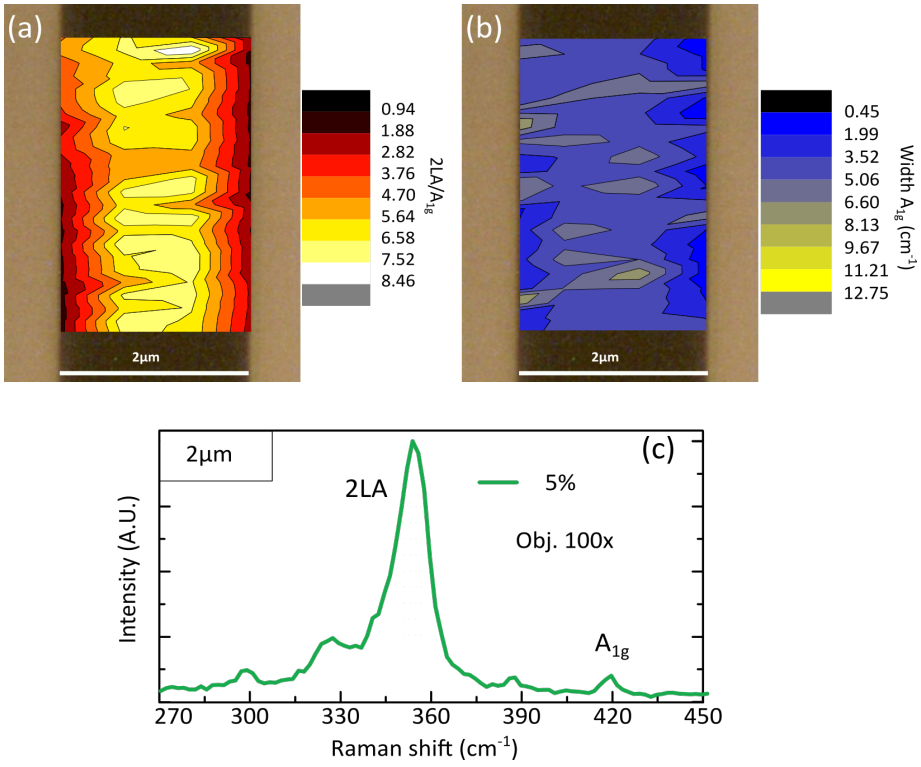

Fig. 6.3 (a) Raman map of 2LA/A1g ratio peak intensity over the device channel. (b) Raman map of A1g peak width. (c)Representative WS_2 spectrum of the investigated area.

It is clearly shown how sharp the interface between the areas is, moreover the graphene exposed area for contacts is free of any contamination. A Raman map of the main peaks of WS_2 – whose position and intensities are

indicative of mono-bilayer[121,122] thickness – is reported in Fig. 6.3. Our fabrication approach allows for the implementation of regular device arrays, as demonstrated in the optical microscope image (Fig. 6.4).

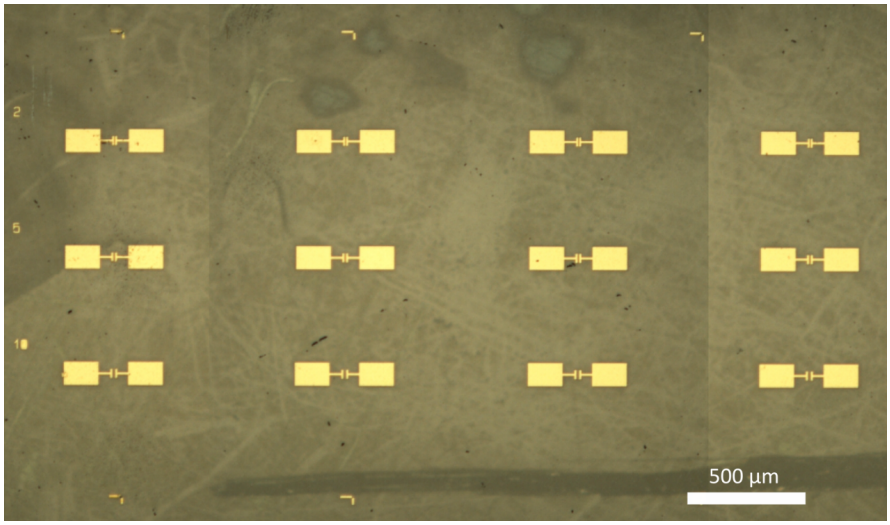

Fig. 6.4 Optical image of a set of devices.

Electrical measurements of representative WS_2/Gr and Gr-only devices are reported in Fig. 6.5 and the linear dependence of the I/V curves confirm the ohmic behavior of the graphene-Ti/Au contacts. The resistance obtained from the curves varies from 1 to 2 kΩ, which includes the contributions from the contact resistance and sheet resistance. Transfer Length Measurement (TLM) measurements allows for extracting contact effective resistivity in the range of a few tens of kΩ · µm (Fig. 6.6), typical for this kind of contact[239,240].

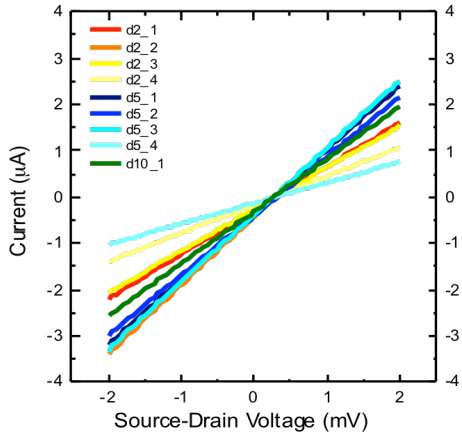

Fig. 6.5 I/V curves for WS_2/graphene and graphene-only devices. d2, d5 and d10 curves are for devices with channel length of 2 μm, 5 μm and 10 μm respectively. Devices number 1,2,3 are WS_2/Gr based and number 4 graphene-only.

We thus conclude that our fabrication process results in a clean interface between the graphene and the metal contacts.

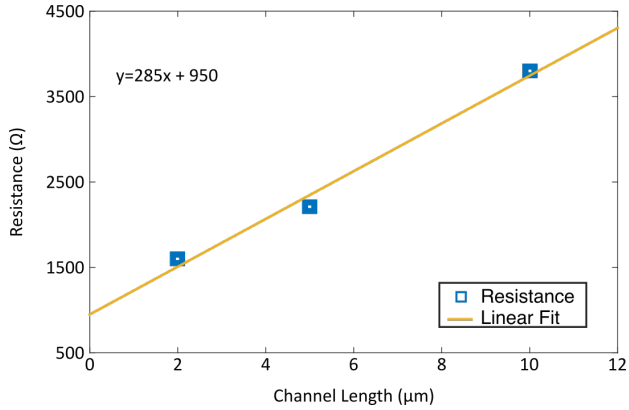

Fig. 6.6 Transfer Length Measurements. The value of the resistance is taken for different length of the device. The equation in the graph is relative to the linear fit

As the whole patterning and device fabrication processes can also be performed via mask-aligner optical lithography, the reported method can be readily extended to wafer-scale. Fig. 6.7(a) reports the device

photoresponsivity measured in DC (stars) and AC (diamonds) at 173 Hz for 638 nm illumination at different photoexcitation intensities.

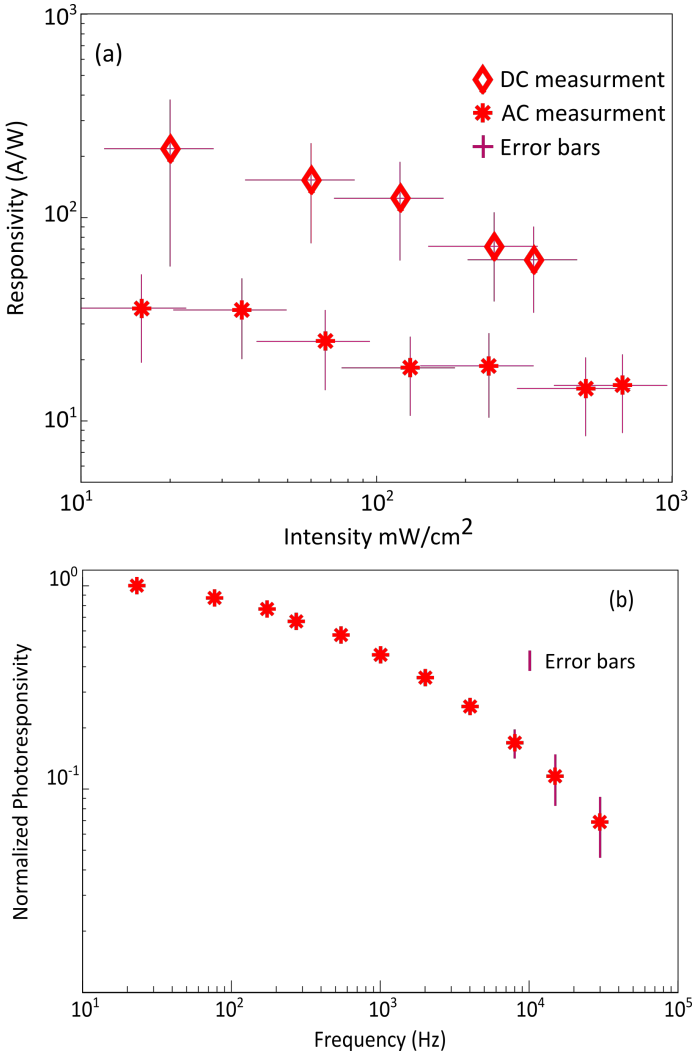

Fig. 6.7 (a) Comparison between photoresponsivity taken with red light in AC (at 173 Hz) and DC measurements. (b) Normalized photoresponsivity in AC measurement in function of the frequency, where the light was modulated by a chopper. Measurements where taken at bias voltage of $V_B = 1.8$ V

The photoresponsivity is calculated using $R = \frac{I_{pc}}{P_{opt}} \frac{\pi}{\sqrt{2}}$, for the AC values, where I_{pc} is the measured photocurrent, P_{opt} is the power incident over the

active area, and the factor $\frac{\pi}{\sqrt{2}}$ takes the lock-in amplifier measurements into account. The photoresponsivity reaches a maximum value of R_{DC}~220 A/W in DC and R_{AC}~ 36 A/W in AC Fig. 6.7(a)). For the detectivity, calculated from $D^* = \frac{\sqrt{A}\cdot R}{S_i}$, where A is the active area and S_i is the noise spectral density calculated considering thermal noise from dark resistance, we obtain a maximum value (in DC) of $D^* \sim 1.6 \times 10^{10}\ Jones$.

Such responsivity and detectivity values are remarkable [231] as they are obtained from a vertical heterostack entirely synthetized via CVD. Devices made using only graphene as active channel have been investigated to compare their performances with respect to those of the hybrid heterostructures. The measured responsivity is R~0.04 A/W, obtained with 638 nm wavelength excitation, bias voltage V_B = 2 V, optical modulation frequency set at 23 Hz and light intensity 250 mW/cm^2. The correspondent value obtained for the detectivity is $D^* \sim 7.3 \times 10^6\ Jones$. The photoresponse of graphene-only devices is barely detectable at this wavelength. Hence, the WS_2/graphene device manifests an improvement of three orders of magnitude with respect to graphene-only devices. The response time of the devices has been investigated by studying the dependence of the photoresponsivity signal dependence on the AC frequency, as reported in Fig. 6.7(b). Although the displayed behavior, typical for hybrid system[241,242], cannot be exactly outlined with a RC circuitt,[243] the response time of the device can be estimated by using the -3dB bandwidth figure of merit, *i.e.* the point at which the signal has dropped to 70% of its initial value[233]. The obtained value is $\tau_r = \frac{1}{2\pi fc}$~0.6 ms (corresponding to a bandwidth of 250 Hz calculated with respect to the maximum value at 20 Hz). To the best of our knowledge, this response time is among the fastest obtained for TMD/graphene devices.[231] It is

worth noticing that a significant signal can be detected also above 10 kHz, where the responsivity is ~10% of the maximum value. We believe that the clean ohmic contact obtained with our approach is at the basis of the fast response time of our devices. Furthermore the epitaxial relation in our heterostack[27] could have a positive impact as well.

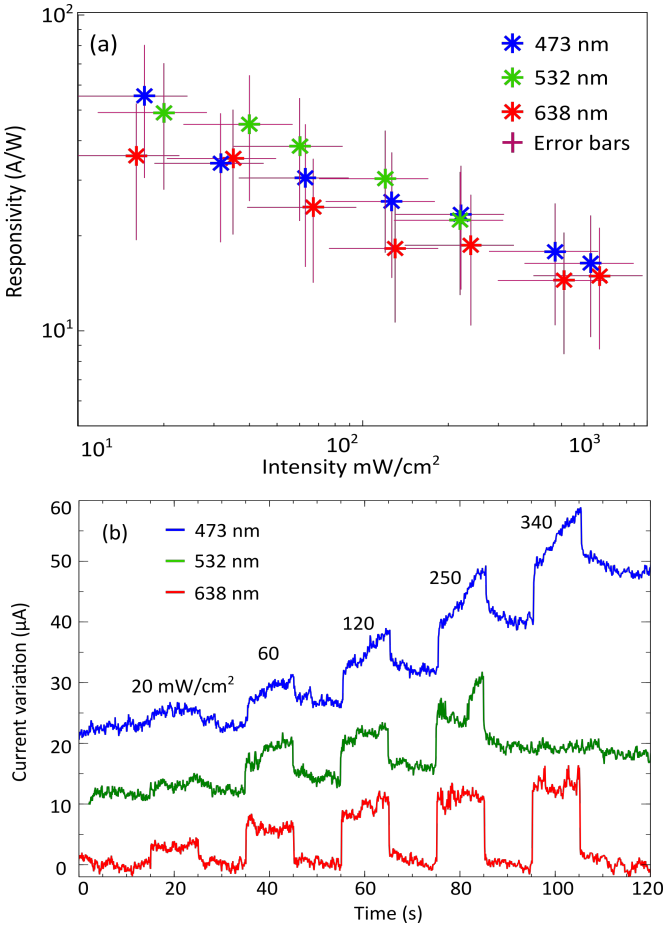

Fig. 6.8 (a) Responsivity vs power intensity taken at different wavelengths in AC measurements (at 173 Hz). (b)DC measurements of photocurrent at different wavelength in function of time. PPC progressively with longer wavelength of the excitation light. With each light on/off cycle the light intensity was increased, as indicated by the values above the blue curve . With increasing light intensity, the PPC increases under blue light illumination. Measurements taken at bias voltage $V_B = 1.8\ V$

In Fig. 6.8 the wavelength-dependent behavior of the device is reported Fig. 6.8(a) shows the WS_2/graphene device responsivity in AC at 173 Hz, for three different illumination wavelengths.

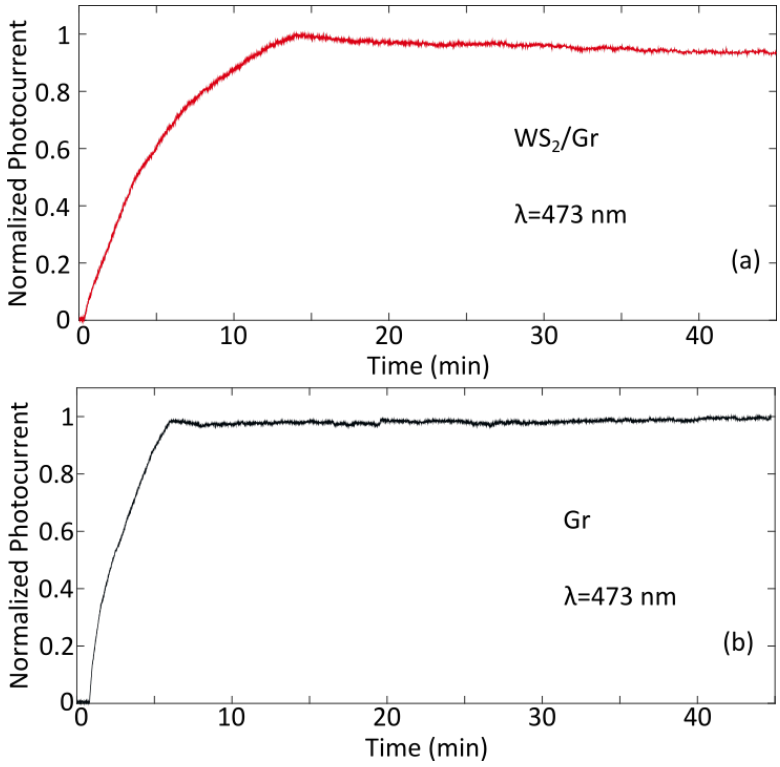

Fig. 6.9 DC photocurrent measurements vs time for WS2/graphene(a) and Gr-only (b) device under 473 nm light irradiation at bias voltage VB=1.8 V .

The responsivities, within the error bars, are generally unaffected by the change in wavelength and, overall, responsivity decreases with increasing light intensity. Fig. 6.8(b) reports the temporal response of the photocurrent under DC illumination at different wavelengths for on/off cycles with period of 20 s. The three curves collected at different wavelength are offset on the vertical axis for sake of clarity. In this case, the response changes dramatically when we switch from blue (473 nm)

to red (638 nm) light. With the excitation at 473 nm once the light is switched off, there is a PPC that remains even on a time scale of hours (Fig. 6.9(a)). The PPC is observed (although to a lesser extent) also for the green illumination, while for excitation with the red laser at 638 nm no PPC is recorded. The incident power dependence has been addressed by increasing the power at each on/off cycle. Although the photocurrent (the number of carriers) increases for all the three wavelengths the dark status is immediately restored for the red one only, even under the highest illumination intensity. This suggests the presence of a slow mechanism that retains the exceeding carriers, which keep accumulating increasing the power at each cycle.

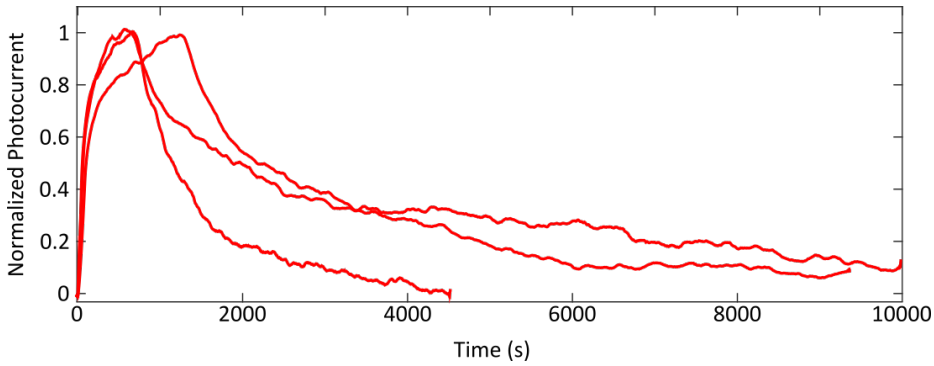

Fig. 6.10 DC photocurrent measurement vs time, under 532 nm light irradiation on devices with a channel length of 10μm at bias voltage VB=1 V and incident power of 10 mW. The diameter of the laser spot is ~1 μm.

Photocurrent measurements with a smaller illuminating spot (1 μm diameter) on devices with channels of 10μm width were also carried out and allowed us to exclude the contribution of the contacts to the observed behavior (Fig. 6.10). Graphene-only devices displayed the same PPC observed for the WS_2/graphene devices (Fig. 6.9(b)). Hence, the observed PPC – differently from what reported in [232] – is not an intrinsic property of the hybrid heterostack.

In order to understand the mechanism behind the PPC, the temporal response has been measured when illuminating the WS_2/graphene 2µm device with a spot diameter larger than the channel length, but smaller than the channel width (diameter 15 µm, 532 nm laser). The illumination was switched off only when approaching current saturation. As can be seen in Fig. 6.11(a), the device shows a slowly decaying "off" current, but after several minutes the dark condition of the device is restored. The observed finite decay is attributed to the smaller illuminated area of the device. Before discussing in detail, the measured temporal response of the photocurrent, we analyze the band alignment of our structure, *i.e.* of the WS_2 on epitaxial graphene on 4H-SiC, which we have directly measured via angle-resolved ARPES as discussed in chapter 4.

The electronic properties reported in chapter 4 for this heterostack are valid also for the case investigated in this work, since the doping level of the epitaxial graphene on hexagonal 4H/6H-SiC(0001) is not influenced by the polytype[191]. Furthermore, assuming that high purity semi-insulating (HPSI) 4H-SiC used as a substrate has the Fermi level at midgap, the total band alignment is the one sketched in Fig. 6.11(b). HPSI 4H-SiC displays several deep levels with activation energies ranging between 0.7 eV and 0.9 eV below the SiC conduction band[244], which are known to have a fundamental role in the semi insulating behavior of 4H-SiC. These intrinsic deep levels are either acceptor-like levels or negative-U centers generated from C-vacancies complexes (e.g., $Z_{1/2}$ levels), and act as recombination centers and life-time killers in charge transport experiment[245–247]. These defects in the 4H-SiC substrate are responsible for the photogating mechanism in our devices, which prevents the decay of the photocurrent. As depicted in Fig. 6.11(c) if the impinging light has enough energy (i.e. larger than 2.2 eV corresponding to a wavelength

shorter than 563 nm), it is not only responsible for photocurrent in the graphene/WS_2 heterostructure, but it also promotes electrons into the aforementioned 4H-SiC deep levels.

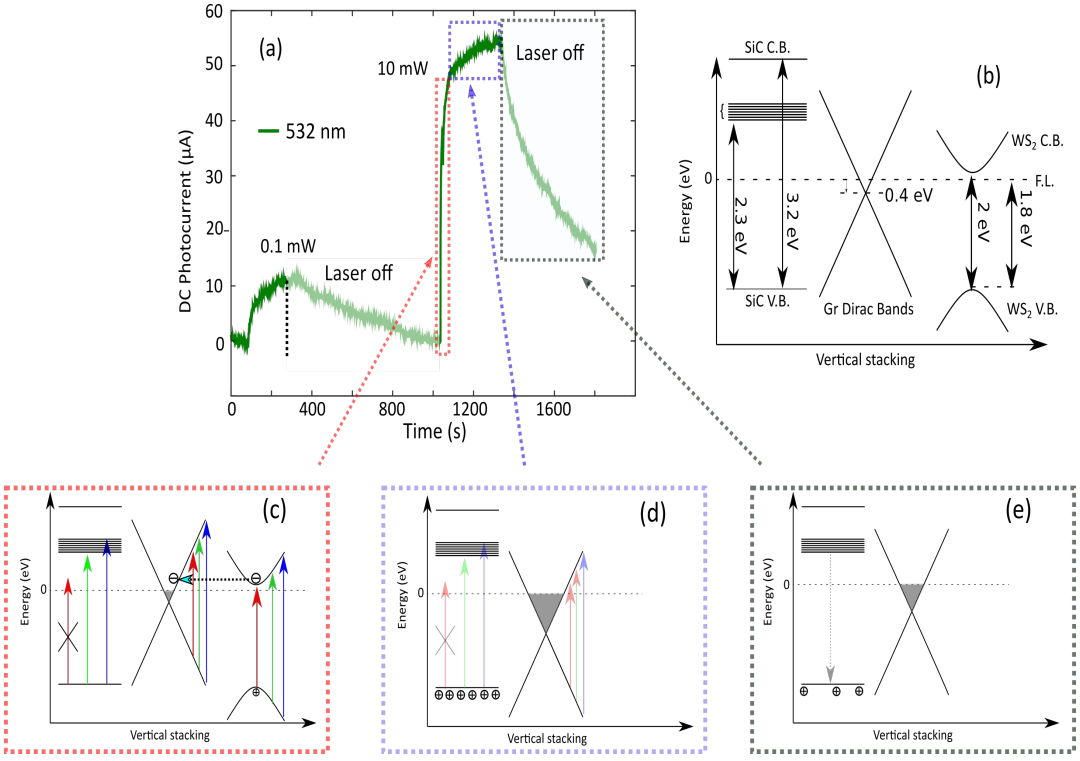

Fig. 6.11 DC photocurrent vs time using 532nm excitation wavelength. The curve is taken for two different incident light intensities, at a bias voltage of $V_B = 1V$. Opaque areas are relative to "light-off" state. (b) Scheme of the band alignment of the system with the relative energies. (c) Scheme of the mechanism involved in the generation of photocurrent and photogating at different wavelengths in the rising part of the signal (red dashed box). (d) Gating effect on graphene from SiC substrate relative to the saturating part of the rising curve (blue dashed box). (e) Recombination in VB occurring with light off in falling curve (gray dashed box).

By acting as recombination centres, such levels capture and neutralize electrons and leave charged holes behind. The accumulated holes generate an electric field that leads to a Fermi Level shift in graphene, enhancing the number of carriers (Fig. 6.11(d)). Since the trapping lifetime of these defects is extremely long[248], PPC is observed.

Nevertheless, eventually the trapped carriers recombine Fig. 6.11(e)), thus the related gate voltage decays and the initial position of the Fermi level is restored. The presence of defect levels with different activation energies is responsible for the distinct behavior observed for blue and green light, e.g. when $Z_{1/2}$ deep levels are involved, a PPC lasting for several hours is obtained. Red light does not induce any deep level transition[249], and therefore no photogating and no PPC occur. However, the energy of the red light is sufficient to excite the transition from VB to CB in WS_2. Subsequently charge transfer from the active layer (WS_2) to graphene occurs, injecting carriers in the transport layer (graphene). Hence, the role of WS_2 is crucial to enhance the responsivity of the system making the device "active" in the visible range.

6.3 CONCLUSIONS

To summarize, this chapter describes a novel approach for the implementation of scalable graphene/WS_2 photoresponsive devices. The use of a mask during the growth is crucial to controllably deposit WS_2 just on the optical channel in order to create an effective ohmic contact to the graphene channel. The devices created with this scalable approach show – when illuminated with red light – a DC responsivity reaching 220 A/W and an AC response time of $\tau_r \sim 4$ ms. PPC is measured for shorter illumination wavelengths, and a nearly perfect charge retention is observed for blue light. Such PPC originates from deep levels in the SiC substrate. The findings reported in chapter 4 resulted to be fundamental to understand the nature of this effect. The combination of wavelength-selective memory effect, enhanced responsivity and fast detection is of interest for the fabrication of 2d based optical memories, which might be realized by exploiting a transparent top gate[233] to reset the memory state and depopulate the traps.

7 BILAYER WS_2 ON GRAPHENE AND H-BN: AN ALL 2D PLATFORM FOR VALLEY-SPINTRONICS

In the previous chapters, the cutting-edge electronic and tribological properties of monolayer WS_2 on epitaxial graphene have been investigated. As discussed in chapter 1, monolayer WS_2 displays a direct band gap of about 2 eV at the $\boldsymbol{K}$ and $\boldsymbol{K'}$ symmetry points of the BZ[18,123,124], exhibits long exciton life and coherence times, causing remarkable PL[18], and therefore it has been appreciated as the TMD of choice for photoactive devices[8,52,53]. On the other hand, bilayer WS_2 presents an astonishing preservation of polarization at RT[28], *i.e.* when a polarized light is shined on the material, its PL emission preserves the polarization of the impingin light. This means that the carriers are selectively excited from one valley or the other, which implies that they are also spin-polarized[55]. Hence, WS_2 represents an exciting playground for light-matter interaction studies and a promising platform for valley-spintronic applications. Interestingly, to date, only a few works have addresses the optical properties of bilayer WS_2[28,65].

Before our work, most of these studies were carried on by using flakes mechanically exfoliated on conventional solid-state systems and adopting technologically unpractical cryogenic temperatures[28,250].The scalable synthesis of continuous WS_2 films displaying high polarization coherence is instrumental in the implementation of a WS_2-based valleytronic technology, where light allows for selecting a specific valley of the two in $\boldsymbol{K}$ and $\boldsymbol{K'}$ and therefore, also a specific spin. Moreover, incorporation of such WS_2 films within vdWH would pave the way for the realization of novel all-2D opto-spintronic devices.

In this chapter, we report the synthesis of atomic-thick WS_2 on EG, CVD graphene and h-BN by using CVD. These heterostacks were synthesized with the ultimate goal of analyzing their optical properties and assess their potential for valley- and spintronic applications. We characterize the material thickness and homogeneity via spectroscopic, microscopic and photoluminescence measurements, which indicate that the WS_2 synthetized is mostly bilayer. On h-BN, PL measurements reveal that the polarization of the incident light is highly retained. The polarization anisotropy retrieved from PL polarization maps over areas of thousands of square-microns peaks at 74% at room temperature. These results indicate the suitability of bilayer CVD-grown WS_2 films to absorb and conserve quantum information in the form of polarized light. Interestingly, at the same time of our findings, similar values of polarization conservation were reported for isolate grains of CVD grown WS2 on SiO_2[65]. For WS_2 on CVD graphene we find that the PL signal is highly quenched, and therefore a PL resolved analysis cannot be extracted. The quenching is caused by the metallic-like nature of the graphene substrate. However, when on CVD graphene, the WS_2 structural properties and Raman signal are found to be similar to those retrieved on h-BN. Therefore, one could hypothesize a polarization conservation similar to that observed on h-BN, although in this case charge transfer from the TMD to graphene is involved (as demonstrated for photodetectors in chapter6). This hypothesis is further confirmed by additional studies performed on WS_2/EG heterostacks. By adopting a bottom-up strategy for the design of photoconductive and photoemitting patterns we find that the polarization conservation of bilayer WS_2 on buffer layer graphene is indeed about 74%.

The findings reported in this chapter open exciting prospects for the adoption of vdWH in valley-spintronics.

7.1 METHODS

7.1.1 BILAYER WS_2 GROWTH

To synthesize WS_2, we used also in this case a vapor-phase reaction from solid S and WO_3 powders in a horizontal quartz tube as described in the previous chapters. The stoichiometric ratio between the WO_3 and S powders was kept the same as in the other chapters (i.e., 1:100 WO_3:S). The substrates were placed face-up < 1 cm away from the WO_3 powder (i.e., with the geometry described in chapter 3). In this case the growth temperature within the hot-zone was set to 900 °C, optimized to obtain a bilayer coverage. This final temperature was reached at a rate of 1 °C/s and was kept for 1 hour. Before the temperature ramp up, the chamber was pumped down to a pressure of ~$5x10^{-2}$ mbar. Argon was flowed during the temperature ramp with a flux of 500 s.c.c.m., leading to a pressure of 4.5 mbar, which kept the sulfur solid. After reaching 900°C, the Ar flux was suddenly reduced to 80 s.c.c.m., which reduced the furnace pressure to 1.3 mbar thus initiating sulfur evaporation and WO_3 sulfurization. The combination of a sudden evaporation of S at the growth temperature of 900 °C and high reactant flow rates, were found to direct the reaction in favor of fast and dense WS_2 growth. WS_2 synthesis was performed on h-BN flakes exfoliated on quartz, CVD graphene transferred on quartz, and epitaxial graphene on insulating 4H-SiC(0001)[50,251]. The choice of transparent substrates anticipates the use of the investigated heterostacks for optoelectronic applications. The substrates were prepared as follows:

(i) h-BN flakes were obtained via mechanical exfoliation on quartz substrates by scotch tape method as introduced in chapter 1 and reported in Ref[85]. Before exfoliation, the quartz substrate was cleaned in acetone, isopropanol, and in O_2 plasma (5 min, 80W). After the exfoliation, the sample was cleaned again in acetone and isopropanol, and treated with O_2 plasma to remove possible scotch tape residue.

(ii) CVD growth of large single-crystals of monolayer graphene was performed on Cu foil as discussed in Chapter 3 and reported in Ref.[50]. Graphene was then transferred onto a quartz substrate via dry transfer.

(iii) EG was grown on nominally on-axis 6H–SiC(0001) in a resistively heated cold-wall reactor (BM, Aixtron) as reported in chapter 3. Hydrogen etching at ~ 1250°C was used to prepare an atomically-flat 6H–SiC(0001) surface[141] and graphene was subsequently obtained in argon atmosphere at 780 mbar and at about 1700 K [142].

7.1.2 INVESTIGATION TECHNIQUES

Photoluminescence microscopy experiments were carried out with a Leica SP5 confocal laser scanning microscope using a 63x (NA 1.2) water-immersion objective. As light source, a pulsed solid state laser diode at 640 nm was used (Picoquant). The luminescence arising from the sample was collected through the objective and filtered with a 640 nm notch filter and with a 610 nm long pass filter (Chroma). To measure luminescence polarization, a broadband (420-680 nm) polarizer beam splitter was introduced in the light path. The two arising beams are collected with two identical fiber couple SPAPDs (Picoquant). The alignment of the polarizer beam splitter principal axis and the excitation laser polarization plane was proved by an additional internal polarizer filter to be better than 5°.The

atomic force microscopy (AFM). images were acquired with a Bruker Dimension Icon microscope used in ScanAsyst tapping mode. The LEEM and μLEED measurements were carried out at the Nanospectroscopy beamline (Elettra Synchrotron, Italy) using the SPELEEM set-up thoroughly described in chapter 4. Raman spectroscopy was performed using a standard Renishaw inVia system equipped with a 532 nm green laser and 100x objective lens. The laser spot size was ~1µm and the accumulation time was 1s. SEM imaging was performed at 5 keV using a Zeiss Merlin microscope, equipped with a field emission gun. TEM was carried out on a Zeiss Libra 120 transmission electron microscope operating at 120 kV and equipped with an in-column Omega filter for energy filtered imaging. Both electron diffraction patterns and bright field images were recorded energy filtered, with a 20 eV slit centered on the zero loss peak. Electron diffraction patterns were collected with a parallel beam in micro-diffraction mode, by selecting the diffracting area through the appropriate condenser aperture. For sample preparation, graphene was transferred on a gold grid. Subsequently, WS_2 was directly grown onto this system.

7.2 RESULTS AND DISCUSSION

7.2.1 ATOMIC-THICK WS_2 ON H-BN: STRONG LIGHT POLARIZATION CONSERVATION

Before carrying out optical characterization, we first report on the morphology, quality and thickness of WS_2 synthesized on h-BN. Fig. 7.1(a) shows a SEM micrograph of a representative h-BN flake exfoliated on quartz and fully covered with WS_2. No isolated triangular crystal[24,68,252]is observed and the uniform distribution of WS_2 on the flake is confirmed by Raman spectroscopy. The intensity ratio of the in-plane vibrational mode

E_{2g}^1 and of the out-of-plane vibrational mode A_{1g} is indicative of the thickness of WS_2 when using specific excitation wavelengths such as that adopted in this work, i.e., 532 nm[121,253,254]. As visible in Fig. 7.1(b), the A_{1g}/E_{2g}^1 ratio is approaching 1, indicating bilayer coverage[126].

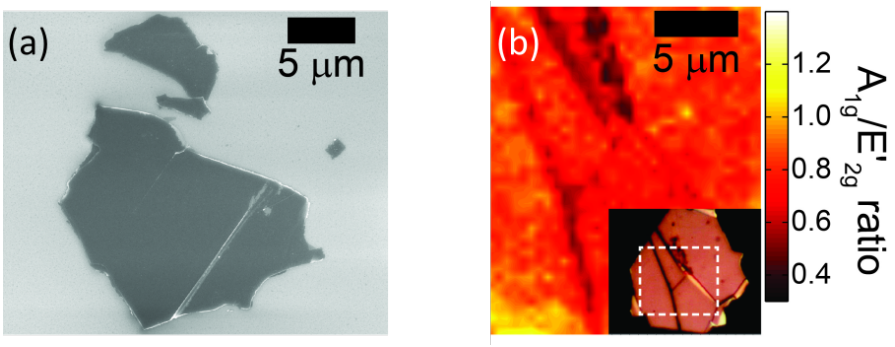

Fig. 7.1 (a) SEM image of h-BN flakes exfoliated on quartz and fully covered by WS_2 crystals. (b) Raman map of the ratio between the intensities of A_{1g} and E_{2g}^1 peaks taken in the area shown in the optical image in the inset.

Interestingly, only along crystal anomalies (clearly visible in the optical image reported in the inset in panel (b)), a smaller ratio is observed, suggesting monolayer-thick regions.

We further corroborate the monolayer/bilayer nature of the synthesized film by analyzing the overtone peak located at 310 cm^{-1}.This peak, which is attributed to rigid interlayer shear forces, diminishes with the number of layers, and ultimately disappears when approaching the monolayer limit[164,255]. Indeed, as shown in Fig. 7.2, the 310 cm^{-1} peak is barely detectable.

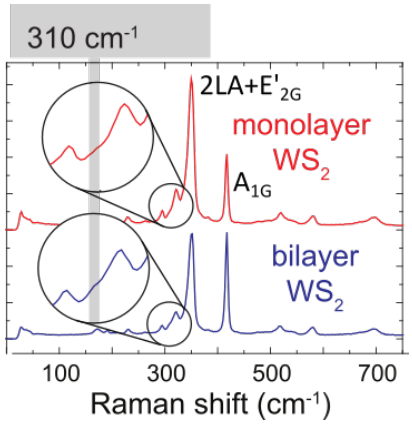

Fig. 7.2 Raman spectra of WS_2 taken in area mostly bilayer (blue) and monolayer (red). The zoom-in inset is taken around 310 cm^{-1}, where the overtone is expected.

In order to gain additional information about the thickness and morphology of WS_2 on exfoliated h-BN, we performed AFM analysis on a sample with partial WS_2 growth as that depicted in the SEM micrograph reported in Fig. 7.3(a). The white areas in the SEM micrograph are representative of exposed hBN, whereas the dark ones indicate the presence of the WS_2 film. Representative AFM micrograph and related line profiles for such partial growth are reported in panels (b) and (c). Line profiles collected atop of holes (e.g., red line in panel (c)) consistently show that they are 1.6 ± 0.3 nm in height, which confirms the bilayer thickness of our film. Between holes the film is flat within a range of a few Angstroms (black line in panel(c)). A RMS roughness of a few Å was similarly retrieved on AFM micrographs performed on films with complete coverage as that reported in Fig. 7.1(a). The crystal quality of WS_2 films obtained with a partial growth on h-BN flakes was also assessed via μ-LEEM/LEED analysis. Fig. 7.4(a) shows the LEEM micrograph of a representative analyzed h-BN flake.

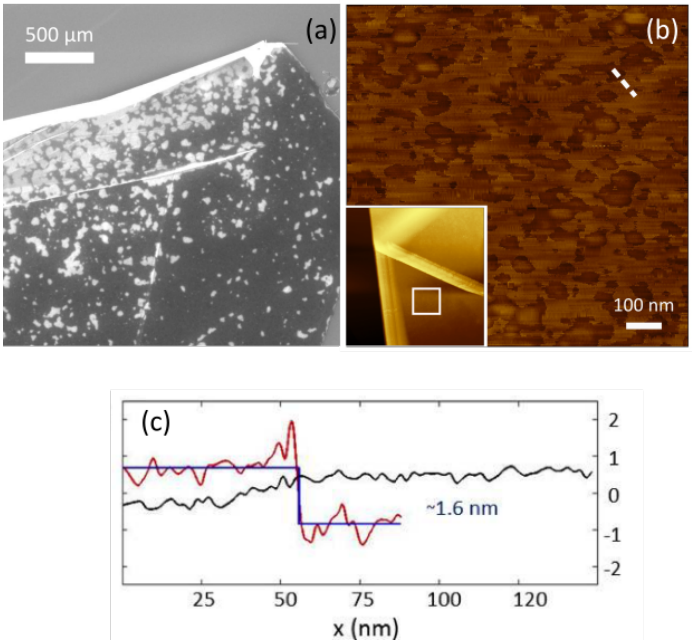

Fig. 7.3 AFM analysis of WS_2 on hBN: (a) SEM image of a selected hBN flake, showing partial growth of WS_2 (black areas). (b) 1x1 µm AFM topography micrograph displaying partial WS_2 growth (holes in the film are visible as darker regions). The micrograph is a zoom-in of the larger area reported in the figure inset. Dashed lines indicate the position of the line profiles reported in panel (c). (c) The red line indicates that the hole depth matches that of a bilayer WS_2, whereas the continuous area appears to be flat in the order of a few Angstroms (black line).

The corresponding µLEED micrograph reported in Fig. 7.4(b) shows that an epitaxial relation holds between the WS_2 and h-BN. Hence, also h-BN flakes, as already observed for EG substrates, impress a well-defined register to the growth of WS_2Time- and polarization-resolved PL spectroscopy was used to investigate the optical properties of the synthesized WS_2 film. This technique allows us to extract the conservation of the polarization of the light emitted from the recombination of the exciton. PL measurements were performed by using linearly polarized laser light with a near-resonant excitation energy (1.94 eV).

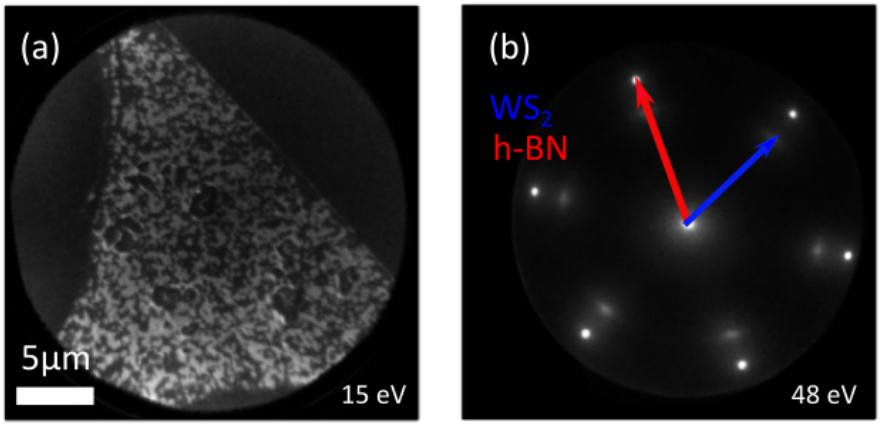

Fig. 7.4 (a) LEEM image of a h-BN flake (white area) with partial growth of WS_2 on top (dark area). (b)

To quantify the degree of polarization anisotropy of the emission, *P*, the following relation is used:

$$P = \frac{I_{\parallel} - I_{\perp}}{I_{\parallel} + I_{\perp}}, \qquad (1)$$

where $I_{\parallel}$ ($I_{\perp}$) is the intensity of PL with parallel (perpendicular) polarization with respect to the polarization of the excitation. As expected, PL emission is observed across the entire h-BN flake (Fig. 7.5(a)). A significantly stronger intensity – compatible with a transition to direct band-gap – is observed along h-BN crystal boundaries (compare map to inset in panel (a)), where monolayer WS_2 patches were indeed detected via Raman. In Fig. 7.5(c), we plot the PL intensity histogram (vertical graph), the PL polarization histogram (horizontal graph) and a 2D correlation histogram (intensity plot) obtained by analyzing the

representative flake in panel (a). Remarkably, the peak polarization anisotropy is about 74% over an area of thousands of square micrometers.

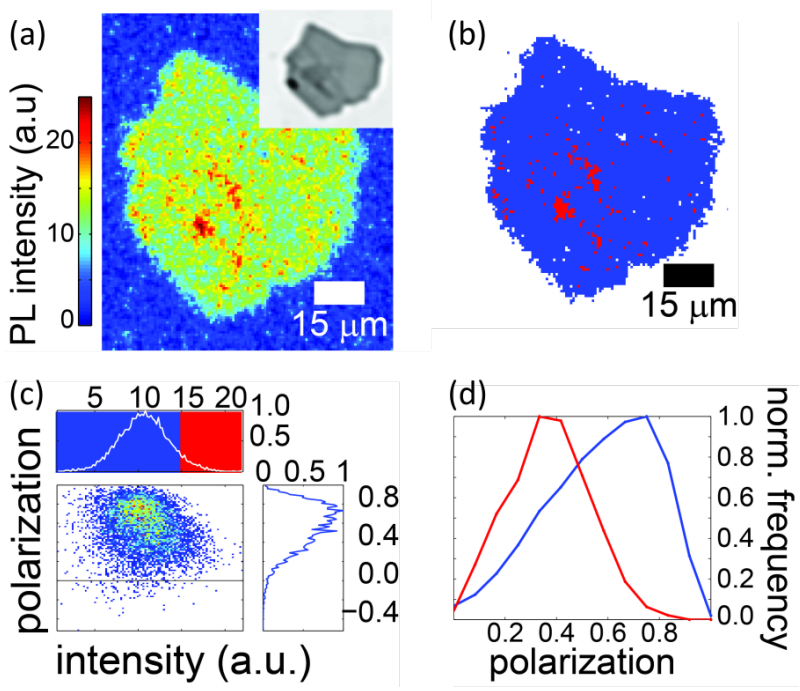

Fig. 7.5(a) Raw PL intensity map of a selected h-BN flake (also shown in the optical micrograph in the inset). (b) Binary PL intensity map, where the high PL intensity areas (in red) near the domain edges of the h-BN flakes are separated from the lower intensity values (in blue) elsewhere by defining a threshold, as shown in the intensity graph in (c). (c) 2D histogram of PL polarization vs. PL intensity with respective projections, revealing a correlation of the two quantities. (d) Histograms of the PL polarization within the high (red) and low (blue) PL intensity areas as shown in panels (b) and (c).

The elongated 2D histogram indicates a strong correlation between intensity and polarization, which we elaborate further by plotting separate histograms for areas attributed to monolayer WS_2 and bilayer WS_2 (red and blue in panel (c)), based on the PL intensity. The two histograms are shown in Fig. 7.5(d) and define the polarization

conservation to be 43% for monolayer WS_2 and 74% for bilayer WS_2, respectively. These values are in close agreement with those measured for isolated mono- and bilayer WS_2 crystals on SiO_2 (i.e., 30% and 80%) with circularly polarized light[65].The slightly higher (lower) values measured for monolayer (bilayer) found in this work can be explained by the fact

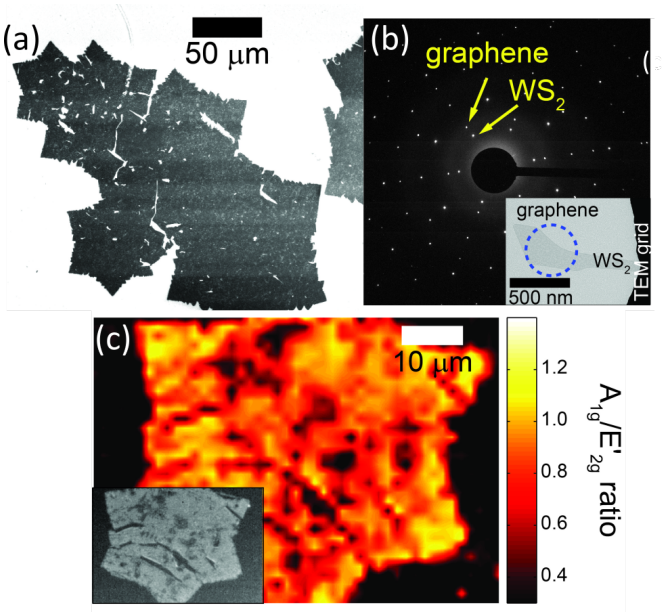

Fig. 7.6 (a) SEM image of CVD graphene crystals transferred on quartz and fully covered by WS_2. (b) Selected area electron microdiffraction pattern of the heterostack collected from the area enclosed by the dotted circle in the bright field image reported in the inset. (c) Raman map of the ratio between the intensities of A1g and E2g1 peaks. Inset: optical image of the selected flake used for Raman.

that both thicknesses occur below the resolution threshold of the PL setup (~ 250 nm), as also indicated by the wide tails of the histograms.

It is to note that a continuous atomically-thick polycrystalline WS_2 film such as that presented in this work does not pose an obstacle for coherent photoabsorption/emission, since the exciton radius in WS_2 is as small as ~1-2 nm[256].

7.2.2 ATOMIC-THICK WS_2 ON CVD GRAPHENE: A POSSIBLE PLATFORM FOR OPTICAL SPIN INJECTION

We now turn to the analysis of bilayer WS_2 synthesized on CVD graphene. Fig. 7.6(a) reports a SEM micrograph of CVD graphene single-crystals after growth of a continuous WS_2 film with the process parameters reported in paragraph 7.1.1. The crystallinity of the WS_2 layer is evaluated by analyzing a partial growth via TEM imaging and selected area electron microdiffraction. As shown in Fig. 7.6(b), the partial process leads to the formation of WS_2 single-crystals with an epitaxial relation to the graphene substrate. The single-crystal domains appear to be several hundreds of nanometers in size (see inset in panel(b) showing the analyzed area). It is worth noticing that for TEM analyses WS_2 growth was directly performed on graphene transferred over a TEM grid, with holes 10 μm wide (Fig. 7.7). It is remarkable that WS_2 growth occurred on suspended graphene, which hence stood the growth conditions.

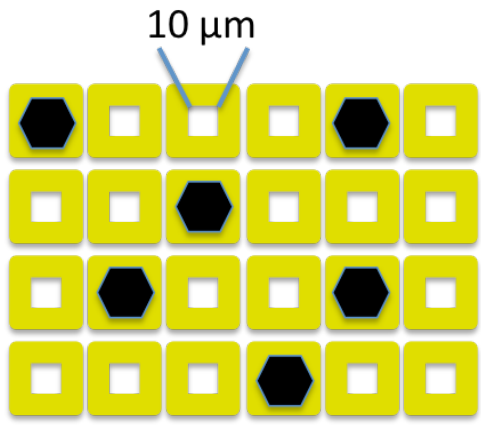

Fig. 7.7 Scheme of the TEM grid with transferred graphene on top. The grid is made of gold, ideal to sustain growth conditions of WS_2

The Raman map reported in panel (c) indicates that most of the graphene grains are covered by bilayer WS_2 (i.e., $I(A_{1g}/E_{2g}^1) \sim 1$)[126]. Local monolayer inclusions are observed especially in proximity and within transfer-generated tears of graphene (which are visible in the optical image in panel (c)). AFM analysis and line profile for continuous WS_2 films grown on top of CVD-graphene allow for WS_2 thickness estimation and morphology evaluation (Fig. 7.8). Different from the case of exfoliated h-BN flakes, where the thickness of the flake is unknown, in this case thickness of the supporting graphene layer is known (i.e. a monolayer). Hence, the thickness of WS_2 can be simply extracted by measuring the height of the heterostack.

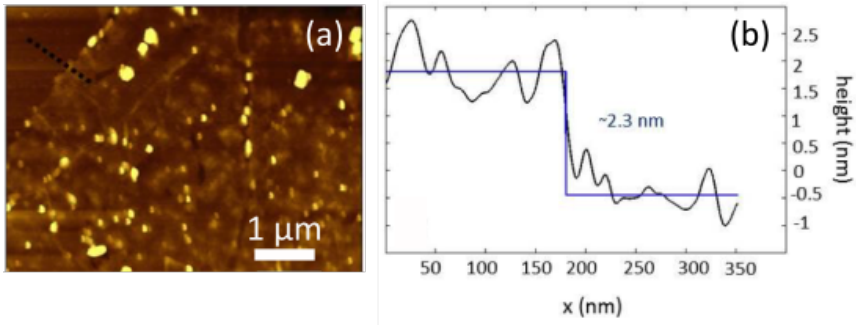

Fig. 7.8 AFM analysis of WS_2 on CVD graphene: (a) AFM topography micrograph of a flake of CVD graphene transferred on quartz with a WS_2 film grown on top. The number of layers of the system is estimated by tracking a line profile at the edge of the flake (b). The height measured matches the sum of one layer of graphene plus two layers of WS_2.

The line profile reported in Fig. 7.8(b) indicates a height of 2.3 ± 0.5 nm, compatible with that of a graphene monolayer with atop a WS_2 bilayer. The morphology of the film is in this case rougher (see Fig. 7.8(a)), with a RMS roughness of 5.3 nm, which is due to contaminations brought by the transfer process. Fig. 7.9 shows the Raman spectra measured for CVD

graphene after WS_2 growth, demonstrating that the underlying graphene is not damaged by the growth process, however a broadening of the 2D peak and the presence of a small D peak suggest that the flake has been altered with respect the pristine one. Interestingly, already with the Raman setup a PL signal should be present, since the corresponding peak falls near the 2D Raman peak. Nevertheless, no PL is retrieved. This is due to the already low PL emission coming from bilayer WS_2 combined with the metal quenching arising from the graphene layer underneath. Indeed, graphene gathers the photoexcited carrier, preventing the radiative recombination. Considering the results reported in chapter 6, it appears that charge is efficiently transferred between WS_2 and the underlying graphene. Therefore, if the polarization conservation observed for WS_2 on SiO_2[65] and h-BN would be verified also for WS_2 on graphene, this system would gain enormous appeal for implementing optical spin injection and optospintronic devices.

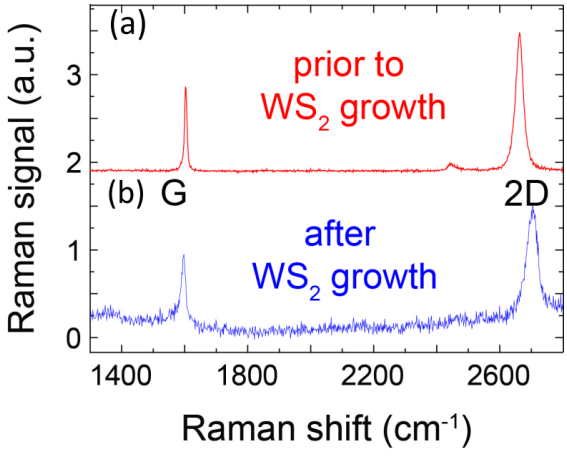

Fig. 7.9 Raman spectrum of CVD graphene before (a) and after (b) the growth of WS_2

7.2.3 PHOTO-EMITTING/PHOTO-CONDUCTIVE PATTERNS OF WS_2 ON EPITAXIAL GRAPHENE.

As discussed above, PL is quenched in WS_2/graphene stacks because of enhanced electron transfer to gapless graphene[257]. Therefore a compelling open question is whether the synthesized WS_2 film still presents a robust polarization conservation.

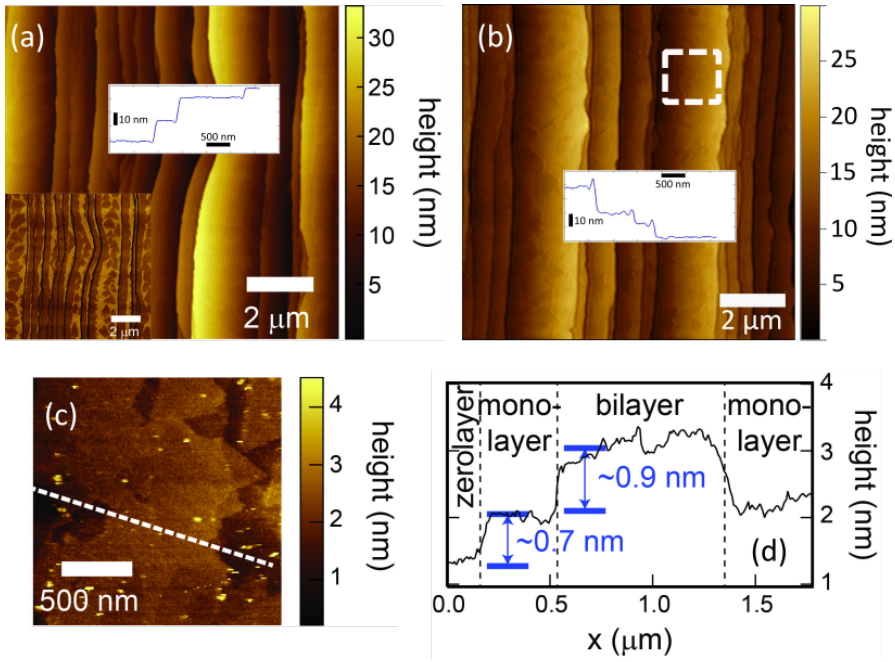

Fig. 7.10 AFM analysis of WS_2 on epitaxial graphene: (a) Representative AFM micrograph showing a typical topography of epitaxial graphene on SiC. The inset shows the phase trace, highlighting the difference between zero layer (bright) and monolayer (dark) graphene. (b) Topography of the surface after the growth of WS_2. The growth process does not affect terraces. (c) Height scan of the same sample in the dashed area in panel (b) after WS_2 growth. (d) Profile of the highlighted line, showing monolayer and bilayer regions.

To gain insight into this, we devised a tailored experiment by using EG on SiC(0001)[45], a perfect platform to investigate WS_2 optical properties. On a

typical epitaxial monolayer graphene sample, monolayer areas alternate with buffer layer areas following the atomic terraces of the SiC surface[143]. As discussed in paragraph 3.1.1, buffer layer graphene is the first carbon-rich layer forming on top of SiC and, although the hexagonal lattice is retained, 30% of the constituting atoms are covalently bonded to the substrate[48]. Local breaking of the sp^2 hybridization disrupts the semi-metallic nature of the layer and hence its quenching properties. The epitaxial graphene topography was investigated before and after WS_2 growth. Fig. 7.10(a) is a characteristic AFM micrograph of an atomically flat SiC surface presenting single steps of about 10 nm height after graphene growth. The phase image reported in the inset of Fig. 7.10(a) shows typical monolayer (darker) and zerolayer (brighter) graphene regions along the atomic terraces of SiC[48,141]. Fig. 7.10 (b) shows the sample after the synthesis of WS_2 adopting the growth process reported in this chapter. The morphology of the sample appears overall unaltered, although finer structures can be detected within the atomic terraces. Indeed, a more detailed analysis of the WS_2 film is possible by analyzing the region within the atomic terraces, as shown in panel (c). The merging WS_2 islands, showing a triangular symmetry, present a mono to bilayer WS_2 height (see relative line profile in panel (d)). In the SEM micrograph reported in Fig. 7.11(a), one can appreciate triangular WS_2 grains (obtained with a partial growth) covering monolayer graphene (light gray contrast) and zerolayer (or buffer layer) graphene (mid gray contrast). Also in this case, as for h-BN and CVD graphene substrates, the grown WS_2 is azimuthally aligned with the substrate (see chapter 4).

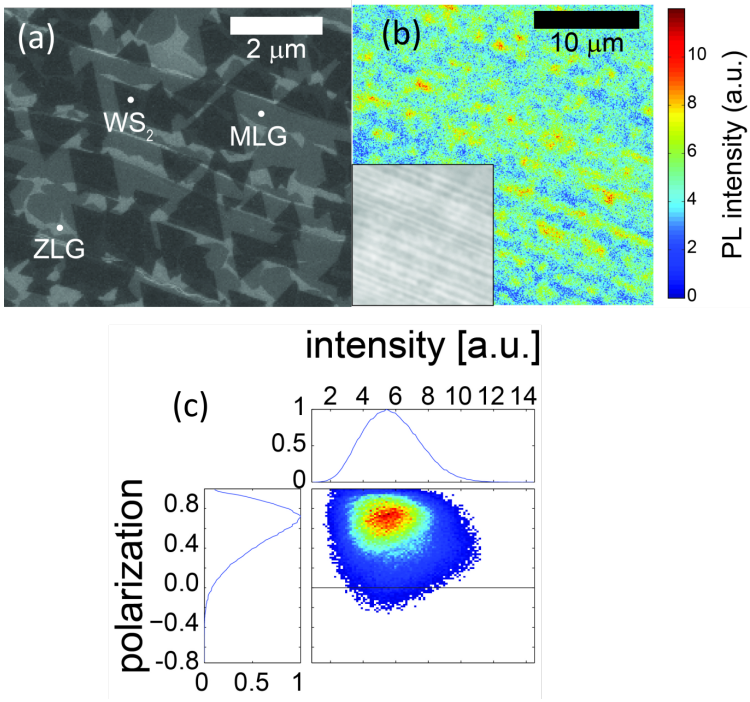

Fig. 7.11 (a) SEM image of WS_2 on epi-graphene. Brighter areas are attributed to buffer (ZLG) layer, intermediate grey to graphene and darker triangles to WS_2 crystals. (b) PL polarization vs. PL intensity 2D histogram. The polarization peaks at ~70%. (c) PL intensity map taken from the area shown in the inset. The emission in stronger where WS_2 is on top of buffer layer regions.

As expected, the PL intensity from a sample covered with WS_2 bilayers is altered along lines parallel to the terrace directions (see panel (b)). A measurable photoemission is detected only in correspondence of WS_2/buffer layer stacks. Analogously to the h-BN substrate, an elongated 2D histogram of PL polarization and intensity is observed and the polarization conservation is again peaked at 72% (Fig. 7.11(c)). Conversely, no significant PL signal is retrieved over monolayer EG areas. Hence, by synthesizing WS_2 on EG, patterned photoconductive and photoemitting ribbons can be obtained in a bottom-up and straightforward fashion. The outstandingly high mobility and free path

length in graphene could potentially allow to transport the quantum information from the absorbed light via spin-polarized electrons.

7.3 CONCLUSIONS

In this chapter, we have demonstrated the CVD synthesis of continuous atomic-thick WS_2 films on 2d substrates. Remarkably, the adopted synthetic approach yields films which are (mostly) bilayer thick on all the analyzed substrates. Hence, the presented approach appears to be robust.

In all instances, the synthesized WS_2 films are azimuthally aligned with the underlying substrate. Furthermore, on h-BN and EG they display remarkable polarization conservation at room temperature, as high as 74%. By adopting EG as growth substrate, one can define in a bottom-up fashion photoemitting and photoconducting ribbons. The scalable synthesis and design on 2D substrates of WS_2 films with outstanding optical properties is instrumental in the development of novel all-2d quantum optoelectronic and valleytronic devices. Indeed, the measured high polarization conservation indicates that the carriers promoted in conduction band are highly spin-polarized. In chapter 6 the charge transfer from WS_2 to graphene in a photodetector geometry was demonstrated. In light of this, one can think of a device geometry where spin-polarized carriers can be injected from WS_2 to graphene by means of polarized light. The WS_2 layer would allow for spin manipulation by light transduction mechanisms while the long spin-life time in graphene[258] would allow for spin transport.

8 SUMMARY AND PERSPECTIVE

Graphene has proven to be an extraordinary material, with outstanding electronic and mechanical properties and is – as a matter of fact – the most famous and most studied 2d crystal. However, a large portfolio of 2d materials exists, each with different electronic, mechanical and optical features. Combining them together in vertical heterostructures allows for creating novel functional materials whose properties and applicative potential await to be discovered.

This work focuses in synthetizing and unveiling the properties of vdW heterostructures of interest for optoelectronics and potentially appealing for spin-valleytronics applications. We have chosen to study vdW heterostructures created with WS_2 as a building block. This TMD is a semiconductor with direct bandgap in its monolayer form, it shows a strong spin-orbit coupling and light adsorption substantially higher than graphene. A large part of this thesis concentrates on the heterostructure WS_2 on EG, as the combination of a 2d semiconducting layer (WS_2) and a 2d quasi-metallic substrate (graphene) is enticing for the implementation of a new generation of optoelectronic devices.

The major findings of this work are represented by: (i) the development of a growth process for flexibly synthetizing WS_2 in isolated grains and continuous films on graphene and h-BN; (ii) the first direct experimental visualization of the electronic band structure of the WS_2/EG heterostructure; (iii) the report of superlubricity of WS_2 flakes on EG triggered by an STM tip; (iv) the development of a scalable process for the fabrication of photodetectors with remarkable performance; (v) the report of light polarization conservation in bilayer WS_2 films on h-BN and buffer layer graphene.

(i) In the first part of this thesis the WS_2 growth mechanism has been introduced and discussed. Starting from solid reactants such as sulfur and tungsten trioxide makes the growth process very delicate, with a number of variables that play a major role in the process. A first modeling of the growth mechanism of WS_2 has been addressed on a classical bulk substrate – SiO_2/Si^{++} – adopted also by other groups for synthesizing WS_2[26,68].This has facilitated the material benchmarking process and the development of a robust synthetic approach. It has been found that the growth of WS_2 in either continuous film or isolated crystal depends dramatically on the substrate roughness, temperature and pressure. Particular conditions of high pressure and high temperature lead to the formation of vertical platelets of WS_2, whereas in the opposite situation of low pressure and low temperature, the chemical reaction is unbalanced, giving rise to the formation of unwanted byproducts. Optimal recipes to obtain from time to time continuous films or isolated crystals were found for a number of bulk substrates (i.e., SiC, SiO_2). Remarkably, it was found that by adopting the same parameters that led to isolated crystals on bulk substrates yielded continuous growths on 2d layers. WS_2 growth was optimized to an extent where isolated crystals, continuous films and even bilayers could be obtained on EG, CVD graphene and exfoliated h-BN.

(ii) The structural and electronic properties of CVD-grown WS_2 crystals on monolayer EG on SiC(0001) were thoroughly explored. Microscopy techniques such as LEEM/PEEM and AFM as well as laterally averaging methods as ARPES and XPS have allowed for the full characterization of the system. The set of measurements we carried out converged on defining WS_2/EG to be a low-

interacting system. Indeed, μLEED did not show moiré-like diffraction spots and neither μARPES nor ARPES showed replica bands. DFT calculations supported the experimental findings by evidencing the absence of gaps (either due to band anticrossing or to superperiodicity effects). The analysis of core level confirmed as well the weak interaction between WS_2 and graphene. Finally, the band alignment between WS_2 and graphene was determined. Moreover, this study allowed for recording the highest value (at the time of the experiment) of spin-orbit splitting of the VB, i.e. 462 meV. These findings suggest that this system has a strong appeal for realizing optical spin-injection and optospintronic applications in general.

(iii) The interest for the structural properties of this system initially has motivated the study via STM of the interface WS_2/EG. However, the obtainment of atomically resolved images was found to be extremely challenging, due to tip-triggered superlubric sliding of monolayer WS_2 on EG. We attributed the activation of the sliding transition to tip-sample interactions, as also supported by molecular dynamics calculations. The observation of the superlubric sliding of the WS_2 flakes on the graphene substrate is a further indication of the cleanliness of the CVD growth of WS_2, since contaminants at the interface can hinder superlubricity. Finally, we propose suggestions on how to obtain atomic resolution for such system and provide the first atomically resolved STM micrographs for WS_2 on graphene. Notably, this is the first report of superlubricity between a 2d TMD and graphene and suggest that the applicative potential of this interface can be extended by novel mechanical prospects. In principle, it is reasonable to think that such sliding effect can controlled to create

specific patterns, e.g. by creating a design of “defective” points acting as sliding barriers.

(iv) We reported a novel approach for the implementation of scalable graphene/WS_2 photoresponsive devices. A new strategy was employed to controllably deposit WS_2 on a defined pattern. The implementation of a growth mask allowed for depositing WS_2 on the optical channel only, in order to leave graphene unaltered and open for direct contact. The devices created with this scalable approach showed – when illuminated with red light – a DC responsivity reaching 220 A/W and an AC response time of $\tau_r \sim 4$ ms. When a shorter wavelength excitation light was implemented, a PPC photocurrent arising from deep levels in SiC and lasting for hours was detected. The combination of wavelength-selective memory effect, enhanced responsivity and fast detection is of interest for the fabrication of 2d based optical memories, which might be realized by exploiting a transparent top gate to reset the memory state and depopulate the traps.

(v) In the last part of the thesis the optical properties of continuous bilayer WS_2 synthesized on EG, CVD graphene and h-BN were studied. We retrieved a conservation of polarization of the incident light up to 74% when PL experiments were carried out. The valley-selective transitions involved are responsible for promoting spin-polarized carriers. We showed that by adopting EG on SiC as growth substrate, one can define in a bottom-up fashion photoemitting and photoconducting ribbons. The synthesis on 2d substrates of continuous WS_2 films with outstanding optical properties is instrumental in the development of novel all-2d quantum-optoelectronic and valleytronic devices.

The findings reported in this thesis suggest numerous enticing developments which are worth exploring. In particular, many of these results (band alignment, efficient charge transfer, light polarization conservation) strongly indicate the WS_2/graphene system is as an extremely appealing platform for the realization of optical spin-injection and spintronic devices more in general. At present, in order to fully unveil the potential of WS_2/graphene for (opto)spintronic applications we are concentrating on deepening the following studies:

I. The electron dynamics of WS_2 on quasi-freestanding graphene are currently being studied by adopting a time-resolved ARPES equipment at the MPI of Hamburg, in collaboration with Dr. Isabella Gierz. First results demonstrate a fast charge transfer (~1 ps) from graphene to WS_2, showing how the systems are intimately connected when charge transfer effects are taken into account. Moreover, a shrinking or renormalization of WS_2 band gap has been demonstrated when, by means of optical pumping, carriers are promoted and excitonic levels are filled. In fact, a vertical shift of the valence band has been observed reducing the optical band gap at around ~1.8 eV (see appendix C).

II. Spintronic devices have been fabricated and measured in collaboration with Prof. Bart van Wees. Specifically spin valve measurements have been being carried out to demonstrate the spin lifetime anisotropy in graphene when WS_2 is placed in contact with the transport channel. The systems under investigation are WS_2 on CVD graphene and on QFSMLG. The choice of the latter with respect EG, has been dictated by the possibility to rule out any contribution from buffer layer[259]. Despite being very promising, this study needs a deeper investigation in order to understand what measured so far.

The ultimate goal would be to exploit the optical properties of WS_2 to directly inject spin polarized carriers in graphene by means of polarized radiation.

Furthermore, a beamtime proposal for time-and-spin resolved measurements at the Diamond Light Source synchrotron facility (UK) was awarded and is expected to be carried on at the beginning of 2018. The objective of the proposal is to resolve spin polarized photocarriers in WS_2/graphene. If successful, these experiments will provide direct evidence for the existence of spin polarized photocarriers and their relaxation dynamics. The successful completion of these research projects stemmed from my thesis work might realistically pave the way towards devising a novel class of 2d optospintronic devices.

APPENDIX A:

DOUBLE-PIPE GEOMETRY FOR HIGH PRESSURE GROWTH

Here a new strategy for the growth of large grain WS_2 is proposed. As described in chapter 4, the growth mechanism is highly affected by temperature and pressure. In particular, it is possible for a molecule to explore a number of minima in the potential profile related to the surface landscape when enough energy is given to the system, residing on the most favorable. However, the surface mobility is also related to the pressure, which affect the mean free path of the molecules on the surface. In particular, low pressure means high mean free path. Conversely, high pressure means that the molecule will not explore the whole surface and will enlarge crystals already existing rather than forming new ones.

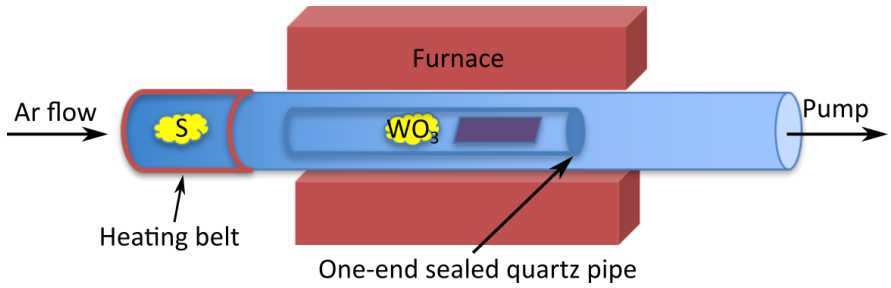

Fig. A 1 Scheme of the furnace with the inside inner pipe. The inner pipe is one-end sealed ensuring a local higher pressure in the system.

Nevertheless, the practical limitations of our set-up do not allow for exploring a wide range of pressure, and therefore a different strategy has to be implemented. A possible expedient is to use a one-end sealed quartz pipe. In this way, the incoming Ar flow will stay in the pipe ensuring a local

over pressure. The sample and the powder are therefore placed together inside the pipe (Fig. A 1).

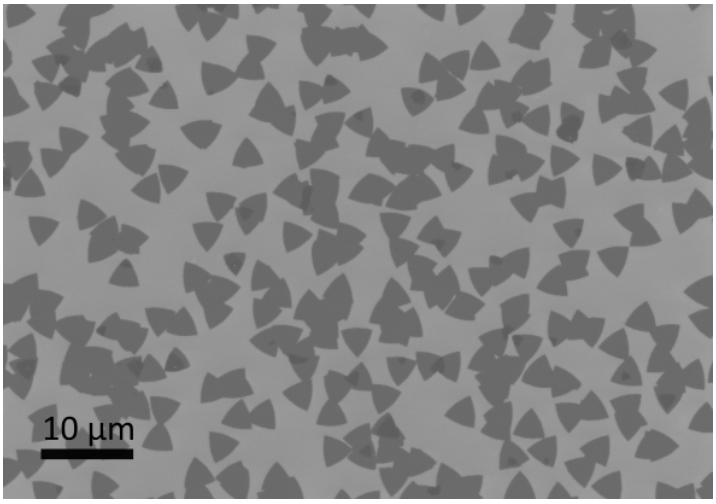

Fig. A 2 SEM micrograph of WS_2 on SiO2. Small patches of darker contrast indicate bilayer area.

METHODS

The growth is performed at 900°C with a base pressure of 1 mbar. The substrate is SiO_2/Si^{++} as the one used in chapter 4 to model the growth mechanism. The substrate has been cleaned in acetone and isopropanol for 3 minutes respectively. As a last cleaning step it has been treated with oxygen plasma. SEM micrograph have been obtained at 5keV using a Zeiss Merlin microscope, equipped with a field emission gun.

RESULTS AND DISCUSSION

The resulting outcome is reported in Fig. A 2. The average size of the crystals is substantially higher than what reported in chapter 4, clearly displaying the typical crystal triangular shape. This confirms our hypothesis regarding the growth working principle.

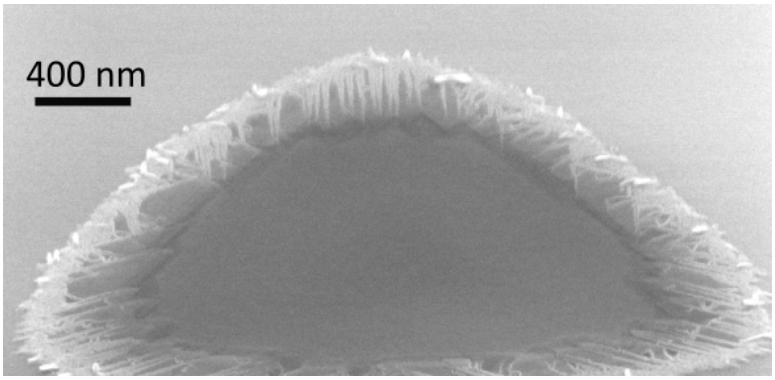

Fig. A 3 Tilted SEM micrograph of WS_2 crystal sunk in the SiO_2 substrate. An indented crown is surrounding the WS_2 crystal

It worthy noticing that such an approach presents a side effect. In some areas of the SiO_2 sample it seems that the WS_2 crystal is somehow sinking in the substrate, showing an indented crown surrounding the WS_2 surface (Fig. A 3). However, a deeper study is needed to clarify this phenomenon.

APPENDIX B:

DISTANCE DEPENDENCE OF WS_2 GROWTH OUTCOME ON EXFOLIATED H-BN

In this appendix, the dependence of the WS_2 growth mechanism from the substrate distance with respect the reactants is reported. The choice of the substrate has been dictated by its availability and the reproducibility. Therefore, exfoliated h-BN on SiC has been explored. The commercial source (*HQ graphene*) ensures the homogeneity of the crystal quality. However, the thickness of the investigated flakes is not taken into account, assuming that different multilayer h-BN flakes will behave in the same way, irrespective of the number of layers. The choice of SiC as substrate is due to the fact that on hydrogen-etched SiC the growth is not favorable and therefore the nucleation will occur on the h-BN flakes only.

METHODS

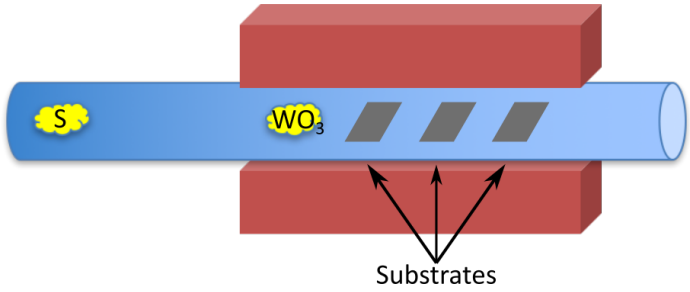

Fig. B 1 Furnace scheme, showing the relative distances between reactants and substrates

The SiC substrate has been treated with hydrogen, as described in chapter 4, in order to obtain atomically flat surface. The h-BN flakes have been

exfoliated and cleaned with oxygen plasma as described also for chapter 8. The WS_2 growth has been perfomerd at 900°C and 1mbar pressure for 1 hour for all the four cases reported here. SEM micrograph have been obtained at 5keV using a Zeiss Merlin microscope, equipped with a field emission gun

RESULTS AND DISCUSSION

As reported in chapter 4 the growth of WS_2 on other 2D materials is extremely favorable. Nevertheless, a perfect 2d surface will now show any favorable nucleation point acting as a seed. Therefore, the growth has to start from a defect present on the surface.

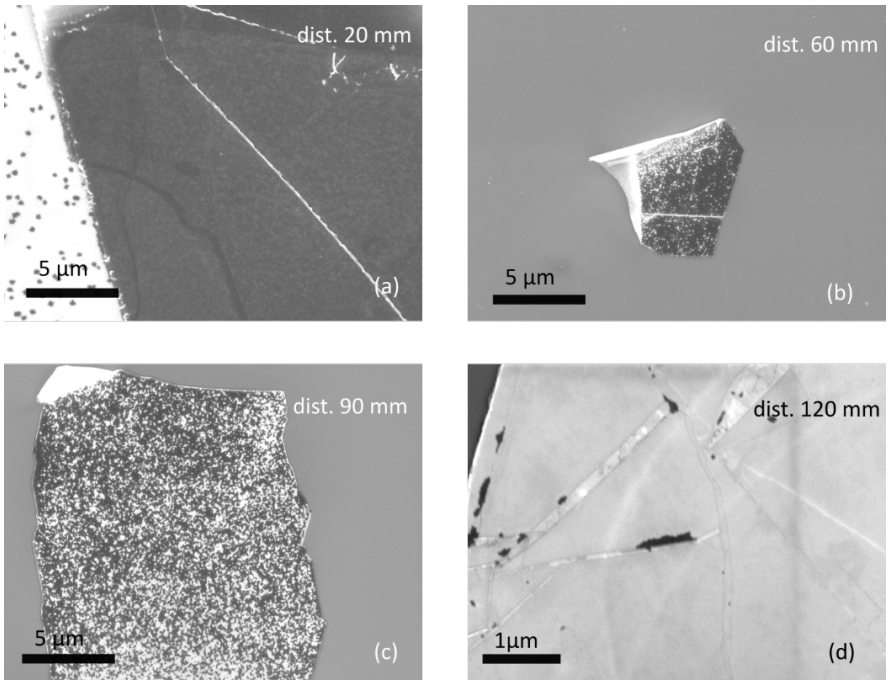

Fig. B 2 SEM micrograph of h-BN flakes after WS2 growth for different distances of the substrate from the reactants: (a) 20mm, (b) 60 mm, (c) 90 mm, (d) 120 mm

In the case of exfoliated h-BN such defect are represented by the edge of the flake itself. When he sample is place close to the reactants (closest edge of the substrate slab at 1 cm with respect the WO_3 powder), the reaction is very favorable leading to the formation of a bilayer film (explored in chapter 7). However, changing the distance as schematized in Fig. B 1, alter the way the molecules are delivered on the surface. Thus, the growth proceeds towards partial growth of the substrate. In Fig. B 2 the outcome of the growth at different distances is reported. When the substrate is placed close to reactants (panel (a)), the growth displays a full coverage. However, the contrast present on the surface of the flake suggests that the growth has both monolayer and bilayer patches. Interestingly enough in this case a partial growth is displayed also outside the flake, however with a way lower coverage. Putting the distance further away, the coverage goes progressively disappearing, down to few cluster shown in panel (d) when the distance is set 120 mm away.

CONCLUSION

We can therefore conclude that the further the sample is placed the less favorable the deposition of the molecules is. This suggest that distance is also a good parameter to play with, even though it is strongly depending on the gas flow choice and on the fluid-dynamic model of the furnace, not addressed in this work.

APPEDINX C

TIME-RESOLVED ARPES ON THE WS_2/QUASI-FREESTANDING MONOLAYER GRAPHENE INTERFACE

ARPES study reported in chapter 4 was focused to the study of WS_2 on EG. However also QFMLG can be used as growth substrate for WS_2. As showed in chapter 3, the structure differs by the presence of the buffer layer at the interface between SiC and graphene. In the case of QFMLG there is no buffer layer and the Si dangling bonds at the interface are saturated by hydrogen (H) atoms[138]. This difference affects the features of the two systems, for instance the doping level changes from n-type of EG to p-type of QFMLG[260] (highlighting the role of buffer layer in shifting the chemical potential), the mobility in QFMLG is higher[139], spin transport is more efficient[259]. As it will be described in chapter 6, the WS_2/EG can be used to fabricate large-scale efficient photodetectors. Due to its better performances in terms of mobility, QFMLG can be a valid candidate to enhance the performances of such a device. Therefore, it is crucial to study how WS_2/QFMLG interact with light to understand the mechanism behind the charge transfer responsible for photodetection.

In this appendix the carriers dynamics in WS_2/QFMLG heterostructure is shown. The aim of this short report is to display preliminary results collected in the very last part of my thesis. However, a deeper and more accurate scientific discussion is needed, since more data have to be collected and analyzed.

In order to reveal the dynamics of the charge carriers, we exploited the potential provided by time-resolved ARPES (tr-ARPES) as an

investigation technique. tr-ARPES is a technique that allows for the investigation of excited state and electrons dynamics in a system.

It is a pump-and-probe technique, in which by mean of an external excitation the system is put out of equilibrium. For instance, the system can be perturbed by a laser source (pump), which promotes the electrons from the ground level to an excited state. Experiments of selected samples (see appendix C) were carried out at the "Center for Free-Electron Laser Science –CFEL" at Max Plank Institute (MIP) in Hamburg.

Recently, a work on MoS_2/EG via tr-ARPES has been published[199], showing the band-gap renormalization occurring in MoS_2 due to the screening from excited carrier. However, no interlayer interaction is displayed, treating the two layers as independent. This might be due to the azimuthal angle between the two layers, i.e. 30°, which implies the misalignment of the BZs. As a consequence, mapping around the **K**-point for graphene and MoS_2 becomes impossible, since they are not aligned along the same high-symmetry direction. Conversely, the WS_2/QFMLG heterostructure reported in the following shows a preferential relative orientation at 0°, which allows for investigating the VB and CB of WS_2 at the same time together with graphene Dirac cone. Also in this case the band-gap shrinking is observed and attributed to density of excited carriers. Moreover, a clear charge transfer between the 2d layers is displayed, confirming the suitability for this heterostructure for light detection.

METHODS

QFMLG has been obtained annealing in H_2 the buffer layer grown from SiC(0001) via thermal decomposition. The SiC substrate has been first hydrogen-etched, in order to obtain atomically flat surface, as described in chapter 3. The growth process, occurring at ~1300 °C, has been tuned

to stop the surface decomposition to the formation of buffer layer only. Subsequently, in the same reactor, the sample has been treated in H_2/argon (Ar) environment with a flow of 500 s.c.c.m. for each gas, at 900 °C for 20 min. WS_2 growth was carried out in a horizontal hot-wall furnace. The reaction occurred at 900 °C and 8 sccm, corresponding to a chamber pressure of 0.6 mbar, for 1 hr.

A first characterization has been given using Raman Renishaw spectroscopy. Raman characterization was performed using a standard Renishaw inVia system equipped with a 532 nm green laser and 100x objective lens. The laser spot size was ~1 μm and the accumulation time was 2s. SEM imaging was performed at 5 keV using a Zeiss Merlin microscope, equipped with a field emission gun.

Spatially averaged LEED measurements were carried out using an ErLEED system from SPECS GmbH. All measurements were performed at room temperature.

Pump and probe experiments have been performed at Center for Free Electron Laser Science at Max Plank Institute for the Structure and Dynamics of Matter in Hamburg (Germany).

Pump and probe pulses are generated by the same Titanium:Sapphire amplifier (1kHz repetition rate, central wavelength 790nm, 40fs pulse duration, 12mJ output power)

- probe pulse: 2mJ in the high harmonic generation(HHG) beamline in Argon to produce extreme ultraviolet (XUV) light. A single harmonic is selected with time-preserving monochromator at ~26eV. The XUV pulses are stretched to 100 fs.
- pump pulse: 1eV pulses are generated with an optical parametric amplifier (OPA). Pulses are frequency doubled in a beta barium

borate (BBO) crystal to produce 2eV pump pulses. Pump fluence was 2mJ/cm^2

RESULTS AND DISCUSSION

The system has been characterized already after the H-intercalation to assess the presence of graphene. Fig. C 1 shows the two Raman spectra. The graphene 2D peak is observed at (Raman Shift) in Fig. C 1(a).

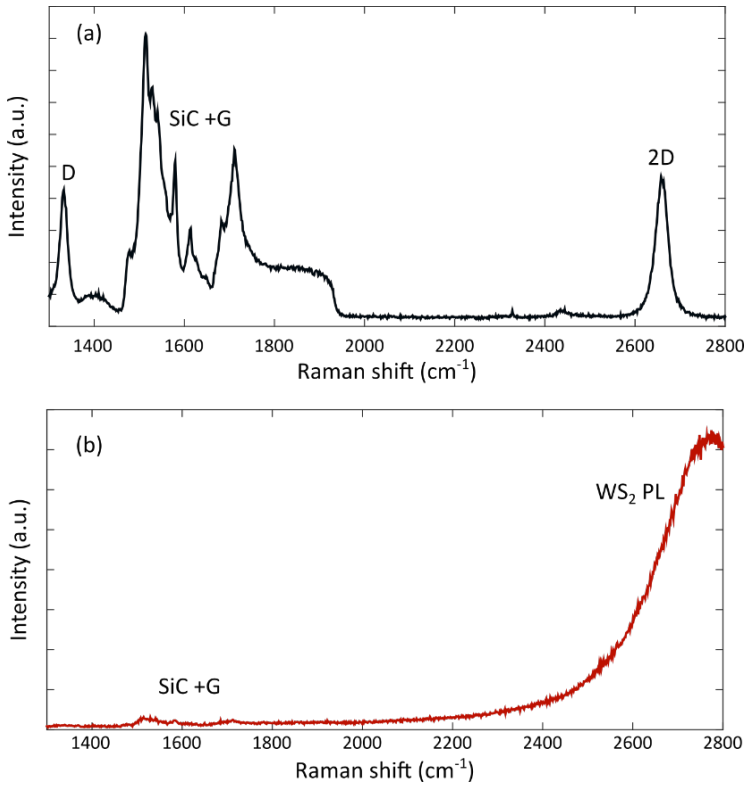

Fig. C 1(a) Raman spectrum of QFMLG. (b) PL arising from WS_2 obtained under the same conditions of (a).

This confirms that the first step indeed allowed for obtaining the buffer layer from SiC decomposition. This is not trivial, since Raman spectrum of buffer layer is very similar to the one from SiC (see chapter 3), however

just the presence of the buffer layer gives rise to the QFMLG once annealed in hydrogen environment. In addition, also a D peak is observed. This is expected and attributed to the partial elimination of the buffer layer[261]. A further optical analysis was carried out after the growth of WS_2, showing the clear signature of WS_2 monolayer coming from its strong PL[121](Fig. C 1(b)).

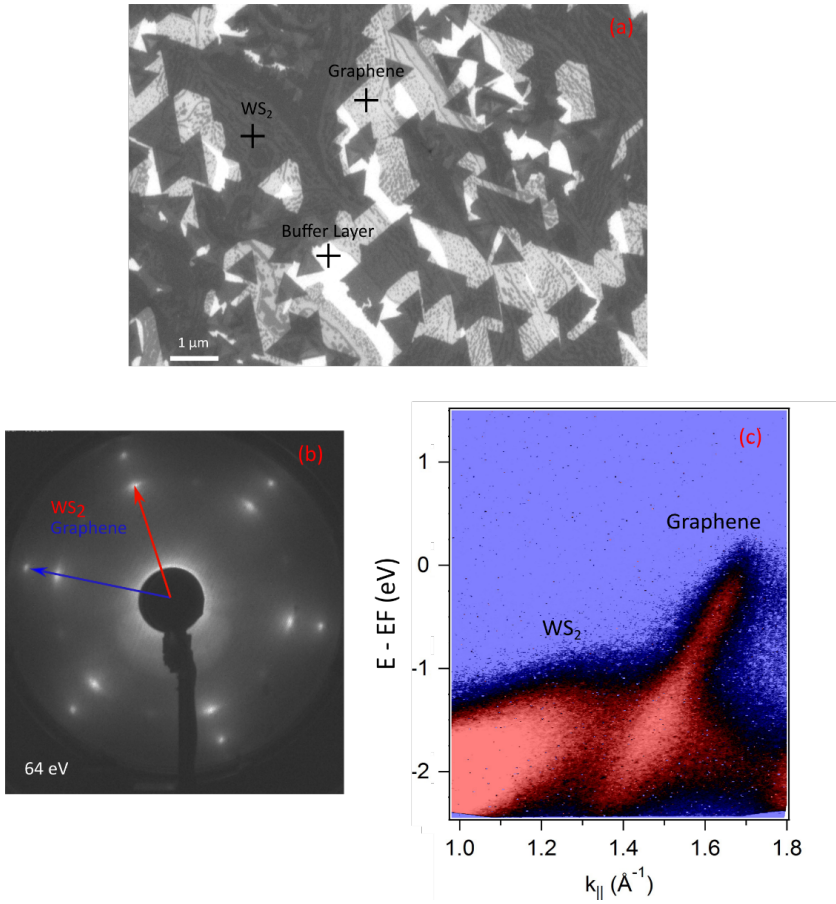

Fig. C 2 (a) SEM micrograph of the investigated system. The three different layers are highlighted in the image. (b) LEED diffraction pattern showing both WS_2 and QFMLG first order diffraction spots. (c) tr- ARPES acquired at negative time, showing the ground state of the system.

The crystal distribution has been investigated via a first SEM imaging and LEED study. The SEM micrograph Fig. C 2(a) shows the well-defined triangular crystal structure of WS_2 on terrace-like surface of QFMLG on SiC. The LEED pattern reported in Fig. C 2(b) shows the preferential relative orientation of the two crystals at 0°, confirming what reported above regarding WS_2/EG interface. An additional spot at 30° is recorded, indicating a second stable configuration of the WS_2 on graphene.

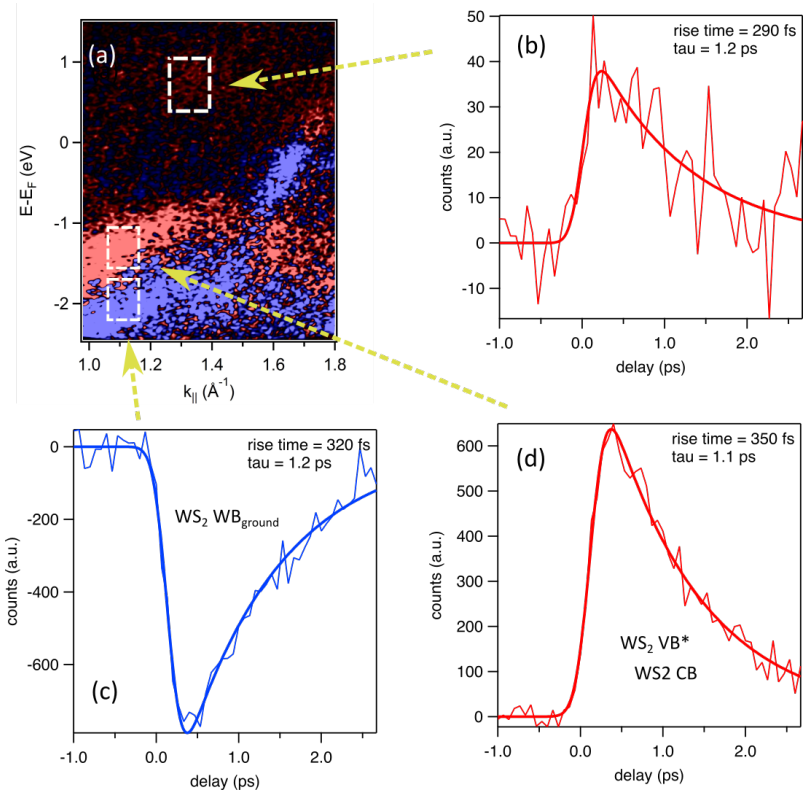

Fig. C 3 (a) tr- ARPES spectrum obtained subtracting the signal from negative time signal. (b-d) Time response of the gain/loss signal arising from the correspondent squared areas in (a), yielding the lifetimes of the corresponding regions.

The importance of the relative orientation at 0° is clear when one has to investigate the band structure of the system via ARPES measurements. Most of ARPES system does not allow for exploring more than a narrow

range around a specific point of the BZ, therefore having materials not aligned put a limit in exploring the K-points of the two materials at the same time.Having the crystal aligned allows for studying the Dirac cone of graphene together with the CB and VB band of WS_2, around its narrowest gap region, i.e. at **K**. Tr-ARPES at negative times, that is when the system is not yet excited, shows the typical band structure of WS_2 on graphene (Fig. C 2(c)). The different band alignment with respect what was reported in chapter 4 for WS_2 on EG can be attributed to the lack of buffer layer at the interface with SiC. As it has been shown in Ref [191], this is due to a dipole field at the interface that changes the doping in graphene and, in this case, it affects also the alignment with WS_2. In order to investigate the charge-carrier dynamics, the system is excited out of equilibrium by means of photons at 2 eV, matching the optical band gap of WS_2, therefore promoting the electrons from VB to an excited state. Whether this state represents the CB minimum or an excitonic level it is still under debate. The work of Ulstrup and co-workers[199], measured at Arthemis facility, Rutherford Appleton Labs (Uk) using a very similar set-up (Ti:Sapphire amplified laser 1 kHz repetition rate, central wavelength 785 nm,30fs pulse duration, 12 mJ output power, probe energy 25 eV), shows the excited electrons forming a non-dispersive level. This suggests that the excitonic level is been being populated. This is also corroborated by another work due to Zhu, Chen and Cui, where they show that the quasi-free particle band gap is located 2.7 eV above the VB maximum, assigning a binding energy of 0.7 eV[124] to the exciton. The excited band structure reported Fig. C 3(a) shows the response of the system under optical pumping. It is obtained subtracting the signal from the negative time acquisition, therefore gain and loss values can be retrieved. In the context of carrier dynamics, gain and loss represent the particle and hole states of the excited many-body system. Graphene's linearly dispersing bands

allow for optical transitions and the ground state is hence depopulated by exciting electrons from the π to the π* bands. Optical adsorption is observed for WS_2 as well. It is worth noting that the VB of WS_2 is shifted up with respect the ground state of about 70 meV.

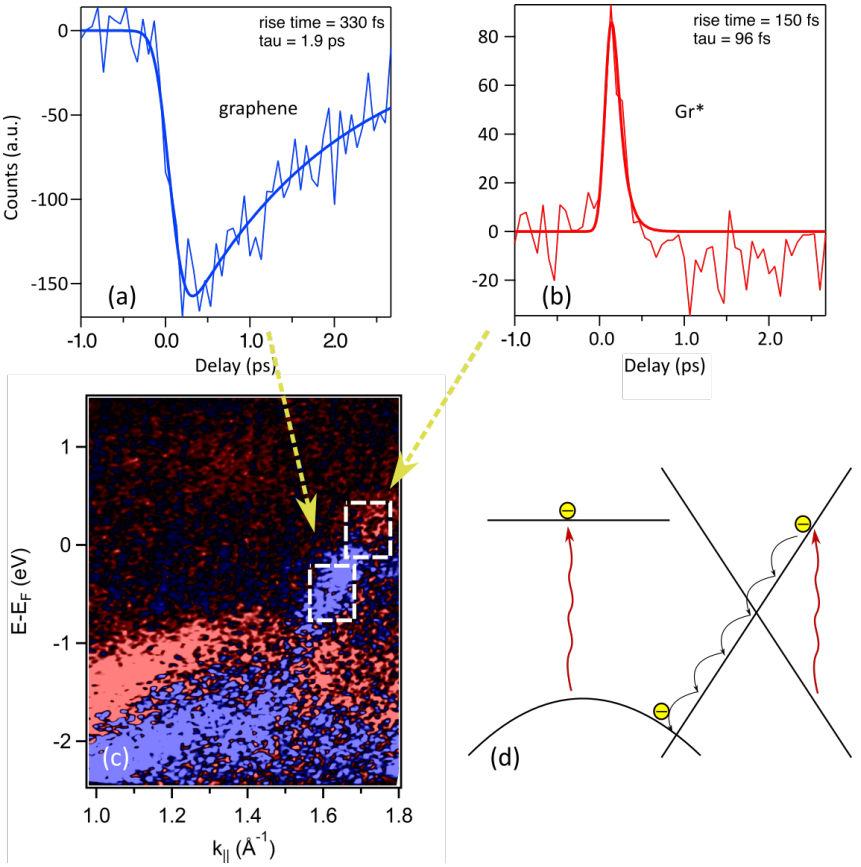

Fig. C 4 (a-b) Time response of the gain/loss signal arising from the correspondent squared areas in (c). (d) Sketch illustrating the charge transfer from QFMLG to WS_2

This behavior was already observed for MoS_2 on graphene[199] and attributed to the different electronic screening arising from the electronic distribution of the excited system. The position previously occupied by the VB shows a clear loss signal, matching the one from the gain of the

band shifted upwards. The probe signal allows for extraction of the quasiparticles' lifetimes (Fig. C 3(b-d)). The gain-loss signal coming from WS_2 VB indicates that the carriers bare the same lifetime, observed also in the excited state. However, graphene exhibits a very different behavior (Fig. C 4(a-b)). The lifetime of the loss signal is about one order of magnitude longer (1.9 ps) than the gain which is 96 fs, comparable with graphene-only relaxation time under optical pumping due to electron-phonon scattering[262,263].

CONCLUSIONS

In summary, the vertical heterostructure WS_2/QFMLG has been explored via pump and probe experiments. The excitation of the system has displayed a band gap renormalization of WS_2 already observed for similar systems. Moreover, by analyzing the lifetime of gain/loss signal with respect the ground state, it has been possible to attribute the longer lifetime of holes in the graphene as side effect of charge transfer from graphene to WS_2 following the thermal relaxation of photoexcited carriers in graphene. The azimuthal alignment at 0° is crucial to enable this effect, not observed in misaligned systems[199]. This behavior is of fundamental importance when considering the implementation of 2d materials for high performing device for light detection, demonstrated in chapter 6.

BIBLIOGRAPHY

1. Banszerus, L. *et al.* Ballistic Transport Exceeding 28 μm in CVD Grown Graphene. *Nano Lett.* **16,** 1387–1391 (2016).

2. Balandin, A. A. *et al.* Superior Thermal Conductivity of Single-Layer Graphene. *Nano Lett.* **8,** 902–907 (2008).

3. Bonaccorso, F., Sun, Z., Hasan, T. & Ferrari, A. C. Graphene photonics and optoelectronics. *Nat. Publ. Gr.* **4,** (2010).

4. Berry, V. Impermeability of graphene and its applications. *Carbon N. Y.* **62,** 1–10 (2013).

5. Lee, C., Wei, X., Kysar, J. W. & Hone, J. Measurement of the Elastic Properties and Intrinsic Strength of Monolayer Graphene. *Science (80-.).* **321,** 385–388 (2008).

6. Novoselov, K. S. Nobel Lecture: Graphene: Materials in the Flatland. *Rev. Mod. Phys.* **83,** 837–849 (2011).

7. Kormányos, A., Zólyomi, V., Drummond, N. D. & Burkard, G. Spin-orbit coupling, quantum dots, and qubits in monolayer transition metal dichalcogenides. *Phys. Rev. X* **4,** 1–16 (2014).

8. Komsa, H.-P. & Krasheninnikov, A. V. Electronic structures and optical properties of realistic transition metal dichalcogenide heterostructures from first principles. *Phys. Rev. B* **88,** (2013).

9. Calandra, M. 2D materials: Charge density waves go nano. *Nat. Nanotechnol.* **10,** 737–738 (2015).

10. Qi, Y. *et al.* Superconductivity in Weyl semimetal candidate MoTe2. *Nat. Commun.* **7,** 11038 (2016).

11. Fei, Z. *et al.* Edge conduction in monolayer WTe2. *Nat. Phys.* (2017). doi:10.1038/nphys4091

12. Yu, P. Y. & Cardona, M. *Fundamentals of semiconductors :*

physics and materials properties. (Springer, 2010).

13. Eisenstein, J. P., Cooper, K. B., Pfeiffer, L. N. & West, K. W. Insulating and Fractional Quantum Hall States in the First Excited Landau Level. **88,** (2002).

14. Geim, A. K. & Grigorieva, I. V. Van der Waals heterostructures. *Nature* **499,** 419–425 (2014).

15. Georgiou, T. *et al.* Vertical field-effect transistor based on graphene–WS2 heterostructures for flexible and transparent electronics. *Nat. Nanotechnol.* **8,** 100–103 (2012).

16. Britnell, L. *et al.* Electron tunneling through ultrathin boron nitride crystalline barriers. *Nano Lett.* **12,** 1707–10 (2012).

17. Liu, L., Kumar, S. B., Ouyang, Y. & Guo, J. Performance Limits of Monolayer Transition Metal Dichalcogenide Transistors. *IEEE Trans. Electron Devices* **58,** 3042–3047 (2011).

18. Gutiérrez, H. R. *et al.* Extraordinary Room-Temperature Photoluminescence in Triangular WS 2 Monolayers. *Nano Lett.* **13,** 3447–3454 (2013).

19. Zhu, Z. Y., Cheng, Y. C. & Schwingenschlögl, U. Giant spin-orbit-induced spin splitting in two-dimensional transition-metal dichalcogenide semiconductors. *Phys. Rev. B* **8422,** (2011).

20. Moody, G., Schaibley, J. & Xu, X. Exciton Dynamics in Monolayer Transition Metal Dichalcogenides. **33,** (2016).

21. Dean, C. R. *et al.* Boron nitride substrates for high-quality graphene electronics. *Nat. Nanotechnol.* **5,** 722–726 (2010).

22. Britnell, L. *et al.* Strong Light-Matter Interactions in Heterostructures of Atomically Thin Films. *Science (80-.).* **340,** 1311–1314 (2013).

23. Avsar, A. *et al.* Spin–orbit proximity effect in graphene. *Nat. Commun.* **5,** 4875 (2014).

24. Zhang, Y. *et al.* Controlled Growth of High-Quality Monolayer WS_2 Layers on Sapphire and Imaging Its Grain Boundary. *ACS*

Nano **7,** 8963–8971 (2013).

25. McCreary, K. M., Hanbicki, A. T., Jernigan, G. G., Culbertson, J. C. & Jonker, B. T. Synthesis of Large-Area WS 2 monolayers with Exceptional Photoluminescence. *Sci. Rep.* **6,** 1–7 (2016).

26. Elías, A. L. *et al.* Controlled Synthesis and Transfer of Large-Area WS 2 Sheets: From Single Layer to Few Layers. *ACS Nano* **7,** 5235–5242 (2013).

27. Forti, S. *et al.* Electronic properties of single-layer tungsten disulfide on epitaxial graphene on silicon carbide. *Nanoscale* **9,** 16412–16419 (2017).

28. Zhu, B., Zeng, H., Dai, J., Gong, Z. & Cui, X. Anomalously robust valley polarization and valley coherence in bilayer WS2. *Proc. Natl. Acad. Sci.* **111,** 11606–11611 (2014).

29. Rossi, A. *et al.* Scalable synthesis of WS 2 on graphene and h-BN: an all-2D platform for light-matter transduction. *2D Mater.* **3,** 31013 (2016).

30. Geim, A. K. & Novoselov, K. S. The rise of graphene. *Nat. Mater.* **6,** 183–191 (2007).

31. Wallace, P. R. The Band Theory of Graphite. *Phys. Rev.* **71,** 622–634 (1947).

32. Peierls, R. *Annales de l'institut henri poincaré*. *Annales de l'institut Henri Poincaré* **5,** (Gauthier-Villars, 1930).

33. Landau. Zur Theorie der phasenumwandlungen II. *Phys. Z. Sowjetunion* **11,** (1937).

34. Novoselov, K. S. *et al.* Electric field effect in atomically thin carbon films. *Science* **306,** 666–9 (2004).

35. The Nobel Prize in Physics 2010. Available at: https://www.nobelprize.org/nobel_prizes/physics/laureates/2010/. (Accessed: 22nd September 2017)

36. Ashcroft, N. W. & Mermin, N. D. *Solid state physics*. (Brooks/Cole Cengage Learning, 2003).

37. Castro Neto, A. H., Guinea, F., Peres, N. M. R., Novoselov, K. S. & Geim, A. K. The electronic properties of graphene. *Rev. Mod. Phys.* **81,** 109–162 (2009).

38. Novoselov, K. S. *et al.* Two-dimensional gas of massless Dirac fermions in graphene. *Nature* **438,** 197–200 (2005).

39. Katsnelson, M. I., Novoselov, K. S. & Geim, A. K. Chiral tunnelling and the Klein paradox in graphene. *Nat. Phys.* **2,** 620–625 (2006).

40. Novoselov, K. S. *et al.* Two-dimensional atomic crystals. *Proc. Natl. Acad. Sci. U. S. A.* **102,** 10451–3 (2005).

41. Park, S. & Ruoff, R. S. Chemical methods for the production of graphenes. *Nat. Nanotechnol.* **4,** 217–224 (2009).

42. Hernandez, Y. *et al.* High-yield production of graphene by liquid-phase exfoliation of graphite. *Nat. Nanotechnol.* **3,** 563–568 (2008).

43. Bonaccorso, F. *et al.* Production and processing of graphene and 2d crystals. *Mater. Today* **15,** 564–589 (2012).

44. Torrisi, F. *et al.* Inkjet-Printed Graphene Electronics. *ACS Nano* **6,** 2992–3006 (2012).

45. Berger, C. *et al.* Ultrathin Epitaxial Graphite: 2D Electron Gas Properties and a Route toward Graphene-based Nanoelectronics. *J. Phys. Chem. B* **108,** 19912–19916 (2004).

46. Emtsev, K. V *et al.* Towards wafer-size graphene layers by atmospheric pressure graphitization of silicon carbide. *Nat. Mater.* **8,** (2009).

47. Emtsev, K. V., Speck, F., Seyller, T., Ley, L. & Riley, J. D. Interaction, growth, and ordering of epitaxial graphene on SiC{0001} surfaces: A comparative photoelectron spectroscopy study. *Phys. Rev. B* **77,** 155303 (2008).

48. Goler, S. *et al.* Revealing the atomic structure of the buffer layer between SiC(0001) and epitaxial graphene. *Carbon N. Y.* **51,** 249–254 (2013).

49. Li, X., Cai, W., Colombo, L. & Ruoff, R. S. Evolution of Graphene Growth on Ni and Cu by Carbon Isotope Labeling. *Nano Lett.* **9,** 4268–4272 (2009).

50. Miseikis, V. *et al.* Rapid CVD growth of millimetre-sized single crystal graphene using a cold-wall reactor. *2D Mater.* **2,** 14006 (2015).

51. Li, J. *et al.* Facile growth of centimeter-sized single-crystal graphene on copper foil at atmospheric pressure. *J. Mater. Chem. C* **3,** 3530–3535 (2015).

52. Hua Wang, Q., Kalantar-Zadeh, K., Kis, A., Coleman, J. N. & Strano, M. S. Electronics and optoelectronics of two-dimensional transition metal dichalcogenides. *Nat. Nanotechnol.* **7,** (2012).

53. Chhowalla, M. *et al.* The chemistry of two-dimensional layered transition metal dichalcogenide nanosheets. *Nat. Chem.* **5,** 263–275 (2013).

54. Koppens, F. H. L. *et al.* Photodetectors based on graphene, other two-dimensional materials and hybrid systems. *Nat. Nanotechnol.* **9,** 780–793 (2014).

55. Xu, X., Yao, W., Xiao, D. & Heinz, T. F. Spin and pseudospins in layered transition metal dichalcogenides. *Nat. Phys.* **10,** 343–350 (2014).

56. Omar, S. & van Wees, B. J. Graphene- WS 2 heterostructures for tunable spin injection and spin transport. *Phys. Rev. B* **95,** 81404 (2017).

57. Luo, Y. K. *et al.* Opto-Valleytronic Spin Injection in Monolayer MoS $_2$ /Few-Layer Graphene Hybrid Spin Valves. *Nano Lett.* **17,** 3877–3883 (2017).

58. Manzeli, S., Ovchinnikov, D., Pasquier, D., Yazyev, O. V. & Kis, A. 2D transition metal dichalcogenides. *Nat. Rev. Mater.* **2,** 17033 (2017).

59. Ouyang, B., Lan, G., Guo, Y., Mi, Z. & Song, J. Phase engineering

of monolayer transition-metal dichalcogenide through coupled electron doping and lattice deformation. *Appl. Phys. Lett.* **107,** 191903 (2015).

60. Lee, C.-H. *et al.* Tungsten Ditelluride: a layered semimetal. *Nat. Publ. Gr.* (2015). doi:10.1038/srep10013

61. Kormányos, A. *et al.* k.p theory for two-dimensional transition metal dichalcogenide semiconductors (2015 2D Mater. 2 022001). **109,** (2015).

62. Kuc, A., Zibouche, N. & Heine, T. Influence of quantum confinement on the electronic structure of the transition metal sulfide T S 2. *Phys. Rev. B* **83,** 245213 (2011).

63. He, Z. *et al.* Layer-Dependent Modulation of Tungsten Disulfide Photoluminescence by Lateral Electric Fields. **9,** 2740–2748 (2015).

64. Gong, P., Yu, H., Wang, Y. & Yao, W. Optical selection rules for excitonic Rydberg series in the massive Dirac cones of hexagonal two-dimensional materials. *Phys. Rev. B* **95,** 1–8 (2017).

65. Nayak, P. K., Lin, F. C., Yeh, C. H., Huang, J. S. & Chiu, P. W. Robust room temperature valley polarization in monolayer and bilayer WS2. *Nanoscale* **8,** 6035–6042 (2016).

66. Coleman, J. N. *et al.* Two-dimensional nanosheets produced by liquid exfoliation of layered materials. *Science* **331,** 568–71 (2011).

67. Choi, W. *et al.* Recent development of two-dimensional transition metal dichalcogenides and their applications. *Mater. Today* **20,** 116–130 (2017).

68. Rong, Y. *et al.* Controlling sulphur precursor addition for large single crystal domains of WS 2. *Nanoscale* **6,** 12096–12103 (2014).

69. Bianco, G. V. *et al.* Direct epitaxial CVD synthesis of tungsten disulfide on epitaxial and CVD graphene. *RSC Adv.* **5,** 98700–

98708 (2015).

70. Briggs, N. *et al.* (Invited) Realizing 2D Materials Via MOCVD. *ECS Trans.* **75,** 725–731 (2016).

71. Kim, H., Ovchinnikov, D., Deiana, D., Unuchek, D. & Kis, A. Suppressing Nucleation in Metal–Organic Chemical Vapor Deposition of MoS 2 Monolayers by Alkali Metal Halides. *Nano Lett.* **17,** 5056–5063 (2017).

72. Kalanyan, B. *et al.* Rapid Wafer-Scale Growth of Polycrystalline 2H-MoS 2 by Pulsed Metal–Organic Chemical Vapor Deposition. *Chem. Mater.* **29,** 6279–6288 (2017).

73. Song, J.-G. *et al.* Layer-Controlled, Wafer-Scale, and Conformal Synthesis of Tungsten Disulfide Nanosheets Using Atomic Layer Deposition. **7,** 11333–11340 (2013).

74. Liu, H. J. *et al.* Molecular-beam epitaxy of monolayer and bilayer WSe_2: a scanning tunneling microscopy/spectroscopy study and deduction of exciton binding energy. *2D Mater.* **2,** 34004 (2015).

75. Zhan, L., Wan, W., Zhu, Z., Shih, T.-M. & Cai, W. MoS 2 materials synthesized on SiO 2 /Si substrates via MBE. *J. Phys. Conf. Ser.* **864,** 12037 (2017).

76. Greber, T. Graphene and Boron Nitride Single Layers. (2009).

77. Topsakal, M., Aktürk, E. & Ciraci, S. First-principles study of two-and one-dimensional honeycomb structures of boron nitride. **22,**

78. Wang, J., Ma, F. & Sun, M. Graphene, hexagonal boron nitride, and their heterostructures: properties and applications. *RSC Adv.* **7,** 16801–16822 (2017).

79. Watanabe, K., Taniguchi, T. & Kanda, H. Direct-bandgap properties and evidence for ultraviolet lasing of hexagonal boron nitride single crystal. *Nat. Mater.* **3,** 404–409 (2004).

80. Yang, H. *et al.* Dielectric nanosheets made by liquid-phase exfoliation in water and their use in graphene-based

electronics. *2D Mater.* **1,** 11012 (2014).

81. Song, X. *et al.* Wafer-scale CVD Growth of Monolayer Hexagonal Boron Nitride with Large Domain Size by Cu Foil Enclosure Approach. (2015).

82. Wang, L. *et al.* Monolayer Hexagonal Boron Nitride Films with Large Domain Size and Clean Interface for Enhancing the Mobility of Graphene-Based Field-Effect Transistors. *Adv. Mater.* **26,** 1559–1564 (2014).

83. Park, S. *et al.* Facile Synthesis of Highly Crystalline and Large Areal Hexagonal Boron Nitride from Borazine Oligomers. *Sci. Rep.* **7,** 40260 (2017).

84. Auwärter, W., Suter, H. U., Sachdev, H. & Greber, T. Synthesis of One Monolayer of Hexagonal Boron Nitride on Ni(111) from B-Trichloroborazine (ClBNH) 3. *Chem. Mater.* **16,** 343–345 (2004).

85. Mishra, N. *et al.* Rapid and catalyst-free van der Waals epitaxy of graphene on hexagonal boron nitride. *Carbon N. Y.* **96,** 497–502 (2016).

86. Taniguchi, T. & Watanabe, K. Synthesis of high-purity boron nitride single crystals under high pressure by using Ba–BN solvent. *J. Cryst. Growth* **303,** 525–529 (2007).

87. Dingle, R., Wiegmann, W. & Henry, C. H. Quantum States of Confined Carriers in Very Thin AlxGa1−xAs-GaAs-AlxGa1−xAs Heterostructures. *Phys. Rev. Lett.* **33,** 827–830 (1974).

88. Mimura, T., Hiyamizu, S., Fujii, T. & Nanbu, K. A New Field-Effect Transistor with Selectively Doped GaAs/n-Al $_{x}$ Ga $_{1-x}$ As Heterojunctions. *Jpn. J. Appl. Phys.* **19,** L225–L227 (1980).

89. Jaegermann, W. *et al.* Thin film solar cells based on layered chalcogenides: fundamentals and perspectives of van der Waals epitaxy. *Proc. 1994 IEEE 1st World Conf. Photovolt. Energy Convers. - WCPEC (A Jt. Conf. PVSC, PVSEC PSEC)* 357–360 (1994). doi:10.1109/WCPEC.1994.519975

90. Chen, J.-H., Jang, C., Xiao, S., Ishigami, M. & Fuhrer, M. S. Intrinsic and extrinsic performance limits of graphene devices on SiO2. *Nat. Nanotechnol.* **3,** 206–209 (2008).

91. Castellanos-Gomez, A. *et al.* Deterministic transfer of two-dimensional materials by all-dry viscoelastic stamping. *2D Mater.* **1,** 11002 (2014).

92. Soo Kim, K. *et al.* Large-scale pattern growth of graphene films for stretchable transparent electrodes. *Nature* **457,** (2008).

93. Koma, A. Van der Waals epitaxy for highly lattice-mismatched systems. *J. Cryst. Growth* **201–202,** 236–241 (1999).

94. Okada, M. *et al.* Direct Chemical Vapor Deposition Growth of WS 2 Atomic Layers on Hexagonal Boron Nitride. **8,** 8273–8277 (2014).

95. Miwa, J. A. *et al.* Van der Waals Epitaxy of Two-Dimensional MoS2-Graphene Heterostructures in Ultrahigh Vacuum. *ACS Nano* **9,** 6502–6510 (2015).

96. Li, X. *et al.* Van der Waals Epitaxial Growth of Two-Dimensional Single-Crystalline GaSe Domains on Graphene. **9,** 8078–8088 (2015).

97. Lim, H., In Yoon, S., Kim, G., Jang, A.-R. & Suk Shin, H. Stacking of Two-Dimensional Materials in Lateral and Vertical Directions. doi:10.1021/cm502170q

98. Ilatikhameneh, H., Klimeck, G. & Rahman, R. 2D tunnel transistors for ultra-low power applications: Promises and challenges. in *2015 Fourth Berkeley Symposium on Energy Efficient Electronic Systems (E3S)* **60,** 1–3 (IEEE, 2015).

99. Britnell, L. *et al.* Field-Effect Tunneling Transistor Based on Vertical Graphene Heterostructures. *Science (80-.).* **335,** 947–950 (2012).

100. Georgiou, T. *et al.* Vertical field-effect transistor based on graphene-WS2 heterostructures for flexible and transparent

electronics. *Nat. Nanotechnol.* **8,** 100–3 (2013).

101. He, J. *et al.* Electron transfer and coupling in graphene–tungsten disulfide van der Waals heterostructures. *Nat. Commun.* **5,** 5622 (2014).

102. Hüfner, S. *Photoelectron Spectroscopy*. **82,** (Springer Berlin Heidelberg, 1996).

103. Tanuma, S., Powell, C. J. & Penn, D. R. Calculations of electron inelastic mean free paths. IX. Data for 41 elemental solids over the 50 eV to 30 keV range. *Surf. Interface Anal.* **43,** 689–713 (2011).

104. Berglund, C. N. & Spicer, W. E. Photoemission Studies of Copper and Silver: Experiment. *Phys. Rev.* **136,** A1044–A1064 (1964).

105. Turner, D. W. Photoelectron Spectroscopy. *Annu. Rev. Phys. Chem.* **21,** 107–128 (1970).

106. Damascelli, A. Probing the Electronic Structure of Complex Systems by ARPES. *Phys. Scr.* **T109,** 61 (2004).

107. Forti, S. Großflächiges epitaktisches Graphen auf SiC(0001): von der Entkopplung bis zum Maßschneidern der Grenzfläche.

108. Hulst, H. C. Van de & Reesinck, J. J. M. Line Breadths and voigt profiles. *Astrophys. J.* **106,** 121 (1947).

109. Doniacht, S. & Sunjic$, M. Many-electron singularity in X-ray photoemission and X-ray line spectra from metals Many-electron singularity in x-ray photoemission andx-ray line spectra from metals. *J. Phys. C Solid State Phys. J. Phys. C Solid State Phys* **3,**

110. Ertl, G. (Gerhard) & Küppers, J. (Jürgen). *Low energy electrons and surface chemistry*. (VCH, 1985).

111. Tevfik Onur & Locatelli, A. Angle-resolved X-ray photoemission electron microscopy. *J. Electron Spectros. Relat. Phenomena* **185,** 323–329 (2012).

112. Locatelli, A., Aballe, L., Mentes, T. O., Kiskinova, M. & Bauer, E. Photoemission electron microscopy with chemical sensitivity: SPELEEM methods and applications. *Surf. Interface Anal.* **38,** 1554–1557 (2006).

113. Menteş, T. O., Zamborlini, G., Sala, A. & Locatelli, A. Cathode lens spectromicroscopy: methodology and applications. *Beilstein J. Nanotechnol.* **5,** 1873–1886 (2014).

114. Binnig, G. & Rohrer, H. Scanning tunneling microscopy. *Surf. Sci.* **126,** 236–244 (1982).

115. Ferrari, A. C. & Basko, D. M. Raman spectroscopy as a versatile tool for studying the properties of graphene. *Nat. Nanotechnol.* **8,** 235–246 (2013).

116. Beams, R., Cançado, L. G. & Novotny, L. Raman characterization of defects and dopants in graphene. *J. Phys. Condens. Matter* **27,** 83002 (2015).

117. Neumann, C. *et al.* Raman spectroscopy as probe of nanometre-scale strain variations in graphene. *Nat. Commun.* **6,** (2015).

118. Tonndorf, P. *et al.* Photoluminescence emission and Raman response of monolayer MoS_2, $MoSe_2$, and WSe_2. *Opt. Express* **21,** 4908–16 (2013).

119. Zhang, X. *et al.* Phonon and Raman scattering of two-dimensional transition metal dichalcogenides from monolayer, multilayer to bulk material. *Chem. Soc. Rev.* **44,** 2757–2785 (2015).

120. Saito, R., Tatsumi, Y., Huang, S., Ling, X. & Dresselhaus, M. S. Raman spectroscopy of transition metal dichalcogenides. *J. Phys. Condens. Matter* **28,** 353002 (2016).

121. Berkdemir, A. *et al.* Identification of individual and few layers of WS2 using Raman Spectroscopy. *Sci. Rep.* **3,** 183–191 (2013).

122. Zhao, W. *et al.* Lattice dynamics in mono- and few-layer sheets

of WS2 and WSe2. *Nanoscale* **5,** 9677 (2013).

123. Ye, Z. *et al.* Probing excitonic dark states in single-layer tungsten disulphide. *Nature* **513,** 214–218 (2014).

124. Zhu, B., Chen, X. & Cui, X. Exciton Binding Energy of Monolayer WS2. *Sci. Rep.* **5,** 9218 (2015).

125. Allen, M. J., Tung, V. C. & Kaner, R. B. Honeycomb Carbon: A Review of Graphene. doi:10.1021/cr900070d

126. Thangaraja, A., Shinde, S. M., Kalita, G. & Tanemura, M. An effective approach to synthesize monolayer tungsten disulphide crystals using tungsten halide precursor. *Cit. Appl. Phys. Lett. Appl. Phys. Lett* **108,** (2016).

127. Dendzik, M. *et al.* Growth and electronic structure of epitaxial single-layer WS2 on Au(111). *Phys. Rev. B* **92,** 245442 (2015).

128. Van Bommel, A. J., Crombeen, J. E. & Van Tooren, A. LEED and Auger electron observations of the SiC(0001) surface. *Surf. Sci.* **48,** 463–472 (1975).

129. Soe, W.-H. *et al.* Surface phonon and valence band dispersions in graphite overlayers formed by solid-state graphitization of 6H-SiC (0001). *Phys. Rev. B* **70,** 115421 (2004).

130. Hass, J. *et al.* Highly ordered graphene for two dimensional electronics. *Appl. Phys. Lett.* **89,** (2006).

131. Cheung, R. *Silicon carbide micro electromechanical systems for harsh environments*. (Imperial College Press, 2006).

132. Son, N. T. *et al.* Electron effective masses and mobilities in high-purity 6H–SiC chemical vapor deposition layers. *Appl. Phys. Lett.* **65,** 3209–3211 (1994).

133. Son, N. T. *et al.* Electron effective masses in 4H SiC. *Appl. Phys. Lett.* **66,** 1074–1076 (1995).

134. Shen, T. *et al.* Observation of quantum-Hall effect in gated epitaxial graphene grown on SiC (0001). *Appl. Phys. Lett.* **95,** 10–13 (2009).

135. Castro, E. V *et al.* Limits on Charge Carrier Mobility in Suspended Graphene due to Flexural Phonons. doi:10.1103/PhysRevLett.105.266601

136. Fromm, F. *et al.* Contribution of the buffer layer to the Raman spectrum of epitaxial graphene on SiC(0001). *New J. Phys.* **15,** (2013).

137. Ray, N., Shallcross, S., Hensel, S. & Pankratov, O. Buffer layer limited conductivity in epitaxial graphene on the Si face of SiC. *Phys. Rev. B* **86,** (2012).

138. Riedl, C., Coletti, C., Iwasaki, T., Zakharov, A. A. & Starke, U. Quasi-free-standing epitaxial graphene on SiC obtained by hydrogen intercalation. *Phys. Rev. Lett.* **103,** 1–4 (2009).

139. Pallecchi, E. *et al.* High Electron Mobility in Epitaxial Graphene on 4H-SiC(0001) via post-growth annealing under hydrogen. *Sci. Rep.* **4,** 4558 (2015).

140. Monk, D. J., Soane, D. S. & Howe, R. T. Invited Review A review of the chemical reaction mechanism and kinetics for hydrofluoric acid etching of silicon dioxide for surface micromachining applications. *Thin Solid Films* **232,** 1–12 (1993).

141. Frewin, C. L., Coletti, C., Riedl, C., Starke, U. & Saddow, S. E. A Comprehensive Study of Hydrogen Etching on the Major SiC Polytypes and Crystal Orientations. *Mater. Sci. Forum* **615–617,** 589–592 (2009).

142. Convertino, D., Rossi, A., Miseikis, V., Piazza, V. & Coletti, C. Thermal decomposition and chemical vapor deposition: a comparative study of multi-layer growth of graphene on SiC(000-1). *MRS Adv.* **1,** 3667–3672 (2016).

143. Coletti, C. *et al.* Surface studies of hydrogen etched 3C-SiC(001) on Si(001). *Appl. Phys. Lett.* **91,** 61914 (2007).

144. Forti, S. & Starke, U. Epitaxial graphene on SiC: from carrier density engineering to quasi-free standing graphene by atomic intercalation. *J. Phys. D. Appl. Phys.* **47,** 94013 (2014).

145. Starr, D. E., Pazhetnov, E. M., Stadnichenko, A. I., Boronin, A. I. & Shaikhutdinov, S. K. Carbon films grown on Pt(111) as supports for model gold catalysts. *Surf. Sci.* **600,** 2688–2695 (2006).

146. Coraux, J., N'Diaye, A. T., Busse, C. & Michely, T. Structural Coherency of Graphene on Ir(111). *Nano Lett.* **8,** 565–570 (2008).

147. Reina, A. *et al.* Large area, few-layer graphene films on arbitrary substrates by chemical vapor deposition. *Nano Lett.* **9,** 30–5 (2009).

148. Kim, K. S. *et al.* Large-scale pattern growth of graphene films for stretchable transparent electrodes. *Nature* **457,** 706–710 (2009).

149. Li, X. *et al.* Large-Area Synthesis of High-Quality and Uniform Graphene Films on Copper Foils. *Science (80-.).* **324,** 1312–1314 (2009).

150. Lander, J. J., Kern, H. E. & Beach, A. L. Solubility and Diffusion Coefficient of Carbon in Nickel: Reaction Rates of Nickel-Carbon Alloys with Barium Oxide. *J. Appl. Phys.* **23,** 1305–1309 (1952).

151. Zhang, J., Safarzadeh, M. & Young, D. J. Carbon Permeability of Nickel and Ni–Cu Alloys. *Oxid. Met.* **70,** 15–24 (2008).

152. Hao, Y. *et al.* The Role of Surface Oxygen in the Growth of Large Single-Crystal Graphene on Copper. *Science (80-.).* **342,** 720–723 (2013).

153. Li, X. *et al.* Large-Area Graphene Single Crystals Grown by Low-Pressure Chemical Vapor Deposition of Methane on Copper. *J. Am. Chem. Soc.* **133,** 2816–2819 (2011).

154. Miseikis, V. *et al.* Deterministic patterned growth of high-mobility large-crystal graphene: a path towards wafer scale integration. *2D Mater.* **4,** 21004 (2017).

155. Fu, Q. *et al.* Controllable synthesis of high quality monolayer

WS 2 on a SiO 2 /Si substrate by chemical vapor deposition. *RSC Adv.* **5,** 15795–15799 (2015).

156. Morrish, R., Haak, T. & Wolden, C. A. Low-Temperature Synthesis of *n* -Type WS $_2$ Thin Films via H $_2$ S Plasma Sulfurization of WO $_3$. *Chem. Mater.* **26,** 3986–3992 (2014).

157. Jagminas, A. *et al.* Laser Light Induced Transformation of Molybdenum Disulphide-Based Nanoplatelet Arrays. *Nat. Publ. Gr.* (2016). doi:10.1038/srep37514

158. Benz, K.-W. & Neumann, W. *Introduction to Crystal Growth and Characterization*. (WILEY-VCH Verlag, 2014).

159. Deng, S. & Berry, V. Wrinkled, rippled and crumpled graphene: An overview of formation mechanism, electronic properties, and applications. *Mater. Today* **19,** 197–212 (2016).

160. Mayorov, A. S. *et al.* Micrometer-scale ballistic transport in encapsulated graphene at room temperature. *Nano Lett.* **11,** 2396–9 (2011).

161. Banszerus, L. *et al.* Ultrahigh-mobility graphene devices from chemical vapor deposition on reusable copper. *Sci. Adv.* **1,** (2015).

162. Kretinin, A. V *et al.* Electronic Properties of Graphene Encapsulated with Different Two-Dimensional Atomic Crystals. *Nano Lett.* **14,** 3270–3276 (2014).

163. Kuc, A., Zibouche, N. & Heine, T. How does quantum confinement influence the electronic structure of transition metal sulfides TmS2. **245213,** 1–4 (2011).

164. Zhao, W. *et al.* Evolution of electronic structure in atomically thin sheets of WS2 and WSe2. *ACS Nano* **7,** 791–7 (2013).

165. Jiang, H. Electronic Band Structures of Molybdenum and Tungsten Dichalcogenides by the GWApproach. *J. Phys. Chem. C* **116,** 7664–7671 (2012).

166. Jo, S., Ubrig, N., Berger, H., Kuzmenko, A. B. & Morpurgo, A. F.

Mono- and Bilayer WS 2 Light-Emitting Transistors. *Nano Lett.* **14,** 2019–2025 (2014).

167. Chernikov, A. *et al.* Exciton Binding Energy and Nonhydrogenic Rydberg Series in Monolayer WS2. *Phys. Rev. Lett.* **113,** 76802 (2014).

168. Fraser, M. D., Höfling, S. & Yamamoto, Y. Physics and applications of exciton–polariton lasers. *Nat. Mater.* **15,** 1049–1052 (2016).

169. Scrace, T. *et al.* Magnetoluminescence and valley polarized state of a two-dimensional electron gas in WS2 monolayers. *Nat. Nanotechnol.* **10,** 603–607 (2015).

170. He, J. *et al.* Electron transfer and coupling in graphene–tungsten disulfide van der Waals heterostructures. *Nat. Commun.* **5,** 5622 (2014).

171. Tan, H. *et al.* Ultrathin 2D Photodetectors Utilizing Chemical Vapor Deposition Grown WS2 with Graphene Electrodes. *ACS Nano* **10,** 7866–7873 (2016).

172. Bauer, E. *Surface Microscopy with Low Energy Electrons*. (Springer New York, 2014). doi:10.1007/978-1-4939-0935-3

173. Riedl, C., Coletti, C. & Starke, U. Structural and electronic properties of epitaxial graphene on SiC(0 0 0 1): a review of growth, characterization, transfer doping and hydrogen intercalation. *J. Phys. D. Appl. Phys.* **43,** 374009 (2010).

174. Giannozzi, P. *et al.* QUANTUM ESPRESSO: a modular and open-source software project for quantum simulations of materials. *J. Phys. Condens. Matter* **21,** 395502 (2009).

175. Cavallucci, T. & Tozzini, V. Multistable Rippling of Graphene on SiC: A Density Functional Theory Study. *J. Phys. Chem. C* **120,** 7670–7677 (2016).

176. Vanderbilt, D. Soft self-consistent pseudopotentials in a generalized eigenvalue formalism. *Phys. Rev. B* **41,** 7892–

7895 (1990).

177. Rappe, A. M., Rabe, K. M., Kaxiras, E. & Joannopoulos, J. D. Optimized pseudopotentials. *Phys. Rev. B* **41,** 1227–1230 (1990).

178. Perdew, J. P. *et al.* Restoring the Density-Gradient Expansion for Exchange in Solids and Surfaces. *Phys. Rev. Lett.* **100,** 136406 (2008).

179. Grimme, S. Semiempirical GGA-type density functional constructed with a long-range dispersion correction. *J. Comput. Chem.* **27,** 1787–1799 (2006).

180. Rossi, A., Piccinin, S., Pellegrini, V., de Gironcoli, S. & Tozzini, V. Nano-Scale Corrugations in Graphene: A Density Functional Theory Study of Structure, Electronic Properties and Hydrogenation. *J. Phys. Chem. C* **119,** 7900–7910 (2015).

181. Wang, Z. *et al.* Strong interface-induced spin–orbit interaction in graphene on WS2. *Nat. Commun.* **6,** 8339 (2015).

182. Popescu, V. & Zunger, A. Extracting E versus $\vec{k}$ effective band structure from supercell calculations on alloys and impurities. *Phys. Rev. B* **85,** 85201 (2012).

183. Dendzik, M. *et al.* Growth and electronic structure of epitaxial single-layer WS 2 on Au(111). *Phys. Rev. B* **92,** 245442 (2015).

184. Pierucci, D. *et al.* Self-organized metal-semiconductor epitaxial graphene layer on off-axis 4H-SiC(0001). *Nano Res.* **8,** 1026–1037 (2015).

185. Ulstrup, S. *et al.* Spin and valley control of free carriers in single-layer <math> <msub> <mrow> <mi mathvariant='normal'>WS</mi> </mrow> <mn>2</mn> </msub> </math>. *Phys. Rev. B* **95,** 41405 (2017).

186. Katoch, J. *et al.* Giant spin-splitting and gap renormalization driven by trions in single-layer WS2/h-BN heterostructures. *Nat. Phys.* (2018). doi:10.1038/s41567-017-0033-4

187. Yuan, H. *et al.* Evolution of the Valley Position in Bulk

Transition-Metal Chalcogenides and Their Monolayer Limit. *Nano Lett.* **16,** 4738–4745 (2016).

188. Hibino, H. *et al.* Microscopic thickness determination of thin graphite films formed on SiC from quantized oscillation in reflectivity of low-energy electrons. *Phys. Rev. B* **77,** 75413 (2008).

189. Srivastava, N. *et al.* Low-energy electron reflectivity of graphene on copper and other substrates. *Phys. Rev. B* **87,** 245414 (2013).

190. Feenstra, R. M. & Widom, M. Low-energy electron reflectivity from graphene: First-principles computations and approximate models. *Ultramicroscopy* **130,** 101–108 (2013).

191. Ristein, J., Mammadov, S. & Seyller, T. Origin of Doping in Quasi-Free-Standing Graphene on Silicon Carbide. *Phys. Rev. Lett.* **22,** 1–5 (2012).

192. Kopylov, S., Tzalenchuk, A., Kubatkin, S. & Fal'ko, V. I. Charge transfer between epitaxial graphene and silicon carbide. *Appl. Phys. Lett.* **97,** 112109 (2010).

193. Riley, J. M. *et al.* Negative electronic compressibility and tunable spin splitting in WSe2. *Nat. Nanotechnol.* **10,** 1043–1047 (2015).

194. Jo, S., Costanzo, D., Berger, H. & Morpurgo, A. F. Electrostatically Induced Superconductivity at the Surface of WS 2. *Nano Lett.* **15,** 1197–1202 (2015).

195. Zhang, R. *et al.* Superconductivity in Potassium-Doped Metallic Polymorphs of MoS 2. *Nano Lett.* **16,** 629–636 (2016).

196. Tombros, N., Jozsa, C., Popinciuc, M., Jonkman, H. T. & van Wees, B. J. Electronic spin transport and spin precession in single graphene layers at room temperature. *Nature* **448,** 571–574 (2007).

197. Wu, Q. *et al.* Efficient Spin Injection into Graphene through a

Tunnel Barrier: Overcoming the Spin-Conductance Mismatch. *Phys. Rev. Appl.* **2,** 44008 (2014).

198. Pierucci, D. *et al.* Band alignment and minigaps in monolayer MoS2-graphene van der Waals heterostructures. *Nano Lett.* **16,** 4054–4061 (2016).

199. Ulstrup, S. *et al.* Ultrafast Band Structure Control of a Two-Dimensional Heterostructure. *ACS Nano* **10,** 6315–6322 (2016).

200. Oviedo, J. P. *et al. In Situ* TEM Characterization of Shear-Stress-Induced Interlayer Sliding in the Cross Section View of Molybdenum Disulfide. *ACS Nano* **9,** 1543–1551 (2015).

201. Wang, L. *et al.* Superlubricity of a graphene/MoS_2 heterostructure: a combined experimental and DFT study. *Nanoscale* **9,** 10846–10853 (2017).

202. Ye, Z., Otero-de-la-Roza, A., Johnson, E. R. & Martini, A. Oscillatory motion in layered materials: graphene, boron nitride, and molybdenum disulfide. *Nanotechnology* **26,** 165701 (2015).

203. Hod, O. Graphite and Hexagonal Boron-Nitride have the Same Interlayer Distance. Why? doi:10.1021/ct200880m

204. Hirano, M. & Shinjo, K. Atomistic locking and friction. *Phys. Rev. B* **41,** 11837–11851 (1990).

205. Kontorova, T. A. & Frenkel, Y. I. On the theory of plastic deformation and crystal twinning. *Zh. Eksp. Teor. Fiz.* **8,** 1340–1348 (1938).

206. van den Ende, J. A., de Wijn, A. S. & Fasolino, A. The effect of temperature and velocity on superlubricity. *J. Phys. Condens. Matter* **24,** 445009 (2012).

207. Jinesh, K. B., Krylov, S. Y., Valk, H., Dienwiebel, M. & Frenken, J. W. M. Thermolubricity in atomic-scale friction. *Phys. Rev. B* **78,** 155440 (2008).

208. Zhao, X., Phillpot, S. R., Sawyer, W. G., Sinnott, S. B. & Perry, S.

S. Transition from Thermal to Athermal Friction under Cryogenic Conditions. *Phys. Rev. Lett.* **102,** 186102 (2009).

209. Dienwiebel, M. *et al.* Superlubricity of Graphite. *Phys. Rev. Lett.* **92,** 126101 (2004).

210. Feng, X., Kwon, S., Park, J. Y. & Salmeron, M. Superlubric Sliding of Graphene Nanoflakes on Graphene. *ACS Nano* **7,** 1718–1724 (2013).

211. Li, H. *et al.* Superlubricity between MoS_2 Monolayers. *Adv. Mater.* **29,** 1701474 (2017).

212. Liu, S.-W. *et al.* Robust microscale superlubricity under high contact pressure enabled by graphene-coated microsphere. *Nat. Commun.* **8,** 14029 (2017).

213. Nečas, D. & Klapetek, P. Gwyddion: an open-source software for SPM data analysis. *Cent. Eur. J. Phys.* **10,** 181 (2012).

214. Damnjanović, M., Dobardžić, E., Milošević, I., Viršek, M. & Remškar, M. Phonons in MoS_2 and WS_2 Nanotubes. *Mater. Manuf. Process.* **23,** 579–582 (2008).

215. Lindsay, L. & Broido, D. A. Optimized Tersoff and Brenner empirical potential parameters for lattice dynamics and phonon thermal transport in carbon nanotubes and graphene. *Phys. Rev. B* **81,** 205441 (2010).

216. Camiola, V. D., Farchioni, R., Pellegrini, V. & Tozzini, V. Hydrogen transport within graphene multilayers by means of flexural phonons. *2D Mater.* **2,** 14009 (2015).

217. Smith, W. & Forester, T. R. DL_POLY_2.0: A general-purpose parallel molecular dynamics simulation package. *J. Mol. Graph.* **14,** 136–141 (1996).

218. Xu, P. *et al.* Electronic transition from graphite to graphene via controlled movement of the top layer with scanning tunneling microscopy. *Phys. Rev. B* **86,** 85428 (2012).

219. Xu, P. *et al.* Graphene Manipulation on 4H-SiC(0001) Using Scanning Tunneling Microscopy. *Jpn. J. Appl. Phys.* **52,** 35104

(2013).

220. Kobayashi, Y., Taniguchi, T., Watanabe, K., Maniwa, Y. & Miyata, Y. Slidable atomic layers in van der Waals heterostructures. *Appl. Phys. Express* **10,** 45201 (2017).

221. Michel, K. H., Costamagna, S. & Peeters, F. M. Theory of anharmonic phonons in two-dimensional crystals. *Phys. Rev. B* **91,** 134302 (2015).

222. Perea-López, N. *et al.* CVD-grown monolayered MoS $_2$ as an effective photosensor operating at low-voltage. *2D Mater.* **1,** 11004 (2014).

223. Yoshida, S. *et al.* Microscopic basis for the band engineering of Mo1−xWxS2-based heterojunction. *Sci. Rep.* **5,** 14808 (2015).

224. Lin, Z. *et al.* Defect engineering of two-dimensional transition metal dichalcogenides. *2D Mater.* **3,** 22002 (2016).

225. Parkin, W. M. *et al.* Raman Shifts in Electron-Irradiated Monolayer MoS $_2$. *ACS Nano* **10,** 4134–4142 (2016).

226. Fabbri, F. *et al.* Novel near-infrared emission from crystal defects in MoS 2 multilayer flakes. *Nat. Commun.* **7,** (2016).

227. González, C., Biel, B. & Dappe, Y. J. Theoretical characterisation of point defects on a MoS $_2$ monolayer by scanning tunnelling microscopy. *Nanotechnology* **27,** 105702 (2016).

228. Füchtbauer, H. G. *et al.* Morphology and atomic-scale structure of single-layer WS2 nanoclusters. *Phys. Chem. Chem. Phys.* **15,** 15971–80 (2013).

229. Dong, Y., Wu, X. & Martini, A. Atomic roughness enhanced friction on hydrogenated graphene. *Nanotechnology* **24,** 375701 (2013).

230. Buscema, M. *et al.* Photocurrent generation with two-dimensional van der Waals semiconductors. *Chem Soc Rev* **44,** 3691–3718 (2015).

231. Xie, C., Mak, C., Tao, X. & Yan, F. Photodetectors Based on Two-Dimensional Layered Materials Beyond Graphene. *Adv. Funct. Mater.* **27,** 1603886 (2017).

232. Roy, K. *et al.* Graphene-MoS_2 hybrid structures for multifunctional photoresponsive memory devices. *Nat. Nanotechnol.* **8,** 826–830 (2013).

233. Mehew, J. D. *et al.* Fast and Highly Sensitive Ionic-Polymer-Gated WS_2 -Graphene Photodetectors. *Adv. Mater.* **1700222,** 1700222 (2017).

234. Tan, H. *et al.* Ultrathin 2D Photodetectors Utilizing Chemical Vapor Deposition Grown WS 2 With Graphene Electrodes. *ACS Nano* **10,** 7866–7873 (2016).

235. Lan, C. *et al.* Highly responsive and broadband photodetectors based on WS_2 –graphene van der Waals epitaxial heterostructures. *J. Mater. Chem. C* **5,** 1494–1500 (2017).

236. Ovchinnikov, D., Allain, A., Huang, Y.-S., Dumcenco, D. & Kis, A. Electrical Transport Properties of Single-Layer WS 2. *ACS Nano* **8,** 8174–8181 (2014).

237. Kang, J.-H. *et al.* MBE growth of self-assisted InAs nanowires on graphene. *Semicond. Sci. Technol.* **31,** 115005 (2016).

238. Fiori, S. *et al.* Li-intercalated Graphene on SiC(0001): an STM study. *Phys. Rev. B* **96,** 1–8 (2017).

239. Nagashio, K., Nishimura, T. & Kita, K. Density-of-States Limited Contact Resistance in Graphene Field-Effect Transistors. *Jpn. J. Appl. Phys.* **50,** (2011).

240. Giubileo, F. *et al.* Contact Resistance and Channel Conductance of Graphene Field-Effect Transistors under Low-Energy Electron Irradiation. *Nanomaterials* **6,** 206 (2016).

241. Konstantatos, G. *et al.* Ultrasensitive solution-cast quantum dot photodetectors. *Nature* **442,** 180–183 (2006).

242. Robin, A. *et al.* Engineering the Charge Transfer in all 2D Graphene-Nanoplatelets Heterostructure Photodetectors. *Sci. Rep.* **6,** 24909 (2016).

243. Xia, F., Mueller, T., Lin, Y., Valdes-Garcia, A. & Avouris, P. Ultrafast graphene photodetector. *Nat. Nanotechnol.* **4,** 839–843 (2009).

244. Dalibor, T. *et al.* Deep Defect Centers in Silicon Carbide Monitored with Deep Level Transient Spectroscopy. *Phys. Status Solidi* **162,** 199–225 (1997).

245. Son, N. T. *et al.* Negative-U system of carbon vacancy in 4H-SiC. *Phys. Rev. Lett.* **109,** 23–27 (2012).

246. Kawahara, K. *et al.* Investigation on origin of Z1/2 center in SiC by deep level transient spectroscopy and electron paramagnetic resonance. *Appl. Phys. Lett.* **102,** (2013).

247. Kawahara, K. *et al.* Quantitative comparison between Z1 / 2 center and carbon vacancy in 4H-SiC Quantitative comparison between Z 1 = 2 center and carbon vacancy in 4H-SiC. *J. Appl. Phys.* **115,** 2–8 (2014).

248. Kalabukhova, E. N. *et al.* Trapping Recombination Process and Persistent Photoconductivity in Semi-Insulating 4H SiC. *Mater. Sci. Forum* **527–529,** 563–566 (2006).

249. Kalabukhova, E. N., Lukin, S. N., Savchenko, D. V., Mitchel, W. C. & Mitchell, W. D. Photo-EPR and Hall Measurements on Undoped High Purity Semi-Insulating 4H-SiC Substrates. *Mater. Sci. Forum* **457–460,** 501–504 (2004).

250. Zeng, H., Dai, J., Yao, W., Xiao, D. & Cui, X. Valley polarization in MoS2 monolayers by optical pumping. *Nat. Nanotechnol.* **7,** 490–493 (2012).

251. Bianco, F. *et al.* Terahertz detection by epitaxial-graphene field-effect-transistors on silicon carbide. *Tredicucci Cit. Appl. Phys. Lett.* **107,** (2015).

252. Cong, C. *et al.* Synthesis and Optical Properties of Large-Area

Single-Crystalline 2D Semiconductor WS 2 Monolayer from Chemical Vapor Deposition. *Adv. Opt. Mater.* **2,** 131–136 (2014).

253. Li, H. *et al.* From Bulk to Monolayer MoS2: Evolution of Raman Scattering. *Adv. Funct. Mater.* **22,** 1385–1390 (2012).

254. Peimyoo, N. *et al.* Thermal conductivity determination of suspended mono- and bilayer WS2 by Raman spectroscopy. *Nano Res.* **8,** 1210–1221 (2015).

255. Gao, Y. *et al.* Large-area synthesis of high-quality and uniform monolayer WS2 on reusable Au foils. *Nat. Commun.* **6,** 8569 (2015).

256. Berkelbach, T. C., Hybertsen, M. S. & Reichman, D. R. Theory of neutral and charged excitons in monolayer transition metal dichalcogenides. *Phys. Rev. B* **8820,** (2013).

257. Kasry, A. *et al.* Highly Efficient Fluorescence Quenching with Graphene. *J. Phys. Chem. C* **116,** 2858–2862 (2012).

258. Cummings, A. W., Garcia, J. H., Fabian, J. & Roche, S. Giant Spin Lifetime Anisotropy in Graphene Induced by Proximity Effects. *Phys. Rev. Lett.* **119,** 206601 (2017).

259. Maassen, T. *et al.* Localized States Influence Spin Transport in Epitaxial Graphene. *Phys. Rev. Lett.* **110,** 67209 (2013).

260. Speck, F. *et al.* The quasi-free-standing nature of graphene on H-saturated SiC(0001). *Appl. Phys. Lett.* **99,** 122106 (2011).

261. Robinson, J. A. *et al.* Epitaxial graphene transistors: Enhancing performance via hydrogen intercalation. *Nano Lett.* **11,** 3875–3880 (2011).

262. Winzer, T., Knorr, A. & Malic, E. Carrier multiplication in graphene. *Nano Lett.* **10,** 4839–4843 (2010).

263. Gierz, I. Probing carrier dynamics in photo-excited graphene with time-resolved ARPES. *J. Electron Spectros. Relat. Phenomena* **219,** 53–56 (2017).

Acknowledgements

The Ph.D. training has been a challenging experience that gave me the chance to learn, travel and accomplish many interesting results.

Nevertheless, none of this could have been possible without the extreme support, patience, help and inspiration of my supervisor. Therefore, I want to thank Dr. Camilla Coletti for having walked with me during these three and a half years.

I desire to also thank the people who daily worked with me. Friends more than colleagues, who were by my side for all or part of my training. I want to thank them for the precious life moments more than the working hours we shared together. Thanks to Domenica (Nica), Vaidas and Neeraj, the first people I met during the first steps through lab life. A special thank goes to Holger and Stiven, to me the mentors without whom I could have never accomplished what I did. Finally, I want to acknowledge Filippo, Ylea, who joined our group during the final months of my Ph.D., Giulia and Sara, who gave me the opportunity to test myself as a mentor (even if for a short time).

At NEST I found a group of people who were to me much more precious than what I could show them. Together they contributed to make this place like home, even during the rainy weekends. Therefore, I want to thank: Domenico, Melissa, Filippo, Tommaso, Cecilia, Ambra, Paola, Paolo, Dave, Lale, Ilir, Luca, Federica, Sergio, Gina, Matteo, Marco, Figaro, Mirko, Valeria, Eleonora, Sara, Federico, Francesca, Bazza, Paola, Antonio, Antonella, Rosy, Fulvio, Luca, Olga, Frank, Pasquale, Alessandro, Stefano, Francesco, Giuliano, Mauro, Giovanni, Valerio, Leonardo, Andrea, Kimberly, Simone, Katia, Abhishek, Valentina and the whole NEST community. Special thanks go to Marianna for designing and drawing the

cover of this book. I also want to acknowledge Silvia and her infinite patience for the support and for sharing valuable moments of daily life.

I want to thank Prof. van Wees, Alexey, Jorge, Christian, Pep, Martjeen, Carmem, Julian, Jantje, Xu and all the people from Groningen for giving me the opportunity to expand my research activity and for making my abroad experience remarkably delightful.

Finally, I need to spend few words about Carmine, whose absence today is louder than ever. He infected me with the passion for research showing the immense joy of harvesting results coming from hard work.

Un doveroso ringraziamento va ai miei genitori senza i quali non avrei nemmeno iniziato il percorso che mi ha portato fino a questo punto, ai quali consegno il frutto della mia ultima fatica. Ringrazio mia sorella, fonte di ispirazione continua, per i numerosi momenti condivisi a distanza e quelli meno numerosi ma più preziosi, condivisi dal vivo. Ringrazio inoltre tutta la mia famiglia, nonni, zii e cugini per avermi accompagnato lungo questo lunghissimo percorso.

Ringrazio Simone per avermi ospitato questi anni e aver condiviso con me l'ebbrezza della vita quotidiana.

Ringrazio inoltre tutti gli amici di Pisa e Latina il cui elenco sarebbe davvero interminabile, come la stima e l'affetto che mi lega ad ognuno di loro.

Finalmente quiero agradecer a mi novia, Cristina. Tú has sido el regalo más precioso que esta experiencia me dio. Gracias por estar a mi lado y en el mi futuro.